Very high energy gamma-ray observations of a few Fermi detected blazars using TACTIC telescope

By

Krishna Kumar Singh

PHYS01201004006

Bhabha Atomic Research Centre, Trombay, Mumbai,

A thesis submitted to the

Board of Studies in Physical Sciences

In partial fulfillment of requirements

For the Degree of

DOCTOR OF PHILOSOPHY

of

HOMI BHABHA NATIONAL INSTITUTE

2015

Homi Bhabha National Institute
Recommendations of the Viva Voce Board

As members of Viva Voce Board, we certify that we have read the dissertation prepared by "**Krishna Kumar Singh**" entitled "**Very high energy gamma-ray observations of a few Fermi detected blazars using TACTIC telescope**" and recommend that it may be accepted as fulfilling the dissertation requirement for the Degree of Doctor of Philosophy.

Chairman- Dr V. M. Datar
Tata Institute of Fundamental Research
Homi Bhabha Road, Mumbai - 400005, Maharashtra, India

Datar

________________________ **Date:** 4-6-2015

Guide- Dr A. K. Tickoo
Bhabha Atomic Research Centre
Trombay, Mumbai, Maharashtra - 400085, India

Ontickoo ________________________ **Date:** 27-05-2015

Member- Dr B. S. Acharya
Tata Institute of Fundamental Research
Homi Bhabha Road, Mumbai - 400005, Maharashtra, India

BSAcharya 29/5/2015

________________________ **Date:**

Member- Dr R. C. Rannot
Bhabha Atomic Research Centre
Trombay, Mumbai - 400085, Maharashtra, India

________________________ **Date:** 28/5/2015

Invitee- Sh R. Koul
Bhabha Atomic Research Centre
Trombay, Mumbai - 400085, Maharashtra, India

________________________ **Date:** 28.05.2015

Final approval and acceptance of this dissertation is contingent upon the candidate's submission of the final copies of the dissertation to HBNI.
I hereby certify that I have read this dissertation prepared under my direction and recommend that it may be accepted as fulfilling the dissertation requirement.

Guide- Ontickoo (AK TICKOO)

Date: 27-05-2015 **Place:** Mumbai

STATEMENT BY AUTHOR

This dissertation has been submitted in partial fulfillment of requirements for an advanced degree at Homi Bhabha National Institute (HBNI) and is deposited in the Library to be made available to borrowers under rules of the HBNI.

Brief quotations from this dissertation are allowable without special permission, provided that accurate acknowledgement of source is made. Requests for permission for extended quotation from or reproduction of this manuscript in whole or in part may be granted by the Competent Authority of HBNI when in his or her judgment the proposed use of the material is in the interests of scholarship. In all other instances, however, permission must be obtained from the author.

Krishna Kumar Singh

DECLARATION

I, *Krishna Kumar Singh*, hereby declare that the investigation presented in the thesis has been carried out by me. The work is original and has not been submitted earlier as a whole or part for a degree/diploma at this or any other Institution/University.

Krishna Kumar Singh

I dedicate this thesis to my beloved father

.... Late Shri Rajendra P. Singh

ACKNOWLEDGEMENTS

While it is impossible to mention the name of every individual who has contributed in one way or the other to my thesis work, there is always the risk of having inadvertently forgotten somebody. My apologies, in advance, for such a lapse. To begin with, I would like to express my heartiest gratitude to my thesis advisor and doctoral committee convener Dr. A. K. Tickoo for his continuous support, guidance and encouragement throughout the course of this research work. I am extremely indebted to Sh. R. Koul, Head, Astrophysical Sciences Division, Bhabha Atomic Research Centre, Mumbai, for providing me enormous learning opportunities and for motivating me to pursue my PhD. He has been a constant source of inspiration to me ever since I joined this division. I am deeply grateful to my doctoral committee members, Prof. V. M. Datar, Prof. B. S. Acharya and Prof. R. C. Rannot for providing their valuable suggestions and encouragement during my thesis work, despite their busy schedules. Their suggestions have helped me to significantly improve the quality of the work presented in the thesis.

I sincerely thank Dr. R. C. Rannot and Dr. K. K. Yadav for their guidance concerning the *TACTIC* data analysis and other useful suggestions related to the work presented in the thesis. I also thank my colleagues from GOALS, Mt. Abu, Sh. P. Chandra, Sh. H. C. Goyal, Sh. M. Kothari, Smt. A. Goyal, Sh. N. Kumar, Sh. K. K. Gour, Sh. P. Marandi, Sh. N. K. Agarwal and other technical staff for participating in the observations with *TACTIC*. I am thankful to my other colleagues Sh. S. R. Kaul, Sh. M. K. Koul, Dr. V. K. Dhar, Sh. M. Sharma, Sh. K. Venugopal, Sh. K. Chanchalani, Sh. C. Borwankar, Dr. N. Mankuzhiyil, Dr. S. Godambe and Sh. B. Ghosal for their support and creating a healthy and positive environment in the division.

I am deeply grateful to my senior colleagues Sh. N. Bhatt and Dr. S. Bhattacharyya for spending their valuable time in crucial discussions with me and for stimulating my thinking at every stage of my research work. I also thank Dr. S. Sahayanathan for numerous fruitful discussions regarding the blazar emission models and for sharing his emission code for spectral energy distribution modelling. Special thanks to Dr. H. Bhatt for useful discussions regarding X-ray and optical data used in my thesis work. I also wish to thank my senior colleagues Dr. A. K. Mitra, Dr. C. K. Bhat, Dr. A. Razdan and Dr. D. K. Koul for their encouragement and motivation. I am grateful to my colleague and dearest friend Sh. Sandeep Godiyal for being there with me always in moments of joy and distress. Thanks are also due to Sh. D. K. Nehru, Sh. N. Venkataraman, Sh. R. C. Raina, Sh. Ravi, Sh. Madan Lal and Sh. P. M. Jadhav for their support and cooperation.

Finally, I take this opportunity to express my heartiest gratitude to all my family members and especially to my eldest brother Sh. A. K. Singh for his support and encouragement. Without their love and prayers, it would have been impossible for me to have achieved anything in my life.

List of Publications

Publications in Refereed Journal : 8

1. **Search for TeV γ–ray emission from blazar 1ES 1218+304 with TACTIC telescope during March-April 2013**
   K K Singh, K K Yadav, A K Tickoo, R C Rannot, P Chandra, N K Agarwal, K K Gaur, A Goyal, H C Goyal, N Kumar, P Marandi, M Kothari, H Bhatt, K Chanchalani, N Chouhan, V K Dhar, B Ghosal, S R Kaul, M K Koul, R Koul, K Venugopal, C K Bhat, C Borwankar, J Bhagwan, A C Gupta
   New Astronomy 36 (2015) 1-8

2. **Multi-wavelength study of Mrk 421 TeV flare observed with $TACTIC$ telescope in February 2010**
   K K Singh, K K Yadav, P Chandra, S Sahaynathan, N Bhatt, R C Rannot, A K Tickoo, R Koul
   Astroparticle Physics 61 (2015) 32-40

3. **Intrinsic VHE gamma-ray spectra of blazars as a probe for extragalactic background light**
   K K Singh, S Sahaynathan, A K Tickoo, N Bhatt
   New Astronomy 27 (2014) 34-40

4. **XMM-Newton view of radio loud narrow line Seyfert1 galaxy PMN J0948+0022**
   S Bhattacharyya, H Bhatt, N Bhatt, **K K Singh**
   MNRAS 440 (2014) 106-118

5. **Long term performance evaluation of the TACTIC imaging telescope using $\sim$ 400 h Crab Nebula observation during 2003-2010**
   A K Tickoo, R Koul, R C Rannot, K K Yadav, P Chandra, V K Dhar, M K Koul, M Kothari, N K Agarwal, A Goyal, H C Goyal, S Kotwal, N Kumar, P Marandi, K Venugopal, K Chanchalani, N Bhatt, S Bhattacharyya, C Borwankar, N Chouhan, S R Kaul, A K Mitra, S Sahaynathan, M Sharma, **K K Singh**, C K Bhat
   Pramana Journal of Physics 82 (2014) 585-605

6. **Study of X-ray and γ-ray flare from Mkn-421 during February 2010 using Swift and Fermi observations**
   K K Singh, S Bhattacharyya, N Bhatt, A K Tickoo
   New Astronomy 17 (2012) 679-686

7. **TeV gamma-ray observations of Markarian 421 using TACTIC during 2009-10**
   P Chandra, R C Rannot, K K Yadav, A K Tickoo, **K K Singh**, K Chanchalani, M Kothari, N K Agarwal, A Goyal, H C Goyal, S Kotwal, N Kumar, P Marandi, K Venugopal, C K Bhat, N Bhatt, S Bhattacharyya, C Borwankar, N Chouhan, V K Dhar, S R Kaul, S K Koul, M K Koul, R Koul, A K Mitra, S Sahaynathan, and M Sharma
   J. Phys.G: Nucl. Part. Phys. 39 (2012) 045201

8. **TeV observations of Mrk 421 with the TACTIC γ-ray telescope during 2006-8**
   P Chandra, K K Yadav, R C Rannot, **K K Singh**, A K Tickoo, M Sharma, K Venugopal, C K Bhat, N Bhatt, S Bhattacharyya, K Chanchalani, V K Dhar, S V Godambe, H C Goyal, M Kothari, S Kotwal, M K Koul, R Koul and S Sahaynathan
   J. Phys.G: Nucl. Part. Phys. 37 (2010) 125201

Publications in Symposium/Conferences : 11

1. **Study of TeV γ–ray emission from Mrk 501 observed with TACTIC telescope during 2011-13**
   K K Singh, K K Yadav, P Chandra, A K Tickoo, R C Rannot, A Goyal, H C Goyal, N Kumar, P Marandi, M Kothari, N K Agarwal, N Chouhan, V K Dhar, B Ghosal, S R Kaul, M K Koul, R Koul, C K Bhat, C Borwankar, K Venugopal, K Chanchalani
   Presented at ***"32nd Astronomical Society of India Meeting (ASI-2014)", Mohali, India, (2014)***

2. **Blazars help in constraining Extragalactic Background Light**
   K K Singh, S Sahayanathan, A K Tickoo, N Bhatt,
   Presented at ***"National Symposium on Gamma-Ray Astronomy (NSGRA-2013)", BARC Mumbai, India, (2013)***

3. **Understanding the spectral break in GeV-TeV spectra of some selected blazars using *Fermi*-LAT and TeV observations**
   K K Singh, S Bhattacharyya, N Bhatt, A K Tickoo
   Presented at ***"31st Astronomical Society of India Meeting (ASI-2013)", Trivandrum, India, (2013)***

4. **Sensitivity improvement of the TACTIC gamma-ray telescope**
   A K Tickoo, S R Kaul, K Venugopal, N K Agarwal, H C Goyal, P Chandra, N Chouhan, V K Dhar, K K Yadav, R C Rannot, **K K Singh**, N Kumar, P Marandi, K Chanchalani, K K Gaur, M Kothari, A Goyal, A K Mitra, B S Sahayanathan, M Sharma, C K Bhat, N Bhatt, S Bhattacharyya, C Borwankar, M K Koul
   Presented at ***"TeVPA-2012", TIFR Mumbai, India, (2012)***

5. **Transparency of the Universe to VHE gamma-rays and EBL models**
   K K Singh, S Sahayanathan, A K Tickoo and N Bhatt
   Presented at ***"39th COSPAR Scientific Assembly (COSPAR-2012)", Mysore, India, (2012)***

6. **Constraints on the Extragalactic Background Light using Fermi-LAT and TeV observations of blazars**
   K K Singh, A K Tickoo, N Bhatt
   Presented at ***"Symposium on High Energy Astrophysics (HEAP12)", HRI Allahabad, India, (2012)***

7. **Compatibility of various EBL models with recent ground based sub-TeV observations of extragalactic sources**
K K Singh and A K Tickoo
Presented at ***"29th Astronomical Society of India Meeting (ASI-2011)", Raipur, India, (2011)***

8. **Analysis of Fermi-LAT data on Mrk 421 during its high state in February 2010**
K K Singh, A K Tickoo and N Bhatt
Presented at ***"29th Astronomical Society of India Meeting (ASI-2011)", Raipur, India, (2011)***

9. **Extragalactic gamma-ray absorption and the intrinsic spectra of distant TeV- selected AGNs**
K K Singh, A K Tickoo and N Bhatt
Presented at ***"16th National Space Science Symposium (NSSS-2010)", Rajkot, India, (2010)***

10. **Feasibility of operating TACTIC telescope during partial moonlit conditions**
K K Singh, A K Tickoo, K K Yadav, R C Rannot, V K Dhar and R Koul
Presented at ***"16th National Space Science Symposium (NSSS-2010)", Rajkot, India, (2010)***

11. **Methodology for selecting Fermi detected blazars for VHE observations with TACTIC telescope**
A K Tickoo, **K K Singh** and N Bhatt
Presented at ***"16th National Space Science Symposium (NSSS-2010)", Rajkot, India, (2010)***

Homi Bhabha National Institute

SYNOPSIS OF Ph. D. THESIS

1. **Name:** Krishna Kumar Singh
2. **Name of the Constituent Institution:** Bhabha Atomic Research Centre, Mumbai
3. **Enrollment No.:** PHYS01201004006
4. **Title of the Thesis:** Very high energy gamma-ray observations of a few Fermi detected blazars using TACTIC telescope
5. **Board of Studies:** Physical Sciences

SYNOPSIS

Very High Energy (VHE) gamma-ray astronomy (also referred to as TeV gamma-ray astronomy) is concerned with the observational and theoretical studies of astrophysical sources in the energy range above 100 GeV [1,2]. It provides information that is not only complementary to what is being provided by the more conventional astronomies (Radio, Optical and X-ray), but is also unique in the sense that it gives insight as to how γ–rays of very high energies are produced in exotic astrophysical settings: viz, Pulsars, Supernova remnants and Active Galactic Nuclei. VHE γ–rays are thus unique probes of the high energy phenomenon in the Universe and can place stringent limits on the underlying particle acceleration mechanisms which produce these γ–rays.

VHE γ–rays are the highest energy photons in the electromagnetic spectrum and their detection presents unique challenges. At energies above 100 GeV, a typical γ–ray source is generally too weak for detection using satellite based detectors and thus ground based atmospheric Cherenkov detection technique is used. The telescope gets triggered when Cherenkov photons produced in a γ/hadron induced extensive air shower arrive at its focal plane. The idea of the imaging Cherenkov telescope proposed in late 1970s by the Whipple group [3], allows removal of more than 99.5% cosmic-ray background events. In this technique, one records the spatial distribution of Cherenkov photons in the focal plane of the telescope by using a close-packed array of photomultiplier tubes. Gamma-ray events give rise to shower images which apart from being narrow and compact in shape have their major axes preferentially oriented towards the source position in the image plane [4]. In comparision, Cherenkov light produced by cosmic-rays gives rise to images that are, on an average, broader and randomly oriented within the field of view of the camera.

As an important part of the on-going global effort to observe VHE γ–ray emission from celestial sources, scientists from Astrophysical Sciences Division, Bhabha Atomic Research Centre, Mumbai, India, have been actively engaged in the observation and collection of useful data on potential γ–ray sources with the *TACTIC* (TeV Atmospheric Cherenkov Telescope with Imaging Camera) gamma–ray telescope [5,6]. The telescope is operational at Mt. Abu (24.6° N, 72.7° E, 1300 m asl), Rajsthan for the last 12 years. *TACTIC* is equipped with a light collector of $\sim$ 9.5 m^2 area and an imaging camera of 349 pixels. With a 5σ sensitivity in 25 hours for detecting the steady γ–ray signal from the Crab Nebula above 1 TeV energy threshold, the telescope has detected TeV γ–ray emission from Mrk 421, and Mrk 501 on several occasions during their strong flaring activity. A major upgrade of the telescope, involving replacement of signal & high voltage cables and installation of new compound parabolic concentrators was taken up during November-December 2011. The upgrade has resulted in lowering the threshold energy of the telescope and improving its sensitivity. At present telescope has a 5σ sensitivity of detecting the Crab nebula in $\sim$ 15 hours of observation time. With enhanced sensitivity, the upgraded *TACTIC* provides opportunity to detect VHE γ–ray emission from blazars in flaring state as well as long term moitoring of blazars in quiscent state over the energy range 0.8–15 TeV. With the *Fermi*, *Swift* and other satellite observatories simultaneously in orbit, complemented by the ground based observatories, it has now become possible to collect high quality data in order to build simultaneous and well sampled spectral energy distribution (SED) of a large sample of blazars.

The research presented in the thesis involves results of VHE γ–ray observations of two blazars Mrk 421 and 1ES 1218+304 using *TACTIC* along with multi-wavelength observations with *Fermi*-Large Area Telescope (LAT) and other instruments in X–ray, optical and radio energy bands. The thesis will also cover analysis of the data recorded on Crab Nebula to validate the proper functioning of *TACTIC* after its upgrade. The observational results of Mrk 421 and 1ES 1218+304 are discussed in the context of multi-wavelength emission from blazars and are used to understand the emission model involving synchrotron and synchrotron self Compton (SSC) processes. The thesis also discusses the applications of VHE observations of distant blazars for probing the extragalactic background light (EBL). The VHE γ–ray absorption (caused by interaction of TeV photons with low energy UV/Optical/IR photons from EBL via pair production) distorts the intrinsic VHE spectra of sources at cosmological distances and hence carries an imprint of EBL. The main scientific results of the thesis are reported in Chapter 4, 5, & 6, which have resulted in several publications in referred journals.

Blazars are a small subclass of active galactic nuclei characterized by distinct and extreme observational properties, such as rapid variability with large amplitude and strong emission over the entire electromagnetic spectrum. The SEDs of blazars are dominated by non-thermal emission and consist of two distinct, broad components. Blazars often show flux variability from radio to VHE γ–rays at different time scales which may or may not be correlated. Therefore, simultaneous multi-wavelength observations are important to understand the underlying physics of blazars.

Mrk 421 is the first extragalactic source detected in the TeV energy range using ground based imaging atmospheric Cherenkov telescope [7]. It is the closest (redshift z=0.031) known and best studied TeV γ–ray emitting blazar. Since its detection, the source has been a frequent target for all existing ground based imaging atmospheric Cherenkov telescopes and other multi-wavelength campaigns. Flux variations on different time scales from minutes to years have turned this source into a unique laboratory for understanding the particle acceleration mechanisms which produce γ–rays. Mrk 421 is also a very bright source in MeV-GeV energy range and the spectrum measured by *Fermi*-LAT is described by a simple power law of spectral index 1.78$\pm$0.04. The work presented in the thesis uses TeV observations with *TACTIC* together with other multi-wavelength data on Mrk 421, to study the variability and spectral properties of the source during its high state of activity observed in February 2010 [8]. The enhanced activity of the source was also observed in high energy γ–rays and X-ray with *Fermi* and *Swift* satellites respectively [9]. Apart from discussing the results from the *TACTIC*, *Fermi*-LAT and *Swift*-XRT (X-Ray Telescope) observations during February 10-23, 2010, the thesis will also cover analysis of the simultaneous archival data from *Swift*-BAT (Burst Alert Telescope), *MAXI* (Monitor of All sky X-ray Image), optical V-band and radio observations at 15 GHz.

1ES 1218+304 is a high-synchrotron peaked blazar at redshift z=0.182. The source was discovered as a candidate BL Lac object on the basis of its X-ray emission and was also predicted to be a possible TeV candidate blazar from the position of the synchrotron peak in its spectral energy distribution. The VHE γ–ray emission from 1ES 1218+304 was first detected by the *MAGIC* telescope in 2005 [10]. The *Fermi*-LAT spectrum of the source is described by a power law with spectral index 1.71$\pm$0.07, making it one of the hardest spectrum source in MeV-GeV range. The blazar 1ES 1218+304 has been monitored with the *TACTIC* from March 1, 2013 to April 15, 2013 for a total observation time of $\sim$ 40 hours and no evidence of TeV γ–ray activity is found from the source [11]. For the study of multi-wavelength emission from the source, we use near simultaneous Optical, UV, and X-ray data collected from the UVOT and XRT instruments onboard the *Swift* satellite. The analysis results of the high energy γ–ray data collected by *Fermi*-LAT are also reported in the thesis.

The contents of the thesis are organized as follows. In Chapter 1, we provide an introduction to the field of VHE γ–ray astronomy. Main processes responsible for production of γ–rays and their detection using different observational techniques will be discussed in this Chapter. Chapter 2 will cover general properties and morphology of active galactic nuclei and blazars in particular. This Chapter will also include description of *Fermi*-LAT with its results and observational programs on blazars. In Chapter 3, we discuss the physics of the extensive air shower and present details of atmospheric Cherenkov radiation produced by the secondaries in the air shower. A description of the *TACTIC* γ–ray telescope will also be presented in this Chapter. Chapter 4 will focus on the observational results of Mrk 421 which was observed in a high state during February 2010 with *TACTIC* [8, 9]. In Chapter 5, we present results of TeV γ–ray observations of another blazar 1ES 1218+304 with the *TACTIC* [11]. The analysis and interpretation of multi-wavelength data in the UV, optical, X-ray and high energy γ–ray bands will also be discussed in this Chapter. Chapter 6 deals with the application of blazar observations as a probe for extragalactic background light [12]. Finally in Chapter 7, we present the main conclusions of the thesis. Apart from giving future scientific and experimental prospects in the field, we also discuss the potential of future ground based telescopes in this Chapter.

References

1. J. Holder, 2012, Astropart. Phys., 61, 39-40

2. F. Aharonian et al., 2008, Rep. Prog. Phys., 71, 096901

3. T. C. Weekes et al., 1989, ApJ, 342, 379

4. A. M. Hillas, 1985, ICRC, 3, 445

5. R. Koul et al., 2007, NIM A, 578, 548

6. A. K. Tickoo et al., 2014, Pramana-Journal of Phys., 82, 585

7. M. Punch et al., 1992, Nature, 358, 477

8. K. K. Singh et al., 2015, Astropart. Phys., 61, 32-40

9. K. K. Singh et al., 2012, New Astron., 17, 679-686

10. J. Albert et al., 2006, ApJ, 642, L119

11. K. K. Singh et al., 2015, New Astron., 36, 1-8

12. K. K. Singh et al., 2014, New Astron., 27, 34-40

Publications in Referred Journal :

a. Published 8

b. Accepted X

c. Communicated X

d. Other Publications X

Signature of Student :

Date: 24.04.2015

Doctoral Committee:

S. No.	Name	Designation	Signature	Date
1.	Prof. V M Datar	Chairman		24-04-15
2.	Prof. A K Tickoo	Guide/Convener		24-04-15
3.	Prof. B S Acharya	Member		
4.	Prof. R C Rannot	Member		24/04/15
5.	Sh. R Koul	Invitee		24.04.2015

Contents

List of Figures

List of Tables

Chapter 1

Introduction to VHE Astrophysics

1.1 Developments in Astroparticle Physics

The fields of cosmology, astrophysics and particle physics are collectively referred to as *Astroparticle Physics*. Astrophysics and cosmology are concerned with the structure and evolution of the Universe including the study of the behaviour of matter and radiation on large scales up to 10^{26} m. The most active topics in *Astroparticle Physics* include: origin of cosmic rays, contents and history of the Universe, mass and nature of elusive neutrinos, matter–antimatter asymmetry, star burning and supernova explosion, and nature of gravity. *Astroparticle Physics* has entered an exciting period with the recent development of experimental techniques that have opened new windows of observation and detection of cosmic radiation in all its components: cosmic rays & photons. Among the results and developments in *Astroparticle Physics* are the latest developments in the measurements of the cosmic ray composition and spectra, the results on atmospheric neutrinos and the latest developments in gravitational wave detection. Experimental observations with telescopes on the Earth and on satellites, covering the visible, infrared (IR), and ultraviolet (UV) regions of the electromagnetic spectrum as well as with detectors of radio waves, X–rays, γ–rays and neutrinos have revealed an astonishing range of extraterrestrial phenomena from the most distant regions of the Universe. Galileo in 1609 first looked at the sky using his telescope and this event is regarded as the foundation of modern astronomy. Second revolution occured in the 20th century when the development of new instruments enabled astrophysicists to expand their field of investigation from visible light to the whole electromagnetic spectrum including other messengers from the Universe. After the first pioneering studies, cosmic ray observations gave birth to subnuclear physics in the first half of the 20th century. Cosmic ray physics reflourished in the second half of the century with the advent of space-borne instruments. *Gamma-Ray Astronomy* is the most recent addition to the field of *Astroparticle Physics* in the 20th century and is historically closely connected to the search for origin of cosmic rays. This thesis is devoted to *Gamma-Ray Astronomy* at high energies.

1.2 Cosmic Rays

Cosmic rays (CRs) are defined as charged particles that reach the Earth from interstellar space. They are an essential part of the Universe, but their origin has remained an unresolved problem for a long time. This problem consists of identification of astrophysical sources contributing to observed CR spectrum and understanding the physical processes responsible for their production. The origin of CRs is interrelated with the main processes and dynamics of star formation, stellar evolution, supernova explosions and to the state and conditions of the interstellar matter in the galaxy. The field of cosmic ray research started around the year 1900 after the observation of discharge in electroscopes even if they were kept in the dark well away from sources of natural radioactivity. The origin of ionisation in electroscopes was a major puzzle and various igenious experiments were carried out to discover this ionising radiation. The big breakthrough occurred when Victor Hess in Austria (1912) and Kohlhorster in Germany (1913) decided to measure the ionisation of the atmosphere with increasing altitude using balloons. By late 1912, Hess flew in a balloon to altitudes of 5 km and discovered that ionization of the air strongly increases with altitude [1.1]. The only explanation of this measurement by Hess was that "a radiation of very high penetrating power enters the atmosphere from above". This marked the discovery of CRs for which Hess received the Noble prize in 1936. Kohlhorster contributed a lot to these first measurements with his flights that reached altitude of 9 km. On the other hand, Domenico Pacini performed a series of measurements using an electroscope in a box lowered into the sea. Pacini realized that the ionization intensity decreased with the depth and concluded that the ionizing radiation had no terrestial origin, but a cosmic origin [1.2]. After this discovery the altitude dependence of the ionization became the topic of many measurements at different locations and altitudes. In 1925, Millikan first used the term "cosmic rays" to describe the radiation and thus created the current name of the field. After 20 years since their discovery, Compton proved that CRs are made predominantly from charged particles, through the dependency of CR fluxes on the geomagnetic latitude [1.3].

1.2.1 Types

Cosmic rays are usually distinguished as *Primary* and *Secondary*. Primary cosmic rays are those particles produced directly in astrophysical sources, while secondary cosmic ray particles are produced by interaction of primaries with interstellar gas or atmospheric nuclei. The total flux of primary cosmic rays that hit the Earth's atmosphere is about 10^3 m^{-2} s^{-1} sr^{-1}. The cosmic rays detected so far over wide energy range are classified in four categories: *Solar cosmic rays* (coming from the Sun), *Galactic cosmic rays* (coming from astrophysical objects within our own galaxy Milky Way), *Extragalactic cosmic rays* (coming from outside our galaxy), and *Anomalous cosmic rays* (coming from the edge of our solar system).

1.2.2 Composition

Cosmic rays consist of high energy particles incident on Earth from outer space and the secondary particles they produce during their propagation in space. The chemical composition of CRs is interesting as it may provide clues for understanding their origin and process of propagation from their source to the Earth. The composition of CRs obtained from mass spectrometers on board satellites and balloons is divided into two components namely *Charge* and *Neutral*. The charged components of CRs consist of protons (85.26%), α-particles (11.76%), nuclei of heavier elements up to uranium (0.98%) and electrons (2%). While these come from primary sources, there are also very small proportions of positrons and antiprotons, which are believed to be of secondary origin. The neutral components consist of γ–rays (0.01%), neutrinos and antineutrinos [1.4]. Some of these can be identified as coming from "point" sources in the sky. The chemical composition of CRs exhibits certain differences and similarities to the solar system abundance. The solar system abunadances are derived from the spectral features in the photosphere of the Sun and from the studies of meteorites, which are believed to have the same composition.

1.2.3 Energy Spectrum

The most striking feature of CRs is the fact that their differential energy spectra extend over 13 orders of magnitude in energy and more than 30 orders of magnitude in observed flux. The energy spectra are not of Maxwellian form but can be well represented by power law energy distribution as shown in Figure 1.1. At energies less than 1 GeV nucleon^{-1}, the energy spectra of CRs show a pronounced attenuation relative to the power law observed at higher energies. In the region of the energy spectrum which is unaffected by the geomagnetic field and propagation of particles to the Earth through solar wind, the analytical expression for differential flux is given by

$$\frac{dN}{dE} \propto E^{-\Gamma} \tag{1.1}$$

where Γ is the spectral index. Qualitatively, the present experiments agree that the overall CR spectrum can be divided into the following four regions:

(i) E $<$ 10^9 eV (Γ=0). At 10^8 eV, flux is 1 particle cm^{-2} s^{-1}.

(ii) 10^9 eV $<$ E $<$ 3×10^{15} eV (Γ=2.7). At 3×10^{15} eV (*Knee*), flux is measured to be 1 particle m^{-2} year^{-1}.

(iii) 3×10^{15} eV $<$ E $<$ 4×10^{18} eV (Γ=3.0). At 4×10^{18} eV (*Ankle*), flux is 1 particle km^{-2} year^{-1}.

(iv) E $>$ 4×10^{18} eV (Γ=2.6). The flux in this Ultra High Energy (UHE) region is 1 particle km^{-2} century^{-1}.

The CR spectrum appears to be a unique power law with at least two changes in slope, at the "knee" and at the "ankle". The origin of the *knee* is still poorly

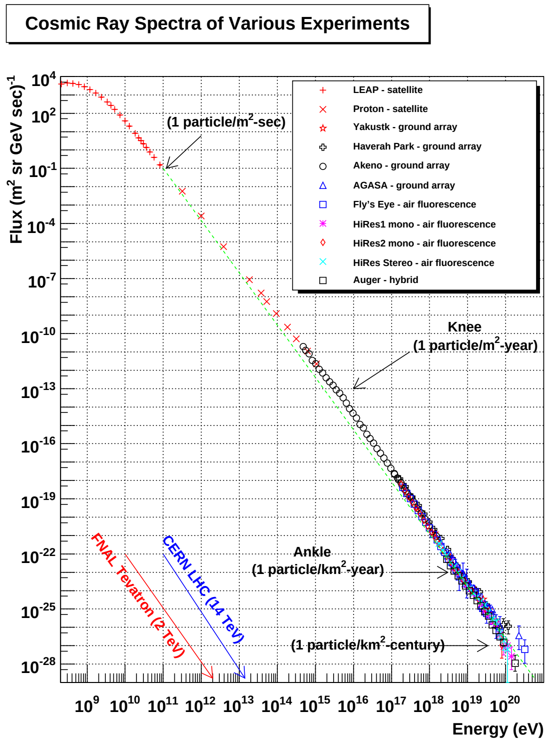

Figure 1.1: Energy spectrum of all cosmic ray nuclei measured with different experiments. (Credit: physics.utah.edu)

understood, it may result from a change in the propagation properties of CRs in the intergalactic medium. As regards the *ankle*, it is clear that UHE cosmic rays (UHECRs) have an extragalactic origin.

Shortly after the discovery of 2.7 °K cosmic microwave background radiation (CMBR), Greisen and Zatsepin & Kuzmin (GZK) predicted that the number of cosmic rays above certain energy threshold should be suppressed via photo–pion production during their propagation to the Earth [1.5,1.6]. The interaction of CR particles with CMBR photons is expressed as

$$\gamma_{CMBR} + p \rightarrow p + \pi^0 \quad or \quad n + \pi^+ \tag{1.2}$$

The energy threshold for the above process is about 10^{20} eV. Because of the mean free path associated with these processes, CRs with E $> 10^{20}$ eV and travelling over distances larger than 50 Mpc (1 Mpc = 3.26$\times$ 10^{19} km) should not be observed on the Earth. This is generally known as "GZK Effect". This is not a true cutoff, but a suppression of the UHECR flux owing to an energy dependent propagation time against energy losses by such interactions.

1.2.4 Origin

The problem of understanding the source and origin of the highest energy CRs still remains unsolved in high energy astrophysics. It is believed that CRs result from the electromagnetic acceleration of ions that originate either in the outer atmospheres of the stars or in interstellar space. Cosmic rays are stored either in the galaxy or in the solar system by magnetic fields. It is argued that there are three "origins" of cosmic rays: origin of the particles, origin of energy, and site of the acceleration. Observationally it is well established that the CRs are ordinary atomic nuclei accelerated to high energies which arive in the neighbourhood of Earth from outside the solar system, together with some electrons and secondary particles. Bulk of CRs observed at mildly relativistic energies upto the *knee* and probably as far as the *ankle* are thought to be of local galactic origin. Galactic CRs are likely to originate in supernova remnants. A transition from galactic to extragalactic should occur somewhere between 10^{15} eV and 10^{18} eV and there are good theoretical and observational reasons to think that at ultra high energies we are in fact observing an extragalactic component. The plausible energy source for the Galactic component is the explosion of supernova. The mechanical energy released per supernova is of the order of 10^{44} Joule and they occur at a rate of one every 30 years. Thus as long as an acceleration process exists which can convert about 10% of this energy into accelerated particles supernovae are a viable power source. The key point is that the energy has to be in a form that is capable of driving particle acceleration and this means that it must be either magnetic field energy (driving acceleration through magnetic reconnection) or kinetic energy (driving Fermi acceleration).

1.3 Gamma–rays as messenger of non-thermal Universe

Most of the CRs are charged particles and any source information contained in the directions of particles arriving at Earth is lost due to their deflection in the galactic magnetic field. It is natural to search for a neutral component which can provide direction information about sources and acceleration sites of cosmic rays. Gamma–rays are electromagnetic radiation of very short wavelength present in the neutral component of CR along with neutrinos and neutrons. Due to the relatively short life time of neutrons, only a small fraction of primary particles can be detected on Earth. The neutron flux observed by ground based detectors is dominated by secondary particles whose study provides only a limited insight of the distant Universe. By contrast, neutrinos are weakly interacting light particles of longer life time. Neutral components like γ–rays are ideal tools to study CR origin. To locate the site of particle acceleration the best suited neutral "messenger" particle is a high energy photon. These particles do not interact with the magnetic fields filling the galactic and intergalactic space while travelling through the Universe. Consequently, their trajectories are not deflected from their initial travel direction and particles preserve information on their origin, pointing back to their source. Thus γ–rays are of interest to astrophysicists because they can provide information about objects producing energetic charged particles, which are the progenitors of γ–rays. Sometimes, very extreme objects in the Universe reveal their most interesting features through the emission of γ–rays. The study of γ–ray emission provides information on fundamental astrophysical problems related to violent and non-thermal processes in the Universe. The γ–rays refer to photons in the energy range 10^6–10^{21} eV. Such a wide energy band implies a variety of emission mechanisms and consequently observation techniques. Gamma–rays are classified into the following energy bands [1.7].

Energy Range	**Definition**
1MeV–10MeV	Low or Nuclear γ–rays
10MeV–30MeV	Medium Energy γ–rays
30MeV–30GeV	High Energy (HE) γ–rays
30GeV–30TeV	Very High Energy (VHE) or TeV γ–rays
30TeV–100PeV	Ultra High Energy (UHE) γ–rays
100PeV–100EeV	Extremely High Energy (EHE) γ–rays

The unit of energy commonly used in astroparticle physics is *electron volt* (eV). This unit (eV) is used with the metric prefixes : kilo (keV: 10^3 eV), mega (MeV: 10^6 eV), gega (GeV: 10^9 eV), tera (TeV: 10^{12} eV), peta (PeV: 10^{15} eV), exa (EeV: 10^{18} eV) and zeta (ZeV: 10^{21} eV). It is interesting to note that the energy carried by a tennis ball moving at 100 km h^{-1} is $\sim 10^{20}$ eV.

1.4 Gamma–ray Production Mechanisms

Most of the cosmic radiation is emitted in thermal processes, which can be described in first approximation as a black-body radiation by Planck's formula with temperature extending upto $\sim 10^6$ °K. The hottest objects emit X–ray photons upto few keV energy. On the other hand, γ–ray photons in high energy regime are produced by non-thermal processes like nuclear decay, nuclear interactions and interactions in strong electromagnetic fields. The most important non-thermal processes responsible for γ–ray production [1.8] are briefly discussed below.

1.4.1 Bremsstrahlung

The radiation emitted in the encounter between the electron and the nuclei of matter through which it passes is called "braking radiation" or "Bremsstrahlung" in German. The physical reason for this radiation is simply the emission of electromagnetic radiation from the acceleration or deceleration of a charged particle. Bremsstrahlung is the radiation associated with the centripetal acceleration of electrons in the electrostatic fields created by the presence of ions and atomic nuclei. The process is identical to *free-free* emission in atomic physics in the sense that the radiation corresponds to transitions between unbound states in the field of the nucleus. The amplitude of Bremsstrahlung emitted by the particle is proportional to its acceleration and the emitted photon spectrum is described by a power law with spectral index same as the accelerated particles. Bremsstrahlung is classified in two types:

thermal and *relativistic*. *Thermal* Bremsstrahlung occurs when the particles are at uniform temperature and are described by Maxwell-Boltzmann distribution. This is the most important emission process in astrophysical environments such as intra-cluster medium (cold ionized plasma) and accretion disk of active galactic nuclei for X–ray emission [1.9,1.10]. *Relativistic* Bremsstrahlung occurs when electrons move with velocity comparable to the speed of light. This process is important when the UHECR electrons described by power law form interact with inter-stellar medium and produce γ–ray photons upto TeV energy. However, Bremsstrahlung is dominant only in dense astrophysical environments such as γ–Cygni supernova remnant [1.11].

1.4.2 Synchrotron Radiation

When a charged particle moves in a magnetic field, it undergoes an acceleration associated with Lorentz force that induces a rotation of the particle around the magnetic field. The particle follows a spiral trajectory at a constant pitch angle (angle between the velocity and the magnetic field lines). During this motion, the charged particle is accelerated towards the guiding center of its orbit and loses energy in the form of electromagnetic radiation. If the particle motion is non-relativistic, its motion is described by Larmor equations and the emitted radiation is referred to as *cyclotron* radiation. When the particle is relativistic, the emission is beamed in a cone along the direction of the motion and is known as *synchrotron* radiation [1.12]. For a relativistic electron with energy $E_e = \gamma m_e c^2$ in the magnetic field B, the gyration frequency is given by

$$\omega = \frac{eB}{\gamma m_e c} \tag{1.3}$$

where m_e is rest mass of electron, γ is its Lorentz factor and γ^{-1} gives the cone angle in which the radiation is beamed. The radiative power emitted by the relativistic electron moving with velocity v at pitch angle α is expressed as:

$$P_{syn} = \frac{2e^4}{3c^3}\frac{\gamma^2 B^2}{m_e^2 c^2} v^2 sin^2\alpha \tag{1.4}$$

Generally, the energy of synchrotron photons ($\propto \gamma^2$) is much less than the energy of parent electrons. If the relativistic electrons are not monoenergetic and are described by power law energy spectrum with index p, the emitted synchrotron photon spectrum will be a power law with spectral index $(p+1)/2$. Synchrotron radiation of acclerated electrons is one of the most important processes for γ–ray production in a magnetized astrophysical environment in the non-thermal Universe. As synchrotron photons are less energetic than their parent elctrons, the emitted radiation typically covers an energy range from radio to X–rays. Proton synchrotron radiation is an inefficient process due to higher mass to charge ratio than an electron.

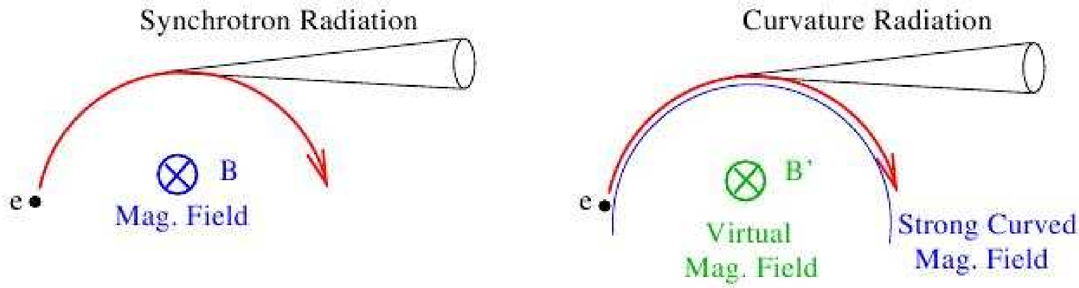

Figure 1.2: Comparision between Synchrotron and Curvature Radiation.

1.4.3 Curvature Radiation

Curvature radiation is produced when charged particles cross very strong magnetic fields. If the magnetic field lines are curved and gyroradius of a charged particle is much smaller than the curvature of the field, the charged particle moves along the curved magnetic field. Due to bending of the trajectory of charged particle by the curvature of magnetic field, particle emits radiation known as curvature radiation in addition to synchrotron radiation. All properties of curvature radiation can be obtained by analogy with synchrotron radiation [1.13] by assuming that the curvature of electron motion is caused by Lorentz force from the virtual magnetic field perpendicular to the curved field plane as shown in Figure 1.2. If the electrons have a power law energy spectrum with spectral index p, the resulting γ–ray spectrum due to curvature radiation will be a power law with an index $(p + 1)/3$. In polarization aspects, curvature radiation is almost linearly polarized. This mechanism is important in astrophysical sources like pulsars with strong magnetic fields (10^8–10^9 Gauss), originating from their magnetic poles, producing γ–ray photons in GeV regime [1.14].

1.4.4 Inverse Compton Scattering

The Compton scattering is a relativistic effect in which photon of electromagnetic radiation is scattered by electron at rest. In this scattering process, electron at rest will gain energy from the incident photon, as it acquires a recoil velocity for satisfying the momentum conservation. As a result, energy of incoming photon decreases after the scattering while electron energy increases. Therefore, the Compton scattering is considered as heating mechanism. When the energy of incoming photon as seen in the electron rest frame is small with respect to the rest mass energy of electron (m_ec^2), the process is known as *Thomson* scattering. The *Thomson* scattering is considered as classical non-relativistic limit of Compton scattering in which there is no change in the photon energy after scattering and recoil of electron is neglected. As the energy of incoming photon increases and becomes comparable or greater than m_ec^2, relativistic and quantum effects appear and the process is referred to as the scattering in *Klein-Nishina (KN)* regime.

When the electron that scatters the photon is not at rest, but has energy greater than typical energy of photon there can be energy transfer from electron to photon. This process is called inverse Compton (IC) scattering. In astrophysics, IC scattering is more important than Compton scattering because this process is very effective for producing energetic photons. As in IC scattering, the low energy photon gains energy and the energetic or hot electron loses energy, the process can be considered as cooling mechanism. In astrophysical environments, part of the kinetic energy of the accelerated electron is transferred to the low energy target photon to produce VHE γ–ray photon and the process may be expressed as

$$e + \gamma_{low} \rightarrow e + \gamma_{high} \tag{1.5}$$

The cross section of this process depends strongly on the energy of relativistic electron ($\gamma m_e c^2$), resulting in two different regimes [1.15]. In *Thomson* regime, the scattering cross section is independent of the energy of target photon (ε) and the energy of scattered photon is given by

$$E_\gamma \approx \gamma^2 \varepsilon \tag{1.6}$$

On the other hand, in *KN* regime the scattering cross section is dependent on target photon energy and the energy of scattered photon is given by

$$E_\gamma \approx \gamma m_e c^2 \tag{1.7}$$

Although in the *Thomson* limit, the characteristic energy ($\sim \gamma^2 \varepsilon$) of scattered photon is very large, it is still small compared with the electron energy, so the electron loses a small fraction of its energy in each scattering. This is not the case in KN limit where the scattered photon carries a large fraction of the electron energy and therefore electron does not lose its energy continuously. For a power law distribution of accelerated electron population with index p, the emitted γ–ray spectrum assumes a power law depending on two different scattering regimes. In case of *Thomson* regime, the spectral index of VHE photons will be $(p+1)/2$ which is similar to the synchrotron spectrum. Compared to the *Thomson* regime, the KN regime provides a much steeper power law spectrum with index $(p+1)$. The IC scattering mechanism is the principal γ–ray production channel in the individual astrophysical objects peaking in GeV–TeV energy range. Besides requiring the presence of seed photons in astrophysical objects, IC sacttering also demands sufficient transparency of the environment, allowing γ–rays to escape from the production site. The IC scattering is apparently more efficient in case of electrons than protons due to lighter mass of electrons.

1.4.5 Neutral Pion Decay

When accelerated hadrons collide with other hadrons or nuclei, pions are produced. Being the lightest mesons, pions are among the end products of nucleonic cascades involving strong interactions. Charged (π^+, π^-) and neutral (π^0) pions are produced with the same probability, thus one third of the pions produced are neuatral. With regards to life-time and decay channel these pions differ among each other. Charged pions (π^+, π^-) decay due to weak interactions after a typical life-time of $\sim 10^{-8}$ s via leptonic decay channel producing muons and neutrinos. Neutral pions (π^0) have a much shorter life of $\sim 10^{-16}$ s and they decay into two gamma photons (p= 99%) or e^-e^+ pairs (p=1%) before interacting with the medium. The decay of neutral pions can be expressed as

$$\pi^0 \rightarrow \gamma + \gamma \quad OR \quad e^- + e^+ + \gamma \tag{1.8}$$

Thus, the neutral pions provide a dominant channel for conversion of kinetic energy of protons as primary particles into VHE γ–rays. To produce the γ–rays through this process, the energy of accelerated proton should exceed the threshold energy given by

$$E_{th} = 2m_{\pi^0}c^2 \left(1 + \frac{m_{\pi^0}}{4m_p}\right) \tag{1.9}$$

With $m_{\pi^0} \approx 135$ MeV and $m_p \approx 938$ MeV as respective rest masses, the threshold energy is 280 MeV. If π^0 is at rest, the energy of emitted photon is

$$E_\gamma = \frac{m_{\pi^0}c^2}{2} \approx 67.5MeV \tag{1.10}$$

and if it is moving with velocity β (= v/c), the energy of photon is given by

$$E_\gamma = \frac{\gamma m_{\pi^0}c^2}{2}(1 + \beta cos\theta) \tag{1.11}$$

where γ is the Lorentz factor and θ is angle between direction of motion of photon and π^0. If pions are described by a power law energy spectrum of index p, the resulting γ–ray spectra is also a power law with same index p. Charged pions produced in proton-proton collisions decay into muons, electrons and corresponding (anti-) neutrinos. The spectra of neutrinos would be similar to the γ–ray spectrum from neutral pion decay. The neutrino and γ–ray spectra are the strongest indicators for the proton or CR accelerator sites.

The dominance of one process over another is decided by the astrophysical environment and energy range. From the above physical mechanisms that involve the production of γ–ray photons only two have the potential to produce VHE photons in astrophysical sources, namely IC scattering and neutral pion decay.

1.5 Gamma–ray Interaction and Absorption Processes

Gamma–ray photons being neutral particles are not affected by magnetic fields. However a large number of possible interaction mechanisms take place during their propagation in the medium. These interaction mechanisms lead to the absorption of γ–ray photons as a function of energy. The distinct absorption and interaction mechanisms of γ–rays are classified in two groups: *Radiation-Matter* and *Photon-Photon* interactions. These processes find very important place in the study of high energy astrophysical phenomena and are described below in brief.

1.5.1 Radiation-Matter Interaction

In the interaction of photons with matter, photon transfers its partial or complete energy to the electron in the matter. This results in sudden and abrupt changes in the photon history and photon either disappears or is scattered through a significant angle. Three main types of interaction mechanisms for γ–ray photon with matter that cause the attenuation are discussed below. The preference of one mechanism over other is strongly energy dependent.

- **Photoelectric Absorption:** The photoelectric absorption process involves absorption of a photon by an atomic electron and the subsequent ejection of an electron from one of the bound shells of the atom. The ejected electron is referred to as *photoelectron* and the process is known as *photoelectric effect* or *bound-free* absorption. Since a free electron can not absorb a photon and also conserve momentum, the photoelectric effect always occurs on bound electrons with the nucleus absorbing the recoil momentum. This process is the predominant mode of interaction for γ–ray photons of relatively low energy. The interaction cross section or probability of photoelectric absorption also depends on the atomic number (Z) of matter and is roughly approximated as

$$\sigma_{PA} \propto \frac{Z^n}{E_\gamma^{3.5}} \tag{1.12}$$

  where E_γ is the energy of γ–ray photon and n varies between 4 and 5 over the energy region of interest. Clearly, higher Z materials are the most favoured absorbers of low energy γ–rays. This absorption is usually observed in X–ray spectra of most of the astrophysical sources at energies below 1 keV representing principal source of opacity in stellar interiors.

- **Compton Scattering:** The Compton scattering process takes place between incident γ–ray photon and free electron in the matter. In matter, the electrons are bound; however if the photon energy is higher than the binding energy, the electron can be considered as essentially free. In Compton scattering, the incident photon is deflected with respect to its original direction and transfers a portion of its energy to the electron, which is then known as *recoil electron*. Since the deflection of photon is possible in all scattering directions, the energy transfer to electron varies from zero to a large fraction of incident photon energy. The process is dominant for γ–ray photons with higher energy and the scattering cross section depends on the number of electrons and increases linearly with the atomic number (Z) i.e.

$$\sigma_{CS} \propto Z \tag{1.13}$$

for γ–ray photons in MeV regime. This interaction takes place in astrophysical environments where matter is present.

- **Pair Production:** The pair production process generally involves transformation of photon into a particle and its antiparticle from the interaction of a photon with matter. The interaction takes place in the Coulomb field of a nucleus and the γ–ray photon disappears. If the energy of photon exceeds twice the rest mass energy of an electron (1.02 MeV), the pair production process is energetically possible and electron-positron (e^-e^+) pair is produced during interaction. All the excess energy carried by the photon above 1.02 MeV goes into kinetic energy of electron and positron. The process is dominant for VHE γ–rays and the magnitude of probability of pair production per nucleus or scattering cross section varies approximately as the square of the atomic number i.e.

$$\sigma_{PP} \propto Z^2 \tag{1.14}$$

As the intergalactic space provides a small matter containment to encounter, the absorption of VHE photons by radiation-matter interaction is negligible.

Attenuation Coefficient : The above reactions for radiation-matter interaction explain two qualitative features of radiation: (i) radiation or photons are more penetrating in matter than charged particles and (ii) a beam of photons is *not* degraded in energy as it passes through the matter, only attenuated in intensity. Each of the three interaction processes removes the photon from the beam entirely either by absorption or scattering and the photons passing through the matter retain their original energy. The interaction processes outlined above are characterized by a fixed probability of occurence per unit path length in the matter. The sum of these individual probabilities gives simply the probability per unit path length that the photon is removed from the beam and is known as *linear attenuation coefficient* (μ). The intensity of photons surviving a distance x in the matter is given by

$$I = I_0 e^{-\mu x} \tag{1.15}$$

where I_0 is the incident intensity of photons. It is more desirable to express the attenuation in terms of the mass of the material encountered by photons rather than in terms of distance because μ varies with the density of material. The *mass attenuation coefficient* is defined as the ratio of linear attenuation coefficient (μ) to the density of the matter (ρ). Thus in terms of mass attenuation coefficient (μ/ρ), the above attenuation law takes the form

$$I = I_0 e^{-(\mu/\rho)\rho x} \tag{1.16}$$

The product ρx, known as *mass thickness* of the absorber, is a significant parameter for describing degree of attenuation in terms of g/cm^2. The photons are also characterized by their *mean free path* λ, defined as the average distance travelled in the matter before an interaction takes place, and is given by

$$\lambda = \frac{1}{\mu} \tag{1.17}$$

1.5.2 Photon-Photon Interaction

The process is also known as γ–γ or *radiation-radiation* interaction. In this process a high energy γ–ray photon interacts with low energy photon and produces e^-e^+ pairs. The process can be expressed as

$$\gamma_{high} + \gamma_{low} \rightarrow e^- + e^+ \tag{1.18}$$

and it has a strict kinematic threshold, since in the center of mass or momentum frame the total photon energy must be greater than twice the rest mass energy of the electron [1.16]. The threshold condition to be satified for above process is given by

$$E_{high} E_{low} (1 - cos\theta) \geq 2m_e^2 c^4 \tag{1.19}$$

where θ is the angle between directions of two photons. The scattering cross section is maximum at threshold. The fundamental process is well understood and its amplitude can be calculated accurately by general perturbation methods using quantum electrodynamics. The existence of the process can not be questioned because all quantum electrodynamical predictions have been verified; moreover the reverse reaction, two photon e^-e^+ annihilation is observed. This interaction is dominant at higher energies affecting VHE γ–rays. In fact, this is the only interaction relevant for VHE γ–ray absorption during their travel across the Universe. A detailed description of this process is given in Chapter 6.

1.6 Gamma–ray Detection Techniques

Gamma–rays from high energy phenomena in the Universe span a wide energy range from 10^6 to 10^{20} eV. Therefore a single type of detector will not be suitable to detect γ–rays over this wide energy range. The detection of photons relies on the interaction with detector medium and γ–rays interact with matter in different ways depending on their energy. The Earth's atmosphere is not transparent to high energy photons due to their absorption and interaction with atmospheric mantle. Therefore, due to the opacity of the atmosphere, γ–rays can not be detected directly from the ground based instruments as is the case for optical light. Nevertheless, at energies < 10 GeV, the atmospheric absorption can be circumvented by placing the detectors in the space above Earth atmosphere using satellites. However, since the γ–ray photon fluxes from astrophysical sources are approximated by a power law spectrum with negative index, the number of photons decreases significantly with increasing energy. Beyond 10 GeV, the γ–ray fluxes are generally extremely low, so that the effective detection area of satellite based instruments can not provide adequate statistics for comprehensive spectral and temporal studies in VHE regime. Thus, for the observation of VHE γ–rays the required detection area should be very large due to the low fluxes, but instruments with required bigger sizes can not be sent into space. The only way to detect VHE γ–rays is using indirect methods from ground, where the detector of desired area can be built. These basic issues related to γ–ray observations, over wide energy range, lead to the development of instruments following different concepts and each characterized by different advantages, weaknesses and systematics. Two principal detection techniques from *Space* and *Earth* used to detect γ–rays from astrophysical objects over a wide energy band are briefly described below.

1.6.1 Space Based Technique

These techniques are based on direct detection of primary HE γ–ray photons in MeV-GeV regime. Three competing processes of γ–ray interaction with matter namely *Photoelectric absorption*, *Compton scattering* and *Pair production* are used by space based telescopes for detection of HE γ–rays. The building of space based detectors relies on these γ–rays interactions in their respective most efficient energy range. These detectors use trackers and calorimeters to measure the direction and energy of primary HE γ–rays. In order to achieve the goal of measuring the source location of the γ-ray photons, some sort of telescope must be designed. The various satellite telescopes designed for γ–ray observations are briefly described below.

- **Explorer XI:** First γ–ray telescope launched by NASA in 1961 to observe photons above 50 MeV. It consisted of a crystal scintillator with Cherenkov counter. Over its less than five months life time, it detected 22 γ–ray photons opening the era of space based gamma–ray astronomy.

- **Third Orbiting Solar Observatory (OSO-3):** Launched in 1967 and contained a γ–ray detector slightly more sophisticated than Explorer XI. It detected 621 events over a period of 16 months and also revealed the anisotropy of γ–ray sky.

- **Vela Satellites:** A set of satellites launched in pairs during 1963-1970 by United States and Soviet Union to detect photons in the energy range 150–750 keV. These detectors discovered Gamma Ray Bursts (GRBs) and 73 such events were recorded during ten years of their operation.

- **Second Small Astronomy Satellite (SAS-2):** A pair production telescope launched by NASA in 1972, exclusively designed for γ–ray astronomy in the energy range 20 MeV–1 GeV with an effective area of 100 cm^2. During its short life time of six months, it discovered emission from discrete sources like Crab and Vela pulsars and measured the HE component of diffuse γ–ray background.

- **COsmic ray Satellite B (COS-B):** A pair production telescope similar to SAS-2, launched in 1975 by European Space Agency (ESA). With an effective area of the order of 50 cm^2 at 400 MeV the telescope extended the results of SAS-2 in the energy range 30 MeV–5 GeV during its operation for more than six years.

- **Granat:** Launched in 1989 by Russian Space Agency to observe both interstellar X-rays and γ–rays. Beside its CR detections, it provided deep imaging of the galactic center.

- **Compton Gamma Ray Observatory (CGRO):** Launched in 1991 by NASA and ramained in its orbit till 2000 providing huge amount of information about γ–ray sources. It carried four instruments on board: *Burst And Transient Source Experiment (BATSE)*, *Oriented Scintillation Spectrometer Experiment (OSSE)*, *COMpton TELescope (COMPTEL)* and *Energetic Gamma Ray Experiment Telescope (EGRET)*, covering a wide energy range from 20 MeV to 30 GeV.

- **High Energy Transient Explorer 2 (HETE-2):** Launched in 2000 by an international collaboration comprising USA, Japan, France and Italy. Primary goals of the instrument are multi-wavelength observations of GRBs in the energy range 1–500 keV using two X-ray and one γ–ray detectors onboard.

- **INTErnational Gamma-Ray Astrophysics Laboratory (INTEGRAL):** Launched by ESA in 2002 for fine spectroscopy and fine imaging of γ–ray sources in the energy range 15 keV to 10 MeV and source monitoring in X–ray (3–35 keV) and optical ranges. The source catalog contains more than 1600 sources during its entire operation.

- **Astro-rivelatore Gamma a Immagini LEggero (AGILE):** An Itallian satellite launched in 2003 for observations in the 10–40 keV band as well as between 20 MeV and 50 GeV with a compact pair production telescope main instrument.

- **Swift:** Launched by NASA in 2004 for multi-wavelength observations of astrophysical transients like γ–ray bursts. The *Swift* satellite payload carries three instruments: *X-ray Telescope (XRT: 0.2–10keV)*, *Burst Alert Telescope (BAT: 15–150 keV)* and *Ultra-violet/Optical Telescope (UVOT: 170–650 nm)*. These instruments will be discussed in detail in Chapter 2 as data from these telescopes have been used for the multi-wavelength study of blazars in this thesis.

- **Fermi:** Launched in 2008 by NASA, it carries the most performing space telescope. The satellite hosts two instruments: *Large Area Telescope (LAT: 20 MeV–500 GeV)* and *Gamma-ray Burst Monitor (GBM: 8 keV-25 MeV)*. Sensitivity of LAT is 50 times better than EGRET. As the thesis is focussed to the observation of *Fermi* detected blazars, a detail dicussion on *Fermi*–LAT is given in Chapter 2.

1.6.2 Ground Based Technique

At energies above 100 GeV, the performance of space based satellite detectors gets seriously constrained by limited collection area ($\sim$ 1 m^2) due to power law nature of γ–ray fluxes from astrophysical sources. Therefore, the ground based detectors with large effective collection area ($\sim 10^5$ m^2) provide the only viable option to observe VHE γ–rays from the astrophysical sources. The limitations of space based detectors can be overridden with ground based detection techniques that observe the VHE γ–rays following a completely different concept: not the direct detection of the primary photons, but the detection of the products of its interaction with atmosphere. Even if the atmospheric absorption prevents the γ–ray photons from reaching the detector at ground, their interactions with the atoms and molecules of the atmosphere create a huge number of secondary particles (muons, electrons, positrons and neutrinos) along with the production of atmospheric Cherenkov and fluorescence radiation that allow to detect indirectly the primary incident photons. These secondary particles are named as *Extensive Air Shower (EAS)*. Two broad classes of experiments: *particle detectors* and *Cherenkov detectors*, have been designed to indirectly observe the VHE γ–rays from the ground.

- **Particle Array Detectors:** A collection of charged particle detectors dispersed over a large area is termed as EAS array. This technique is based on the direct detection of shower particles passing through the detector. The direction of primary particle is determined by measuring the relative arrival time of the EAS as it sweeps across various detectors in the array. The energy can be estimated from the shower size and using shower development curves taken from simulations. Since the showers normally die above sea level, detectors are placed at high altitude on Earth. The energy threshold of array detector depends on the altitude of the experiment, minimum number of detectors for shower reconstruction and size & spacing of the detectors. Particle array detectors are generally used to detect EAS produced by UHE primaries. The main advantage of these detectors include a long duty cycle and a large field of view. The examples of particle based experiments are:

  - *MILAGRO :* Located at 2630 m above sea level, *Milagro* (which is no longer in operation) is a water Cherenkov detector consisting of 5000 m^2 central pond surrounded by an array of 175 instrumented water tanks that span an area of 40000 m^2. An array of photo-multipliers detect the

Cherenkov light produced by EAS particles in the water. The detector has been operated with a 95% duty cycle since 2000.

- *High Altitude Water Cherenkov (HAWC):* Located at an altitude of 4100 m, *HAWC* is a second generation cosmic ray and γ–ray observatory that builds upon the successful water Cherenkov technique pioneered by *Milagro*. It is designed to continuously survey the sky in the energy range 100 GeV to 100 TeV with 1.8 *sr* instantaneous field of view telescope consisting of 300 water tanks, each instrumented with 4 photomultiplier tubes. The detector started science operation in August 2013 with about 100 tanks, and the full array has very recently been completed.
- *Astrophysical Radiation with Ground-based Observatory at Yang-BaJing (ARGO-YBJ):* It is a full coverage array detector located in Tibet at 4300 m above sea level. The detector consists of a square array of 1848 resitive plate counters (RPCs) covering a total area 6700 m^2. The *ARGO-YBJ*, with 130 clusters, collects data above an energy threshold of 100 GeV since 2006 and provides a detailed space-time picture of shower front.
- *Gamma Ray Astronomy at PeV EnergieS (GRAPES):* This experiment loacted in India (Ooty) at 2200 m above sea level contains a large area ($\sim$ 560 m^2) tracking muon detectors. It consists of 16-modules, each 35 m^2 in area that are grouped into four super modules of 140 m^2 each. The experiment records 4×10^9 muons every day above an energy threshold of 1GeV.

- **Atmospheric Cherenkov Detectors:** Cherenkov radiation associated with EAS was first detected by Galbraith & Jelly in 1953 [1.17], and the possibility of using this phenomena to study γ–ray initiated showers led to the development of a number of dedicated facilities. Atmospheric Cherenkov experiments are grouped into two categories depending on the technique they use to detect the Cherenkov light from the EAS produced by primary VHE γ–rays: *Imaging Atmospheric Cherenkov Telescope (IACT)* and *Cherenkov Wavefront Sampling Telescope (CWST)*. A more detailed description of atmospheric Cherenkov techniques and in particular IACT technique will be given in Chapter 3. The current generation of IACTs are allowing to probe the γ–ray sky with greater sensitivity than ever before in the energy range above 40 GeV. The major IACTs running smoothly in the world at present are briefly summarized below.

  - *Very Energetic Radiation Imaging Telescope Array System (VERITAS):* Array of four 12 m diameter telescopes, located in Arizona, USA (31.68° N, 111.95° W, 1268 m asl), has been in operation since the summer of 2007. The telescope has detected γ–rays above 100 GeV from a number of galactic and extragalactic objects during its operation.
  - *High Energy Stereoscopic System (HESS):* Array of four 12 m diameter telescopes, located in Namibia, Gamsberg (23.27° S, 16.5° E, 1800 m asl)

is operational since 2003. The telescope with an energy threshold above 100 GeV has been involved in scanning of galactic plane, monitoring of sources in southern hemisphere and northern hemisphere at large zenith angles. Addition of the largest Cherenkov telescope ever constructed with 28 m diameter (HESS II) in 2012 has greatly enhanced the sensitivity of the system to lower energies up to 30 GeV.

- *Major Atmospheric Gamma ray Imaging Cherenkov (MAGIC):* Telescope with 17 m diameter light collector, loacted at La Palma in Canary islands (28.45° N, 17.54° W, 2231 m asl), is exploring the γ–ray sky in the energy range above 50 GeV since 2004. A second telescope (MAGIC II) with the same diameter 85 m away was added in 2009 for stereoscopic observations. This stereo-pair is providing obsevations above 25 GeV.
- *TeV Atmospheric Cherenkov Telescope with Imaging Camera (TACTIC):* Telescope with a light collector of 3.5 m diameter, located at Mount Abu, India (24.6° N, 72.7° E, 1300 m asl) is operational since 2001 and has detected TeV γ–ray emission from blazars during flaring activity. In 2011, the telescope has undergone a major upgrade program to improve its performance. A detailed description of the *TACTIC* telescope is presented in Chapter 3.
- *First G-APD Cherenkov Telescope (FACT):* A relative newcomer to the field of gamma–ray astronomy, located at *MAGIC* site and operational since 2011. As a single telescope with modest aperture ($9.5m^2$), FACT is scientifically limited to monitoring of the brightest TeV blazars. However, it also serves as an important test bed for some of the technologies which will be employed in the next generation of Cherenkov instruments.

To a large extent, the two types of ground based experiments for VHE γ–ray observations: *particle array detectors* and *atmospheric Cherenkov telescopes*, are complementary in practice. The main advantages of particle detectors include a long duty cycle and a large field of view (wide field survey), while those of Cherenkov telescopes include high sensitivity, low energy threshold, good energy and angular resolution. Because of high background induced by cosmic ray showers, ground based detectors should have capability to suppress this background. The rejection of cosmic ray background while observing a γ–ray source, remains a challenging task in VHE γ–ray astronomy.

1.7 VHE γ–ray Astronomy

VHE γ–ray astronomy is an integral part of high energy astrophysics. It is also referred to as TeV γ–ray astronomy which concerns the study of astrophysical sources of γ–ray photons with energies in the range from 30 GeV to 30 TeV, which is one of the most recent windows of the electromagnetic spectrum to be explored for study. Many experiments in the past aimed both at the search for VHE γ–ray emission sites, as well as at solving fundamental questions concerning the nature of cosmic rays.

1.7.1 Historical Development

Discovery of cosmic rays in 1912 by Austrian physicist Victor Hess showed that some type of high energy radiation is constantly entering the Earth's atmosphere from outer space. Shortly before and after the Second World War in 1939, new windows in energy bands below and above visible light were successfully opened, by observations in radio, infrared (IR), ultraviolet (UV), X–rays and eventually in γ–rays.

Cherenkov radiation associated with large cosmic ray air showers was first detected in 1953 by Galbraith & Jelly [1.17]. The idea of searching for astrophysical VHE γ–ray sources above 100 MeV energies was first proposed by Morrison in 1958 [1.18]. Prediction of TeV photons from various sources including Crab, which might be detectable with an air shower particle array at high altitude was made by Cocconi in 1959 [1.19]. Possibility of using Cherenkov radiation to study the γ–ray initiated showers led to development of number of experimental facilities in 1960s. This effort was boosted by the apparent detection of a γ–ray signal from the black hole binary Cygnus X-3 by particle air shower arrays and atmospheric Cherenkov detectors. Around 1980, it was possible to observe the cosmic radiation in the entire electromagnetic spectrum from 10^{-6} eV upto 10^{9} eV. These multi-wavelength observations demonstrated that besides the thermal Universe dominated by stellar production of radiation, the so called non-thermal Universe with high energy acceleration processes based on particle acceleration constitutes an essential ingredient of the Universe.

The field of VHE γ–ray astronomy reached a firm experimental footing with the development of the imaging technique, which provides an efficient method of discriminating between γ–ray initiated showers and cosmic ray showers based on the morphology of their Cherenkov images [1.20,1.21]. In 1989, the technique was applied by the Whipple collaboration to detect steady TeV γ–ray emission from Crab Nebula using a 10 m reflector with 37 photomultiplier tube camera [1.22]. This seminal observation started a very productive research field in an energy domain which is essentially accessible by ground based instruments. A number of IACTs such as CANGAROO, Telescope Array, SHALON, TACTIC were subsequently developed around the world, with the northern hemisphere instruments leading the field. The 1990s witnessed two important developments in the field: detection of the first extragalactic sources Mrk 421 [1.23] and Mrk 501 [1.24] by Whipple collaboration, and application of stereo imaging technique by HEGRA group [1.25]. HEGRA group demonstrated that the combination of Cherenkov image information from multiple telescopes located within the same Cherenkov light pool could dramatically improve the sensitivity of the technique. The field of VHE γ–ray astronomy has enjoyed rapid growth in the last two decades with the development of new generation ground based telescopes like VERITAS, MAGIC and HESS and number of sources detected has increased from a handful to over 160. As an increasing number of sources are detected at TeV energies, the field has matured and become a viable branch of modern astronomy. Together with observations at lower energies, TeV γ–ray observations have substantially improved our understanding of the Universe.

1.7.2 Scientific Motivation

The primary motivation for development of VHE γ–ray astronomy is to utilize the unique window of opportunity on the ground to push astronomy towards the upper most end of the electromagnetic spectrum. As the history of astronomy has shown, a new window into the Universe nearly always brings about new discoveries. TeV photons are always preciously few in number but carry essential information about the particle acceleration and radiative processes involved in extreme astrophysical environments. The prospects of probing the most energetic and most violent phenomena in the Universe provide strong motivation to develop perfect techniques in the field. VHE γ–ray astronomy also attempts to address many of the questions that other branches of astronomy do. They include cosmic sources of TeV Photons, radiation geometry and mechanism, properties of radiating particles and their environments, and so on. The origin of CRs is an important outstanding question even 100 years after their discovery. VHE γ–rays point back directly to their sources and can reveal the production sites of energetic CRs. Exploring the Universe with VHE γ–rays allows us to explore astrophysical *TeVatrons*–powerful nonthermal sources that accelerate particles to TeV energies and beyond. VHE γ–rays can also be used to probe the physics beyond standard model of particle physics and cosmology.

1.7.3 Connection with Fundamental Physics

The area of VHE γ–ray astronomy is not only concerned about issues in astronomy and astrophysics, but also provides one of the best windows for probing fundamental physics beyond the reach of terrestrial accelerators. The domain of VHE γ–rays is sensitive to energy scales important for particle physics including the 100 GeV scale expected for cold dark matter, the TeV scale where supersymmetry may emerge, and even perhaps the unification scale for the strong and electro–weak forces. Some of the important concepts of fundamental physics, which can be probed with VHE γ–ray observations are discussed below.

- **Quantum Gravity and Lorentz Invariance Violation:** Quantum gravity attempts to describe gravity according to the principles of quantum mechanics and Einsteins's general theory of relativity. A cornerstone of Einstein's special theory of relativity is Lorentz invariance, which postulates that all observers measure exactly the same speed of light in vacuum, independent of photon energy. While special relativity assumes that there is no fundamental length scale associated with such invariance, there is a fundamental scale known as *Planck Scale*, at which quantum effects are expected to strongly affect the nature of space–time and some theories predict that Lorentz invariance might break near the *Planck Scale* (Length: 1.62×10^{-33} cm, Energy: 1.22×10^{19} GeV) [1.26]. A key test of such violation of Lorentz invariance is the detection of variation of photon speed with energy. Even a tiny variation in photon speed, when accumulated over cosmological travel times, may be revealed by observing sharp features in γ–ray burst light curves or flaring episodes in quasars [1.27]. If Lorentz invariance is conserved, the VHE γ–ray photons emitted at the same time should be detected simultaneously on the Earth. If there is a delay in arrival times depending on the energy of γ–rays, a possible Lorentz invariance violation can be claimed.

- **Searching for Dark Matter:** In the standard cosmological model, which has emerged over the last decade, only 4% of the energy density in the Universe is in the form of visible matter or baryons, about 24% is invisible or dark matter and remainder 72% is dark energy [1.28,1.29]. Evidence for the gravitational effects of dark matter is observed on all scales ranging from galaxies, where flat rotation curve requires that visible matter is embedded in extended dark matter halos, to cluster of galaxies. The dark matter particles may interact only through gravitational forces with hadronic matter, some form of weakly interacting massive particle (WIMP) in the mass range of some tens of GeV to TeV is required to explain the existing observations [1.30]. Possible candidates include supersymmetry (SUSY) particles and Kaluza-Klein (KK) particles arising in theories with TeV-scale extra dimensions. One of the best theoretical candidates for dark matter is the neutralino–the lightest supersymmetric WIMP with rest mass above 50 GeV. The neutralino has a property to be the anti-particle of itself so that it can undergo self-annihilation, converting into quarks or into two γ–rays. High energy γ–rays from dark matter annihilation may provide a means of discovering and identifying this invisible component of the Universe.

- **Extragalactic Background Light:** The intergalactic space is filled with the light produced by all the sources in the Universe throughout cosmic history, which in the band 0.1–1000 μm is called Extragalactic Background Light (EBL) [1.31]. The intensity and spectral shape of EBL is an important issue in astrophysics and cosmology, providing unique information about the epochs of formation and the history of evolution of galaxies in the Universe. TeV photons coming from cosmological distances may interact with low energy EBL photons to produce electron-positron pair and thus be effectively absorbed [1.32]. While this represents a problem for detecting distant extragalactic γ–ray sources, it also provides an indirect method to probe EBL. Recent VHE γ–ray observations indicate that the Universe seems to be much more transparent at TeV energies than previously expected [1.33]. We could use distant TeV sources as cosmic beacons to study the diffuse infrared background, which has remain an observational challenge for direct measurements. Application of VHE γ–ray observations of blazars for studying EBL is discussed in detail in Chapter 6.

- **Axion-Photon Oscillation:** Axion is a pseudo-scalar boson predicted by Peccei-Quinn mechanism for solving the strong Charge-Parity (CP) problem in Quantum Chromodynamics [1.34]. The one generic property of axion is two photon coupling with an important feature that its mass and coupling constant are inversely related to each other [1.35]. Other predicted states with same phenomenology but different relationship between mass and coupling constant are known as Axion-Like Particles (ALPs). ALPs, if existing in nature, are expected to mix with photons in the presence of an external magnetic field [1.36]. This photon-ALP mixing leads to intriguing signatures in astrophysical observations of distant sources above 100 GeV and in particular, produces detectable effects in the observation of blazars. The photon-ALP oscillations provide a natural mechanism to drastically reduce the absorption of VHE photons by EBL photons.

1.8 VHE γ–Ray Sources

VHE γ–rays are produced in environments where effective acceleration of particles (electrons, protons, and nuclei) is accompanied by their interactions with the surrounding gas and radiation fields. Different classes of astrophysical sites for emission of VHE γ–rays via non-thermal processes are known from the study of their nature and properties of γ–ray production. The sources of VHE γ–rays are naturally divided into three classes: *Galactic*, *Extragalactic* and *Unidentified* as described below. The distribution of VHE γ–ray sources in the sky discovered till now is shown in Figure 1.3. As can be seen from the Figure 1.3, the VHE γ–ray sky contains a diverse collection of different object classes, despite a modest number of known sources ($\sim$ 160). Numerically dominant are the sources clustered along the plane of our galaxy. The VHE γ–ray sources detected till now have also been summarized in Table 1.1.

1.8.1 Galactic Sources

The γ–ray sources located in our Milky-Way Galaxy are referred to as Galactic sources. The matter in the galaxy is composed of stars, interstellar gas, dust and may be dark matter with unknown composition. A simple model of our Galaxy is that the mass is concentrated mostly in a thin disk of thickness 0.5 kpc and radius 15 kpc. The solar system is 8.5 kpc from the Galactic center. The dynamics of the Galaxy are not fully understood and more than 80 Galactic sources have been detected in VHE regime to date. Being located in our Galaxy, VHE γ–rays from these sources suffer negligible attenuation on their travel to the Earth. The examples of Galactic sources include: *Supernova Remnants*, *Pulsars* (PULSating stARs), *Binary Systems* (Microquasars and Binary pulsars), *Star clusters*, *Galactic Center*, *Solar System* and *Fermi–Bubbles*.

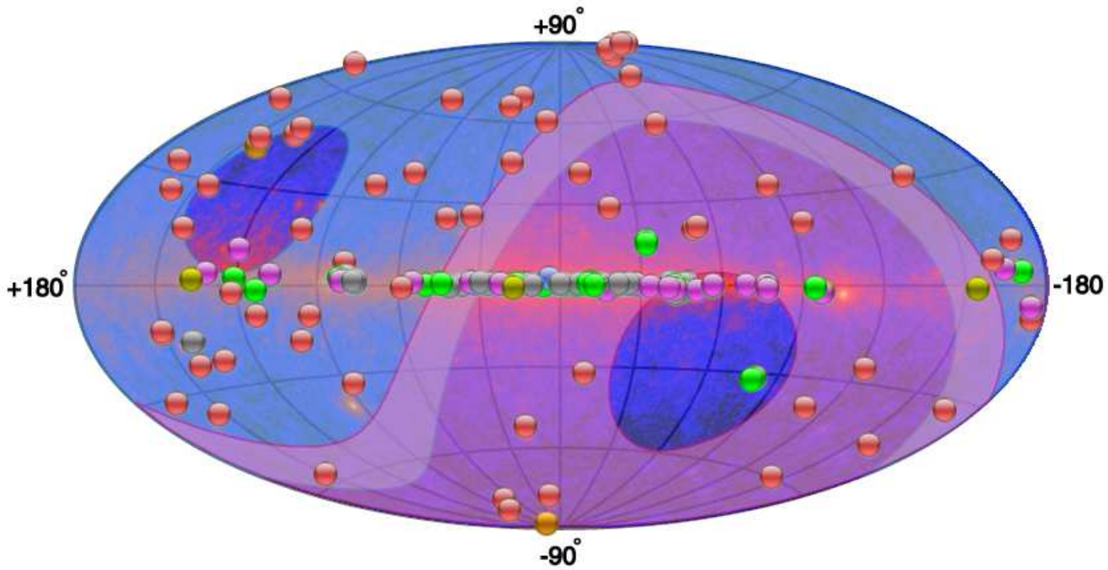

Figure 1.3: Distribution of more than 160 VHE γ–ray sources discovered till now (June 2015). Circles with different colors represent different types of sources in the γ–ray sky. (Credit: tevcat.uchicago.edu)

Table 1.1: Summary of VHE γ–ray sources detected till June 2015.

Sources	Class	No.
Supernova Remnants (SNR)	Galactic	62
Pulsars	Galactic	6
Binary Systems	Galactic	8
Star Clusters	Galactic	6
Active Galactic Nuclei (AGN)	Extragalactic	61
Star Burst Galaxies	Extragalactic	2
Galaxy Clusters	Extragalactic	9
UNID	Unidetified	31

1.8.2 Extragalactic Sources

These sources are located outside the Milky-Way Galaxy. More than 70 extragalactic sources have been discovered as VHE γ–ray emitters till now. From a general point of view, the γ–ray production in extragalactic sources shares much in common with that in Galactic ones. Unlike the Galactic sources, γ–rays of extragalactic origin travel large cosmological distances and suffer significant absorption through $\gamma - \gamma$ interaction and pair production. The class of extragalactic sources involves: *Active Galactic Nuclei (AGN)*, *Star Burst Galaxies*, *Galaxy Clusters* and *Gamma Ray Bursts (GRBs)*. AGN are believed to be the most powerful sources of non-thermal radition in the Universe. The continuum radiation from AGN expands over the entire electromagnetic spectrum from radio to VHE γ–rays. Despite the fact that AGN consist $\sim 1\%$ of the total galaxy population they provide an excellent site of studying unexplored physical processes. AGN with their jets pointing towards the Earth are referred to as **Blazars**. GRBs are frequently observed at a rate of 1-2 per day uniformly distributed in the Universe and more than 1000 GRBs have been detected so far in the extragalactic sky. As the present thesis is mostly related to study of blazars, Chapter 2 is dedicated to a detailed description of blazars.

1.8.3 Unidentified Sources

The VHE γ–ray sources with no counterpart in low energy bands are referred to as unidentified sources. The general characteristics of these sources like spectra, size and position are similar to known VHE γ–ray sources. These sources may be of galactic or extragalactic origin. Multi-wavelength study is required to understand these types of sources. A non-detection of lower energy emission from these sources may be an indication that a new VHE γ–ray source class exists [1.37]. A wide variety of galactic astrophysical objects have been suggested as possible counter parts for some of the unidentified sources. With regard to extragalactic sources, understanding the nature of unidentified sources is important because new γ–ray emitting source classes are likely to be found in addition to well established blazars.

1.9 Summary

The Universe is filled with a large number of energetic particles, electrons and fully ionized atoms, travelling through space very close to the speed of light. Their origin is one of the fundamental unsolved problems in astrophysics. High energy astrophysics studies the most energetic and non-thermal processes in the Universe and explores cosmic objects which produce extreme conditions that can not be created in experiments on the Earth. Many classes of celestial sources have been detected at TeV energies and their observations have shed new light on the physical processes operating in the diverse astrophysical settings. Discoveries in TeV energy band have important consequences for a wide range of topics in astrophysics and astroparticle physics. The development of VHE γ–ray instruments has been driven to a significant extent by questions in the field of astroparticle physics. The current generation of γ–ray instruments has demonstrated that VHE γ–ray astronomy with unique capabilities to reveal the nature of astrophysical objects is a rich field of research today. With the first firm detection of TeV γ–ray emission from Crab Nebula, the VHE γ–ray astronomy has continued to explore the non-thermal Universe with the development of more advanced analysis techniques and instruments such as *AGILE*, *Fermi*, *HESS*, *VERITAS* and *MAGIC* and has made it possible to understand the particle acceleration and study the origin of cosmic rays in the Universe. The connection between ground based IACTs and satellite telescopes is growing strongly and IACTs as the most powerful instruments for pointed observations of VHE γ–ray may lead to the most spectacular discoveries in future.

1.10 References

[1.1] V. F. Hess, 1913, Phys. Z., 13, 1084

[1.2] D. Paciini, 1912, Nuovo Cimento, 3, 93

[1.3] A. H. Compton, 1933, Science, 77, 480

[1.4] T. K. Gaisser, 1990, *Cosmic rays and particle physics*

[1.5] K. Greisen, 1966, Phys. Rev. Lett., 16, 748

[1.6] G. T. Zatsepin, V. A. Kuźmin, 1966, Sov. J. Expt. & Theo. Phys. Lett., 4, 78

[1.7] T. C. Weekes, 1988, Phys. Rep., 160, 1

[1.8] M. S. Longair, 1992, *High Energy Astrophysics: Volume 1*

[1.9] R. Schlickeiser, 2002, *Cosmic Ray Astrophysics*

[1.10] T. Padmanabhan, 2002, *Theoretical Astrophysics: Volume 1*

[1.11] Y. Uchiyama et al., 2002, ApJ, 571, 866

[1.12] J. D. Jackson, 1975, *Classical Elctrodynamics*

[1.13] V. V. Ochelkov & V. V. Usov, 1979, NASA STI Tech. Rep., 80, 30239

[1.14] D. P. Barsukov et al., 2006, Astronomy Reports, 50, 159

[1.15] G. R. Blumenthal & R. J. Gould, 1970, Rev. Mod. Phys., 42, 237

[1.16] R. J. Jauch & F. Rohrlich, 1955, *Theory of Photons and Electrons*

[1.17] W. Galbraith & J. V. Jelly, 1953, Nature, 171, 349

[1.18] P. Morrison, 1958, Nuovo Cimento, 7, 858

[1.19] G. Cocconi, 1959, ICRC, 2, 309

[1.20] T. C. Weekes, K. E. Turver, 1977, *Recent Advances in γ–Ray Astronomy*

[1.21] A. Hillas, 1985, ICRC, 3, 445

[1.22] T. C. Weekes et al., 1989, 342, ApJ, 379

[1.23] M. Punch et al., 1992, Nature, 358, 477

[1.24] J. Quinn et al., 1996, ApJL, 456, 83

[1.25] A. Daum et al., 1997, Astropart. Phys., 8, 1

[1.26] E. Witten, 1996, Nucl. Phys. B, 471, 135

[1.27] G. Amelino-Camelia et al., 1998, Nature, 393, 763

[1.28] A. G. Riess et al., 1998, Astron. J., 116, 1009

[1.29] S. Perlmutter et al., 1999, ApJ, 517, 565

[1.30] L. Bergstrom, 2012, Annalen Phys., 524, 479

[1.31] M. G. Hauser, E. Dwek, 2001, ARA&A, 39, 249

[1.32] R. J. Gould, G. P. Schreder, 1967, Phys. Rev., 155, 1408

[1.33] A. Domínguez et al., 2013, ApJ, 770, 77

[1.34] R. D. Peccei & H. R. Quinn, 1977, Phys. Rev. Lett., 38, 1440

[1.35] S. Weinberg, 1978, Phys. Rev. Lett., 40, 223

[1.36] D. Hooper & P. D. Serpico, 2007, Phys. Rev. Lett., 99, 231102

[1.37] F. A. Aharonian et al., 2005, Science, 307, 1938

Chapter 2

Fermi Observation of Blazars

2.1 Active Galactic Nuclei

The galaxies, in which the nucleus or central core produces powerful electromagnetic radiation, often outshining stars, gas and dust which make up the host galaxy, are known as active galactic nuclei (AGN). If the core or central emission dominates the galaxy emission all over the electromagnetic spectrum, the AGN is known as **quasar** (QUASi-stellAR radio source). The energy source powering AGN is believed to be accretion of gas onto a supermassive black hole (SMBH: 10^6 - 10^9 $M_\odot$) [2.1]. This is a very efficient energy release process potentially able to extract a large fraction of the rest mass energy of infalling matter. The released energy makes AGN visible from cosmological distances. The accretion of matter onto a compact object is often associated with production of collimated bipolar outflows known as jets. Jets carry a fraction of infalling matter and its angular momentum away from the central object.

2.1.1 General Properties

AGNs are focus of observational effort in every wavelength band from radio to γ–rays. The different observational properties of AGN arise, to a large degree, from their intrinsically anisotropic geometry and radiation pattern, from absorption as well as from relativistic effects. The important properties of these objects are described below:

- AGN emit radiation over the entire electromagetic spectrum having a bolometric luminosity $L_{bol} \geq 10^{44}$ erg s^{-1} sometimes reaching upto 10^{48} erg s^{-1}. In comparision, normal galaxies have $L_{bol} \leq 10^{42}$ erg s^{-1} and bulk of their luminosity is emitted in the visible band, essentially produced by stars.

- Their spectra over the whole electromagnetic band are essentially of non-thermal origin contrary to normal galaxies where the spectrum is given by the integration of the stars, thermal spectra.

- Some AGN also reveal strong radio and X–ray emission in the form of spectacular jets.

- The basic characteristic of AGN emission is the variability. The observed emission of these objects is highly variable in all energy bands on time scales ranging from seconds to years.

- According to the best estimations, AGN remain active for more than 10^6 years, this means that an enormous amount of material must be consumed in order to maintain their luminosities.

All these properties indicate that powerful physical mechanisms with very high efficiency (higher than nuclear processes) originate inside these extragalactic objects. Despite the fact that AGN consist $\sim 1\%$ of the total galaxy population they provide an excellent site of studying unexplored processes.

2.1.2 Morphology

Morphology of AGN host galaxy is very important for our understanding about their evolution as a function of redshift and luminosity. At the same time, morphology can play an important role in testing the physical mechanisms for fueling of the central black hole. An AGN is a complex system consisting of central (possibly rotating) SMBH, infalling matter in the form of an inner accretion disk, dusty torus (away from central object and hence colder), clouds of gas orbiting the central object and outflowing matter (moving away from central black hole) in the form of collimated relativistic jets. AGN are generally hosted by spiral or elliptical galaxies and the basic morphological feature of AGN from observed characteristics can be developed as follows.

- **Core:** This is a compact unresolved luminous radio component at the center of the associated galaxy. The emission from the core is mostly described by a flat power law with spectral index < 0.5. Cores are present in almost all quasars and in 80% of radio galaxies.

- **Lobes:** These are a pair of two extended regions of radio emission on opposite side of the host galaxy. They are often several hundred kpc in length and can be separated from the galaxy by a similar distance. The axes of two lobes and center of galaxy generally lie along a common line. Even within the lobes, one often observes local intensity maxima known as *hotspots*.

- **Jets:** These are narrow features connecting the core with the extended lobes of AGN. Jets are observed in most of the AGN as two-sided or one-sided. They may extend from pc scale to kpc scale and are visible over entire electromagnetic spectrum. The bright regions observed along the length of AGN jets are known as *knots*. Jets are assumed to be the medium for transporting energetic particles from the nucleus to extended radio structures at relativistic velocities.

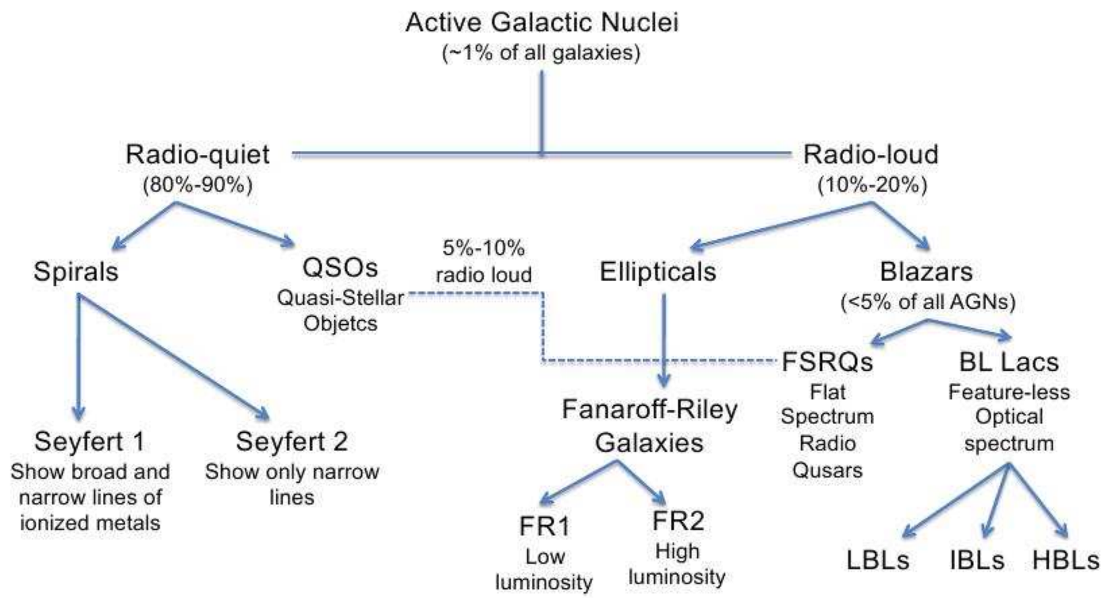

Figure 2.1: AGN classification scheme.

The above description is applicable only to radio morphology of extended sources and quite often the morphology of other sources (like compact radio source or radio-quiet source) becomes too complex to provide an unambiguous separation among different parts. However, it is convenient to consider a radio source built up from the above components and assume any complex or ill-defined features to be produced from perturbations in the source itself, or in interaction with the ambient intergalactic environment. Majority of the compact sources are observed to be surrounded by extended emission prominent at low energies. Therefore, the compact sources may simply be extended sources, seen end-on. The high frequency radio spectra of compact sources are usually flat. Quasars in elliptical galaxies tend to be radio loud, while those in spiral galaxies are radio-quiet.

2.1.3 Classification

AGN are classified in various subclasses according to their observed characteristics. A more simplified classification based on different observational properties is discussed below.

- **Radio and Optical Emission:** AGN are firstly classified in two classes: *radio-loud* and *radio-quiet* (Figure 2.1) according to their radio emission. AGN showing important radio emission are termed as radio-loud, otherwise, they are named as radio-quiet. This classification is based on *radio-loudness* parameter R which is defined as the ratio of radio flux at 5 Ghz to the B-band ($\lambda \approx 440$ nm) optical flux.

The **radio-quiet** AGN are also known as thermal/disk dominated galaxies which do not show significant nuclear radio emission compared to the observed emission in optical or X-ray band. The *radio-loudness* parameter for these AGN is less than 10 and rougly 85% of AGN are hosted in *radio-quiet galaxies*. These AGN are further subdivided into two classes: *quasi-stellar objects* (QSOs) or *radio-quiet quasars* (RQQ) and *Seyfert galaxies* based on their optical emission line widths. *QSOs* exhibit broad emission lines where as *Seyfert galaxies* show narrow emission lines. In *QSOs*, the host galaxy is not resolved however the *Seyfert galaxies* have a visible host galaxy. The commonly observed *radio-quiet* AGN are *Seyfert galaxies* with spiral morphology. The *Seyfert galaxies* are of two different species, type I and type II based on their optical/UV properties. *Seyfert I* galaxies exhibit both narrow and broad emission lines as well as a strong non-stellar continuum and the *Seyfert II* galaxies exhibit only narrow lines and a weaker non-stellar continuum.

The **radio-loud** AGN are also referred to as non-thermal/jet dominated or quasars where non-thermal processes are energetically dominant at all energies. The radio-loudness parameter for these galaxies is assumed to be greater than 10 and approximately 15% of AGN belong to this class. The *radio-loud* AGN are subdivided into the classes of narrow line, broad line and weak emission line objects. Based on their radio morphology *narrow-line radio galaxies* (NLRGs) are distinguished as *Fanaroff-Riley* (FR) type I and II radio galaxies. *FR I* radio galaxies are extended sources where radio emission is core dominated. *FR II* radio galaxies are more luminous than FR I and the emission region is lobe dominated. Broad line objects are subdivided into *broad-line radio galaxies* (BLRG) and *radio quasars* (RQ). *BLRGs* have a continuum and emission lines similar to Seyfert 1 galaxies. Based on their radio spectral index, *RQs* are further classified into *steep spectrum radio quasars* (SSRQs) and *flat spectrum radio quasars* (FSRQs) under the assumption of a simple power law. For SSRQs, the spectral index is less than 0.5 while for FSRQs the index is greater than 0.5. The *radio-loud* objects with weak emission lines and continuum emission are represented by *BL Lacertae* (BL Lacs), named after their prototype that was originally mistaken for a star. BL Lacs have a flat or inverted radio spectra with a smooth and featureless continuum emission.

BL Lacs are analogous to *FSRQs* and both of them form a separate category called *Blazars*. It must be noted that the optical spectra of BL Lacs and FSRQs differ greatly. In fact, whereas FSRQs show strong broad emission lines, BL Lacs have either weak emission lines of typical equivalent width of less than 0.5 nm or no emission lines at all in their optical spectra. The reason for combining them as *blazar* is because they share the same continuum properties such as multifrequency spectra by non-thermal emission, strong variability and high polarization. A special emphasis will be given on blazars, as this work is dedicated to the study of these objects.

- **Orientation Scenario:** All the AGN presented above are usually explained in terms of an orientation scenario with respect to the viewing angle. In general type I AGN are viewed close to the jet axis and type II are viewed perpendicular to it. Concerning the *radio-quiet* galaxies, Seyfert I generally exhibit broad and narrow lines meaning that the AGN is viewed from the observer at a small angle from the jet axis, therefore both the broad-line region (BLR) and the narrow-line region (NLR) are visible. In the opposite case of Seyfert II, the AGN is viewed along the plane of the torus therefore the BLR is obscured and the NLR is visible. In the *radio-loud* regime, blazars are thought to be oriented such as their jets are aligned very close to the line of sight of the observer.

2.1.4 Unification Theory

The unified scheme is the widely accepted theory regarding radio-loud AGN. The unification models of AGN [2.2,2.3] postulate that all the observed differences among different types of objects are due to the orientation effects with respect to the line of sight to the observer. Thus, based on a common axisymmetric structure, AGN can be grouped into one class by implying different observational properties at different aspect angles. The *Unification Theory* of AGN predicts a spinning or stationary black hole with mass in the range 10^6 - 10^9 $M_\odot$ at the center. The black hole with high gravitational potential, is assumed to be the central engine of an AGN which provides an energy release through matter accretion from a surrounding, flat, rotating accretion disk. With an efficiency of the order of 10%, the process is much more efficient than nuclear fusion. Two relativistic jets perpendicular to the disk emanate from the region near to central enegine, extending upto large distances > 100 kpc. The two components, accretion disk and jet form radiation emitting region of AGN. There two radiation absorbing regions: a gas cloud located at $\sim$ 0.1-1 pc from central engine and a dusty torus further away as depicted in Figure 2.2. In the following, the different components of *Unification model* are briefly explained.

- **Central engine or Accretion of matter:** Accretion of gaseous matter in the gravitational field of a massive object is the standard scenario for energy generation in most of the astrophysical objects. In AGN, the central SMBH accretes the matter from the surroundings and if the black hole is spinning, the angular momentum considerations lead to the formation of a disk around the black hole. When the accreting matter approaches towards the SMBH, the rotation velocity of matter increases and the velocity structure of the disk is correlated with the temperature. Therefore, the disk thermal emission can be assumed as black body radiation at a given temperature. Consequently, the observed radiation from the disk is a superposition of several black body spectra that appears as *blue bump* in the UV/optical band of the spectrum [2.4]. The radiation process strongly depends on the mass of SMBH and the accretion rate. The disk emission is limited by an important quantity known as *Eddington limit*, which is associated with spherical accretion. Radiation emitted during accretion exerts an outward pressure on the electrons in the matter due to Compton scattering, while gravity exerts an inward force on the protons in the matter (gravitational force on the electrons is negligible). As the luminosity of an object increases, the radiation pressure on the electrons can increase so much that the net force on electron-proton pairs acts outwards, so that there is no further accretion. This reduces the luminosity until the forces again become equal. The luminosity at which this happens is the maximum achievable luminosity and is known as the *Eddington limit* given by

$$L_{Edd} = 1.25 \times 10^{38} \frac{M}{M_{\odot}} \quad erg \;\; s^{-1} \tag{2.1}$$

where M is the mass of SMBH.

- **Corona:** Corona contains extremely hot electrons surrounding the disk. The population of hot electrons interacts via IC scattering with the UV photons leading to the emission of hard X–ray continuum.

- **Broad Line Region (BLR):** Due to the strong gravitational field, the gas clouds move very fast in the potential of the SMBH and a cloud of highly ionized gas is created upto a radius of 10^{-2} pc as shown in Figure 2.2. The emission lines produced from the moving ionized gas are widened due to Doppler broadening. Therefore, this compact region around the central part of AGN is referred to as *Broad Line Region*.

- **Torus:** The molecular torus is a dusty region located well outside the accretion disk and BLR at 1-10 pc from AGN center. This region obscures the BLR emission by the absorption via an idealized dust along the transverse line of sight. Due to this absorption property, the absence of broad emission lines can be explained for those AGN where line of sight crosses this structure when viewed from the equatorial plane. The emission from torus region mainly occurs in the IR band.

- **Narrow Line Region (NLR):** Clouds from interstellar medium move slowly outside the molecular torus and are ionized by the radiation which flows from the central engine. These slower motion clouds generate narrow emission lines in their optical spectrum. Therefore, this zone is denoted as narrow line region but it consists of an extensive region. It is located at $\sim$100 pc from the AGN center and is not blocked by the torus.

- **Jets:** In radio loud AGN, a pair of relativistic jets pointing in opposite direction and perpendicular to the disk plane appears. The radio jets become prominent beyond the narrow line region and extend up to large distances $>$ 100 kpc. The jet formation process is still not well understood, but it is commonly assumed that they are generated in the disk region very close to SMBH and are strictly connected to the accretion disk. Jets are thought to be mainly consisting of ionized matter outflow, which includes electrons, protons

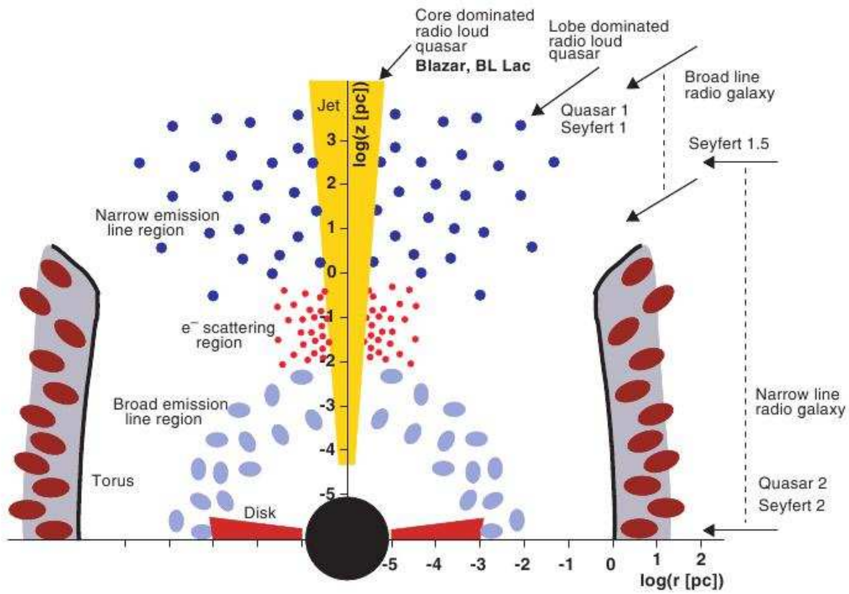

Figure 2.2: An artistic view of AGN unification scheme in a single black hole case.

and their interaction products entangled in a magnetic field. The emission from the jet is assumed to be originating from this relativistic matter outflow along the jet.

2.2 Blazars

Blazars are the most enigmatic class of radio loud active galactic nuclei, which host a jet oriented at an acute angle to the line of sight of the observer. They are characterized by distinctive and extreme properties, such as large amplitude and rapid variability, superluminal motion and strong emission over the entire electromagnetic spectrum. Blazars represent the most abundant population of extragalactic sources at TeV energies, but not all blazars have been established as TeV γ–ray emitters. These sources are known to produce flares of duration as short as few minutes or outbursts of duration as long as many months. This, coupled with the non-thermal nature of their emission, implies that the photons from blazars most likely originate in the jets that are directed roughly towards us.

2.2.1 General Properties

Blazars are excellent laboratories for studying physical processes in the jets and black hole systems in general. Due to production of GeV to TeV photons in their relativistic jets, these objects are particularly relevant to the field of γ–ray astronomy. The important observational characteristics of blazars are mentioned below.

- The name *blazar (blazing quasar)* goes back to the astronomer Ed Spiegel, who originally used it to denote a combination of Optically Violent Variable (OVV) quasars, FSRQs and and BL Lacs.

- It is widely accepted that the relativistic jet is the key element of the observed blazar emission. A convenient definition for the pointing of blazar jet is to require that the viewing angle $< 1/\Gamma$, where Γ is the bulk Lorentz factor of the jet emitting plasma.

- Virtually, every blazar exhibits superluminal motion of jet in high resolution radio maps which is easily explained by relativistic bulk motion along the line of sight.

- Acceleration processes in the jet generate non-thermal, high energy emission over wide energy range covering almost 20 orders of magnitude from radio to VHE γ–rays, which completely masks the thermal emission from the surrounding host galaxy.

- The broadband emission from blazars is characterized by high and variable polarization and very high luminosities coupled with a flat radio spectrum that steepens in the IR-optical bands and a rapid variability from radio to γ–ray bands with weak or absent emission lines.

2.2.2 Spectral Energy Distribution

The spectral energy distribution (SED) is a graphical representation of bolometric luminosity *vs* emission frequency or energy. This is a broad band spectrum covering the whole range of frequencies, from radio to VHE γ–rays. Such a plot has the advantage of showing approximately the emitted energy per unit logarithmic frequency interval, indicating immediately the band in which most of the energy is released. The observed SED of blazars is characterized by two humps: the first occuring at low energy in IR to X–ray regime, and second one located at GeV-TeV energies in HE/VHE regime. The observed SED of a candidate blazar is shown in Figure 2.3 as a representative example. The total energetic output is dominated by the high energy component and the position of HE/VHE hump is shifted according to the low energy hump. The SED of blazars are mainly characterized by three important features: flux level, peak frequencies and spectral slopes. The emission at low energies in IR to X–rays is highly polarized which gives a hint that it is mainly produced by synchrotron radiation of relativistic charged particles in magnetic fields. The emission at high energies is supposed to originate from IC scattering of low energy *seed* photons coming either internally from the synchrotron radiation of the jet or externally from various radiating sources. However, the origin of HE/VHE peak can also be described by hadronic processes, where VHE photons are generated by interaction of protons in the jet. The exact mechanism driving the high energy emission from blazars still remains poorly understood.

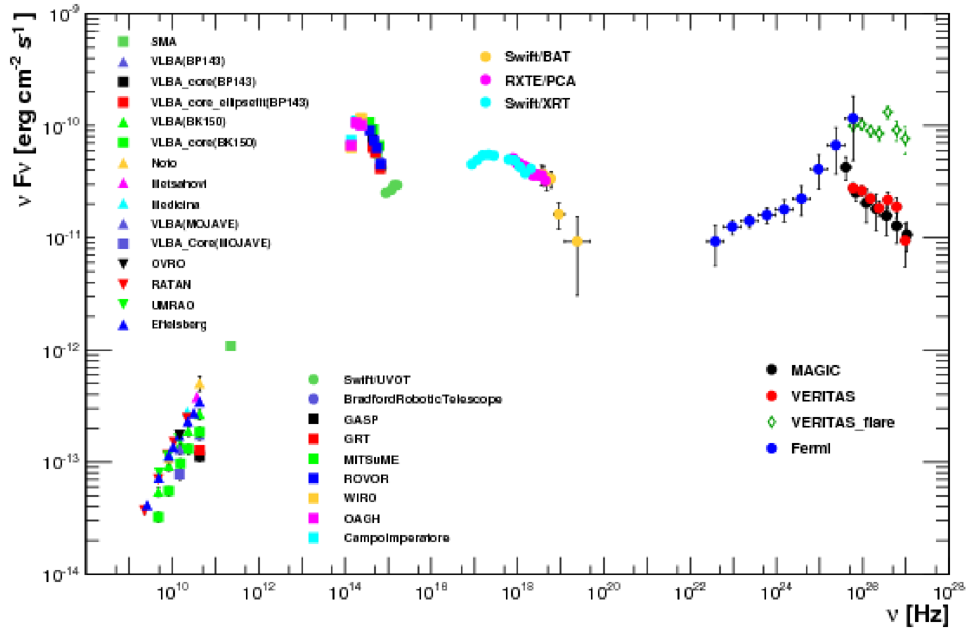

Figure 2.3: SED of a typical blazar (Mrk 501) observed during an extensive multi-wavelength campaign (Figure adopted from [2.5]).

2.2.3 Classification

While all blazars share the same property of emitting variable, non-thermal radiation across the entire electromagnetic spectrum, they also display diversity. Blazars are mainly divided into two subclasses: FSRQs and BL Lacs depending on their optical spectral properties. Blazars have been classified in the past according to heterogeneous criteria, often based on observational properties related to the energy band where they were first discovered. This lack of a stable and clear definition can lead to multiple classification of the same object and may cause subtle selection effects and biases in statistical analyses. The current blazar classification depends on the details of their appearance in the optical band where they emit a mix of three types of radiation: light from the host giant elliptical galaxy, thermal radiation from accretion disk & BLR region and non-thermal jet emission. The strong non-thermal radiation spanning the entire electromagnetic spectrum, is composed of two basic components (synchrotron and IC scattering) forming two humps at low and high energy in the SED of blazars. The peak of low energy hump due to synchrotron radiation (ν_{peak}) can occur at different frequencies from 10^{12} to 10^{18} Hz, reflecting the maximum energy at which particles can be accelerated [2.6]. Based on the position of synchrotron peak ferquency in the SED, all types of non-thermal dominated AGNs and blazars in particular are classified in three subgroups [2.7]:

- *Low synchrotron peaked blazars* or **LSP :** Synchrotron power peaks at low energy in the IR band or $\nu_{peak} \leq 10^{14}$ Hz. X–ray emission is flat and IC scattering occurs in Thompson regime.

- *Intermediate synchrotron peaked blazars* or **ISP :** Synchrotron emission peaks at intermediate energies i.e $10^{14} \leq \nu_{peak} \leq 10^{15}$ Hz. X–ray band includes both the tail of synchrotron emission and the rise of IC component.
- *High synchrotron peaked blazars* or **HSP :** The peak of synchrotron power reaches UV or higher energies i.e $\nu_{peak} \geq 10^{15}$ Hz. Emitting particles are accelerated at much higher energies so that the synchrotron emission dominates the observed flux in X–ray band and IC scattering occurs in the Klein Nishina regime.

2.2.4 Blazar Sequence and Evolution

The SED of blazars form a spectral sequence which implies the existence of a strong anticorrelation between bolometric luminosity and synchrotron peak frequency [2.8]. The peaks of two components of blazar SED are governed by a single parameter called bolometric luminosity. The main suggested trend is that with increasing luminosity both the synchrotron peak and IC peak move to lower frequencies and that the latter becomes energetically more dominant. As the bolometric luminosity increases, the synchrotron peak of blazar SED moves to lower frequencies and it follows the sequence: HSP BL Lac (HBL)→ LSP BL Lac (LBL)→ FSRQ. This implies that the sequence FSRQs→LBLs→HBLs goes in decreasing order of luminosity and increasing order of peak frequency. According to the blazar sequence, the bolometric power output of FSRQs is strongly γ–ray dominated, especially during flaring states, while HBLs are expected to be always synchrotron dominated.

The difference in redshift distribution and cosmological evolution between BL Lacs and FSRQs is a long standing blazar puzzle. FSRQs are typically found at redshifts 0.432 to 5.5, while BL Lac objects are much closer with very few cases at redshift greater than 0.6. FSRQs show a redshift distribution that peaks at redshift $z > 1$. The cosmological evolution of two blazar subclasses is very different, with FSRQs evolving strongly and BL Lac objects showing moderate or negative evolution in the X–ray band.

2.2.5 Unusual Activities in Blazars

Blazars are known to be highly variable across nearly the entire electromagnetic spectrum, producing flares of duration as short as a few minutes or outbursts of duration as long as many months. The high energy emission and the erratic, rapid and large amplitude variability observed in all accessible spectral regimes are two main defining properties of blazars. This coupled with the non-thermal nature of their emission, make blazars excellent laboratories for studying some interesting physical processes in their jets. Two important and interesting activities happening in blazars are described below.

- **Variability :** Blazars are known to be variable at all wavelengths. They are characterized by strong and chaotic variability, occasionally producing spectacular flares. Typically, the variability amplitudes are the largest and variability time scales are the shortest at the high frequency ends of the two SED components. In HSPs, this refers to the X–ray and VHE γ–ray regimes. The nature of blazar variability is stochastic and is characterized by a very high duty cycle [2.9]. The study of variability is particularly important in gamma-ray astronomy because most of the bolometric luminosity is emitted as γ–rays. Based on the time scale, blazar variability is classified into three classes: (i) intraday variability (IDV), also known as micro or intranight variability with time scales from a few tens of minutes to less than a day [2.10], (ii) short time variability (STV), characterized by time scales from several days to a few months and (iii) long time variability (LTV) covers changes from several months to many years [2.11]. The variability time scale of blazars can be used to constrain the emission region size through light travel time effects.

- **Flaring :** The intermittent episodes of major brightening in blazars on time scales of days or even shorter with substantial flux surges are known as *flares*. The flaring activity where blazars undergo apparently random flux increase is a very promising and interesting characteristic of these sources. In a very simple way, the flare can be defined as a contiguous period of time, associated with a given flux peak, during which the flux exceeds half of the peak value, and this lower limit is attained exactly twice-at the begnning and at the end of the *flare*. The precise mechanism that causes flaring in blazars is not yet understood. The flares could ultimately be related to internal shocks in the jets, or to major ejection of new components of relativistic plasma, or to magnetic reconnection events like solar flares. The amplitude and duration of flares probably reflect the energetics and physical time scales involved in the processes. The SED of TeV-blazars is known to evolve significantly during a major outburst or *flare* with duration of weeks or months. The large γ–ray flares with no counterparts in low energy bands are referred to as “orphan TeV flares”.

2.2.6 VHE Blazar Candidates

Blazars emitting γ–rays in VHE regime are known as TeV or VHE blazars. The number of blazars from which TeV γ–rays have been detected so far is more than 60 and is continuously increasing with the advent of new generation high sensitivity ground based telescopes. Most of the detected extragalactic γ–ray sources belong to the blazar class and currently they are the largest source population for TeV gamma-ray astronomy.

- **Prediction from X–ray Observations:** The strong connection between TeV and X–ray emission was first observed from two blazars Mrk 421 and Mrk 501 during their high activity state. In 1998, Mrk 421 showed a tight correlation between the emission in the X–ray and TeV bands, implying that the radiation produced in the two bands is co-spatial and produced by the same population of electrons [2.12]. The connection between TeV and X-ray emission was also clearly evident during the 1997 flare of Mrk 501, when this source was observed by the X–ray satellite *Beppo*SAX in an extreme spectral state [2.13]. At the same time, the source underwent a major flare in TeV band and continued to be active at TeV energies for several months [2.14]. Motivated with these observations, Costamante and Ghisellini (2002) considered several published samples of BL Lac objects, and proposed a simple and handy tool to identify and select the most promising TeV candidates [2.15]. The main point they emphasized concerns the requirement of both: high energy electrons and sufficient seed photons to originate the TeV emission. Therefore, the candidate BL Lac objects must not only have their synchrotron peak located at high energies, but also have sufficient radio through optical flux. A simple homogeneous emission model was applied to fit the synchrotron component of the SED of the best TeV candidate BL Lac and to predict the IC spectrum for its VHE emission.

- **TeV Blazar Catalog :** The discovery of TeV γ–ray emission from more than 60 blazars, is one of the most remarkable achievements of the last two decades in *Astrophysics*. The first extragalactic source discovered at TeV energies was Mrk 421 [2.16], a blazar of BL Lac subclass. The blazars discovered so far in the TeV catalog[1] are shown in the Figure 2.4 and their number continues to increase steadily. The majority of the known TeV blazars are HSPs, in part because of inherent biases in the target selection: initially, objects were chosen based primarily upon their radio and X–ray spectral properties [2.15]. More recently, the ground based TeV observatories have expanded their selection criteria, using additional guidance from *Fermi*-LAT observations, and multi-wavelength observation triggers. This has broadened the catalog to include ISPs and LSPs. Recently three FSRQs: PKS 1222+21, PKS 1510-089 and 3C 279 have been detected by ground based TeV instruments. M87 is the largest known radio galaxy at a redshift of z=0.0044, discovered to emit TeV γ–rays. A unique additional case is the TeV detection from IC 310. The source, originally classified as head-tail radio galaxy, was identified as VHE emitter in an analysis of the highest energy *Fermi* photons [2.17] and then subsequently detected from the ground by *MAGIC* telescope [2.18]. From very high resolution radio observations, there are little indication for jet bending [2.19], supporting the case that IC 310 may be a weakly beamed blazar [2.20].

2.3 VHE γ–ray emission from Blazars

The mechanisms which drive the high energy emission from blazars remain poorly understood. Several scenarios have been proposed to explain the VHE emission from blazars. However, none of them is fully self consistent and the current data are not sufficient to firmly rule out or confirm a particular mechanism. The origin

[1] http://tevcat.uchicago.edu/

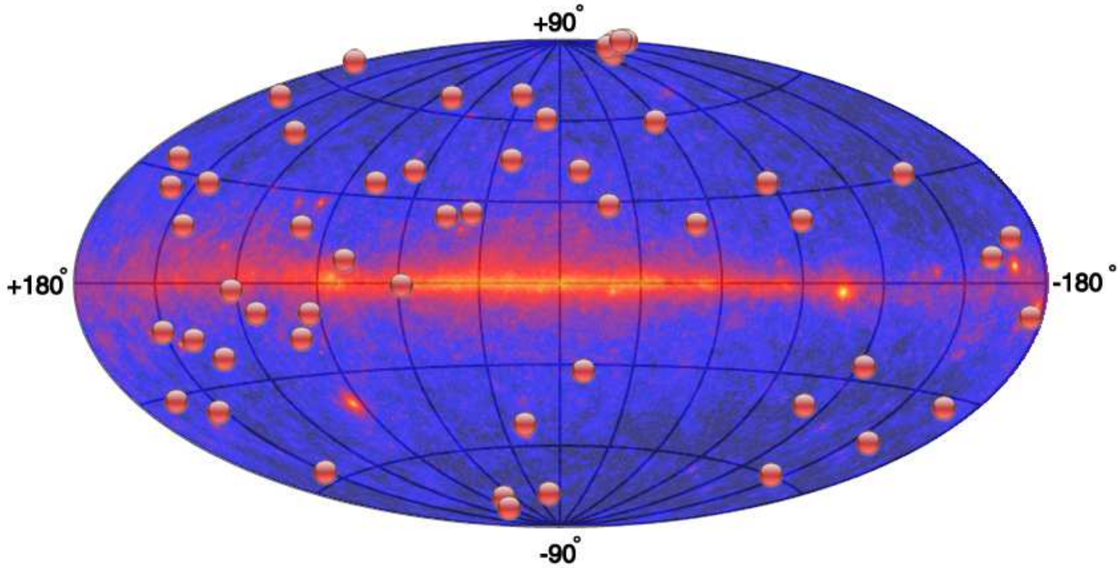

Figure 2.4: The TeV catalog of blazars detected above 100 GeV along with the *Fermi* sky map in the background. (Credit:http://tevcat.uchicago.edu)

of low energy component is well established and is beleived to be synchrotron radiation from relativistic leptons in the co-moving frame. The nature of high energy hump is a controversial issue and poorly understood. Since the accelerated particles responsible for TeV γ–ray emission can be either leptons (electrons or positrons) or hadrons (mostly protons), the existing emission models are grouped into three families: *Leptonic*, *Hadronic* and *Hybrid*. All the three models attribute the low energy peak of blazar SED to synchrotron radiation from relativistic electrons and positrons in the jets, but they differ on the origin of high energy peak. The basic characteristics of acceleration mechanism and various radiation processes for TeV γ–ray production in blazars are briefly described below.

2.3.1 Particle Acceleration

Independent of the emission mechanism, the only way to produce VHE or TeV γ–rays is to accelerate charged particles to higher energies. Among the various acceleration mechanisms, the most promising process for particle acceleration to high energies in blazar jet is "*Fermi* Acceleration" at strong magnetohydrodynamic shocks. Shock fronts arise when the relativistic flows encounter the ambient material. Variability in the central engine of blazars may also result in internal shock waves along the jet. First order *Fermi* process operating at collisionless relativistic shocks is the most widely accepted mechanism of particle acceleration in astrophysics. It is based on the idea that the particles undergo stochastic elastic scatterings both upstream and downstream of the shock front [2.21]. This causes particles to wander across the shock repeatedly. On each crossing, they receive an energy boost as a result of the relative motion of the upstream and downstream plasmas and a particle distribution with characteristic spectral index is produced. Several factors, such as the life time of the shock front, or its spatial extent, can limit the energy to which particles can be accelerated in this process. However, even in the absence of these, acceleration will ultimately cease when the radiative energy losses that are inevitably associated with the scattering process overwhelm the energy gains obtained upon crossing the shock. Exactly when this happens depends on the complexity of the scattering process.

2.3.2 Relativistic Effects

The emission from the blazar jet is assumed to come from accelerated charged particles moving at relativistic velocities along the jet. Relativistic jets in blazars transport energy in the form of bulk motion of protons, leptons and magnetic field. When part of this power is dissipated, the particles emit the beamed radiation we observe, consisting of two broad humps in the SED. Due to high velocities, the physically measured values are affected by *relativistic beaming* effect. This effect is responsible for an apparent brightening of the relativistically moving sources. For a source moving at velocities close to the speed of light (Lorentz factor: $\Gamma >>1$) three main relativistic effects appear:

- **Light Aberration:** Aberration of light is an astronomical phenomenon which produces an apparent motion of the celestial objects. The apparent speed of source inferred by observer is given by :

$$\beta_{app} = \frac{\beta sin\theta}{1 - \beta cos\theta} \tag{2.2}$$

  where β is the speed of source (in units of speed of light in vacuum) moving towards the observer. This equation represents superluminal motion of the jet in blazars.

- **Doppler Boosting and Beaming:** For a source emitting isotropically in its rest frame, the observed emission is collimated in a cone of angle $\sin\theta=1/\Gamma$. For highly relativistic speeds $\Gamma >>1$ and $\theta \approx 1/\Gamma$. Thus, higher the speed of emitting object, the observed radiation will be more collimated in the forward direction within a cone of half angle $1/\Gamma$. This is called *beaming effect*. The frequency of the emitted photons from the moving source will be observed blue-shifted or redshifted depending on the direction of movement. In case of blazars, emission region moves towards the observer and the observed frequency is given by:

$$\nu_{obs} = \delta \nu_{em} \tag{2.3}$$

  where $\delta = 1/\Gamma(1 - \beta cos\theta)$, is called Doppler factor or beaming factor. The fluxes from blazars are dramatically enhanced by the effects of Doppler boosting and the observed flux is related to emitted flux as:

$$F_{obs} = \delta^4 F_{em} \tag{2.4}$$

- **Arrival time contraction:** The time difference detected by observer is not same as the time difference in the rest frame of source. The observed time difference is given by:

$$\Delta t_{obs} = \frac{\Delta t_{em}}{\delta} \tag{2.5}$$

  This relation represents the arrival time dilation in blazar observations.

2.3.3 Leptonic Models

The leptonic models assume the direct emission from relativistic electrons or electron-positron pairs via the synchrotron and IC mechanism. The leptons are accelerated to ultra-relativistic velocities by shock acceleration. The high energy radiation is produced via Compton upscattering of soft photons off the same ultra-relativistic leptons producing the synchrotron, through IC process. The seed soft photons can come either from synchrotron emission of the same electron population (SSC: Synchrotron Self Compton models) or from an external region (EC: External Compton models). These two models in leptonic scenario are qualitatively described below.

- **Synchrotron Self Compton (SSC) model:** The SSC model [2.22,2.23,2.24] is one of the simplest models for understanding the VHE γ–ray emission from many astrophysical systems. The one zone homogeneous SSC models assume that the soft photons of IC scattering for VHE γ–ray emission are the synchrotron photons in the same region within the jet. The emission region is characterized by a spherical blob moving at relativistic speed in the tangled magnetic field along the jet with a small viewing angle to the line of sight. The blob contains relativistic electrons accelerated by shock acceleration processes. Assuming that a diffusive shock acceleration mechanism is responsible for the initial electron acceleration, the electron injection spectrum is described by a power law $dN/dE \propto E^{-p_1}$ with $p_1 \sim 2$. Due to synchrotron cooling effects, the spectrum is modeled to show a break where radiative cooling becomes dominant. At this point the electron spectrum steepens by one ($p_2 = p_1 + 1$) and can be described by three parameters E_{min}, E_{max} and E_{break}. In the presence of randomly oriented magnetic field of constant strength B, the isotropic electron population with above spectrum produces isotropic synchrotron photons in the source frame. The upscattering of synchrotron photons by the same relativistic electron population gives rise to the emission of VHE γ–ray photons in the source. The observed radiation is strongly affected by relativistic beaming effects. The SSC model is completely described by seven parameters: magnetic field strength, size of blob, Doppler factor (characterizing the emission region) and electron injection spectrum (E_{min}, E_{max}, E_{break}) plus the variability time scale. The leptonic SSC models predict a close temporal flux correlation between the synchrotron and Compton components.

- **External Compton (EC) model:** In EC mechanism, the seed photons for IC scattering are assumed to be ambient optical/IR photons, CMB photons or thermal radiation from different regions of the blazar. The possible sources of external seed photons include the accretion disk radiation [2.25,2.26], reprocessed optical-UV emission from circumnuclear material or BLR [2.27,2.28,2.29], IR emission from warm dust [2.30] or synchrotron emission from other regions of the jet itself [2.31]. The average energy of external photons as measured in local stationary frame lies in the range 0.1-10 eV. The importance of EC process strongly depends on the position of relativistic electrons with respect to the external radiation fields. As the emission region moves down the jet at relativistic speed, the electrons see an anisotropic distribution of target photons due to Doppler boosting. The observed SED of high luminosity blazars like FSRQs requires Compton upscattering of external photons to explain its high energy component.

While leptonic models under these assumptions have been successful in modeling blazar SEDs, they lack a self consistent basis for the shape of the electron distribution. In order to produce broad band SED as well as variability patterns, the time dependent electron dynamics and radiative transfer problems have to be solved self consistently. Such time dependent SSC models [2.32,2.33] have been developed and external radiation fields have been included in such treatments [2.34,2.35,2.36].

2.3.4 Hadronic Models

The hadronic models invoke the presence of highly relativistic protons, directly emitting high energy photons by proton synchrotron process and the low energy radiation is emitted by synchrotron radiation of co-accelerated electrons. The acceleration of protons to ultra-relativistic energies requires high magnetic fields of several tens of Gauss. In the presence of such high magnetic fields, the direct synchrotron radiation of the primary protons contributes to the emission of high energy radiation [2.37]. When the relativistic protons reach the threshold for photo-meson production via $p-\gamma$ or $p-p$ interactions, generation of mesons like electrically and neutrally charged pions takes place [2.38]. The neutral pions (π^0) decay into photons, while charged pions ($\pi^{\pm}$) generate charged muons ($\mu^{\pm}$). In the presence of high magnetic fields, the secondary muons and mesons produce high energy synchrotron photons [2.39]. Thus, in order to construct a self-consistent synchrotron-proton blazar (SPB) emission model, the contributions from proton-synchrotron cascade, π^0 cascade, $\pi^{\pm}$ cascade and ($\mu^{\pm}$) synchrotron cascade must be taken into account. It has been shown that the π^0 cascades and $\pi^{\pm}$ cascades generate featureless γ–ray spectra [2.39], in contrast to proton-synchrotron cascades and ($\mu^{\pm}$) synchrotron cascades that produce a double-humped γ–ray spectra. In general, direct proton and $\mu^{\pm}$ synchrotron radiation is mainly responsible for the high energy hump in blazars, whereas the low energy hump is dominated by synchrotron radiation from the primary electrons, with a contribution from secondary electrons. In case the γ–ray radiation is of hadronic origin, one also expects to detect VHE neutrinos from blazars. The detection of neutrinos would clearly favour this model.

Hadronic models are attractive, as they are characterized by particle acceleration up to extreme energy of 10^{19} eV and thus they explain cosmic ray acceleration to the highest energies. Leptonic models generally lack this virtue. Hadronic blazar models also offer a physical interpretation for the spectral sequence of BL Lac subclasses [2.39]. The spectra of HSPs are well reproduced by proton synchrotron dominated SPB models where the intrinsic primary synchrotron photon energy density is small, consistent with the low bolometric luminosity of those objects. As the synchrotron photon energy density increases towards the LSP-like synchrotron properties, protons suffer increasingly strong $p\gamma$ pion production loses, and the contributions from the $\pi^{\pm}$ and $\mu^{\pm}$ synchrotron cascades become dominant at higher energies. This results in a decreasing SED peak frequency of the γ–ray component. One of the biggest problems with hadronic models is that the acceleration and cooling processes involved are rather slow, while flux variability in blazars is observed over very short time spans from minutes to day.

2.3.5 Hybrid Models

The leptonic and hadronic models described above are certainly only to be regarded as extreme idealizations of a blazar jet. Realistically, both types of processes might play a role to some extent and should thus be considered to a comparable level of sophistication. Observations of orphan TeV flares in few blazars [2.40,2.41] provide strong support for the importance of hadronic processes in objects which other spectral and variability features are generally well reproduced by leptonic jet model. The orphan TeV flare preceeded by an ordinary, correlated X-ray and TeV flare suggests the need for models that explain flares dominated by leptonic interactions as well as flares where non-leptonic components might play an important role within the same system. The emission models based on leptonic and hadronic interactions together in the blazar jet are referred to as hybrid models. Following processes in the context of hybrid models have been proposed:

- A runaway pair production avalanche is initiated by mildly relativistic protons interacting with reflected synchrotron photons via $p\gamma$ pair production, as the primary pair injection mechanism in blazar jets [2.42]. This model is known as "superpile model" and spectral characteristics resulting from the model have been considered in gamma-ray bursts [2.43].

- The conversion of ultra-relativistic protons into neutrons via $p\gamma$ pion production on external soft photons provides a mechanism to overcome synchrotron losses of protons near the base of blazar jets and, thus allow blazar jets to remain collimated out to kpc scales [2.44].

- A fully self consistent, time dependent homogeneous one zone model has been developed for the radiation from a relativistic plasma which assumes electron and proton injection into a power law distribution and includes the self consistent cooling of protons by $p\gamma$ pion production processes and their contributions to the pair populations [2.45].

- A model specifically developed to explain "orphan" TeV flares in blazars assumes that the primary, correlated X-ray and TeV flare is explained by a standard SSC model while the secondary TeV flare is explained by π^0-decay γ–rays as a result of photomeson production from relativistic protons interacting with synchrotron photons that have been reflected off clouds located at pc-scale distances from the central engine [2.46,2.47]. This model is known as "hadronic synchrotron mirror model".

2.3.6 Magnetic Field Equipartition

When fitting the SED of blazars, consideration should be given to the energy balance between the magnetic field and the particle content in the jet, as this contains information on the jet launching and acceleration mechanisms. If the relativistic jets are powered by the rotational energy of the central black hole, the jets are expected to be initially Poynting flux dominated. The energy thus carried primarily in the form of magnetic fields then needs to be transferred to the relativistic particles which can then produce the observed high energy emission. This energy conservation is expected to cease when the energy densities in the magnetic field and in relativistic particles approach equipartition. At equipartition magnetic field, the jets are not expected to become matter dominated within the central few parsecs of AGN, where the high energy emission in blazars is believed to be produced. If magnetic pressure plays an essential role in collimating and confining the jets out to kpc scales, the energy density (pressure) of particles in the jet cannot dominate over magnetic field pressure, otherwise the jets would simply expand conically. If SED fits require far sub-equipartition magnetic fields, this may indicate that the jets are magneto-hydrodynamically powered by the accretion flow. In this case, magnetic fields may be self generated in shear flows in the case of a fast inner spine surrounded by a slower, mildly relativistic out flow (sheath). The magnetic field for which the total energy of the system is minimum differs with equipartition magnetic field by a factor less than 10% and the total energy derived from both the magnetic fields is almost same. Hence it is desirable to use equipartition condition while modeling the blazar SED to ensure the minimum energy condition [2.48].

2.4 Fermi-Large Area Telescope

The Fermi Gamma-ray Space Telescope *(Fermi)*, formerly the Gamma-ray Large Area Space Telescope (GLAST), is an international and multi-agency observatory class mission to explore the γ–ray sky in the energy range from 8 keV to 300 GeV

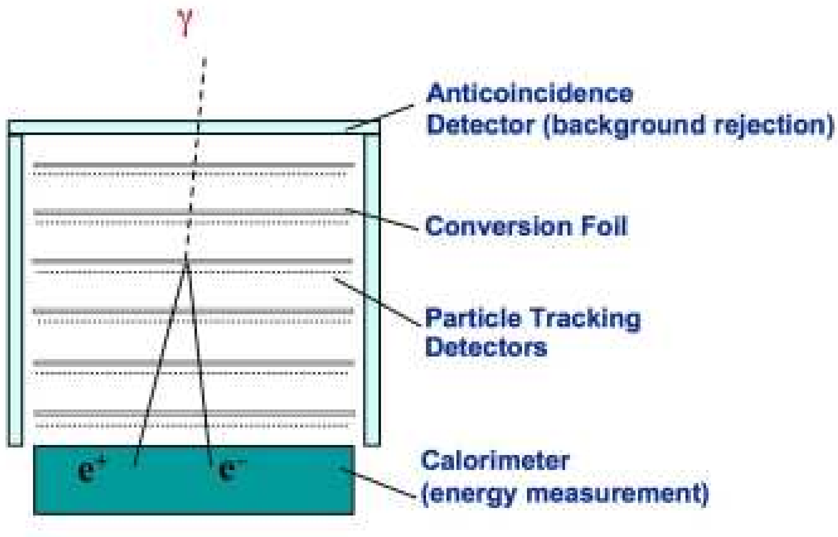

Figure 2.5: Scheme of *Fermi*-LAT design (Credit:glast.stanford.edu/instrument.html)

[2.49]. The *Fermi* satellite was successfully launched by NASA on June 11, 2008 from the launch pad 17-B at Kennedy Space Flight Center (Florida, USA), into an initial orbit at about 565 km altitude with a 25.3° inclination and an eccentricity < 0.01. The satellite hosts two instruments: Large Area Telescope (LAT) and GLAST Burst Monitor (GBM). The main instrument *Fermi*-LAT operates in an energy range from 20 MeV to more than 300 GeV and the GBM records transient phenomena in the sky over the energy band 8 keV-40 MeV .

2.4.1 Science Objectives of LAT

The *Fermi*-LAT provides an increase in sesitivity by more than an order of magnitude over its predecessor *EGRET* and *AGILE*. Unlike *EGRET*, LAT is also able to observe the whole sky several times per day allowing a much deeper and dynamic monitoring of high energy phenomena in the sky. The main scientific objectives addressed by the LAT include (i) determining the nature of the unidentified sources and the origins of diffuse emission revealed by *EGRET*, (ii) understanding the mechanisms of particle acceleration operating in celestial sources, particularly in AGN, pulsars, supernovae remnants, and the Sun, (iii) understanding the HE behavior of GRBs and transients, (iv) using γ–ray observations as a probe of dark matter, (v) using HE γ–rays to probe the early universe and cosmic evolution of high energy sources beyond the redshift z=6.

2.4.2 LAT Design

The LAT is a satellite based pair conversion imaging telescope, designed to measure the directions, the energies, and exact time of arrival of HE γ–rays, while rejecting the background from cosmic rays, incident on the detector. The design of the detector is based on the principle of conversion of incident γ–rays into e^-e^+ pairs while interacting with high Z material as shown in the Figure 2.5. The major subsystems of LAT are briefly described below.

- **Precision converter-tracker:** The converter-tracker subsystem is the central detector of LAT to detect HE γ–rays and to determine the direction of incident γ–ray photons. This subsystem is composed of 16 planes of high Z material (tungsten) in which the incident γ–rays can produce e^-e^+ pair [2.49]. The converter planes are interleaved with position sensitive silicon strip detectors that record the passage of charged particles, thus measuring the tracks of particles produced in pair conversion. The conversion signature is also used to reject the much larger background of charged cosmic rays.

- **Calorimeter:** The main purposes of the calorimeter are two fold : measurement of energy deposition due to electromagnetic particle shower resulting from pair production in converter-tracker and imaging of the shower development profile [2.49]. The calorimeter with modular structure consists of 16 identical modules. Each calorimeter module has 96 scintillating CsI(T1) crystal detector elements providing a total vertical depth of 8.6 radiation lengths for a total instrument depth of 10.1 radiation lengths. Each crystal element is read out by PIN photodiodes, mounted on both ends of the crystal, which measure the scintillation light that is transmitted to each end. The difference in light travel provides a determination of the position of energy deposition along the CsI crystal. The requirement of measuring photon energy upto at least 500 GeV leads to the presence of a heavy calorimeter ($\sim$ 1800 kg) to absorb enough of the photon induced shower energy to make this measurement.

- **Anticoincidence detector:** The purpose of anticoincidence detector (ACD) is to provide charged particle background rejection [2.49]. This purpose dictates its main requirement to have high charged particle detection efficiency. The ACD is required to provide at least 0.9997 efficiency for detection of charged particles entering the field of view of the LAT detector.

  The as-built dispostion of LAT with the three main subsystems converter-tracker, calorimeter and ACD is shown in Figure 2.6.

- **Data Acquisition System :** The Data Acquisition (DAQ) System collects the data from other subsystems, implements the multi-level event trigger, provides on-board event processing to filter events in order to reduce the number of downlinked events, and provides an on-board science analysis platform to rapidly search for transients [2.49]. The DAQ architecture is hierarchical with 16 tower electronic modules (TEM) providing the interface to tracker

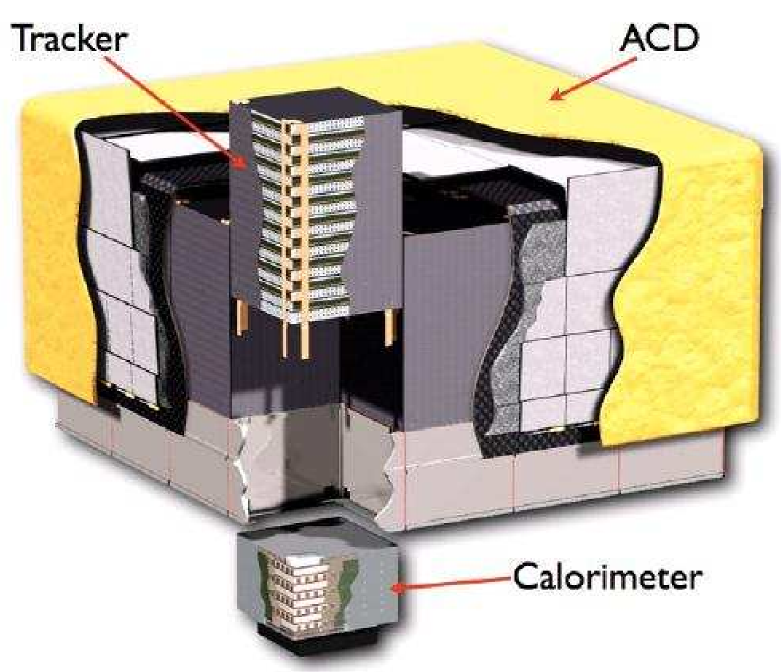

Figure 2.6: *Fermi*-LAT with three main subsystems: Tracker, Calorimeter and Anticoincidence Detector.(Credit:glast.stanford.edu/instrument)

and calorimeter pair. Each TEM generates instrument trigger primitives from combinations of tower subsystem triggers, provides event buffering to support event readout and communicates with the instrument-level event builder module (EBM).

- **Event Classification:** All events detected by the LAT are divided into three classes: *Transient, Source* and *Diffuse*. For the *Transient class*, the background rejection is set to allow a background rate of < 2 Hz, that corresponds to no more than one background event every five second within a 10° radius about a source. The *Source class* is designed to have a residual background contamination similar to that expected from the extragalactic γ–ray background flux over the entire field of view. Finally, the *Diffuse class* has the best background rejection where harsher cuts would not significantly improve the signal to noise ratio.

2.4.3 LAT Performance

The scientific performance of *Fermi*-LAT is defined by the design of its hardware, the event reconstruction and selection algorithms. The Instrument Response Functions (IRFs) are a set of analytical functions that describe the response of a detector to an incoming flux of particles. The IRFs depend not only on the instrument itself, but also on the reconstruction algorithms, on the background rejection algorithm,

Table 2.1: Summary of *Fermi*-LAT performance parameters

Parameters	Value
Orbit	Cirular (Altitude: 565 km)
Orbital Period	96 minutes
Energy Range	20 MeV–500 GeV
Effective Area	6500 cm^2 at 1 GeV
Live Time	76%
Timing Accuracy	$< 10\ \mu$s
Field of View	2.4 sr (20% of the sky) at 1 GeV
Energy Resolution	10% at 1 GeV
Single Photon Angular Resolution	0.6° at 1 GeV
Point Source Sensitivity	3×10^{-9} ph cm^{-2} s^{-1} (for spectral index $\sim$ 2.1)

and on any eventual selection of the events. The pre-launch response of LAT was tuned using simulation and beam test data. The performance parameters are subject to change due to the optimization of the selection algorithms. The main in-orbit performance parameters of *Fermi*-LAT at present are summarized in Table 2.1.

2.5 *Fermi* Blazar Observation Program

The *Fermi* satellite is in a 565 km altitude orbit with an inclination of 25.6°. The orbit has a period of 96 minutes, and its pole precesses about the celestial pole with a period of 53.4 days. At this inclination, satellite spends about 15% of the time inside the South Atlantic Anomaly (SAA). The radiation intensity is greater within SAA region than elsewhere for a given altitude. Therefore, science data taking is suspended while *Fermi* is within the SAA to avoid damage to the instruments. Physical run starts when satellite goes out from the SAA and stops when it re-enters in SAA. *Fermi* spends most of the time in sky survey mode with remainder split between pointed observations and calibrations. In sky survey mode, the azimuthal orientation of the LAT is constrained by the need to keep the spacecraft solar panels pointed towards the Sun and the radiators away from the Sun. Also, in order to reduce the contamination from the γ–ray bright Earth limb, time when the rocking angle of spececraft is larger than 52° and events with zenith angles larger than 100°, are collected.

2.5.1 LAT Detected Blazars

The first three months of sky-survey operation (August 4-October 30, 2008) with the LAT revealed 132 bright sources [2.50]. 106 of these sources indicated high confidence association with known AGN. This sample was referred to as the LAT

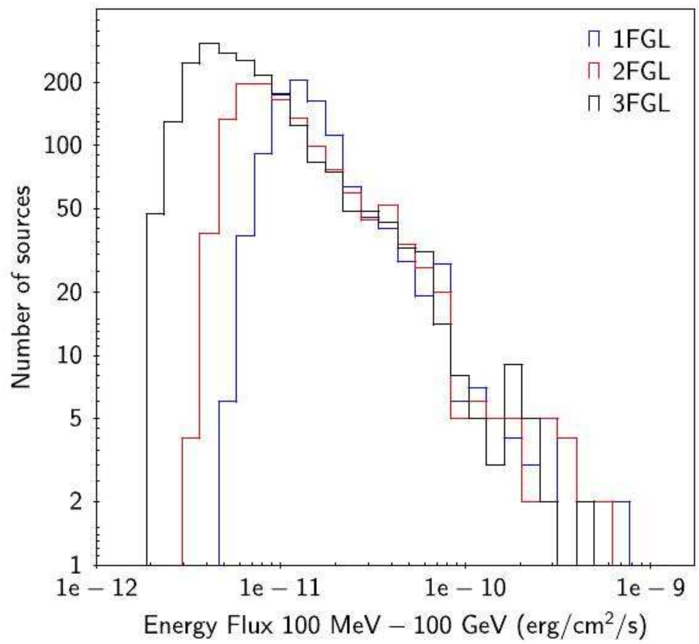

Figure 2.7: Distribution of energy flux for 3 catalogs: 1FGL (Blue), 2FGL (Red) and 3FGL (Black) [2.54].

Bright AGN Sample (LBAS). It contains 2 radio galaxies (Cen A and NGC 1275) and 104 blazars consisting of 58 FSRQs, 42 BL Lac objects and 4 blazars with unknown classification. Four new blazars were discovered on the basis of LAT detections. The source catalogs from LAT observations till today are summarized below.

- **1FGL catalog :** The First *Fermi*-LAT catalog (1FGL) of high energy γ–ray sources [2.51] contains 1451 sources detected by LAT during first 11 months of the science phase of the mission (August 4, 2008 - July 4, 2009) in the energy range 100 MeV to 100 GeV. Among the 1451 sources, 573 blazar candidates are identified in 1FGL catalog.

- **2FGL catalog :** The Second *Fermi*-LAT catalog (2FGL) of high energy γ–ray sources [2.52] contains 1873 sources detected and characterized during first 24 months of the mission (August 4, 2008 - August 1, 2010) in the 100 MeV to 100 GeV range of energy. Out of 1873 sources in 2FGL catalog, 802 objects are identified as blazars whereas 575 sources remain unassociated. The second LAT AGN catalog (2LAC) includes 1017 γ–ray sources located at high galactic latitudes detected during first two years of scientific opertaion [2.53]. A clean sample of 886 AGN from 2LAC catalog includes 395 BL Lac objects, 310 FSRQs, 157 candidate blazars of unknown type, 8 misaligned AGN, 4 NLS1 galaxies, 10 AGN of other type, and 2 starburst galaxies.

- **3FGL catalog :** The Third *Fermi*-LAT catalog (3FGL) of high energy γ–ray sources [2.54] in the energy range 100 MeV–300 GeV is based on the

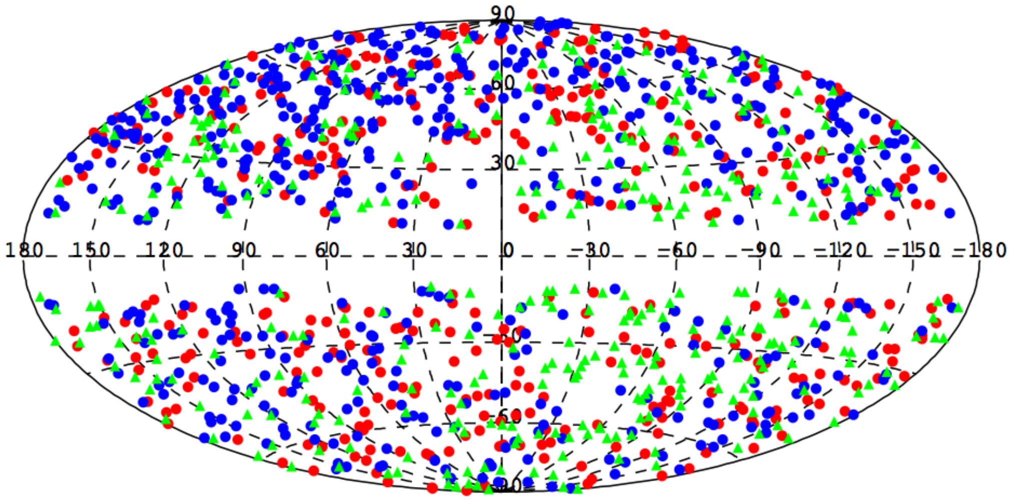

Figure 2.8: *Fermi*-LAT 4 year AGN catalog in galactic coordinates. Red: FSRQs, Blue: BL Lacs, Magenta: Radio Galaxies, Green: AGN of unknown type. (Credit:asdc.asi.it)

first four years (August 4, 2008 - July 1, 2012) of science data from *Fermi* mission. This catalog represents the deepest yet in this energy range. The 3FGL catalog incorporates twice as much data as 2FGL catalog and number of analysis improvements including an updated model for Galactic diffuse γ–ray emission, a refined procedure for source detection and improved calibrations at the event reconstruction level. The catalog contains a total of 3033 sources above 4σ significance with spectral properties and monthly light curves. More than 1100 of the identified sources are AGNs of blazar class; several other classes of non-blazar AGN are also reported in the 3FGL catalog. For 1009 sources, no plausible counterparts at other wavelengths have been found and pulsars represent the largest Galactic source class in this catalog.

The energy flux distribution in 1FGL, 2FGL and 3FGL catalogs is depicted in Figure 2.7. It is evident from the figure that the flux threshold in 3FGL is down to 3×10^{-12} erg cm^{-2} s^{-1}, from 5×10^{-12} erg cm^{-2} s^{-1} in 2FGL, and 8×10^{-12} erg cm^{-2} s^{-1} in 1FGL. Above this flux 2FGL and 3FGL distributions are entirely compatible.

The third AGN catalog (3LAC) is also based on the sources in 3FGL catalog with a significance greater than 5σ using the first four years of data [2.55]. The 3LAC includes 1591 AGN with large majority of these being blazars. The general properties of 3LAC sample confirm previous findings from earlier catalogs, but some new subclasses (ISP and HSP FSRQs) have been significantly detected. The location of AGN in the clean sample of 3LAC is shown in the Figure 2.8.

- **1FHL catalog :** Motivated with the study of γ–ray sky at even higher energies in the LAT data to find the hardest spectrum sources, catalog of sources

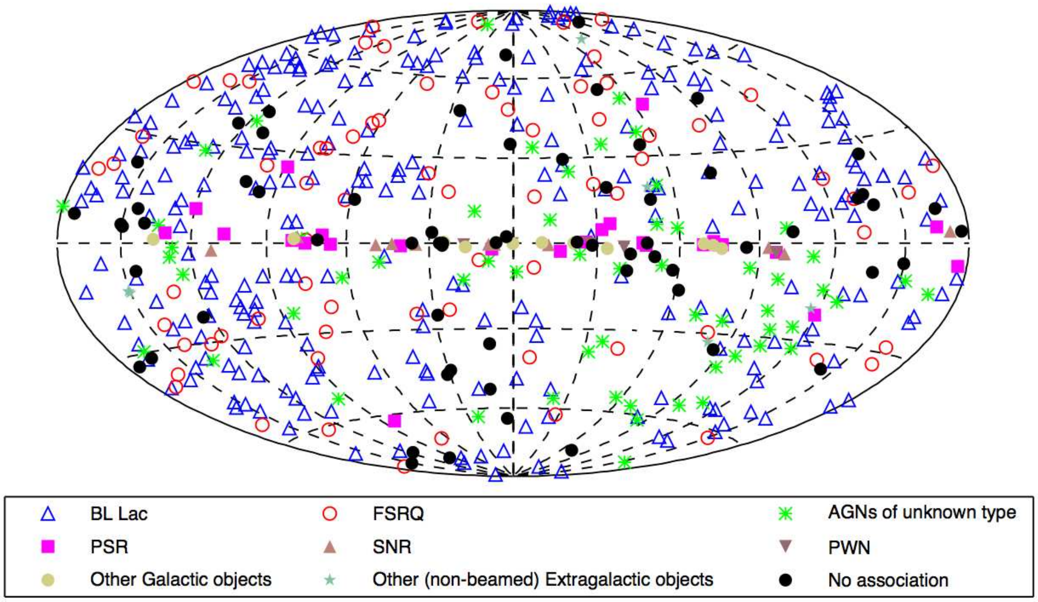

Figure 2.9: The First *Fermi*-LAT 3 year high energy (1FHL) catalog of sources above 10 GeV.(Credit:www.asdc.asi.it)

detected above 10 GeV has been presented. The first *Fermi* high energy catalog (1FHL) or GeV catalog [2.54] is based on data from LAT above 10 GeV accumulated during first three years of *Fermi* mission. The 1FHL catalog contains 514 sources, of which 449 sources are associated with the known sources. Among 514 sources, 393 are AGN and 27 are associated with known pulsars. Of the 1FHL sources not already detected in VHE range, 212 sources are flagged as good candidates for TeV observations based on their average properties for 3 years. The sources in 1FHL catalog are shown in Figure 2.9 in galactic coordinates.

2.5.2 Multi-wavelength Blazar Observation

The key objectives of *Fermi*-LAT are largely motivated by the discoveries of *EGRET* in the energy range 30 MeV-10 GeV. To probe the astrophysics of the sources it is important to make correlated observations across the electromagnetic spectrum. Progress in several areas requires coordinated multi-wavelength observations with both ground and space based telescopes. A number of observing programs have been established by *Fermi Science* effort to provide either regular monitoring or targeted observations of the sources. The multi-wavelength campaigns involving radio, optical, X–ray and gamma–ray observatories used in the present thesis are described below.

- **Radio:** In 2007, the 40 M radio Telescope at the Owens Valley Radio Observatory (OVRO) embarked on a new research campaign. In anticipation of the unique opportunities offered by the *Fermi*-LAT sky monitoring at γ–ray energies, the OVRO 40 M Telescope is monitoring more than 1800 blazars about twice per week at 15 GHz [2.57].

- **Optical:** To help in comprehensive understanding of the source structure and non-thermal emission mechanisms in blazars, *Steward Observatory* of the *University of Arizona* contributes optical data for the LAT monitored blazars [2.58]. The optical data include spectropolarimetry at a resolution of ~ 20 A°, broad band polarization & flux measurements and flux calibrated spectra spanning 4000–7600 A°. These data provide a comprehensive view of the optical variability of an important sample of objects during the *Fermi* Era. The observtaions are made from either of the *Steward Observatory* telescopes: 2.3 m Bok telescope or 1.54 m Kuiper telescope. For both telescopes, the southern declination limit is $\sim 40°$, whereas targets with declinations higher than 61° are not accessible with Kuiper telescope. All observations are obtained using the SPOL CCD Imaging/Spectropolarimeter.

- **X-Ray:** The broadband monitoring of blazars at many wavelengths, particularly the X–ray band where synchrotron peak often lies is very important for understanding the different emission processes and particle acceleration in the dynamic environments. *Swift* observations provide near real time results of *Fermi*-LAT *sources of interest* that are dominated by blazars and flaring sources. *Swift* is equipped with a co-pointed X-ray Telescope (XRT:0.2-10 keV) [2.59], a Burst Alert Telescope (BAT: 15-150 keV) [2.60], and a Ultraviolet/Optical telescope (UVOT: 180-600 nm) [2.61], providing inherent multi-wavelength coverage. Apart from *Swift*, a Japanese satellite, Monitor of All-sky X-ray Image (MAXI) provides X-ray observations is the energy range 2-20 keV [2.62].

- **VHE γ–ray:** The VHE or TeV observations, coming at the extreme end of the spectrum, are unique and generally stretch the models to their limits. The launch of *Fermi* has opened the possibility of combined studies of astrophysical sources above 100 GeV with existing ground based VHE γ–ray experiments such as $HESS$, $VERITAS$, $MAGIC$ and $TACTIC$. These observatories provide complementary capabilities for spectral, temporal, spatial and population studies of the high energy γ–ray sources. Joint observations cover a huge energy range from 20 MeV to over 50 TeV.

2.6 Summary

The potential scientific impact of observing VHE emission from extragalactic objects and blazars in particular is substantial. A significant fraction of the power released from these objects is within the VHE band. This makes the observation of VHE blazar spectra an important component of the overall understanding of these objects. With a better sample of well determined VHE blazar spectra available for study, a population based investigation of γ–ray production in these objects through broadband SED modeling will provide means to answer the long standing question of whether the VHE γ–rays have leptonic or hadronic origin in the jet. Model inferred properties of these new discoveries can also be used to understand how the γ–ray production may differ among various blazar subclasses, exploring the apparent blazar sequence and evolution of AGN.

The current catalog of VHE objects largely contains relatively nearby AGNs and only three have redshift above z=0.3. At energies above 100 GeV, BL Lac objects, and in particular HSPs constitute the largest known population of TeV extragalactic sources, detected by ground based Cherenkov telescopes. The search for new TeV candidate blazars is complicated by the fact that many of these objects do not yet have known redshifts. Initially, objects were selected based on radio and X–ray spectral properties. More recently, the TeV observatories have expanded their selection criteria, using additional guidance in the form of *Fermi*-LAT and other multi-wavelength observations. Also the information from time averaged spectra of blazars measured by *Fermi* can be used to predict the flux above 100 GeV observable with ground based TeV instruments. A catalog of TeV blazars from *Fermi* detected sources for ground based observations can be prepared by extrapolating the LAT spectrum to TeV energies taking into account the unavoidable EBL absorption of VHE γ–ray photons. The underlying assumption of this approach is that the extrapolation of LAT spectrum to VHE band is either a good estimate or an upper limit for the intrinsic VHE spectrum of the source, since they belong to the same hump in the SED.

The present understanding of the emitting high energy radiation is now gaining new insights from multi-wavelength observations. These observations allow to explore the SED of blazars across the entire electromagnetic spectrum, therefore granting the best acheivable understanding of physical processes that originate the observed radiation and their mutual relationship. The simultaneous multi-wavelength data are crucial in order to rule out or support some of the selected models out of many that compete in the effort of describing the physical processes at work.

2.7 References

[2.1] M. J. Rees, 1984, ARA&A, 22, 471

[2.2] R. Antonucci, 1993, ARA&A, 31, 473

[2.3] C. M. Urry & P. Padovani, 1995, PASP, 107, 803

[2.4] J. H. Krolik, 1999, Nature, 398, 678

[2.5] A. Abdo et al., 2011, ApJ, 727, 129

[2.6] P. Giommi et al., 2012, A&A, 541, 160

[2.7] A. Abdo et al., 2010, ApJ, 716, 30

[2.8] G. Fossati et al., 1998, MNRAS, 299, 433

[2.9] A. Abdo et al., 2010, ApJ, 722, 520

[2.10] S. J. Wagner & A. Witzel, 1995, ARA&A, 33, 163

[2.11] A. C. Gupta et al., 2004, A&A, 422, 505

[2.12] L. Maraschi et al., 1999, ApJ, 526, 81

[2.13] E. Pian et al., 1998, ApJL, 492, 17

[2.14] F. A. Aharonian et al., 1997, ApJL, 327, 5

[2.15] L. Costamante & G. Ghisellini, 2002, ApJ, 384, 56

[2.16] M. Punch et al., 1992, Nature, 358, 477

[2.17] A. Neronov et al., 2010, ApJL, 519, 6

[2.18] J. Aleksić et al., 2010, ApJL, 723, 207

[2.19] M. Kadler et al., 2012, ApJL, 538, 1

[2.20] T. A. Rector et al., 1999, ApJ, 516, 145

[2.21] J. G. Kirk & P. Duffy, 1999, J. Phys. G: Nuc. Phys, 25, 163

[2.22] L. Maraschi et al., 1992, ApJL, 397, 5

[2.23] S. D. Bloom & A. P. Marscher, 1996, ApJ, 461, 657

[2.24] A. Konopelko et al., 2003, ApJ, 597, 851

[2.25] C. D. Dermer & R. Schlickeiser, 1993, ApJ, 416, 458

[2.26] C. D. Dermer et al., 1992, A&A, 256, L27

[2.27] M. Sikora et al., 1994, ApJ, 421, 153

[2.28] G. Ghisellini & P. Madau, 1996, MNRAS, 280, 67

[2.29] C. D. Dermer et al., 1997, ApJS, 109, 103

[2.30] M. Błażejowski et al., 2000, ApJ, 545, 107

[2.31] M. Georganopoulos & D. Kazanas, 2003, ApJ, 594, 27

[2.32] A. Mastichiadis & J. G. Kirk, 1997, A&A, 320, 19

[2.33] A. Sokolov et al., 2004, ApJ, 613, 725

[2.34] M. Sikora et al., 2001, ApJ, 554, 1

[2.35] M. Böttcher & J. Chiang, 2002, ApJ, 581, 127

[2.36] A. Sokolov & A. P. Marscher, 2005, ApJ, 629, 52

[2.37] F. A. Aharonian et al., 2000, ApJ, 539, 317

[2.38] K. Mannheim & P. L. Biermann, 1992, A&A, 253, L21

[2.39] A. Mücke et al., 2003, APh, 18, 593

[2.40] H. Krawczynski et al., 2004, ApJ, 601, 151

[2.41] M. Błażejowski et al., 2005, ApJ, 630, 130

[2.42] D. Kazanas & A. Mastichiadis, 1999, ApJL, 518, 17

[2.43] A. Mastichiadis & D. Kazanas, 2006, ApJ, 645, 416

[2.44] A. M. Atoyan et al., 2003, ApJ, 586, 79

[2.45] A. Peér & E. Waxman, 2005, ApJ, 628, 857

[2.46] A. Reimer et al., 2005, ApJ, 630, 186

[2.47] M. Böttcher, 2005, ApJ, 621, 176

[2.48] G. R. Burbidge, 1959, ApJ, 129, 849

[2.49] W. B. Atwood et al., 2009, ApJ, 697, 1071

[2.50] A. A. Abdo et al., 2009, ApJ, 700, 597

[2.51] A. A. Abdo et al., 2010, ApJS, 188, 405

[2.52] P. L. Nolan et al., 2012, ApJS, 199, 31

[2.53] M. Ackermann et al., 2011, ApJ, 743, 171

[2.54] F. Acero et al., 2015, arXiv:1501.02003

[2.55] M. Ackermann et al., 2015, arXiv:1501.06054

[2.56] M. Ackermann et al., 2013, ApJS, 209, 34

[2.57] J. L. Richards et al., 2011, apJS, 194, 29

[2.58] P. S. Smith et al., 2009, arXiv:0912.3621

[2.59] D. N. Burrows et al., 2005, Space. Sci. Rev., 120, 165

[2.60] S. D. Barthelmy et al., 2005, Space. Sci. Rev., 120, 153

[2.61] P. W. A. Roming et al., 2005, Space. Sci. Rev., 120, 95

[2.62] M. Matsuoka et al., 2009, PASJ, 61, 999

Chapter 3

VHE γ–ray Observation Technique and *TACTIC* Telescope

3.1 The Earth Atmosphere

The atmosphere of the Earth consists of Nitrogen, Oxygen and other gases with the volume fraction of 78%, 21% and 1% respectively. In the U.S. standard atmosphere, the density profile is well approximated by a simple slab model whereby the difference in pressure on either side of a vertical slab of atmosphere must balance the gravitational force on the slab. This assumption gives rise to the density function

$$\rho(h) = \rho_0 e^{-h/h_0} \tag{3.1}$$

where ρ_0=1.2× 10^{-3} gm cm^{-3} is the atmospheric density at sea level, h is the height above sea level, $h_0=k_B T/mg$ is local scale height, k_B is Boltzman constant, T is temperature in Kelvin (°K), m is mean molecular mass and g is acceleration due to gravity. The local scale height (h_0) can be defined as the altitude of the atmosphere where density at sea level is reduced by a factor of $1/e$ and it has a value of 8.5 km for mean temperature T=250 °K and m=28 gm/mol. Average standard pressure at sea level is 101.325 Pascal. In an isothermal atmosphere, the pressure decreases exponentially with height in the same way as the density. Some of the important parameters of the atmosphere relevant to the development of extensive air showers and production of atmospheric Cherenkov light are defined below.

- **Atmospheric Depth :** Atmospheric depth (in g/cm^2) is an important parameter to describe the interactions and subsequent propagation of particles in the atmosphere. In an isothermal atmosphere, the *vertical atmospheric depth* is defined as the integral of atmospheric density in altitude above the sea level and can be expressed as

$$X = \int_h^\infty \rho(h')dh' \tag{3.2}$$

Using the density profile given by equation 3.1, the atmospheric depth corresponding to an atmospheric height h is given by

$$X = X_g e^{-h/h_0} \tag{3.3}$$

where $X_g(=\rho_0 h_0)$= 1030 gm/cm^2 is the total atmospheric depth. For zenith angles z < 70°, for which Earth atmosphere is flat, the atmospheric depth is scaled with $1/cos(z)$ giving the *slant atmospheric depth*

$$X_s = X sec(z) \tag{3.4}$$

where $sec(z)$ with z=90°–altitude, is also referred to as *airmass*, which is basically the path length through the Earth atmosphere. The atmospheric depth represents the amount of material penetrated by a charged particle or *grammage*. A charged particle moving along slant depth will traverse more than 1030 gm/cm^2 to reach the sea level. For a more realistic model of the atmosphere [3.1], the relationship between *vertical atmospheric depth* (in gm/cm^2) and altitude h (in km) above sea level is

$$h = \left(\frac{6740 + 2.5X}{1000}\right) ln \left(\frac{1030}{X}\right) \tag{3.5}$$

- **Refractive Index :** Refractive index (n) of the atmosphere is an important parameter in the production of atmospheric Cherenkov light and detection of VHE γ–rays from ground based instruments, which use the atmosphere as a giant calorimeter. For the atmosphere with exponential density profile, the refractive index as a function of altitude can be written as

$$n(h) = 1 + \eta_0 e^{(-h/h_0)} \tag{3.6}$$

where h$_0$ is the scale height and $\eta_0 = 2.7 \times 10^{-4}$. A general expression for refractive index as a function of atmospheric depth and temperature is known to be

$$n(h) = 1 + \eta_0 \left(\frac{X}{1030}\right) \left(\frac{273.2}{T(^\circ K)}\right) \tag{3.7}$$

where T(°K)=(204 + 0.091 X) is the temperature at atmospheric depth X (gm/cm^2).

- **Critical Energy :** The critical energy (E$_c$) is an important parameter to characterize the effectiveness of a medium as radiator. The energy loss of a charge particle by radiation strongly depends on the medium in which the particle is moving. For a given medium critical energy can be defined as the energy at which the energy loss by radiation (Bremsstrahlung for e$^\pm$) equals the energy loss by collision or ionization. Above E$_c$, radiation loss will dominate over collision loss and vice-versa below E$_c$. In a gaseous medium with atomic number (Z), the critical energy for electron or positron is expressed as

$$E_c(MeV) = \left(\frac{710}{0.92 + Z}\right) \tag{3.8}$$

In air (Z=8), e^+(or e^-) has a critical energy of $\sim$ 86 MeV. In liquid or solid medium E_c is given by

$$E_c(MeV) = \left(\frac{610}{1.24 + Z}\right) \tag{3.9}$$

For water the critcal energy is 55 MeV and for Copper E_c has a value of 20 MeV [3.2].

- **Radiation Length :** When a charge particle travels in a dissipative medium, it loses its energy via radiation or bremsstrahlung. Radiation length describes the mean diastance over which a high energy electron loses its initial energy by a factor $1/e$ or 0.368. Thus for a charge particle with initial energy E_0, the energy after traversing a distance X through a medium can be written as

$$E_X = E_0 e^{-X/X_0} \tag{3.10}$$

where X_0 is called *radiation length*. The energy loss by electron is a stochastic process and it is convenient to characterize it in terms of X_0. For a medium with atomic number Z and atomic weight A, an approximate formula for computing radiation length is found to be

$$X_0(gm/cm^2) = \frac{716.4}{Z(Z+1)ln\left(\frac{287}{\sqrt{Z}}\right)} \tag{3.11}$$

Radiation length in *cm* can be derived by dividing X_0 (gm/cm^2) by the density of medium ρ (gm/cm^3). Radiation length for high energy electron is 36 gm/cm^2 in air at standard temperature and pressure. The vertical atmospheric depth at sea level X_g (=1030 gm/cm^2) can also be expressed in terms of X_0 (36 gm/cm^2) and the relationship turns out to be $X_g \approx 28\ X_0$.

The mean distance travelled by a particle along the vertical tarjectory without suffering a collision or interaction is called *mean free path* (λ). It depends on the density of medium and interaction cross section. Majority of heavy nuclei have shorter mean free paths relative to protons, because their interactioc cross sections are much larger. High energy photons predominantly lose energy in matter by pair production, where as electrons lose energy by bremsstrahlung. The mean free path for pair production of high energy photon (λ_p) is related to the radiation length (X_0) of relativistic electron as [3.2]

$$\lambda_p = \frac{9}{7} X_0 \tag{3.12}$$

This reflects the similarity of bremsstrahlung and pair production according to quantum electrodynamics. These two processes are the main interactions in the development of air showers in the Earth atmosphere.

- **Moliere Radius :** When an electron travels in the medium, the direction of propagation is changed in a major way by scattering. At critical energy E_c the electron undergoes an r.m.s. scatter of about 14° as it traverses one radiation length X_0. The lateral distance (in unit of X_0) by which an electron at critical energy is scattered as it travels one radiation length is called *Moliere Radius* (R_m). The Moliere Radius in the unit of radiation length is given by

$$R_m = \frac{21}{E_c(MeV)} \tag{3.13}$$

For air, R_m=0.25 radiation lengths or about 77 m at sea level.

3.2 Extensive Air Shower

Extensive air showers (EAS) were discovered in 1930 by French physicist Pierre Victor Auger. Whenever high energy cosmic ray nuclei or photons enter the terrestrial atmosphere, they interact with the molecules and atoms in the atmosphere and produce large cascades with a huge number of secondary particles. This cascade of secondary particles is called *Extensive Air Shower*. The number of particles in the shower grows up rapidly and attains a maximum till the secondary particles have enough energy to create new particles. The point at which the number of particles in the shower reaches a maxiumum is called shower maxima. Beyond shower maximum, the energy of secondary particles falls below the critical energy resulting in the exponential decay of secondary particles and finally the shower dies out. The typical height of this maximum depends on the type and energy spectrum of primary cosmic ray particle. Depending on the type of primary particles and their interaction, EAS can be classified in two main groups: *electromagnetic* and *hadronic* as shown in Figure 3.1. The two types of EAS are discussed below.

3.2.1 Electromagnetic Air Shower

Electromagnetic showers are produced by high energy γ–ray photons or electrons and positrons. The dominant interaction processes in the development of γ–ray or electron induced showers are electromagnetic in nature. In an electromagnetic cascade, three processes dominate the longitudinal shower development in the atmosphere. Pair production and electron bremsstrahlung within the electric field of air constituents cause the shower development while ionization of air molecules lead to the expiration of a shower. VHE γ–rays penetrating the atmosphere convert into electron-positron pairs in the Coulomb field of atomic nuclei. The electrons (and positrons) subsequently are deflected by nuclei and emit photons via bremsstrahlung.

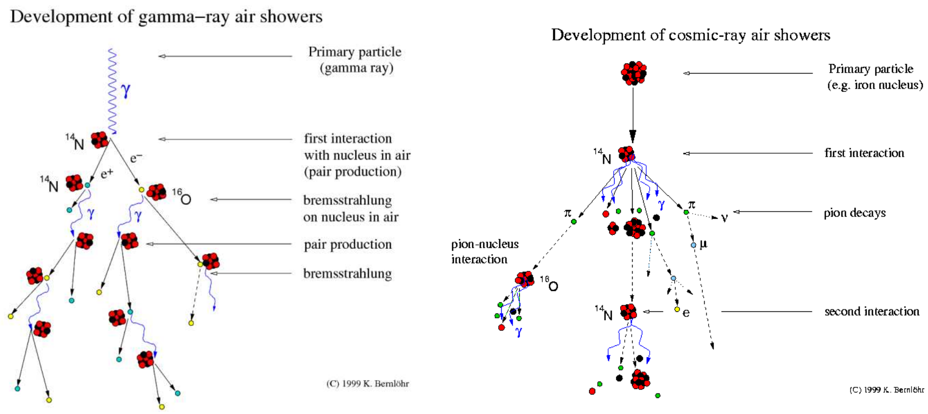

Figure 3.1: Development of extensive air shower by a primary cosmic ray nuclei and γ–ray photon. (Credit:mpi-hd.mpg.de)

Thus, both processes in turn set off an avalanche of particles and result in an electromagnetic air shower. The propagation of the shower continues until the mean energy of $e^{\pm}$ in the shower drops below the critical energy of 86 MeV. The electromagnetic shower will reach its maximum particle number at this stage and no new particle would be created any more. Accordingly, all of the shower energy is eventually dissipated by ionization of the medium and the shower is absorbed.

The small transverse momentum of the secondary electrons in γ–ray induced showers cause the electromagnetic cascades to be beamed along the direction of the primary photon. Multiple Coulomb scattering of cascade electrons determine the lateral distribution of the shower. The radial spread of the electromagnetic shower is determined by Moliere radius (R_m). Therefore, the shower particles move within a cone around the shower axis. This cone has a radius of 80-120 m at sea level and it contains 90% of the total energy of the shower. On an average, 99% of the energy of a shower is contained in a cylinder around the shower axis with radius $3.5R_m$.

Heitler model of shower development : This model illustrates a simplified picture of the characteristic longitudinal shower development of a γ–ray photon [3.3]. This model can be used to infer the basic properties of the development of an electromagnetic shower. In this model, only pair production and bremsstrahlung are considered for secondary particle creation. According to this model, the electromagnetic cascade by a primary γ–ray with energy E_0 starts with pair production, which radiate bremsstrahlung in the second step, and so forth. Every particle undergoes a splitting after it travels a fixed distance related to the radiation length and number of particles is doubled. After n splittings there are 2^n total particles in the shower. The multiplication process abruptly ceases when the energy of individual particle drops below the critical energy E_c. Energy of shower particles in n steps is given by

$$E_n = \frac{E_0}{2^n} \tag{3.14}$$

The cascade reaches maximum size when all particles have energy E_c so that

$$E_0 = N_{max} E_c \tag{3.15}$$

where $N_{max}=2^{n_{max}}$ is the total number of particles at shower maxima and n_{max} is the number of splittings required for the energy per particle to be reduced to critical energy. The position of shower maximum X_{max} (atmospheric depth at which the shower reaches maximum size) is obtained by determining n_{max}. Using above relations, we can show that

$$n_{max} = \frac{1}{ln2} ln(E_0/E_c) \tag{3.16}$$

and

$$X_{max} = n_{max} R_0 = X_0 ln(E_0/E_c) \tag{3.17}$$

where R_0=X_0 ln 2 is referred to as shower unit. It is the characteristic radiation length at which probability for pair production and bremsstrahlung will be same and it represents the splitting length in the development of an air shower. A γ–ray photon of energy 1 TeV incident from zenith will create an air shower reaching its maximum X_{max} typically at $\sim$ 300 gm/cm^2 atmospheric depth which corresponds to a height of $\sim$ 10 km above sea level. Despite the simplicity of this toy model, two important features of electromagnetic air showers are reproduced: while the number of particles at the shower maximum N_{max} is proportional to the energy of the primary particle E_0, the depth of the shower maximum X_{max} depends logarithmically on the primary energy.

All shower particles are strongly collimated along the incident direction due to their relativistic energies. The main process that broadens the shower in transverse direction is multiple Coulomb scattering and, in second order, the deflection by the Earth's magnetic field. The longitudinal evolution of the air shower depends on the energy of the incident particle and the path traveled in the atmosphere. A widely accepted analytic approximation called "Rossi Approximation B" [3.4] for total number of particles as a function of atmospheric depth or *longitudinal distribution* is given by

$$N_e(t, E_0) = \frac{0.31}{\sqrt{ln(E_0/E_c)}}.e^{t(1-1.5lns)} \tag{3.18}$$

where t is the atmospheric depth in units of radiation length and s corresponds to a dimensionless parameter known as shower age and is defined as

$$s = \frac{3t}{t + 2ln(E_0/E_c)} \tag{3.19}$$

The age parameter (s) indicates the level of shower development. At the beginning of shower s = 0, while s = 1 at shower maxima and s = 2 when the shower dies out. Together with the longitudinal development, a *lateral evolution* in transverse direction takes place in the shower. The multiple scattering affects electrons and positrons in the shower development, translating into a dispersion from the central axis of the cascade. The *lateral evolution* of the electromagnetic shower is modelled by the Nishimura-Kamata-Greisen (NKG) formula [3.4, 3.5] to determine the electron and positron density

$$\rho(r,t,E_0) = K.\frac{N_e(t,E_0)}{R_m^2}\left(\frac{r}{R_m}\right)^{s-2}\left(1+\frac{r}{R_m}\right)^{s-4.5} \tag{3.20}$$

where r is the distance to the cascade axis and K is the normalization constant. This formula however is valid only in the range $1 < s < 1.4$.

3.2.2 Hadronic Air Shower

The air showers initiated by protons or nuclei are called nuclear or *hadronic cascades*. The interactions in hadronic cascades are strong interactions, weak decay processes and electromagnetic interactions as shown in Figure 3.1. Hadronic showers are produced by the collision between a cosmic ray particle (protons or atomic nuclei) with an atom in the Earth atmosphere. In the first interaction, new particles (mainly pions and kaons) are produced, which together with the fragments from the primary nucleon form the particle cascade [3.6]. Hadrons and pions initialize a hadronic cascade through further collision and decay of pions into photons, electrons and positrons initiate electromagnetic sub-showers. The hadrons continue to interact with the atmosphere, until the energy per nucleon is reduced to the pion production threshold energy of about 1 GeV. Thus a hadronic cascade can be divided into three main components: *Hadronic*, *Electromagnetic* and *Muonic*. The *hadronic component* comprises the charged fragments of the first and subsequent collisions with further atmospheric molecules. The immediate decay of neutral pions into two energetic photons leads to an *electromagnetic* sub-shower that propagates via the pair production of electrons and positrons. Approximately one third of the hadronic shower energy is transferred to the electromagnetic sub-shower. Charged pions and kaons decay into muons and neutrinos, which are penetrating particles and thus are able to reach the ground level. A 1 TeV proton produces in one single interaction in the atmosphere about 12 secondary low energy pions. Some of these pions may interact again to form finally sub-hadronic showers. The secondary particles of hadronic cascade acquire non-negligible transverse momenta, which lead to substantial lateral spread of the shower. The features of hadronic shower fluctuate more with respect to the shower maximum and a *Superposition model* [3.7] can be used to explain the parameters of hadronic shower.

3.2.3 Difference between Electromagnetic and Hadronic showers

Several major differences between hadron induced showers and γ–ray induced showers have been explored and are very useful in the detection of VHE γ–rays using ground based detection techniques. Some of the important differences are described below.

- All the energy of primary γ–ray is converted into an electromagnetic cascade while a significant part of the primary hadron energy is carried away by muons and neutrions.

- The average transverse momentum of secondary particles in hadronic cascade is higher than electrons and positrons resulting in wider lateral distribution than electromagnetic shower.

- Unlike electromagnetic interactions, hadronic interactions result mainly in pions. Therefore, hadronic showers mainly contain the decaying product of pions, including muons, electrons, positrons and neutrinos from charged pions and γ–rays from neutral pions. In addition, the interactions involved in hadronic showers last longer than those taking place in electromagnetic cascade. Thus, hadronic showers have a larger development with respect to the electromagnetic case leading to a longer temporal shower evolution. Further more, the hadronic showers are more disordered than electromagnetic and produce bigger axial asymmetry and sub-cores.

- Comparing the characteristic radiation length of electromagnetic interactions (~ 37 gm/cm^2) with the interaction mean free path of protons (~ 80 gm/cm^2), the hadronic interactions take place on average deeper than the primary γ–ray interactions. Also, the longitudinal extension of hadronic showers is larger than the electromagnetic showers.

3.2.4 Radiation from Extensive Air Shower

As the extensive air shower develops in the Earth's atmosphere, the charged particles in the cascade produce different types of radiation. The properties of EAS can be exploited by detecting the different kind of radiation from the shower to determine the particle type, energy and direction of primary cosmic rays. The dominant type of radiations produced from the shower are briefly described below.

- **Cherenkov light :** Cherenkov radiation is emitted when a charged particle moves through a transparent medium with a velocity greater than the speed of light in the medium. The emitted radiation or light propagates more or less in the same direction as emitting particle. The Cherenkov emission leads to a characteristic image of an EAS on the ground and is used to detect VHE γ–rays using ground based Cherenkov telescopes. Most of the Cherenkov light is emitted when shower is at its maximum.

- **Fluorescence light :** Fluorescence light is induced by EAS while developing through the Earth atmosphere. The charged particles of EAS, mainly electrons and positrons initiate the emission of fluorescence light by exciting the

Nitrogen molecules in the Earth atmosphere. The emitted spectrum from the de-excitation of Nitrogen molecules has distinct spectral lines in the near UV regime. The fluorescence light is emitted isotropically from any point of shower track.

- **Radio :** Any acceleration of charge particles in EAS leads to the radio emission which is then superimposed for all particles in the cascade. The mechanism for the radio emission from EAS is a coherent geosynchrotron process. Secondary electrons and positrons in the cascade travel with relativistic velocities in the Earth magnetic field and are deflected. This produces dipole radiation beamed into forward direction. The radio signal from EAS is strongly polarized with a median degree of polarization exceeding 99% and has sizable intensity in GHz frequency range.

3.3 Atmospheric Cherenkov Radiation

The Cherenkov radiation in the form of faint blue light was first observed in pools containing radioactive material by Mary and Pierre Curie in 1910, but the nature of such radiation remained ununderstood for a long time. Pavel Alekseyevich Cherenkov in 1934 carried out experimental work to understand the radiation and the name *Cherenkov radiation* was given after him [3.8]. He proposed that the Cherenkov radiation is produced as response of a medium when a relativistic charge particled travels through it at a speed higher than the speed of light in that medium. In 1937, I.E. Tamm and I.M. Frank developed a theoretical interpretation of this phenomena in the framework of special theory of relativity [3.9]. The Cherenkov light involves radiation emitted by the medium under the action of the electric field induced by charged particle moving through the medium and the emission is governed by the refractive index of the medium.

3.3.1 Cherenkov Effect

A charged particle passing through a dielectric medium (e.g. air, water) with velocity exceeding the phase velocity of light in the same medium polarizes the surrounding medium and induces the constructive interferrence of electromagnetic waves produced by the reorientation of electric dipoles. This emission of radiation in the medium is known as *Cherenkov Effect*.

Generally, the atoms and molecules of the medium close to the relativistic particle path are polarized due to the electric field created by the charged particle. Focussing on the single molecule or atom of the medium, during the polarization state, atoms or molecules behave as dipoles and the dipole component appears and disappears once the particle is far from the region. Change in the dipole causes dipole radiation. The electric field due to the motion of charged particle decreases exponentially so that at a point remote from the track, no field will be observed. In normal circumstances (non-relativistic motion of charged particle) no radiation is emitted because the

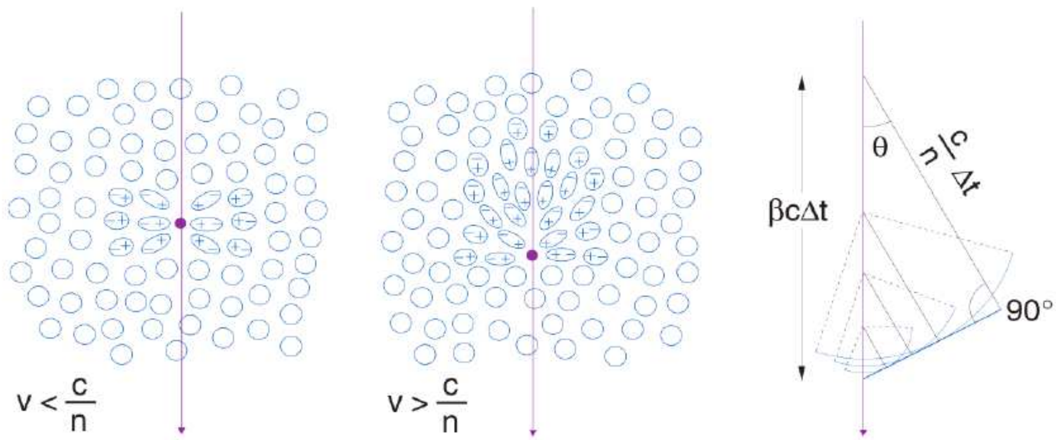

Figure 3.2: Illustration of Cherenkov Effect : Polarization of medium by non-relativistic and relativistic charged particles.

dipoles are organized in a symmetric configuartion, and emission from individual molecules or atoms suppress the electromagnetic radiation of each other. When the speed of charged particle is more than that of light in the medium, the charged particle moves faster than the electromagnetic waves induced by the polarization along its path. As a consequence of asymmetric distribution of dipoles a coherent polarized radiation field known as *Cherenkov light* is produced through constructive interferrence. These two situations are illustrated in Figure 3.2.

The Cherenkov light is emitted in a cone with a characteristic angle between the direction of radiation and the particle track. From geometrical considerations, the Cherenkov angle (θ) is given by

$$cos\theta = \frac{1}{\beta n} \tag{3.21}$$

where β(=v/c) represents the speed of charge particle and n is the refractive index of the medium. From equation 3.21, it is evident that β has to exceed a certain threshold value $\beta_{min} = 1/n$ below which no Cherenkov radiation is observed. This is equivalent to the condition that the charged particle Lorentz factor γ exceeds the threshold value

$$\gamma_{th} = \frac{1}{\sqrt{1-\beta_{min}^2}} = \frac{n}{\sqrt{n^2-1}} \tag{3.22}$$

and this corresponds to a threshold energy E_{min} of the charged particle given by

$$E_{min} = \gamma_{th} m_0 c^2 \tag{3.23}$$

where m_0 refers to the rest mass of charged particle. In the case of ultra-relativistic particle $\beta \approx 1$, the Cherenkov angle is maximum and can be expressed as

$$\theta_{max} = cos^{-1}\left(\frac{1}{n}\right) \tag{3.24}$$

3.3.2 Cherenkov Emission of EAS

The threshold energy for Cherenkov radiation E_{min} is proportional to the rest mass energy of the particle. This implies that the light particles like electrons and positrons dominate the Cherenkov emission. An EAS starts roughly at the point of first interaction (20-25 km altitude) and extends downwards to several km. The secondary charged particles in the shower undergo multiple Coulomb scattering, emitting Cherenkov light until the threshold condition. Since the refractive index of atmosphere depends on the altitude as given by equation 3.6, the condition for Cherenkov emission will depend not only on the energy of particle but also on the height in the atmosphere, so that threshold energy changes as the particle moves downwards. The higher the altitude, lower the refractive index of the atmosphere and higher the energy threshold. For a TeV γ–ray induced EAS, at height of shower maximum the threshold energy of electron is around 50-55 MeV. The secondary electrons and positrons emit Cherenkov light even beyond the shower maximum until their energies fall below a threshold of 21 MeV at sea level. Also the Cherenkov angle is a function of refractive index, the characteristic emission angle increases as the particles move deeper into the atmosphere because the refractive index rises with decreasing altitude. The Cherenkov angle varies between 0.5 and 1.5° within 15 km altitude above sea level and at the shower maximum ($\sim$ 10 km), the common characteristic angle is close to 1°.

Most of the Cherenkov light is generated at heights around the shower maximum, where the number of electrons and positrons reaches its maximum. The light seen from the ground is the superposition of all the light emitted from different heights. For a typical γ–ray shower, the decreasing Cherenkov angle with increasing height due to varying refractive index results in a rough focusing of Cherenkov photons on the ground into a circle called *Cherenkov light pool* with characteristic radius of 120 m depending on the zenith angle. The lateral distribution of Cherenkov photons is uniform or constant within the Cherenkov pool and is characterized by a hump at 120 m from the shower axis, which arises from the focussing effect of increasing emission angle. A Cherenkov flash corresponding to 1 TeV γ–ray shower yields about 100 photons per m^2 within 120 m of the shower axis. The Cherenkov light produced by hadronic showers is dominated by their electromagnetic sub-cascades and features a heterogeneous, and asymmetric lateral profile due to individual muons.

3.3.3 Properties of Atmospheric Cherenkov light

The important characteristics of Cherenkov radiation from EAS are outlined below.

- Most of the charged particles in EAS have energies exceeding the threshold values and thus a copious amount of Cherenkov light is generated. The total photon density inside the Cherenkov light pool is proportional to the energy of primary particle initiating the shower, since nearly a constant fraction of the primary energy is converted into Cherenkov photons. This correlation is a key feature in the detection of VHE γ–rays using ground based telescopes as it allows to determine the energy of primary by measuring the Cherenkov light intensity of the corresponding air shower.

- The time of development of an air-shower from the first interaction until it dies in the atmosphere is about 50 μs. Cherenkov light flashes are very short in duration depending on the type of EAS. In case of electromagnetic showers, it lasts typically 3-10 ns while in case of a hadronic ones, the durations of the light flashes can be longer. For example, a 1 TeV γ–ray induced-shower lasts $\sim$ 5 ns.

- The number of Cherenkov photons emitted by a charge particle of charge Ze per unit of path length (dx) and per unit of photon wavelength (λ) is given by [3.10]

$$\frac{d^2N}{dxd\lambda} = \frac{2\pi\alpha Z^2e^2}{\lambda^2}\left(1 - \frac{1}{\beta^2 n^2}\right) \tag{3.25}$$

where $\alpha(=1/137)$ is fine structure constant. For a dispersive medium the refractive index (n) also depends on wavelength. The $1/\lambda^2$ dependency of Cherenkov photon spectrum indicates that the major contribution to Cherenkov light comes from the short wavelength region.

3.3.4 Absorption of Cherenkov light

The main part of the Cherenkov light from EAS is produced in the upper atmosphere at about 10 km above sea level. On their way down to the ground, the Cherenkov photons undergo several scattering/absorption processes while traveling through the atmosphere. This results in the substantial difference between the observed and emitted Cherenkov spectrum peaking at UV–blue wavelengths [3.11]. The absorption of light strongly depends on the wavelength. For Cherenkov light with the wavelength band 180–600 nm, the attenuation is mainly described by *Rayleigh scattering*, *Mie Scattering* and absorption by ozone. Since the cross section of Rayleigh scattering is proportional to λ^{-4}, this process mainly affects UV/blue part of Cherenkov spectrum. The Mie Scattering is caused by relatively large particles of the atmosphere like aerosols, water droplets and dust with size larger than the wavelenth of Cherenkov light. A more complex Mie Scattering occurs without strong dependence on the photon wavelength with scattering cross section proportional to $\lambda^{-1.2}$. The attenuation of Cherenkov light due to Mie Scattering is small above 2 km height, but poor atmospheric conditions make it a dominant process. At wavelengths below 300 nm, an additional strong absorption caused by ozone molecules takes place. Since ozone molecules widely spread between 10–40 km from the Earth, most of the hard UV photons are absorbed.

3.4 Imaging Atmospheric Cherenkov Telescope

Imaging Atmospheric Cherenkov Telescopes (IACTs) are currently the most efficient ground based γ–ray experiments which complement the space based γ–ray detectors in VHE regime. The overall goal of an IACT is the unambiguous detection of VHE γ–rays from celestial sources. The IACT is a field instrument in which the detector is at a remote location and uses the Earth's atmosphere as its detection medium. Also, IACT unlike conventional radio or optical telescopes is not a wide field survey type instrument and it requires a predetermined potential target which is assumed to be a source of VHE γ–rays. The telescope allows to measure the direction and energy of primary γ–ray above 50 GeV by rejecting the huge hadronic background. A peculiar feature of an IACT is that it does not detect the γ–ray photons directly, but instead detects the Cherenkov light produced from EAS induced by the primary photon. In general, the imaging telescopes are more sensitive than other counter parts for γ–ray detection. The duty cycle of Cherenkov telescopes is limited by the requirement of their operation under good weather on moonless nights. A typical IACT runs for 800–1000 hours in a year with a duty cycle not more than 10%.

3.4.1 Principle of IACT

An IACT is based on the principle of imaging of EAS induced by primary VHE γ–rays and this method is referred to as *imaging atmospheric Cherenkov technique*. The technique involves collecting the Cherenkov photons emitted by an EAS and generating its image to reconstruct the shower development. Reconstructing the shower axis in space and tracing it back onto the sky allows the celestial origin of γ–ray to be determined. The Cherenkov light, emitted from the shower, is reflected by a mirror and focused on the camera at the focal plane. Different emission angles from the shower correspond to different positions in the camera. The angular distribution of longitudinal and lateral emission of the shower determines the image shape in the camera. Showers coming from a point γ–ray source develop parallel to the telescope axis, and the recorded image will be roughly an ellipse pointing towards the position of the γ–ray source in the camera. The image formed in the camera is a geometrical projection of the air shower as shown in Figure 3.3. Light coming from the upper part of the shower, where the secondary particles are more energetic, has smaller Cherenkov angles and is mapped onto a region close to the camera center. Light emitted from the last stages of the showers, from less energetic secondary charged particles, has a larger Cherenkov angle and is therefore mapped further away from the camera center. Most current generation experiments use multiple IACTs to capture the image of shower from different viewing angles for improved reconstruction of γ–ray direction and rejection of hadronic background. These multiple IACTs are known as *Stereoscopic systems*.

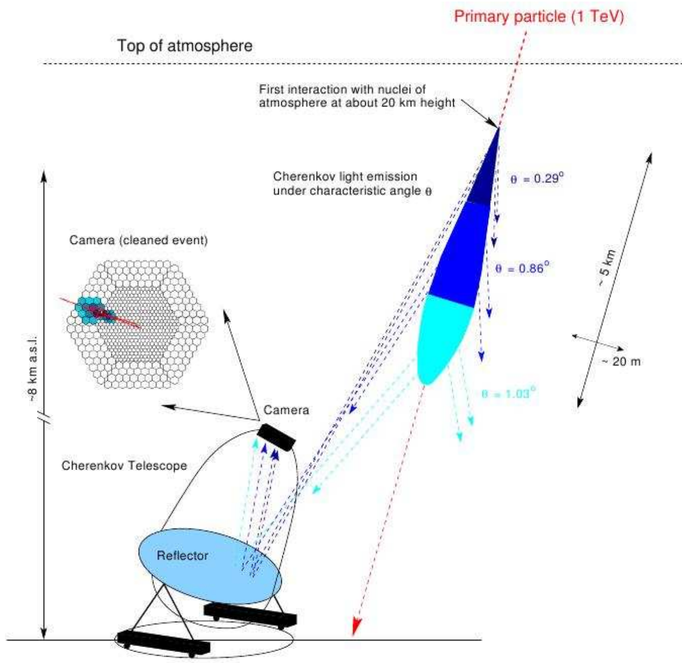

Figure 3.3: Illustration of the principle of an imaging atmospheric Cherenkov telescope. (Credit: http://ihp-lx.ethz.ch/Stamet/magic)

3.4.2 General Design Features of IACTs

As mentioned above, most of the Cherenkov emission from air shower is in the UV-visible range. The faint and brief Cherenkov signal produced during the development of electromagnetic cascades lasts only a few nanoseconds, but it is sufficient for detection using large light reflectors equipped with fast optical detectors. In order to capture an image of the air shower, several important factors have to be taken care of in the telescope design : fast response of the photo-detectors and large collection areas in order to collect maximum number of photons from the Cherenkov light pool. The design of an IACT essentially consists of three components : an optical reflector of large aperture (spherical or parabolic), a wide field of view camera with a matrix of photodetectors (photomultipliers or photodiodes) at the focal plane of mirror and a fast pulse counting electronic system. The light collector of the telescope collects a certain amount of the Cherenkov light from an EAS, if it is physically located somewhere in the Cherenkov light pool on the ground. The reflectors in current IACTs are either parabolic or based on Davies-Cotton (DC) optical design [3.12]. The photodetectors in camera located at the focal plane of the reflector must have high quantum efficiency and spectral response which matches with the Cherenkov spectrum. The high speed electronics is required to minimize the integration time, ideally reducing this down to the shortest intrinsic time scale of the duration of Cherenkov light pulse.

3.4.3 Observation Modes of IACT

When observing a γ–ray source candidate with an IACT, following standard modes of observations can be performed.

- **ON-OFF mode :** In this mode of observation, successive runs for ON and OFF observations are performed. In ON-mode, the γ–ray source is located at the camera center. In OFF mode, a different direction in the sky away from the source is observed for the same duration. This mode of observation requires double the observation time to collect the data on source and background regions.

- **Tracking mode :** In this observation mode, the candidate γ–ray source is continuously tracked without taking any OFF-source run. Thus, this mode collects data on source and background region simultaneously. This mode is utilized to maximize ON-source observation time and to increase the possibility of recording the flaring activity from a source.

- **Wobble mode :** In this mode, the IACT is pointed so that the source position is not in the camera center, but shifted by a known angular distance away from the source. Therefore, a position symmetric to the source position with respect to the camera center is available for background determination. This mode of observation offers the possibility of continuous monitoring of a candidate source along with the background region and without interrupting the observation for collecting OFF data.

3.5 The *TACTIC* Telescope

The *TACTIC* (TeV Atmospheric Cherenkov Telescope with Imaging Camera) VHE γ–ray telescope [3.13] has been in opertaion at Mount Abu, India (24.6° N, 72.7° E, 1300 m asl) since 2001. The *TACTIC* experiment with single imaging telescope has been designed for γ–ray astronomy in the energy range above 1 TeV. The telescope with its prototype 81-pixel camera saw first light in March 1997 when it successfully detected γ–ray flaring activity from one of the most promising blazars Mrk 501 [3.14]. The prototype camera was upgraded in two stages. In the first stage, the camera was upgraded to 144 pixels and in the next stage the final camera configuration was attained in 1999–2000. First successful detection of TeV γ–rays from the Crab Nebula was seen in the data collected with the *TACTIC* for $\sim$ 40 hours during January 19, 2001 and February 23, 2001. Since then, the *TACTIC* experiment has been used for VHE observations of a number of potential TeV blazar candidates like Mrk 421, Mrk 501, H 1426+428, 1ES 1959+650, 1ES 2344+514, 3C 279 and so on [3.15,3.16,3.17,3.18,3.19,3.20].

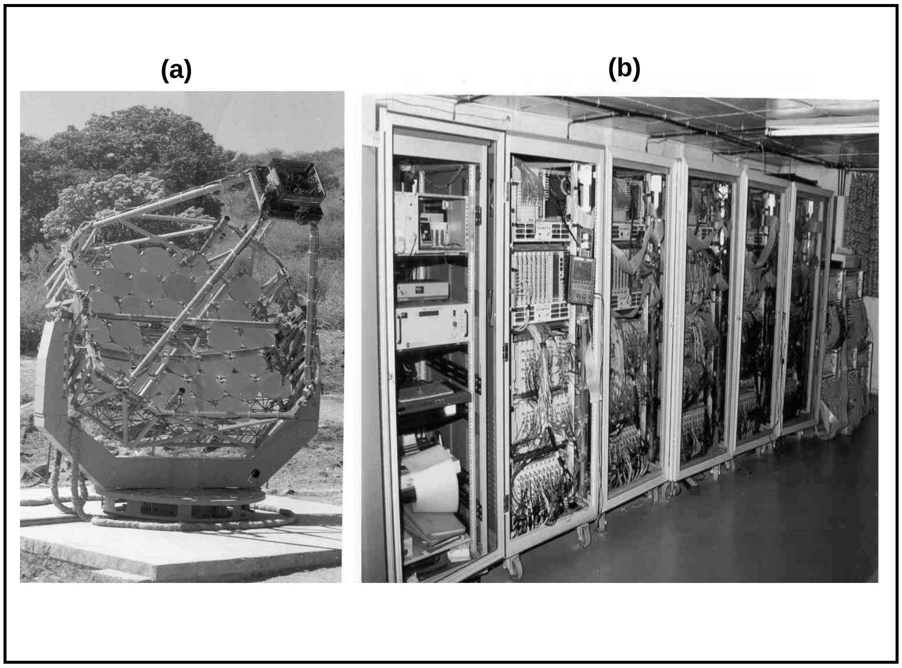

Figure 3.4: Photograph of (a) *TACTIC* with 349 pixel imaging camera and (b) back-end signal processing electronics of the telescope.

3.5.1 Design Features of *TACTIC*

A comprehensive site survey was performed in 1993 at Gurushikhar in Mount Abu, Rajasthan, India to achieve the overall scientific requirements of an IACT observatory. Mount Abu is a hill resort with good logistics and mild climate and it offers maximum number of cloud free nights, reasonably dark site with negligible contribution from artificial sources and dust free atmosphere. The INSAT-1D satellite cloud cover images in the IR and visible bands were studied to derive quantitative information on the percentage of clear nights per year. An analysis of 5 years data during 1986–1991 revealed about 2450 hours of possible observation time per year. Taking the lunar cycle into account, only 48% of this time amounting to ~ 1170 hours of effective observation time was found to be sufficiently dark for observation of EAS induced by cosmic γ–rays. The telescope has been designed for the study of TeV γ–ray emission from celestial sources and the details of overall design of the *TACTIC* can be found in [3.13]. The photograph of *TACTIC* with its back-end signal processing electronics is shown in Figure 3.4 (a) & (b). The salient design features of the *TACTIC* are briefly described below.

- **Mechanical Design :** The main parts of the telescope are: light collector basket, mirror adjustment frame, zenith and azimuth drive assembly, motors/encoders for the motion of two axes, camera support boom assembly and photomultiplier-based camera. A three dimensional truss type structure has

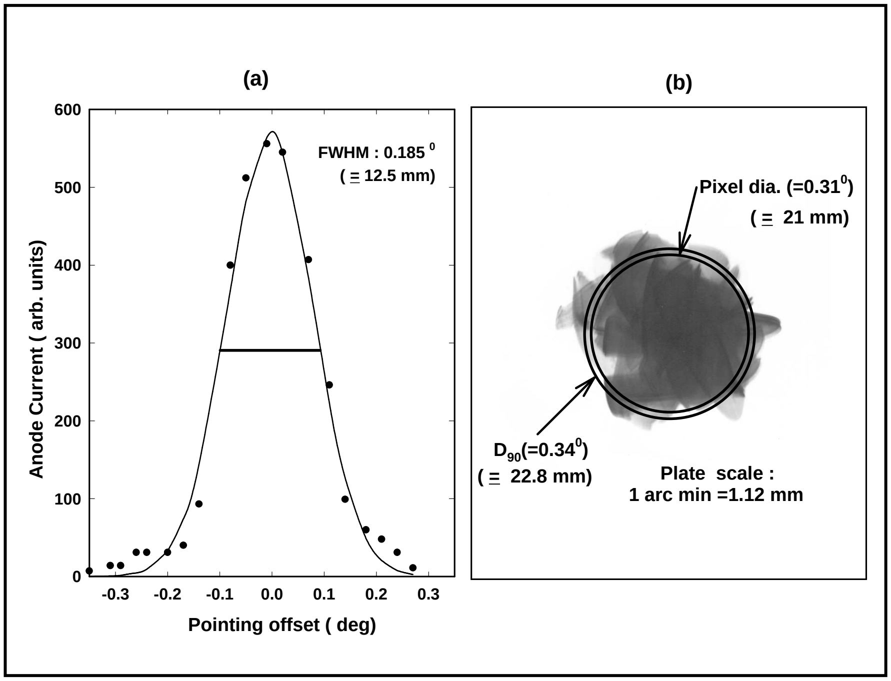

Figure 3.5: (a) Measured PSF of the *TACTIC* light collector and (b) Image of the star Sirius recorded at the focal plane of the telescope.

been used to support the mirror frame. The basket is a three-layer welded mildsteel tubular grid structure fabricated in three parts which are bolted together and is provided with a central tie rod which extends into short stub shafts at the two ends housed in bearings. The complete basket assembly is held by the fork of the telescope and the weight of the moving part of the telescope is around 6.5 tons. The telescope uses an altitude–azimuth (alt-azm) mounting due to its large weight because in this mounting the telescope weight is uniformly supported on a horizontally placed central thrust bearing. The drive system uses hybrid stepper motors, sequence generators and power amplifiers, shaft encoders, programmable stepper motor controller and a GPS clock.

- **Optical Design of the Light Collector :** Unlike optical telescopes, which collect light from objects at “infinity”, an IACT detects Cherenkov light from EAS mainly between 5–15 km above sea level. In order to collect all the Cherenkov photons the field of view of an IACT must be more than the angular extent of Cherenkov light flash ($\sim 1^{\circ}$). Usually the reflector of an IACT is a tessellated mirror made up of smaller mirrors. The light collector of *TACTIC* with $\sim$ 3.5 m diameter uses 34 front face aluminium-coated, glass spherical mirrors of 0.6 m diameter each, to provide a light collection area of $\sim$ 9.5 m^2. The mirror facets used in the telescope are characterized by: focal length of $\sim$ 3.8 m, surface accuaracy of few λ and reflectivity more than 85% at 400 nm. The shorter focal length mirrors are deployed close to the basket center while mirrors with longer focal length are deployed around the periphery. The peripheral mirrors have the effect of increasing the overall spot size as they function in an off-axis mode. In order to make the design close to Davies-Cotton (DC) design, longer studs on the mirror frame structure have been used to raise the pole positions of the peripheral mirrors. This hybrid design of *TACTIC* light collector maintains the spatial distribution of Cherenkov photons from EAS within tolerable limits acheiving minimum blur size at an appropriate focal plane distance. The measured point spread function (PSF) of the *TACTIC* light collector is shown in Figure 3.5.

- **Imaging Camera :** The camera is the most important component of the telescope and is decisive for improving the sensitivity of experiment. Usually, the camera of an IACT is made of photomultiplier tubes (PMTs) followed by back-end signal processing electronics. A single PMT in the camera is called *pixel* and a typical imaging camera consists of a few hundred pixels. The *TACTIC* imaging camera, designed as a square grid, uses 349 pixels (ETL-9083 UVB) of 19 mm diameter with a uniform pixel resolution of $\sim 0.31°$ and the total field of view of the camera is approximately $5.9° \times 5.9°$. The high gain PMTs used in the *TACTIC* camera have a maximum quantum efficiency (expressed as the number of electrons emitted by the cathode divided by the number of photons hitting the PMT) of about 27% at 340 nm and rise time of 1.8 ns, which is compatible with the characteristics of the Cherenkov pulse. A low current zener diode based voltage divider network (VDN) is used with the PMT to ensure the stable volatge for its satisfactory operation. The VDN uses negative voltage and the photocathode of PMT is at a high voltage of 1000–1400 V while the anode is at the ground potential.

  Reflective light concentrators in front of light sensors are a common element used in IACTs to increase the collection area of camera pixels. These light concentrators are designed to maximize the collection efficiency of incoming rays within the angular range subtended by the primary mirror and the camera while at the same time limiting the amount of light reflected from the ground and surrounding objects. The Compound Parabolic Concentrators (CPCs) made of SS-304 were choosen as light guides for *TACTIC* imaging camera. Some of the important geometrical parameters of the CPCs used in *TACTIC* camera are : circular entry aperture diameter 21 mm, exit aperture diameter 15 mm, acceptance angle 45.48° and height 17.6 mm. The light collection efficiency of the CPC (including both the geometrical collection efficiency and the reflectivity of the surface) was experimentally measured to be 65%.

- **Back-end Electronics :** In an IACT, large reflectors and short exposures (preferably < 10 ns) are required to detect the faint flashes of Cherenkov light against the Poisson fluctuations in the night sky background. Therefore high speed electronics is required to record the image of an EAS by detecting the Cherenkov light reflected from the light collector of the telescope. Each image registered in the telescope camera is referred to as a *Cherenkov event*. The event is produced by a group of 5–20 pixels with varying amplitude of 3-60 mV. These voltage pulses are transmitted to the control room using 55 m long high quality RG 58 coaxial cables. The back-end signal processing hardware of the telescope is based on NIM & CAMAC standards. The multi-channel fast NIM-based amplifiers and discriminators have front panel adjustments for gain and threshold, respectively. The charge content and scalar rates are directly read off the CAMAC bus. One of the two outputs of a discriminator channel is used for monitoring the single channel rate (SCR) with a CAMAC scaler while the other output is connected to the trigger generator. Block diagram of the back-end signal processing electronics used in the telescope is shown in Figure 3.6.

- **Trigger Generation :** The innermost 240 pixels (16×16 matrix) or 121 pixels (11×11 matrix) are used for generating the event trigger, based on a predecided trigger criterion which is either nearest neighbour pairs (NN2) or nearest neighbour triplets (NN3). Apart from generating the prompt trigger with a coincidence gate width of ~ 18 ns, the trigger generator has a provision for producing a chance coincidence output based on ${}^{12}C_2$ combinations from various groups of closely spaced 12 channels. The details of design and implementation of the multi-module trigger generator are discussed in [3.21].

- **Data Acquisition System :** The data acquisition and control system of the telescope have been designed around a network of PCs running the QNX real-time operating system and is handled by a network of three personal computers. While one PC is used to monitor the scaler rates and control the high voltage to the PMTs, the other PC handles the acquisition of the event and calibration data and the programming of the *TACTIC* trigger generator (TTG) modules. These two front-end PCs, referred to as the rate stabilization node and the data acquisition node respectively, along with a master node form the multinode data acquisition and control network of the *TACTIC*. The same network is extended to two more LINUX-based PCs which are used for online data analysis and archiving. An event handler module controls the whole process of data acquisition and also provides the link between the *TACTIC* hardware and the application software. The event handler accepts the atmospheric Cherenkov events, calibration and chance trigger outputs from various TTG modules and interrupts the front end data acquisition node. At event occurrence, the event handler also generates a TTL output for latching the system clock and a 20 ns wide NIM pulse for gating the CDC modules. The triggered events are digitized by CAMAC-based 12-bit charge to digital converters (CDC) which have a full scale range of 600 pC. The relative gain of the PMTs is monitored regularly once in 15 min by flashing a blue LED, placed at a distance of about 1.5 m from the camera. Other details regarding hardware and software features of the data acquisition and control system of the telescope are described in [3.22].

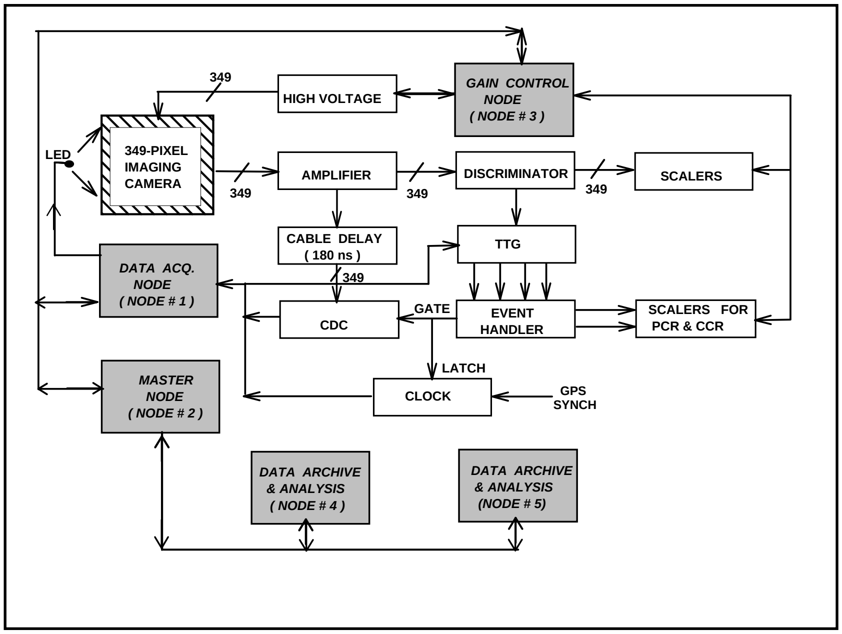

Figure 3.6: Block diagram of the back-end signal processing electronics used in *TACTIC*; TTG–*TACTIC* Trigger Generator, PCR–Prompt Coincidence Rate, CCR–Chance Coincidence Rate.

3.5.2 General Characteristics of *TACTIC*

The performance of the telescope is linked with its basic characteristics, both at hardware and software level. These general characteristics depend on the size of light collector, pixel size, field of view of camera and trigger generation scheme. The important features of the *TACTIC* are described below.

- **Effective Collection Area :** The energy and zenith angle dependent collection area characterizes the efficiency with which γ–rays are detected by an IACT and it is also a measure of the area over which γ–rays trigger the telescope. Typically, single reflectors have relatively uniform detection probability for showers whose cores land upto 125 m away from the telescope. This large effecive collection area ($\sim 10^4$ m^2) makes IACTs more efficient for observation of VHE γ–rays than space borne experiments where the effective area is limited by the geometrical area of the detector. For a point γ–ray source, the effective area is defined as

$$A_\gamma(E) = 2\pi \int_0^\infty R \times P(R,E)dR \tag{3.26}$$

where $P(R,E)$ is the probability that the telescope gets triggered due to a shower of primary energy E and impact parameter R. The effective collection area is computed from the Monte Carlo simulations where γ–ray showers are simulated as a function of energy at a given zenith angle. The trigger probability $P(R, E)$ is defined as the ratio of number of showers triggered to the total number of showers simulated. For isotropic hadronic background, the detection probability also depends on the angle between the direction of primary particle and the telescope axis. The effective area for background cosmic rays can be calculated using the equation

$$A_{CR}(E) = \int_0^\infty 2\pi R dR \int_0^\infty P(R, E, \Omega) d\Omega \tag{3.27}$$

where dΩ=2π sinθ dθ is the solid angle subtended by an element of viewcone with an opening angle between θ and θ + dθ around the shower axis.

- **Threshold Energy :** An IACT triggers on the signal of Cherenkov photons produced in EAS initiated by γ–rays or cosmic rays. More rigorously, the threshold energy of an IACT can be expressed as

$$E_{th} \propto \frac{1}{\rho}\sqrt{\frac{B\Omega}{A_m \varepsilon}} \tag{3.28}$$

where ρ is the Cherenkov photon density on the ground, B is flux of night sky background, Ω is the solid angle subtended by the pixel, A_m is mirror collection area and ε is the quantum efficiency of the PMT in the camera.

The threshold energy of the telescope is the energy at which its differential detection rate reaches the maximum. In actual practice, the threshold energy is determined by multiplying the effective area with the differential spectra of the primary particle. For γ–rays, the differential detection rate is given by

$$\frac{dR_\gamma}{dE} = A_\gamma(E)\frac{dN_\gamma}{dE} \tag{3.29}$$

where dN_γ/dE is the differential energy spectra of primary γ–rays. Similarly, for cosmic ray background (mainly protons) the differential trigger rate is expressed as

$$\frac{dR_{CR}}{dE} = A_{CR}(E)\frac{dN_{CR}}{dEd\Omega} \tag{3.30}$$

where $dN_{CR}/dEd\Omega$ is the differential spectra of primary cosmic rays. The effective collection area and estimated differential rates for γ–ray and proton induced showers for NN3 trigger is shown in Figure 3.7. For a zenith angle of $\sim 15^\circ$ and with a single pixel threshold of $\sim$ 14 photo-electron (pe), the γ–ray threshold energy is obtained to be $\sim$ 1.2 TeV. The threshold energy for cosmic ray protons is higher because Cherenkov photon density due to γ–ray showers is twice that of proton shower of the same energy. Further details of Monte Carlo simulation of γ–ray and cosmic ray proton induced EAS as detected by the *TACTIC* are discussed in [3.23].

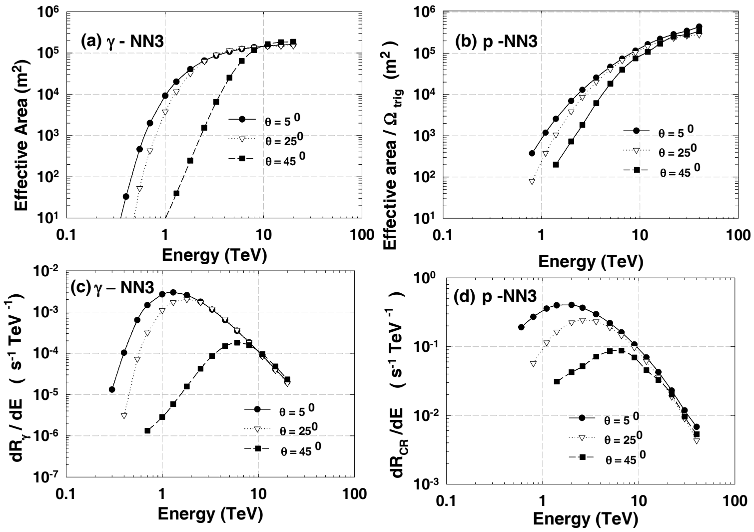

Figure 3.7: Effective collection area for (a) γ–ray and (b) proton induced showers as a function of energy, at various zenith angles with NN3 trigger scheme. Estimated differential trigger rate for (c) γ–ray and (d) proton induced showers at different zenith angles.

- **Sensitivity :** Sensitivity is an important parameter to evaluate the capability of a telescope to detect a γ–ray signal over background fluctuations. In the limit of no background, the flux sensitivity would be simply determined by the collection area of the telescope as a function of energy and observation time. In general, the sensitivity of the telescope is proportional to the square root of the observation time and the minimum time required to detect a source at 5σ level is given by

$$T_{min}(hours) = \frac{25(R_\gamma f_\gamma + 2R_h f_h)}{3600(R_\gamma f_\gamma)^2} \tag{3.31}$$

  where R_γ is the rate of γ–ray photons for a given source with appropriate spectrum and f_γ is the accepted fraction of γ–ray photons. R_h is the rate of hadronic background during the observations and f_h is the accepted fraction of background during the source observation. The sensitivity of *TACTIC* is $\sim 1.0\sqrt{T}$ and the telescope can detect the TeV γ–ray emission from a standard source like Crab Nebula at 5σ level in an observation time of 25 hours.

- **Angular Resolution :** A key characteristic for describing the performance of an IACT is the angular resolution of the telescope. It is a measure of the ability of the telescope to effectively localize the source of γ–ray signals in the sky and is of particular importance for the search of point γ–ray sources. The angular resolution of *TACTIC* is $\sim 0.23°$.

3.6 Gamma/Hadron Separation

The main objective of an IACT is to measure the characteristics of primary VHE γ–rays by means of the Cherenkov light produced in the EAS induced by them. But more than 99% of the air showers in the atmosphere are produced by the isotropic hadronic cosmic rays, which are treated as background in observations with IACTs. The most important sources of background are: hadrons, muons, cosmic electrons and diffuse γ–rays. Therefore, the study of VHE γ–rays with IACTs depends critically on the efficiency of γ/hadron classification methods. Detailed Monte Carlo simulations, pioneered by Hillas [3.24], show that the differences between Cherenkov light produced by air showers initiated by γ–rays and protons are quite pronounced, with proton images being broader and longer as compared to the γ–ray images. This led to the development of successful usage of several image parameters.

3.6.1 Image Parameterization

An effective way to parameterize the shower image in the camera of an IACT was first developed by Hillas in early 1980s [3.24]. The image recorded on camera focal plane can be regarded as a 2 dimensional distribution of intensities and the image parameters can be characterized by the first, second and third order moments of this distribution. The image parameterization is based on a moment fitting approach. The moment analysis is based on the light content of each pixel and its coordinate in the camera plane. The shape and orientation parameters which characterize the image are discussed below and their definition is illustrated in Figure 3.8.

Size (S): Represents the total amount of Cherenkov light captured by the camera for a given event. It is directly related to the shower energy and is calulated as the zeroth order moment of the image.

Length (L) : Represents the longitudinal development of the shower. It is defined as the root mean square (rms) angular size along the major axis of the image and is estimated as second order moment of the image.

Width (W) : Represents the lateral distribution of the shower. It is defined as the rms angular size along the minor axis of the image and is estimated as second order moment of the image.

Distance (D) : It is defined as the angular distance between position of the γ–ray source in the camera and image centroid.

Miss (M) : Measure of shower orientation. It is defined as the perpendicular angular distance from position of the γ–ray in the camera to the major axis of the image.

Concentration (F2) : A meausre of the compactness of the image. It is defined as the ratio of the two highest signal pixels to the sum of all the pixels of the image.

Alpha (α) : Related to the angle between shower axis and axis of telescope. It is defined as the angle between major axis of the image and line connecting image centroid with source position in the camera.

Asymmetry (Asym) : Provides information about the head-tail feature of the

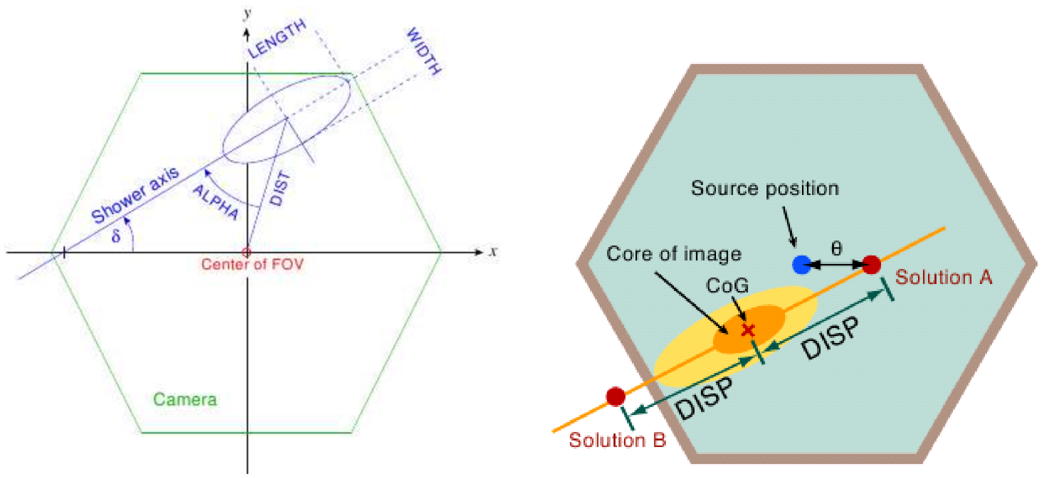

Figure 3.8: Definition of various image parameters and sketch of Disp parameter with two possible source positions. (Credit: https://magic.mpp.mpg.de)

shower image. It is defined as skewness of light distribution along the image axis relative to image centroid.
Disp : It is defined as the distance between the image centeroid and the source position on the camera plane. It uses the information of shower image shape and brightness to reconstruct the direction of an event. The *Disp* analysis is used for reconstructing the γ–ray sky map.
Among the above parameters *S, L, W* are classified as *source independent* and are also known as shape parameters. The *source dependent* parameters like D,α, *Asym, Disp* depend on the position of the γ–ray source in the camera. These parameters are characterized as orientation parameters and are very efficient for γ/hadron separation in VHE γ–ray astronomy with IACTs.

3.6.2 Background Rejection

An IACT has to be capable of rejecting the unwanted hadronic background at a remarkably high level of efficiency, while simultaneously retaining a majority of the genuine γ–ray events. Monte Carlo simulations of both γ and hadronic events are used to optimize the strategies for developing efficient γ/hadron segregation methods. The effectiveness of a particular strategy is quantified in terms of quality factor (QF), defined as

$$QF = \frac{f_\gamma}{\sqrt{f_h}} \tag{3.32}$$

The most widely used method for background rejection in IACT observations is *Dynamic Supercut Method* [3.25]. The supercut procedure is based on optimization of cuts on L, W and orientation parameters of the image for segregating γ–rays from the background cosmic ray events. The idea behind the Dynamical Supercuts is to include the dependence of image parameters on primary energy, core distance

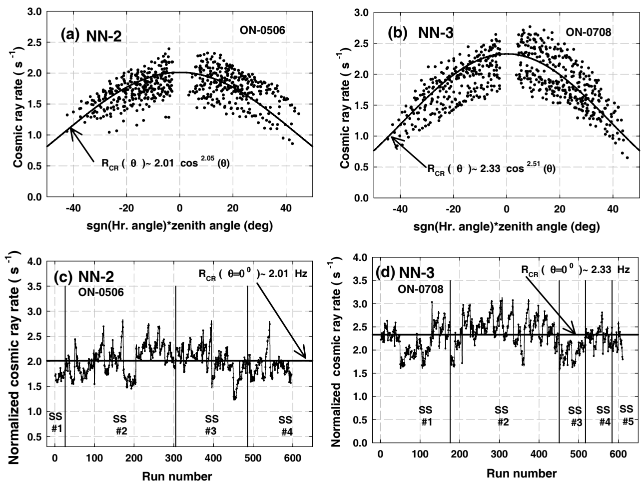

Figure 3.9: Cosmic ray trigger rate measured with *TACTIC* as function of zenith angle with (a) NN2 trigger configuration, (b) NN3 trigger configuration. The spline curve shown in these figures is estimated trigger rate from Monte Carlo simulation. The zenith angle has been multiplied with the sign of hour angle so that pre-upper transit and post-upper transit rates can be distinguished easily. Normalized cosmic ray rate as a function of run number with (c) NN2 trigger and (d) NN3 trigger modes.

and zenith angle. After optimization of the Dynamical Supercuts on Monte Carlo simulated data, γ–ray signal and the residual background events can be derived from the α–distribution.

A standard procedure to extract the γ–ray signal from the cosmic ray background using single imaging telescope is to plot the frequency distribution of α–parameter of shape and distance selected events. This distribution is expected to be flat for the isotropic background of cosmic ray events and for γ–rays coming from a point source, the distribution is expected to show a peak at smaller α–values.

3.7 *TACTIC* Data Analysis

The important goals of *TACTIC* data analysis include : detection of a γ–ray source using efficient background rejection strategy and determining the energy spectrum of the source for understanding the underlying physics. The main tasks performed in the standard data analysis procedure are summarized below.

3.7.1 Data Selection

The data recorded with the telescope (integrated charge of extracted signal) is given in units of digital counts or CDC (charge to digital converter) counts. For *TACTIC*, 1 CDC count is equivalent to 0.125 pC of the charge. The data quality depends on night sky condition and atmospheric dust level. The data selection criteria for *TACTIC* include the following.

- A visual log of night sky conditions is prepared during the observations and is used in offline data handling.
- The trigger rate of the telescope or prompt coincidence rate (PCR) should be compatible with zenith angle (z) and is described by the relation

  $$R(z) = R(0)(cosz)^m \tag{3.33}$$

  where $R(0)$ is the trigger rate at zenith (z=0°). The value of exponent m depends on sky quality and in case of *TACTIC* 1≤ m ≤ 3 for good quality data. The measured values of cosmic ray trigger rate as a function of zenith angle for NN2 and NN3 trigger modes with *TACTIC* are shown in Figure 3.9 as a representative example.
- The arrival times of prompt events follow Poisson distribution and the frequency distribution of arrival time differences of these events is described by a decaying exponential function with the exponent determining the mean event rate detected by the telescope.

  If one or more of the above criteria are not fulfilled, the corresponding data spells are discarded.

3.7.2 Image Preparation

The raw images of air showers corresponding to the clean data, recorded by the telescope, are processed through following steps.

- **Pedestal subtraction :** The pedestal is defined as the output of a channel corresponding to the input without any contribution of Cherenkov light from EAS. Keeping in view that the signals to CDC are AC coupled, the pedestal value is usually set around 100 counts so that the small amplitude positive polarity shot noise fluctuations induced due to light of night sky generate proper CDC counts with value less than 100 counts. The pedestal value for each pixel is determined by artificially triggering the camera, thereby recording the CDC counts in the absence of genuine input signal. The trigger rate is kept high ($\sim$ 400 Hz) during the pedestal data collection to reduce the probability of recording Cherenkov signal. Acquisition of the calibration data in this artificial trigger manner is called *sky pedestal run*. A typical sky pedestal run involves 2000 such trigger events to calculate the mean value of pedestal (CDC counts) and its variance. The pedestal subtraction process includes the subtraction of mean value of sky pedestal from the corresponding counts recorded in response to Cherenkov event.

- **Gain normalization :** The process of accounting for the differences in relative gains of PMTs is referred to as gain normalization or flat fielding. The method followed for *TACTIC* uses a high intensity blue light emitting diode (LED) operating in pulsed mode at distance of $\sim$ 1.5 m from the camera surface. The relative gains of PMTs in the *TACTIC* camera are determined by recording 2000 flashes from the LED. The calibration data collected in this manner is called *relative calibration run* and is used to determine the relative gains of each PMT by comparing their mean signals with respect to a reference pixel.

  In addition to the relative gain calibration of the pixels, an absolute gain calibration is also needed to compute the conversion factors from CDC counts into the number of photo-electrons (pe) arriving at the first dynode of PMT. In *TACTIC* data analysis, the absolute gain calibration is performed following *excess noise factor* (F) method using relative calibration run data. The excess noise factor originates due to statistical fluctuations in the amplification of the electrons in the PMT dynode system. For the PMTs of *TACTIC* camera, the value of conversion factor is found to be 1pe $\approx$ (6.5$\pm$1.2) CDC counts for mean value of excess noise factor F $\sim$ 1.7.

- **Image cleaning :** The signal in each pixel is not only produced by Cherenkov photons, but also due to shot noise fluctuations of the PMT. An image cleaning procedure is applied in order to select only those pixels, which only contain Cherenkov light signal. In case of *TACTIC* analysis, standard 2-level image cleaning method is used. The procedure involves selecting a pixel to be part of the image if it has a signal above a certain higher threshold or is adjacent to such a pixel which has signal above a lower threshold. These two thresholds are referred to as the *picture* and *boundary* thresholds, respectively. These thresholds are multiples of the rms pedestal deviation, which the PMT signal must exceed to be considered as part of the *picture* or *boundary*. All other pixels which do not satisfy this criteria are set to zero. A picture threshold of $\geq 6.5\sigma$ and a boundary threshold of $\geq 3.5\sigma$ have been used to select maximum number of pixels with signal, while at the same time limiting the inclusion of PMTs with shot noise alone.

3.7.3 Event classification and signal extraction

After removing noise dominated pixels, the resulting cleaned images are characterized by the Hillas parameters. The shape and orientation parameters of the image are determined by calculating the first three statistical moments of the cleaned image as already discussed. The derived image parameters are then used to distinguish candidate γ–ray events from the background of cosmic ray events. As already mentioned, these image parameters include *S, L, W, D,* α and *F2*. The dynamic supercut selection criteria used for *TACTIC* data analysis are the following : S $\geq$70 pe, $0.11^\circ \leq$ L $\leq (0.260+0.0265\times\ln \text{S})^\circ$, $0.06^\circ \leq$ W $\leq (0.110+0.0120\times\ln \text{S})^\circ$, $0.52^\circ \leq$ D $\leq 1.27^\circ \cos^{0.88}$ z, $\alpha \leq 18^\circ$ and F2 $\geq$ 0.35.

Defining $\alpha \leq 18°$ as the γ–ray domain and $27° \leq \alpha \leq 81°$ as the background region, the number of γ–ray events is then calculated by subtracting the expected number of backgorund events (calculated from the background region) from the γ–ray domain events. The reason for not including the α bin 18°–27° in the background region is to ensure that the background level is not overestimated because of a possible spill over of γ–ray events beyond 18°. Since the truncation of Cherenkov images recorded at the boundary of imaging camera can distort the flat nature of α–distribution for cosmic rays [3.26] especially when α–parameter is close to 90°, the α bin 81°–90° is also excluded while calculating the expected number of background events in γ–ray domain. This approach of estimating the expected background level in γ–domain is extensively used by all IACT groups when equal amount of OFF-source data is not available. However, this method has also been validated for *TACTIC* by using separate OFF-source data on a regular basis [3.13,3.15–3.20] and the α distribution of these data in the range $\alpha \leq 81°$ is in good agreement with the expected flat distribution. The significance of excess events is finally calculated by using the maximum likelihood ratio method of Li and Ma [3.27]

$$S = \sqrt{2}\left[N_{on}ln\left\{\frac{1+\beta}{\beta}\left(\frac{N_{on}}{N_{on}+N_{off}}\right)\right\} + N_{off}ln\left\{(1+\beta)\left(\frac{N_{off}}{N_{on}+N_{off}}\right)\right\}\right]^{1/2} \tag{3.34}$$

where N_{on} denotes the number of γ–ray events with $\alpha \leq 18°$ and N_{off} is the number of background events with $27° \leq \alpha \leq 81°$. β is normalization factor and is defined as the ratio of number of bins for signal region to the number of bins for estimating the background. If a source is not detected with significant excess in the signal extraction, an upper limit on the excess events must be calculated using observed excess and background events and the related uncertainty. The details of upper limit calculation for *TACTIC* observations is discussed in Chapter 5.

3.7.4 Energy estimation and Determination of energy spectrum

Keeping in view the fact that the Cherenkov light emitted from the electromagnetic cascade is to a first order approximation proportional to the energy of the primary γ–ray, the approach followed in IACTs is to determine the energy on the basis of image size (S). Since the intensity of the Cherenkov light is a function of core distance, which is not possible to obtain with a single imaging telescope, the distance parameter (D) is generally used as an approximate measure of the impact distance. The energy reconstruction procedure with a single imaging telescope thus involves S and D parameters of the Cherenkov event for determining the energy of the primary γ–ray. A novel energy reconstruction procedure, based on the utilization of artificial neural network (ANN), has been developed for the *TACTIC*. While the details of the energy reconstruction procedure can be found in [3.28], brief description regarding its implementation and performance evaluation is given below.

Given the inherent power of ANN to effectively handle the multivariate data fitting, an ANN-based energy estimation procedure has been developed for determining the energy of the primary γ–rays on the basis of their image SIZE, DISTANCE and zenith angle. The procedure followed uses a 3:30:1 (i.e 3 nodes in the input layer, 30 nodes in hidden layer and 1 node in the output layer) configuration of the ANN with resilient back propagation training algorithm to estimate the energy of a γ–ray event. The three nodes in the input layer correspond to zenith angle, SIZE and DISTANCE, while the one node in the output layer represents the expected energy (in TeV) of the event. The activation function chosen is the sigmoid function.

The performance of the ANN-based energy reconstruction procedure has been evaluated by calculating the relative error (Δ_E) in the reconstructed energy, for individual γ–ray events using the test data file. The relative error in the reconstructed energy is defined as

$$\Delta_E = \frac{E_{estm} - E_{true}}{E_{true}} \tag{3.35}$$

where E_true is the true energy and E_estm is the estimated energy yielded by the energy reconstruction procedure. The proposed method yields an energy resolution of ~26% (defined as the rms width of best fit Gaussin to Δ_E) with a negligible bias in the energy.

The differential photon flux (i.e number of γ–ray events per unit area, per unit time, per energy bin) in i^{th} energy bin is computed using the formula

$$\left(\frac{d\phi(E_i)}{dE}\right) = \frac{\Delta N_i}{\Delta E_i \sum_{j=1}^{5} A_{i,j}\eta_{i,j}T_j} \tag{3.36}$$

where ΔN_i is the number of excess events in the i^{th} energy bin ΔE_i over the zenith angle range of 0°–45°. T_j is the observation time in the j^{th} zenith angle bin with corresponding energy dependent effective area ($A_{i,j}$) and γ–ray acceptance ($\eta_{i,j}$). For *TACTIC* observations, five zenith angle bins (j=1-5) used are 0°–10°, 10°–20°, 20°–30°, 30°–40° and 40°–50° with effective collection area and γ–ray acceptance values available at 5°, 15°, 25°, 35° and 45° from Monte Carlo simulation.

3.7.5 Performance Evaluation of *TACTIC*

By virtue of being relatively bright and a stable γ–ray source, the Crab Nebula is usually used as a standard candle[1] in VHE astrophysics. The long term performance of the *TACTIC* has been studied by using the consolidated data collected on Crab Nebula from 2003 to 2010 [3.29]. The total ON-source data for $\sim$ 402 hours, yields 3742±192 γ–ray events with statistical significance of $\sim 20\sigma$. The resulting γ–ray rate is 9.31±0.48 h^{-1} and it can be defined as one Crab Unit (C.U.) for *TACTIC*. The ON-source α–plot for the Crab Nebula, when all the data for $\sim$ 402 hours is analyzed is shown in Figure 3.10(a). The cumulative significance level as a function of the observation time is shown in Figure 3.10(b). The differential energy spectrum

[1]Recent variability observed in Crab Nebula by space and ground based instruments questions its role as standard candle.

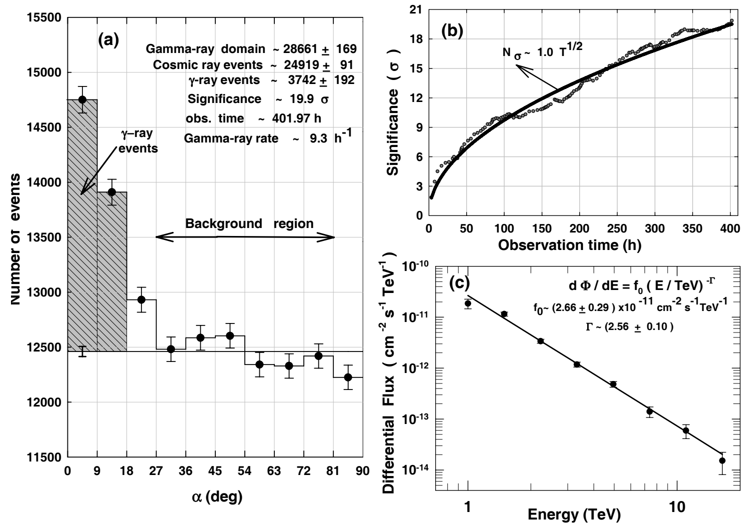

Figure 3.10: (a) ON-source α–plot for the Crab Nebula using $\sim$ 402 hours data, (b) Cumulative significance level as a function of observation time and (c) The differential energy spectrum of Crab Nebula as measured by *TACTIC*, using total ON-source data of $\sim$ 402 hours.

of the Crab Nebula as measured by *TACTIC* using total ON-source data of $\sim$ 402 hours is shown in Figure 3.10(c). A power law fit to the differential spectrum of the Crab Nebula with spectral index 2.56±0.10, matches reasonably well with that obtained by other IACTs and hence validates the overall performance of the *TACTIC*.

3.8 Summary

The imaging atmospheric Cherenkov technique provides an indirect and most efficient detection of VHE γ–rays from the celestial objects. The IACTs with large optical reflectors, multitude of pixels and high speed data acquisition system are certainly not simple experiments for exploring the γ–ray sky from the Earth. The *TACTIC* γ–ray telescope has been in operation at Mt. Abu since 2001 and has so far detected TeV γ–ray emission from the Crab Nebula, Mrk 421 and Mrk 501. The Crab Nebula spectrum measured with TACTIC is described by a power law with spectral index $\Gamma = 2.56 \pm 0.10$ and normalization constant $f_0 = (2.66 \pm 0.29) \times 10^{-11}$ ph cm^{-2} s^{-1} TeV^{-1} [3.29]. The spectrum matches reasonably well with that obtained by other IACT groups like Whipple ($\Gamma = 2.57 \pm 0.12$, $f_0 = (3.12 \pm 0.40) \times 10^{-11}$ ph cm^{-2} s^{-1} TeV^{-1}) [3.25] and HEGRA ($\Gamma = 2.59 \pm 0.03$, $f_0 = (2.79 \pm 0.02) \times 10^{-11}$ ph cm^{-2} s^{-1} TeV^{-1}) [3.30]. Apart from validating the stability of the *TACTIC* subsystems directly with γ–rays from Crab Nebula, matching of its spectrum also validates the full analysis chain, including the inputs used from the Monte Carlo simulations, like, effective area and γ–ray acceptance factors and the energy reconstruction procedure. There is enough scope for *TACTIC* to monitor TeV γ–ray emission from various active galactic nuclei (blazars in particular) on a long term basis.

3.9 References

[3.1] M. V. S. Rao & S. Sinha, 1988, J. Phys. G, 14, 811

[3.2] S. Eidelman et al., 2004, Phys. Lett. B, 592, 1

[3.2] W. Heitler, 1954, *Quantum Theory of Radiation*

[3.4] K. Greisen, 1960, Ann. Rev. Nucl. & Part. Sci., 10, 63

[3.5] K. Kamata & J. Nishimura, 1958, Prog. Theo. Phys. Suppl., 6, 93

[3.6] J. Blümer et al., 2009, Prog. Part. & Nucl. Phys., 63, 293

[3.7] T. Pierog et al., 2006, Czechoslovak J. Phys., 56, 161

[3.8] P. A. Cherenkov, 1934, Doklady Akad. Nauk SSSR, 2, 451

[3.9] I. A. Tamm & I. M. Frank, 1937, klady Akad. Nauk SSSR, 14, 107

[3.10] W. M. Yao et al., 2006, J. Phys. G : Nucl. Phys., 33, 1

[3.11] F. A. Aharonian et al., 2008, Rep. Prog. Phys., 71, 096901

[3.12] J. M. Davies & E. S. Cotton, 1957, Solar Energy, 1, 16

[3.13] R. Koul et al., 2007, NIM A, 578, 548

[3.14] R. J. Protheroe et al., 1997, ICRC, 8, 3.17

[3.15] P. Chandra et al., 2012, J. Phys. G, 39, 045201

[3.16] P. Chandra et al., 2010, J. Phys. G, 37, 125201

[3.17] K. K. Yadav et al., 2009, J. Phys. G, 36, 085201

[3.18] S. V. Godambe et al., 2008, J. Phys. G, 35, 065202

[3.19] K. K. Yadav et al., 2007, Astropart. Phys., 27, 447

[3.20] S. V. Godambe et al., 2007, J. Phys. G, 34, 1683

[3.21] S. R. Kaul et al., 2003, NIM A, 496, 400

[3.22] K. K. Yadav et al., 2004, NIM A, 527, 411

[3.23] M. K. Koul et al., 2011, NIM A, 646, 204

[3.24] A. M. Hillas, 1985, ICRC, 3, 445

[3.25] G. Mohanty et al., 1998, Astropart. Phys., 9, 15

[3.26] M. Catanese et al., 1998, ApJ, 501, 616

[3.27] T. P. Li & Y. Q. Ma, 1983, ApJ, 272, 317

[3.28] V. K. Dhar et al., 2009, NIM A, 606, 795

[3.29] A. K. Tickoo et al., 2014, Pramana J. Phys., 82, 585

[3.30] F. A. Aharonian et al., 2000, ApJ, 539, 317

Chapter 4

Observation of Mrk 421 Flare in February 2010 with *TACTIC*

4.1 Motivation for Observation

Blazars are excellent laboratories for studying multi-wavelength emission. The physics related to VHE blazars is not yet completely understood, despite some of these objects having been studied for more than 20 years. The blazar emission extending from radio to VHE γ–rays is characterized by strong and chaotic variability, ocassionally producing spectacular flares. The flaring events of blazars have attracted a considerable attention, triggering many extensive multi-wavelength campaigns that attempt to characterize the overall behaviour of individual objects. The variability of blazars in VHE regime has been discovered with a time scale of minutes to months. Current experimental data allow for a big inter-model and intra-model degeneracy. Therefore, accumulation of larger and high quality data sample of fast variable blazars is required to constrain and understand the emission models in steady and flaring states. Brightness and variability of blazars make them the best candidate sources for determining the precise energy spectra and time resolved light curves. With the aim of understanding the underlying physics of flaring activity in blazars, we have studied the intense flaring observed from Mrk 421 in February 2010 in this thesis. The main goal of our study is two fold: temporal study of the flux variation of the source and study of broad band SED during flaring activity using near simultaneous multi-wavelength observations including observations from *TACTIC* telescope.

4.2 The source: Mrk 421

Mrk 421 is one of the brightest VHE γ–ray blazars in the Northern hemisphere, located within the Ursa Major region as shown in Figure 4.1. The name *Mrk* comes from the inclusion of the source in the catalog of *Markarian* objects [4.1]. The catalog in turn takes the name from the Aremenian astronomer Benyamin Yerishevich Markarian, who compiled a catalog of 1515 galaxies with a UV continuum

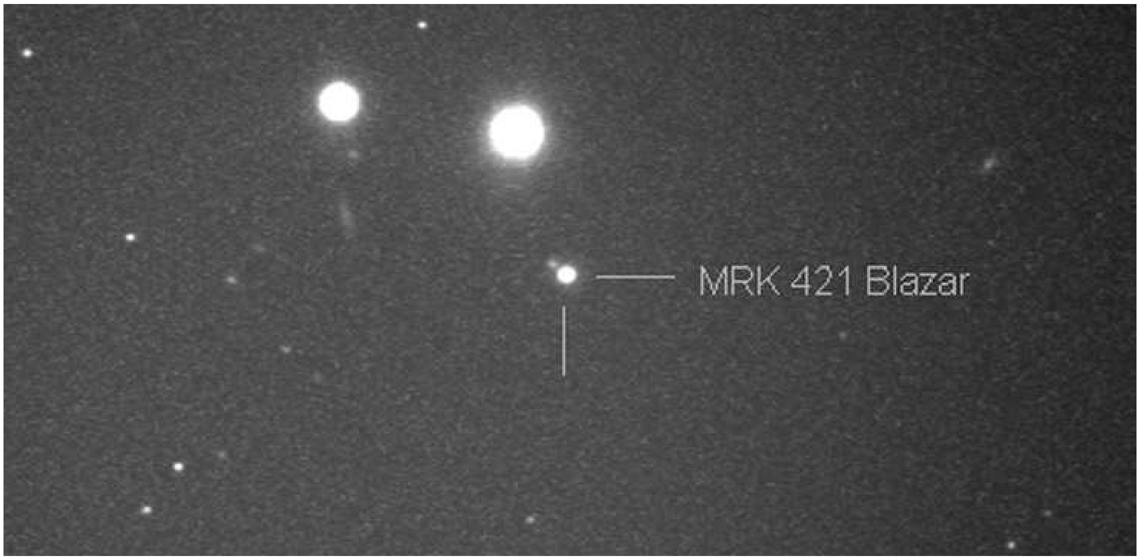

Figure 4.1: Location of Mrk 421 in Ursa Major (Credit: www.theskyscrapers.org).

between 1967 and 1981 [4.2]. The other names of Mrk 421 in the literature are : 1ES 1101+384, 1H 1104+382, H 1105+38, but recent TeV catalog suggests the name TeV J1104+382. The most popular and widely accepted name of the source Mrk 421, will be used in this thesis. In 1972, Mrk 421 was identified with radio source from the second Bolonga survey as B2 1108+38 [4.3]. In 1975, the source was identified as BL Lac object and its distance was measured [4.4]. The source was first noted to be an object with a blue excess which turned out to be an elliptical galaxy with a bright point like nucleus. The object showed optical polarization and the spectrum of the nucleus was seen to be featureless and so it was classified as BL Lac. In 1978, Mrk 421 was the first BL Lac object which was identified with X-ray source 2A 1102+384 [4.5] and had been subsequently followed by several multi-wavelength campaigns.

4.2.1 Basic Properties

Mrk 421 is classified as a high synchrotron peaked (HSP) blazar located at redshift z = 0.031 [4.6] with equatorial coordinates: RA = $11^h\ 04^m\ 19^s$, Dec = $38^\circ\ 11'\ 41''$ and galactic coordinates: l = 179.88°, b = 65.01°. The distance of the source from Earth is estimated to be 134 Mpc. The source is regularly detected by ground based gamma–ray telescopes. Some of the important observational properties of Mrk 421 are described below.

- Mrk 421 is the first extragalactic object detected at VHE by ground based Cherenkov telescopes, and second source after the Crab Nebula.
- It is among the closest and best studied blazars in the multi-wavelength regime and remains one of the most promising source for Target of Opportunity (ToO)

program of all instruments.

- The source has been known to demonstrate rapid, sub-hour flaring behavior at keV and TeV energies during the course of an outburst.

- The VHE flux may vary from a few tenths to a few Crab Units on a time scale of minutes and the flux changes are accompanied with strong spectral variations.

- The variations at X-ray and TeV energies are often very well correlated with no measurable delay, but complex intra-day X-ray variability has also been observed.

4.2.2 Previous Observations

Since 1982, more than 100 instruments world wide have contributed over approximately 3300 observations to the light curve of Mrk 421. This is the first extraglactic object detected at γ–ray energy above 500 GeV by the pioneer *Whipple* Cherenkov telescope in 1992 [4.7]. Few years later, the detection was confirmed by *HEGRA* telescope [4.8]. Since its first detection, Mrk 421 has been the target of many MWL campaigns involving space borne instruments, Cherenkov telescopes and ground based optical and radio facilities.

- **Radio Observations:** Mrk 421 was identified as a radio loud source in 1972. Its radio behavior is rather tame, typical of HSP blazars [4.9]. No variability was detected in more than 30 years of regular monitoring at 14.5 GHz by the University of Michigan Radio Astronomical Observatory (UMRAO) from 1980 to 2010. The source was also monitored from mid 1995 to the end of 2000 at 22, 37 and 87 GHz with 13.7 m Metsähovi radio telescope [4.10] but no evidence for short timescale variability was observed. In 2010, Mrk 421 was monitored with *Very Long Baseline Interferometry* (VLBI) network array at 22 GHz for 20 days between March 7 and May 31 to understand the relativistic jet formation through direct imaging of emitting region [4.11]. A jet component located at 1 milli-arcsec (mas) north-west from the core was able to be identified, and its proper motion was measured to be (-1.66$\pm$0.46) mas yr^{-1}. The negative velocity indicates that the jet component was apparently moving towards the core. In September 2012, Mrk 421 underwent a rapid wideband unprecedented radio flare, reaching nearly twice the brightest level observed in the centimeter (cm) band in over three decades of long radio monitoring history. The flare was detected by OVRO 40 m telescope at 15 GHz [4.12]. In this flare, the 15 GHz flux density increased with an exponential doubling time of about 9 days, then faded to its prior level at a similar rate. This is comparable with the fastest large amplitude centimeter-band radio variability observed in any blazar.

- **Optical Observations:** From archival plates, the first optical light curve of Mrk 421 was obtained in 1975 which contains measurements for almost every year between 1900–1975 [4.13]. This light curve shows strong variability on the time scales of months or less and also variability over time scales of years with a maximum to minimum change by a factor of 76. In other observations, optical variability on time scales down to hours was also seen [4.14] and the apparent magnitude of the source was reported to be ≈ 14. As mentioned earlier, the source is characterized by strong variability in the optical region including long timescale variability of 4.6 magnitude [4.15, 4.16] and extreme rapid optical variability exemplified by a 1.4 magnitude brightness change in only 2.5 hours [4.14]. Intraday and short time scale variability were also observed in the infrared region from the source [4.17].

- **X-ray Observations :** Mrk 421 is a known strong and variable X-ray source up to the hard X-rays and belongs to the complete sample of X-ray blazars. The source has a long history of X-ray observation showing flaring like fluxes and spectral changes. The *Ariel 5* satellite first detected X-rays from Mrk 421 when it flared dramatically in May 1975 [4.18]. The quiescent flux observed with the same instrument was only $\sim 5\%$ of the peak flux of the flare. Subsequent observations were obtained with five other X-ray satellites: SAS 3, OSO 8, HEAO 1 and Ariel 6, in the energy range 1.5-40 keV with proportional counter experiments. X-ray observation with the *HEAO 1* satellite detected a change in spectral index from 2.1 to 3.9 and the disappearance of the hard component above 10 keV by comparing with earlier observations from *OSO 8* and *SAS 3* satellites [4.19]. Between December 1978 and August 1979, the object was observed in the energy range 0.6-4.5 keV with the solid state spectrometer of the *Einstein Observatory* [4.20]. Subsequent to this observation, the source was observed with *Ariel 6* X-ray satellite in January 1980. A single power law of index 1.9 did provide an acceptable fit to the data, but the spectrum appeared to have a broken power law form, with a soft component similar to that seen with the *HEAO 1* in 1978 and a hard component similar to that seen with the *OSO 8* experiment in 1977. Taken together, X-ray observations of Mrk 421 showed a complicated, highly variable source that during 5 years of monitoring has changed in intensity by at least two orders of magnitude and has shown dramatic spectral changes as well. The source got progressively fainter and the dimming was correlated with steepening of the spectrum. Finally, in early 1980, Mrk 421 again got brighter, and this time the overall 1-10 keV spectrum steepened, although it was probably not a single power law but a composite of a steep and a flat power law.

  Over the period January 1984 to June 1985 *EXOSAT* observed Mrk 421 on a total of 14 occasions in the energy range 0.03-10 keV [4.21]. A significant variability on time scale of a day with a minimum e-folding time of 5×10^4 seconds was observed. In 1994, the source was observed with X-ray satellite *ASCA* for 24 hours in the energy range 2-10 keV [4.22]. The *ASCA* observations recorded a high level of X-ray flux peaking at 3.7×10^{-10} erg cm^{-2} s^{-1}, a 10-fold increase over the value observed in 1993, thus implying a flare like behavior. A large well defined flare was observed from Mrk 421 in April 1998 with *BeppoSAX* satellite in the energy range 0.1-300 keV [4.23]. These observations provided the first evidence that the X-ray and TeV emissions from the blazar Mrk 421 were well correlated on time scale of hours. In May 2000, Mrk 421 was observed in a relatively high state with 2-6 keV flux of 1.6×10^{-10} erg cm^{-2} s^{-1} by *XMM-Newton* [4.24]. The 0.2-10 keV spectrum was well fitted by a broken power law and no absorption structure was found in the source spectrum. In April 2006, *Suzaku* satellite observed a large flare from the source [4.25]. During the observation, the X-ray flux was variable, decreasing by 50%, from 7.8×10^{-10} to 3.7×10^{-10} erg cm^{-2} s^{-1} in about 6 hours, followed by an increase by 35%. Four strong X-ray flares were observed from Mrk 421 in the energy range 3-150 keV with *INTEGRAL* in June 2006 [4.26]. A time lag between high energy and low energy X-rays was observed, which allowed an estimation of the magnetic field strength. The *INTEGRAL* observations were triggered by an increase in *RXTE* count rate to more than 30 mCrab. During April-July 2006, Mrk 421 reached its highest X-ray flux recorded until that time. The peak flux was about 85 mCrab in the 2-10 keV band observed with *Swift* and evolution in the spectral parameters as a function of flaring activity was studied [4.27].

Two X-ray instruments onboard *RXTE* satellite namely Proportional Counter Array (PCA) and All Sky Monitor (ASM) started monitoring Mrk 421 since 1996 [4.28, 4.29]. During May-June 2008, Mrk 421 was observed in extremely high state by various X-ray instruments [4.30]. In hard X-rays (20-60 keV) *SuperAGILE* resolved a five day flare peaking at 55 mCrab. *SuperAGILE*, *RXTE*-ASM and *Swift*-BAT data showed a correlated flaring structure between soft and hard X-rays. *Swift*-XRT observation near the flaring maximum revealed the highest 2-10 keV flux ever observed from Mrk 421, of 2.6×10^{-9} erg cm^{-2} s^{-1} ($>$ 100 mCrab). In 2009, the source was again monitored with *Swift* and *RXTE* satellites under long and dense MWL monitoring program of classical TeV blazars [4.31]. The largest variability amplitide was registered in X-rays where variations by a factor of two in flux were seen, still much lower than the maximum values historically registered of 10-20 times variations.

- **HE γ–ray Observations :** The MeV-GeV or HE γ–ray emission from Mrk 421 was discovered by *EGRET* satellite in 1991 [4.32]. During *EGRET* observations the source flux was weak, but still statistically significant. The integrated photon flux above 100 MeV was reported to be $(1.4\pm0.3)\times 10^{-7}$ photons cm^{-2} s^{-1}. The differential photon energy spectrum in the energy range 100 MeV–1 GeV was represented by a power law with index 1.96±0.14. Mrk 421 was the first among 7 out of 24 known BL Lac objects detected with *EGRET*. In the Second *EGRET* catalog, the integral flux above 100 MeV was stated as $(1.57\pm0.14)\times 10^{-7}$ photons cm^{-2} s^{-1} with only insignificant time variability [4.33]. Nine years of observations with *EGRET* resulted in only a few viewing periods with a signal significance of barely 5σ as reported in the third catalog [4.34]. *COMPTEL* (COMpton TELescope) detected Mrk 421 in the energy range 10-30 MeV with 3.2σ significance during the period 1997–2001 [4.35]. Until 2006, only few observations of Mrk 421 between 10 keV and 1 GeV were available.

Since August 2008 after the launch of *Fermi* satellite, Mrk 421 is continuously being monitored by LAT in the energy range 30 MeV to 300 GeV. The HE γ–ray activity of the source during first 1.5 years of *Fermi* operation, from August 2008 to March 2010 was reported in 2011 [4.36]. The *Fermi*-LAT γ–ray spectrum above 300 MeV was well described by a power law function with photon index 1.78±0.02 and average photon flux was reported to be $(7.23\pm0.16)\times 10^{-8}$ photons cm^{-2} s^{-1}. Over this period, a significant variation in the photon flux (up to a factor 3 from the minimum to the maximum flux) was observed with mild spectral variation. The time averaged spectrum reported in the second *Fermi* catalog [4.37] for 24 months of observation (August 2008 to August 2010) is described by a power law with index 1.77±0.01 and integral photon flux above 1 GeV as $(2.97\pm0.06)\times 10^{-8}$ photons cm^{-2} s^{-1}. Observation of Mrk 421 with *Fermi*-LAT in the energy range 10-500 GeV from August 2008 to August 2011 has been reported recently in the first high energy catalog [4.38]. The three years time average spectrum in the energy band 10-500 GeV is represented by a power law index of 1.91±0.05 and flux above 10 GeV is reported to be $(4.55\pm0.22)\times 10^{-9}$ photons cm^{-2} s^{-1}. In the third *Fermi* catalog [4.39] based on four years of observations in the energy range 100 MeV–100 GeV, Mrk 421 is characterized by a power spectral index of 1.772±0.008 and integral flux above 1 GeV as $(3.03\pm0.04)\times10^{-8}$ photons cm^{-2} s^{-1}.

- **VHE γ–ray Observations :** The first VHE γ–ray emission above 500 GeV from Mrk 421 was detected by ground based *Whipple* telescope in 1992 at 6.3σ significance level with a flux approximately 30% of the Crab Nebula flux in 7.3 hours of observation [4.7]. During 1993–94 observation season, the source was again observed by *Whipple* group with an average flux level 20% of the Crab flux. However, in May–June 1994, two consecutive flares were detected from Mrk 421 [4.40]. The first outburst was observed with a rise in the flux by a factor 9±1.5 between May 11-15, 1994. After two weeks, the flux was nearly back to its low preburst level. On June 7, 1994 the second flare followed the first with a flux level of half of the first one and a rise time of two days. In 1995, for the first time other ground based Cherenkov telescope *HEGRA* beisdes the *Whipple* observatory detected TeV γ–ray emission from Mrk 421 and in this way confirmed the existence of the source [4.8]. The data collected by Cherenkov telescopes CT1 and CT2 of the *HEGRA* collaboration for 97 hours of observations yielded a VHE γ–ray signal with 6σ significance. Two major outbursts of VHE γ–rays above 300 GeV were observed by the *Whipple* telescope on May 7, 1996 and May 15, 1996 [4.41]. During the first of these bursts, the flux increased from 2 Crab to about 10 Crab within 2 hours. During the next half hour of observations, the beginning of a decay was visible. The spectrum during the flare was well fitted by a power law with index 2.56±0.07 above 500 GeV [4.42]. On May 8, 1996 the flux level was back to its quiescent value of 0.3 Crab. The second burst reached a peak flux of 5 Crab and was only about 30 minutes in duration. Investigation of large zenith angle data from *Whipple* observatory during June 18, 1995 and July 1, 1995 showed that the emission from Mrk 421 extends above 5 TeV [4.43]. In 1997, Mrk 421 was observed by the recently commissioned *TACTIC* for 29 hours. The observation yielded a conservative 3σ upper limit to the photon flux above 0.7 TeV of 2.2×10^{-11} photons cm^{-2} s^{-1} which was consistent with all earlier measurements of the quiescent state flux. Between January 1, 1997 and May 27, 1998, Mrk 421 was monitored for 165 hours with the *HEGRA* stereoscopic Cherenkov telescope system [4.44]. The mean differential flux at 1 TeV was about one half of the flux of the Crab Nebula. The light curve showed several distinct flares with mean durations of typically one or two days and fluxes at 1 TeV of approximately the Crab level. The time averaged energy spectrum in the range 500 GeV to 7 TeV followed to a good approximation a power law with a differential spectral index of 3.09±0.07.

During February-May 2000, Mrk 421 was observed with the *HEGRA* experiment [4.45]. Several flares with very rapid statistically significant flux variability on a 30 minute time scale were detected from the source. The TeV energy spectrum averaged over all the observations was described by a steep power law with index 2.94±0.06. In April 2001, Mrk 421 entered an extremely active phase. It was observed intensively with the 10 m *Whipple* telescope and exceptionally strong and long lasting flaring activity was revealed [4.46]. Flaring levels of 0.4-13 times that of the Crab Nebula flux provided sufficient statistics for a detailed study of the energy spectrum between 380 GeV and 8.2 TeV as a function of the flux level. These spectra were well described by a power law with an exponential cutoff. There was no evidence for variation in the cutoff energy with flux, and all spectra were consistent with an average value for cutoff energy of 4.3 TeV. The spectral index was observed to vary between 1.89±0.04 in a high flux state and 2.72±0.11 in a low state. Several TeV flares at intermediate flux levels, peaking between 1 and 1.5 times the flux from Crab Nebula were observed by *Whipple* and *HEGRA* experiments during December 2002 and January 2003 [4.47]. The time averaged spectrum was fitted with a power law of index 2.8 and some evidence for spectral variability was found. The *MAGIC* telescope observed VHE γ–ray emission above 100 GeV from Mrk 421 between November 2004 and April 2005 and the integral flux above 200 GeV was found to vary between 0.5 and 2 Crab [4.48]. Although the flux varied day by day, no short term variability was observed. The time averaged energy spectra from 100 GeV to several TeV was described by a power law of index 2.20±0.08 with exponential cutoff energy 1.44±0.27 TeV.

During the period November 2005 and June 2006, Mrk 421 was monitored for a total of 144 hours by 10 m *Whipple* telescope and TeV γ–ray emission was found to be variable on a nightly basis [4.49]. The *TACTIC* telescope also monitored the source during the same period overlapping with *Whipple* observations [4.50]. Although the energy ranges and sensitivities of the two instruments were slightly different, similar trends were present in the two observations. The maximum γ–ray rate of (4.38$\pm$0.49) Crab Unit was recorded for one of the *Whipple* observations on December 29, 2005. The flux on this night was seen to vary between (1.91$\pm$0.42) Crab Unit before reaching its peak value and then decreasing to (1.67$\pm$0.26) Crab Unit. Between January 2006 and June 2008, the source was observed for approximately 47 hours with *VERITAS* telescope and for 96 hours with *Whipple* telescope [4.51]. No evidence for rapid flux variability was found in *VERITAS* observations. However, on May 2-3, 2008, bright TeV flares with fluxes reaching the level of 10 Crab Unit were detected. From December 2007 until June 2008 Mrk 421 was intensively observed in VHE band by *MAGIC-I* telescope [4.52]. The source showed intense and prolonged γ–ray activity during the whole period, with integral fluxes above 200 GeV seldom below the level of the Crab Nebula, and up to 3.6 times this value. The broad band emission from Mrk 421 observed during June 2006 is shown in Figure 4.2 as an illustrative example for spectral energy distribution of the source.

The VHE duty cycle (defined as the fraction of time spent in flaring state) of Mrk 421 was estimated to be $\sim$ 40% using data from different IACTs during 1992–2009 [4.53].

4.2.3 X-ray/TeV Emission from Mrk 421

As mentioned earlier, Mrk 421 is classified as high synchrotron peaked blazar because its X-ray emission via synchrotron radiation peaks between a fraction of a keV to several keV. Its flux variations are accompanied with significant spectral variations. Many studies have demonstrated that the X-ray spectral shape of Mrk 421 is curved and described by a log-parabolic distribution with a mildly curved and symmetric spectral shape [4.54,4.55,4.56,4.57]. This feature is interpreted in the framework of energy dependent acceleration efficiency that naturally corresponds to log-parabolic spectral distributions with a possible power law tail at lower energies [4.56]. It has been shown that a log-parabolic distribution results from a stochastic acceleration scenario with a mono-energetic or quasi-mono energetic particle injection [4.58]. A relativistic Maxwellian electron distribution, produced by a stochastic acceleration process can be used to describe the X-ray/TeV emission of Mrk 421 [4.59, 4.60]. The TeV γ–ray emission arises from particles accelerated in a relativistic jet directed along our line of sight. The absence of strong optical emission lines indicates that photon sources external to the jet (an accretion disk or a dust torus), are modest and do not contribute significantly to the electron cooling. As a consequence, the

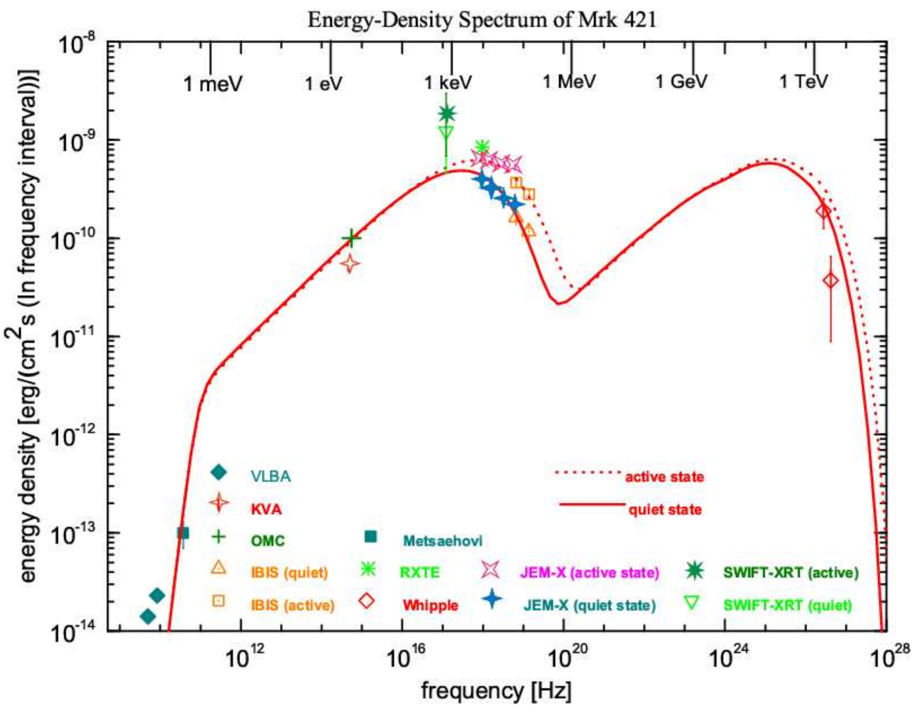

Figure 4.2: Measured multi-wavelength energy density spectrum of Mrk 421 with best fit model curve using one zone SSC process for blazar emission [4.26].

synchrotron component peaks at relatively high energies also during quiescence (soft X-rays) and the synchrotron photons are the main targets for Compton upscattering by the relativistic particles. This synchrotron self Compton component peaks at very high energies, making this blazar a strong TeV emitter, although the TeV spectrum is often heavily suppressed by the Klein-Nishina effect [4.23, 4.29]. The variations at X-ray and TeV energies are often very well correlated with no measurable delay, but complex intra-day X-ray variability has also been observed [4.61]. The correlated multi-wavelength variability of Mrk 421 suggests that a single population of particles may be responsible for radiation over most of the spectrum.

4.3 The Mrk 421 Flare in February 2010

In February 2010, Mrk 421 was observed in extreme flaring state at all energies by almost all instruments world wide. In VHE regime, the source was observed to be in a high state by *VERITAS*, *HESS*, *HAGAR* and *TACTIC*. The *VERITAS* telescope observed an unusual bright flare on February 17, 2010 (MJD 55244) in TeV γ–rays reaching a flux level of approximately 8 Crab Units with a variability time scale of few minutes [5.62]. The flaring episode, comprising about 5 hours of observations, yields presence of a γ–ray signal at statistical significance of 256σ. The spectrum is described by a power law with exponential cutoff: $dN/dE = N_0(E/E_0)^{-\Gamma}exp(-E/E_{cut})$, with normalization N_0=(5.28$\pm$0.09)$\times$ 10^{-10}

photons cm^{-2} s^{-1} TeV^{-1}, spectral index $\Gamma = 1.77 \pm 0.02$ and an exponential cut-off energy $E_{cut} = 4.06 \pm 0.2$ TeV. Triggered by *VERITAS* high state detection, the source was followed up by *HESS* telescope during February 17-20, 2010 (MJD 55244.96 - 55246.96) at an average zenith angle of 62° [4.63]. Analysis of about 5.4 hours of good quality data, obtained after applying various quality checks, yields an excess of 2112 events at statistical significance of 86.5σ with flux level varying from 1.4 to 4.8 Crab Units. The time averaged energy spectrum is characterized by a power law with exponential cutoff with normalization N_0=(1.96±0.32)× 10^{-11} photons cm^{-2} s^{-1} TeV^{-1}, spectral index $\Gamma = 2.05 \pm 0.22$ and an exponential cutoff energy E_{cut}=3.4±0.6 TeV. The source was also observed by *HAGAR* telescope in a bright state. The *HAGAR* observtaions during February 13-19, 2010 at the energies above 250 GeV show an enhancement in the flux level, with a maximum of about 7 Crab detected on February 17, 2010 [4.64].

In X-ray regime, strong flares from Mrk 421 were detected in January-February 2010 through the seven month monitoring with *MAXI* satellite. The maximum 2-10 keV flux in the January and February flares was measured as 120±10 mCrab and 164±17 mCrab respectively [4.65]. A comparision of *MAXI* and *Swift*-BAT data suggested a convex X-ray spectrum with an approximated photon index of ≥ 2. The source exhibited a spectral variation during these flares, slightly different from those in the previous observations, in which the positive correlations between flux and hardness were reported. A detailed spectral and temporal study of the flare along with results from the *TACTIC* are discussed in the following Sections.

4.4 Multi-wavelength Study of February 2010 Flare observed with *TACTIC*

We have performed a detailed temporal study of the VHE data collected during February 10–23, 2010 with *TACTIC*. We supplement this with near simultaneous multi-wavelength data in low energy bands to study the temporal and spectral characteristics of the source. The flaring activity of the source is studied by investigating the properties of daily light curves from radio to TeV energy range and variability amplitude as a function of energy. The TeV flare detected by *TACTIC* on February 16, 2010 is well correlated with the activity in lower energy bands. In addition, we also perform the spectral study of the flaring data recorded on February 16, 2010 (MJD 55243). The broad band spectral energy distribution of the source in flaring state is reproduced using a simple emission model involving synchrotron and synchrotron self Compton processes. The obtained parameters are then used to understand the energetics of the source during the flaring episode. Throughout this study we adopt ΛCDM cosmology with parameters, H_0=70 km s^{-1} Mpc^{-1}, Ω_m=0.27 and Ω_Λ=0.73.

Table 4.1: Dynamic Supercuts selection criteria used for analyzing the *TACTIC* data.

Parameters	Cuts Value
LENGTH (L)	$0.11^{\circ} \leq$ L $\leq (0.235 + 0.0265 \times \ln$ S$)^{\circ}$
WIDTH (W)	$0.065^{\circ} \leq$ W $\leq (0.085 + 0.0120 \times \ln$ S$)^{\circ}$
DISTANCE (D)	$0.5^{\circ} \leq$ D $\leq (1.27$ Cos$^{0.88}$ $\Theta)^{\circ}$ (Θ= Zenith angle)
SIZE (S)	S $\geq$ 485 dc (8.5 digital counts = 1.0pe)
ALPHA (α)	$\alpha \leq 18^{\circ}$
FRAC2 (F2)	F2 $\geq$ 0.38

4.4.1 Multi-wavelength Data Sample and Analysis

Mrk 421 was observed during February 10–23, 2010 with the *TACTIC* at energies above 1.5 TeV. Near simultaneous multi-wavelength data were obtained from high energy (MeV-GeV) γ–ray observations with *Fermi*–LAT, X–ray observations by the *Swift* and *MAXI* satellites, optical V-band observation by SPOL at *Steward Observatory* and radio 15 GHz observation at OVRO 40 meter-telescope. The detailed procedure for the analysis of data of Mrk 421 collected during February 10–23, 2010 (MJD 55237-55250) is outlined below.

- **TACTIC Data :** After performing the standard *TACTIC* data quality checks, around 48.4 hours of clean data, spanning over 12 nights of observation were collected during February 10–23, 2010. The data recorded with *TACTIC* were analysed using standard Hillas parameterization technique as described in Chapter 3. The standard dynamic supercut procedure is used to separate γ–ray like images from background images of cosmic rays. The γ–ray selection cuts, obtained on the basis of Monte Carlo simulations carried out for *TACTIC* telescope are given in Table 4.1. The γ–ray signal is extracted from cosmic–ray background using frequency distribution of α–parameter after applying the set of image parameter cuts presented in Table 4.1. The image parameters given in Table 4.1 are slightly different from the one discussed in Section 3.7.3 for Crab because of variation in SIZE parameter (S) of Cherenkov images recorded by the telescope during different observation seasons. The analysis of *TACTIC* data from Mrk 421 direction during February 10–23, 2010 resulted in an excess of 737$\pm$87 γ–ray like events corresponding to a statistical significance of 8.46σ in nearly 48 hours. Observation of flaring activity on February 16, 2010 (MJD 55243) alone yields 172$\pm$30 γ-like events corresponding to a statistical significance of 5.92σ in $\sim$ 4.9 hours. The α–distribution of one day data collected during the flare on February 16, 2010 is shown in Figure 4.3. The energy of each γ–ray like event is reconstructed using an artificial neural network (ANN) based methodology on the basis of its zenith angle, SIZE and DISTANCE as described in Chapter 3.

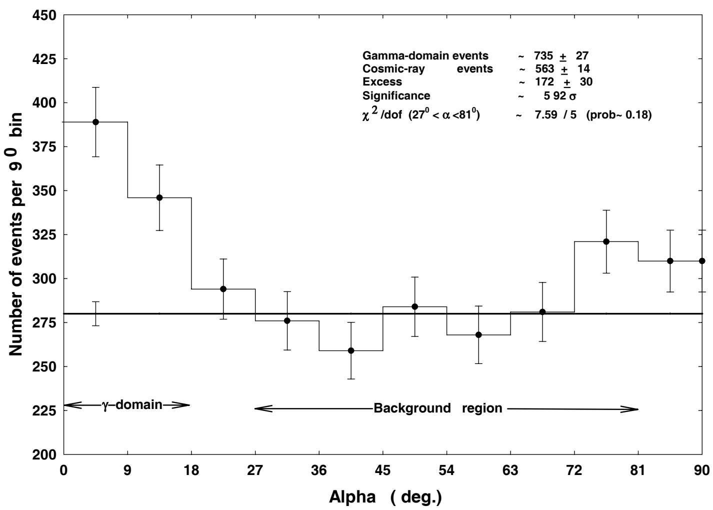

Figure 4.3: On-source alpha distribution of Mrk 421 for $\sim$ 4.9 h of data collected during the flare on February 16, 2010. The horizontal line represents the expected background in γ-domain.

- **LAT Data :** The LAT data used in this work were collected from MJD 55237 (February 10, 2010) to MJD 55250 (February 23, 2010), the period which overlaps with the γ–ray flare of Mrk 421. The data were obtained from FSSC archive[1] and the data analysis was performed using the standard *Fermi* Science-Tools software package (version v9r27p1). Only diffuse class events in the energy range 100 MeV–100 GeV from a circular region of interest (ROI) with radius 15° were included in the analysis. The set of instrument response functions *P7SOURCE_V6* were used. Events with zenith angle $> 105°$ were filtered out to avoid the Earth albedo as suggested by *Fermi*-LAT team. The data obtained in this manner were analyzed using unbinned maximum likelihood algorithm implemented in *gtlike* tool which is also a part of Science-Tools package. The background model used to extract γ–ray signal from the source includes two components: galactic diffuse emission and isotropic background emission. The galactic diffuse component is parameterized by the map cube file *gal_2yearp7v6_v0.fits*. The isotropic background component (sum of residual instrumental background and extragalactic diffuse γ–ray background) was included using the standard model file *iso_p7v6source.txt*. The spectra of Mrk 421 and other point sources in ROI were fitted with a power law defined as:

$$N(E) = \left[\frac{(\Gamma+1)N_o}{(E_{max}^{\Gamma+1} - E_{min}^{\Gamma+1})} \right] E^{\Gamma} \tag{4.1}$$

[1]http://fermi.gsfc.nasa.gov/ssc/data/access

where Γ is the photon index, N_0 is normalization constant, E_{min} and E_{max} are the lower and upper limits of the energy interval selected for Likelihood analysis. We derived the daily light curve and differential photon spectrum of Mrk 421 in the energy range 100 MeV–100 GeV using the methodology described above.

- **XRT Data :** We used *Swift*–XRT archival data from MJD 55237 (February 10, 2010) to MJD 55250 (February 23, 2010) which were analyzed using *xrt-pipeline* utility available with the HEASoft package. We produced the light curves and spectra for each day using spectral analysis package XSPEC.

  A daily average flux in the energy range 15–50 keV detected by *Swift*–BAT was obtained from online data archive [2]. We also used X–ray data in the energy range 2–20 keV observed by X–ray instrument onboard *MAXI* satellite from the website[3].

- **SPOL and OVRO Data :** *Fermi* multi-wavelength observing support program provides data publicly for regular or targeted observation of blazars[4]. We obtained the V–band optical data of Mrk 421 from the SPOL CCD Imaging/Spectropolarimeter at Steward Observatory, University of Arizona[5]. The 15 GHz radio data were obtained from 40m Owens Valley Radio Observatory (OVRO)[6].

4.4.2 Light curve Analysis

The multi-wavelength light curves of Mrk 421 during February 10–23, 2010 (MJD 55237–55250) in TeV, MeV-GeV, X–ray, optical and radio bands are shown in Figure 4.4(a-g). The source was observed in a high state in γ–ray and X–ray energy bands on February 16, 2010 (MJD 55243). Figure 4.4(a) shows the daily averaged light curve of TeV photons detected with the *TACTIC*. We observe that the TeV γ–ray flux starts increasing from February 15, 2010 (MJD 55242), attains a peak on February 16, 2010 (MJD 55243) and finally decays gradually. Figure 4.4(b-g) corresponds to observations with *Fermi*–LAT, *Swift*–BAT, MAXI, *Swift*–XRT, SPOL and OVRO respectively. From the figure it is apparent that the TeV flaring activity detected by *TACTIC* is accompanied by enhanced activity in lower energy bands from MeV-GeV to X–rays and a mild change in V-magnitude. The radio observations are available only for five days and no significant flux variations are observed during this period. If we attribute the observed flare to jet activity, non-detection of radio variation can be associated with the significant absorption at these energies due to synchrotron self absorption process. The multi-wavelength flaring on February 16, 2010 (MJD 55243) is followed by an enhanced activity in

[2]http://heasarc.nasa.gov/docs/swift/results/transients
[3]http://maxi.riken.jp/top/index.php
[4]http://fermi.gsfc.nasa.gov/ssc/observations/multi/programs
[5]http://james.as.arizona.edu/ psmith/Fermi/
[6]http://www.astro.caltech.edu/ovroblazars/data

Table 4.2: Summary of multi-wavelength light curves of Mrk 421 during February 10-23, 2010 (MJD 55237–55250).

Instrument	Energy Band	Constant emission	Flare Emission (16 Feb. 2010)
TACTIC	1.5-11 TeV	(1.0±0.2)×10^{-11} ph $cm^{-2}s^{-1}$	(2.5±0.4)×10^{-11} ph $cm^{-2}s^{-1}$
LAT	0.1-100 GeV	(7.2±0.3)×10^{-8} ph $cm^{-2}s^{-1}$	(3.2±0.9)×10^{-7} ph $cm^{-2}s^{-1}$
BAT	15-50 keV	(5.9±0.1)×10^{-3} cts $cm^{-2}s^{-1}$	(15.7±0.8)×10^{-3} ph $cm^{-2}s^{-1}$
MAXI	2-20 keV	(18.0±2.4)×10^{-2} ph $cm^{-2}s^{-1}$	(46.0±4.0)×10^{-2} ph $cm^{-2}s^{-1}$
XRT	0.2-10 keV	(1.6±0.3)×10^{-9} erg $cm^{-2}s^{-1}$	(2.7±0.6)×10^{-9} erg $cm^{-2}s^{-1}$
SPOL	V-band (Optical)	(13.09±0.02) mag.	(13.04±0.02) mag.
OVRO	15 GHz (Radio)	(0.445±0.004) Jy	–

X–rays on February 22, 2010 (MJD 55249). Thus X–ray data show two consecutive flares during the period February 10–23, 2010. However, because of the absence of TeV data on February 22, 2010, we concentrate only on the flare detected in multi-wavelength regime on February 16, 2010 (MJD 55243) in the present study. The light curves in all energy bands (radio to TeV) shown in Figure 4.4 are fitted with a steady emission during February 10–23, 2010 to identify the corresponding flare on February 16, 2010 (MJD 55243). The results of the light curve analysis in various energy bands are summarized in Table 4.2. We also use e-folding time scale method [4.66] to compute the variability time scale (t_{var}) for each light curve. This method allows computation of variability time using just two flux measurements and it does not require any fitting or minimization procedure. From the light curve analysis, we observe that Mrk 421 shows a time variable broad band emission from X–rays to TeV γ–rays with a temporal variability of approximately one day.

4.4.3 Variability and Correlation Study

To quantify the flux variation in a given energy band, we deduce its fractional variability amplitude (F_{var}) given by [4.67],

$$F_{var} = \frac{[S^2 - \langle\sigma_{err}^2\rangle]^{\frac{1}{2}}}{\langle F\rangle} \tag{4.2}$$

where $\langle F\rangle$ is mean photon flux, S is standard deviation and σ_{err}^2 is mean square error of N-flux points in the light curve. The error in fractional variability amplitude is then given by:

$$\Delta F_{var} = \frac{1}{F_{var}}\sqrt{\frac{1}{2N}}\frac{S^2}{\langle F\rangle^2} \tag{4.3}$$

The fractional variability amplitude as a function of mean observational energy of different instruments is shown in Figure 4.5. Within the frame work of leptonic

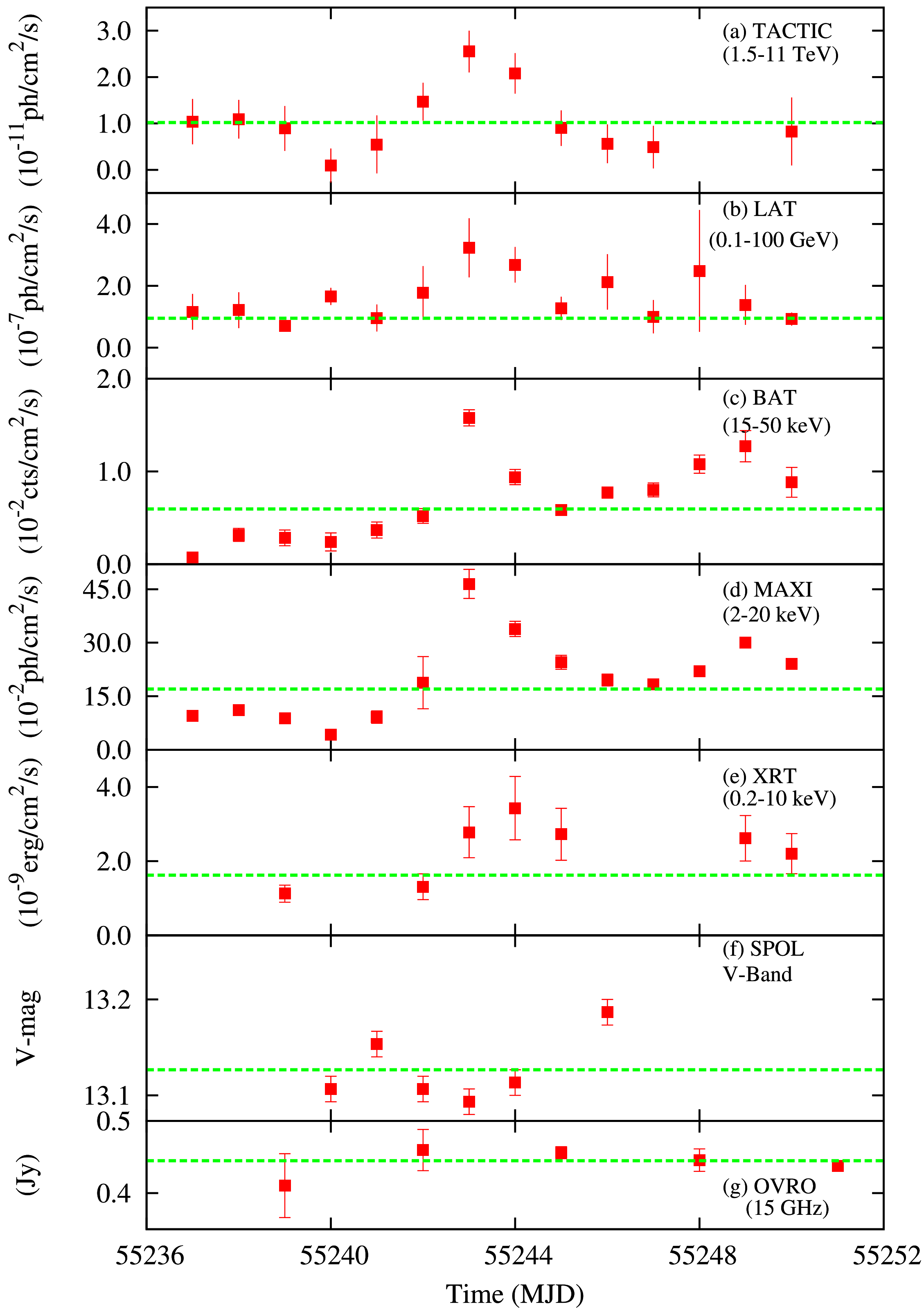

Figure 4.4: Multi-wavelength light curves for Mrk 421 during February 10–23, 2010. The horizontal dotted lines represent the average emission during this period in each energy band.

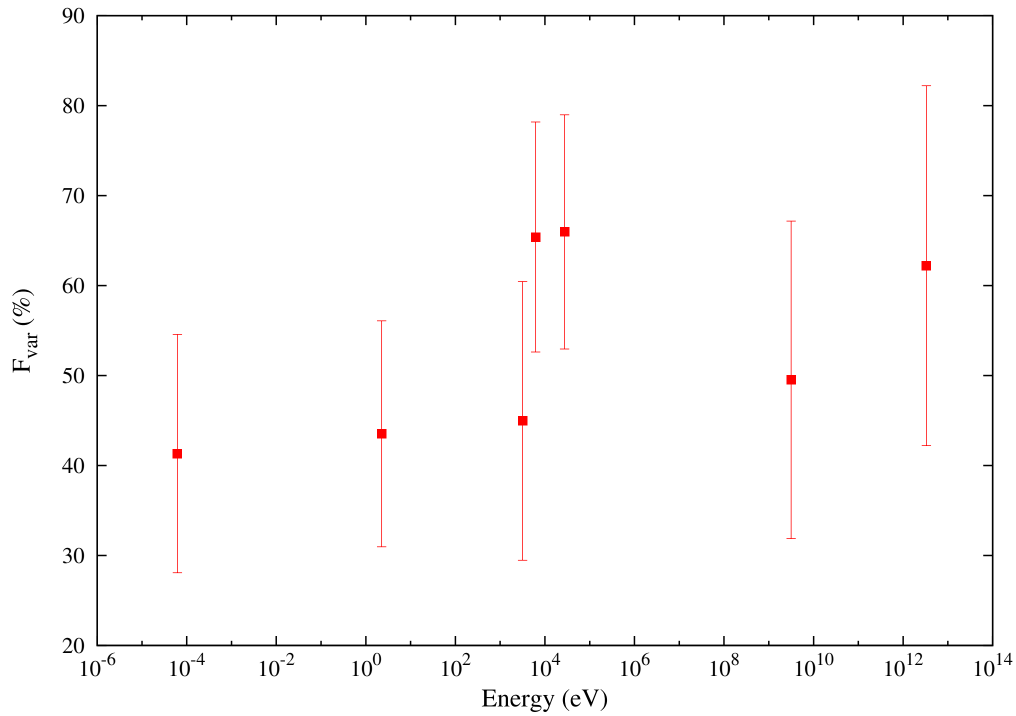

Figure 4.5: Fractional Variability Amplitude in the multi-wavelength observations of Mrk 421 during February 10–23, 2010.

SSC model, the X–ray and γ–ray variabilities give information about the dynamics of relativistic electron population. From the figure, it is clear that the fractional variability amplitudes in various energy regimes are confined in the range 30–80%. The fractional variability measured in X–rays and TeV γ–rays is apparently higher than that observed in other energy bands. This further suggests that these energies may be associated with the same population of relativistic electrons with faster cooling rates, favouring synchrotron and SSC origin of X-rays and TeV γ–rays. Whereas, the emission at other energies, including MeV-GeV, may be associated with low energy electrons with slower cooling rates. However, with the large error bars it is difficult to quantify the exact energy dependence of the fractional variability amplitude during the present flaring activity of the source.

We also compute the variability amplitude parameter (A_{mp}) introduced in [4.68] to characterize the percentage variation in each light curve. The variability amplitude parameter (A_{mp}) is defined as:

$$A_{mp} = \frac{1}{\langle F \rangle} \sqrt{(F_{max} - F_{min})^2 - 2\sigma^2} \tag{4.4}$$

where F_{max} and F_{min} are the maximum and minimum fluxes in each light curve and σ is average measurement error in the light curves. The fractional variability amplitude

Table 4.3: Variability amplitudes for Mrk 421 multi-wavelength observations during February 10-23, 2010 (MJD 55237–55250).

Instruments	Energy Band	F_{var} (%)	A_{mp} (%)
TACTIC	1.5-11 TeV	62.2±20.0	209
LAT	0.1-100 GeV	49.5±17.6	140
BAT	15-50 keV	65.9±13.0	198
MAXI	2-20 keV	65.4±12.8	193
XRT	0.2-10 keV	44.9±15.4	80
SPOL	V-band	43.5±12.5	23
OVRO	15 GHz	41.3±13.2	7

(F_{var}) and variability amplitide parameter (A_{mp}) for observations obtained in the present study are given in Table 4.3. We further study the Pearson correlations between TeV and other simultaneous low energy emissions. The scatter plots for correlations with corresponding correlation coefficients are shown in Figure 4.6(a-f). We observe that variations at X–ray energies observed by *Swift*–XRT/BAT and MAXI are strongly correlated with TeV γ–rays, supporting our earlier inference that the same population of electrons is responsible for emission at these energies.

4.4.4 X-ray Spectral Evolution

The variation of photon spectral index with the integral flux in 1–10 keV energy range as obtained from *Swift*/XRT spectrum is shown in Figure 4.7. It shows a distinct loop structure with clockwise sense. The clockwise loop signifies a soft lag in the spectral evolution [4.69]. The spectrum evolves from hard-to-soft as the flare evolves. The hard-to-soft spectral evolution can be obtained if the evolution of radiation emitting particles is either cooling dominated or the cooling time scale is approximately equal to the acceleration time scale of the particles. If the MeV–GeV photons are produced due to the synchrotron self-Compton process, as it is generally considered for BL Lacs, then a similar loop structure with clockwise sense is also expected for MeV–GeV photons. But such a study is difficult in the MeV–GeV energy range due to the large error bars in the flux data.

4.4.5 Spectral Analysis of Flare on Feb 16, 2010

For detailed spectral analysis during flaring state, we use one night data comprising $\sim$ 5 hours of data collected with *TACTIC* on February 16, 2010 (MJD 55243). This observation reveals an excess of 172±30 γ–ray like events with a statistical significance of 5.92 σ. The corresponding observed differential energy spectrum of the source is presented in Figure 4.8 and the respective flux points are given in Table 4.4. The differential energy spectrum of γ–rays from Mrk 421, in the energy range

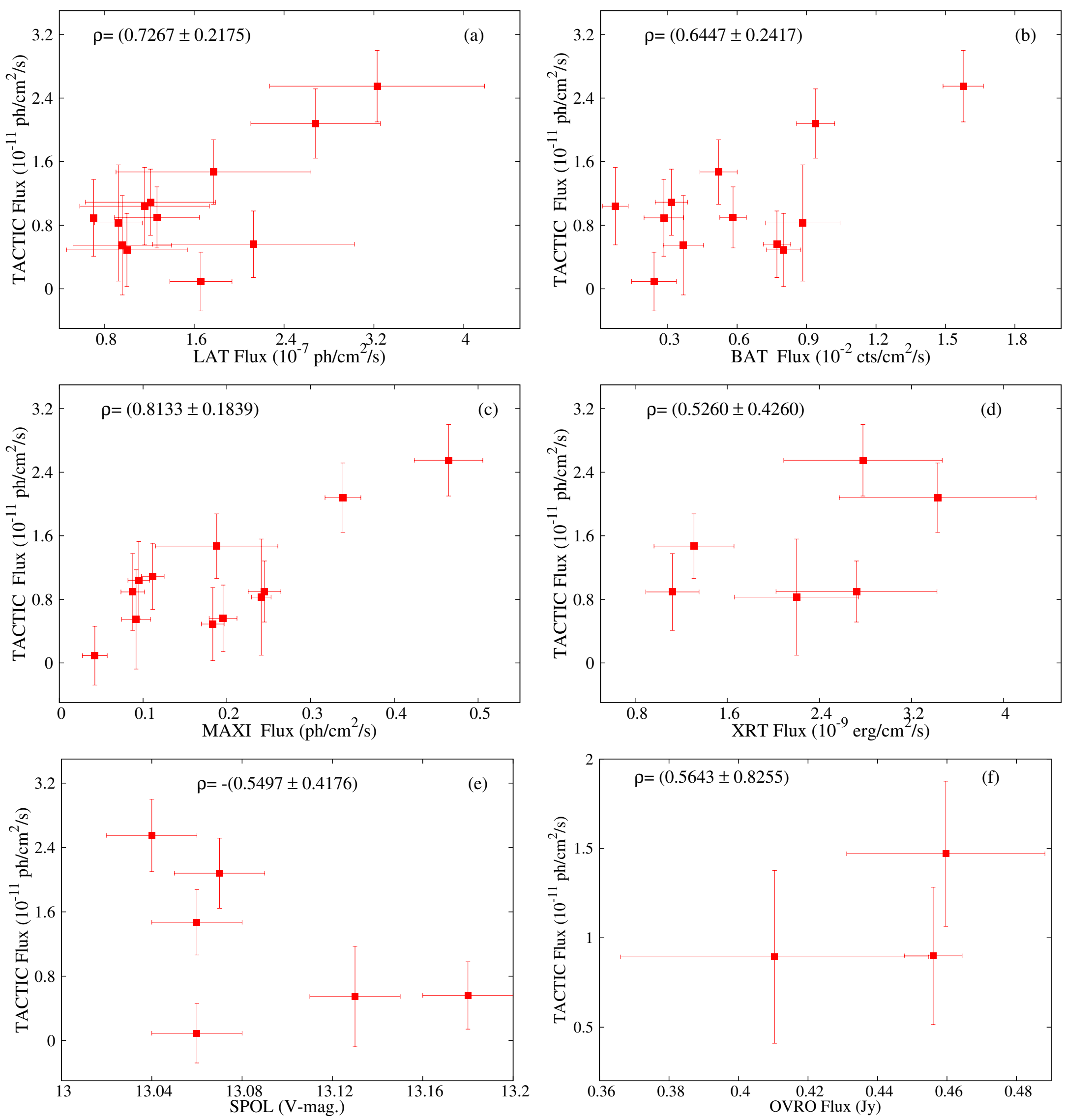

Figure 4.6: Scatter plot for correlation between TeV γ-rays measured by *TACTIC* telescope and near simultaneous low energy observations.

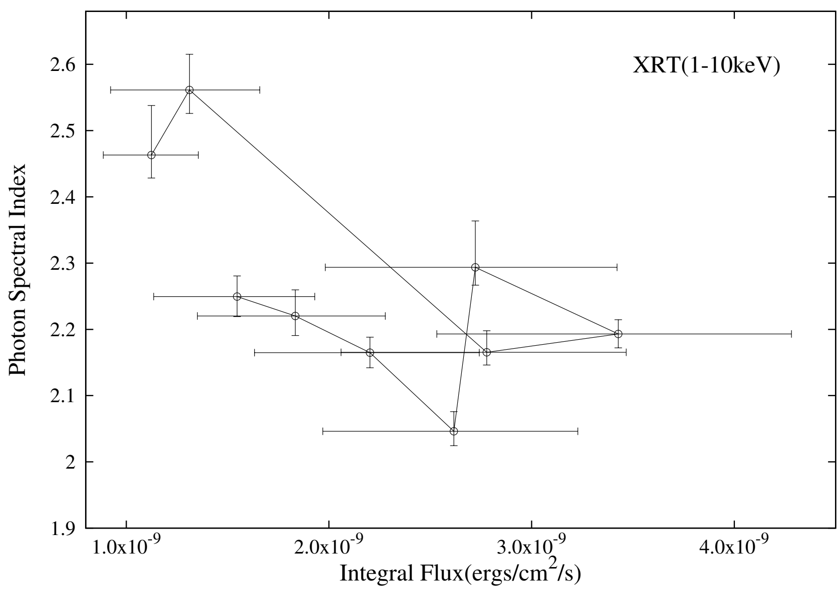

Figure 4.7: Hysteresis pattern of X-ray flux in the energy band 1-10 keV observed by *Swift*-XRT showing the spectral evolution in the source.

1.5-11 TeV, as measured by *TACTIC* on February 16, 2010 is described by a power law of the form

$$\left(\frac{dN}{dE}\right) = (8.13 \pm 2.95) \times 10^{-11} \left(\frac{E}{1TeV}\right)^{-2.60\pm0.35} ph.cm^{-2}s^{-1}TeV^{-1} \qquad (4.5)$$

In order to account for EBL absorption we have used two recent EBL models proposed by Franceschini et al. (2008) [4.70] and Dominguez et al. (2011) [4.71] to estimate the absorption of TeV γ–rays from Mrk 421. The EBL corrected spectrum is again well described by a power law. The observed and intrinsic spectral parameters of the source are given in the Table 4.5. Since the intrinsic spectral indices corresponding to two EBL models are found to be similar, one can use either to model the SED of the source. If we attribute the TeV emission to inverse Compton (IC) emission from a power law distribution of electrons, the obtained intrinsic TeV spectral index corresponds to a particle spectral index $\sim$ 3.6.

The highest activity state of the source on February 16, 2010 was also observed by *Fermi*–LAT in the energy range 0.1–100 GeV with TS value 87 corresponding to statistical significance of 9.3σ. The LAT differential energy spectrum of the source during the flare has been obtained by dividing the LAT energy range into four energy bands: 0.1–1 GeV, 1–3 GeV, 3–10 GeV and 10–100 GeV. The spectrum of Mrk 421 measured on February 16, 2010 by *LAT* detector is described by a power law ($d\Phi/dE = f_0\, E^{-p}$) with $f_0 = (5.73 \pm 0.89) \times\, 10^{-8}$ photons cm^{-2} s^{-1} GeV^{-1} and p= 1.72$\pm$ 0.13. Again, if we consider an IC origin of photons above 100 MeV from a power law distribution of electrons, this spectral index corresponds to a particle

Table 4.4: Differential energy spectrum flux points for Mrk 421 during flare on February 16, 2010 measured with *TACTIC*. Only statistical errors are given.

Energy (TeV)	Differential flux (photons cm^{-2} $s^{-1}TeV^{-1}$)	Statistical error in flux (photons cm^{-2} s^{-1} TeV^{-1})
1.50	2.84×10^{-11}	9.34×10^{-12}
2.22	9.36×10^{-12}	2.84×10^{-12}
3.32	4.21×10^{-12}	1.41×10^{-12}
4.95	1.50×10^{-12}	7.15×10^{-13}
7.38	2.96×10^{-13}	3.75×10^{-13}
11.00	0.75×10^{-13}	2.24×10^{-13}

Table 4.5: Parameters of intrinsic differential energy spectrum of Mrk 421 fitted with power law ($f_0 E^{-\Gamma}$ where f_0 is flux normalization in $photons\ cm^{-2}s^{-1}TeV^{-1}$ and Γ is spectral index, Δf_0 and $\Delta\Gamma$ are the corresponding uncertainties) for two EBL models.

Γ	$\Delta\Gamma$	f_0	Δf_0	Model
2.60	0.35	8.13×10^{-11}	2.95×10^{-11}	observed spectrum
2.35	0.38	9.80×10^{-11}	3.78×10^{-11}	EBL corrected [4.70]
2.36	0.37	1.10×10^{-10}	4.02×10^{-11}	EBL corrected [4.71]

index $\sim$ 2.2. This particle index is considerably flatter than the one obtained from TeV spectral analysis and it cannot be associated with cooling effect, since their difference is not unity. Hence, the underlying particle distribution may be a broken power law probably resulting from multiple acceleration processes [4.72].

4.4.6 SED Modelling

Motivated by the above temporal and spectral behaviour, the time averaged SED of Mrk 421 during the flare on February 16, 2010 is studied using simple leptonic model involving synchrotron and SSC processes since this provides a simple explanation for multi-wavelength emission from blazars [4.73]. The multi-wavelength data are collected from optical, X–ray and VHE γ–rays with SPOL optical telescope, *Swift*–XRT/BAT and *TACTIC* observations respectively. The TeV flux points from *TACTIC* are corrected for EBL absorption using model proposed by Franceschini et al.(2008) [4.70]. To reproduce the broad band SED we adopt a model described in [4.74] where the emission region is assumed to be a spherical blob moving down the jet with bulk Lorentz factor Γ. The radius of blob R is constrained by variability

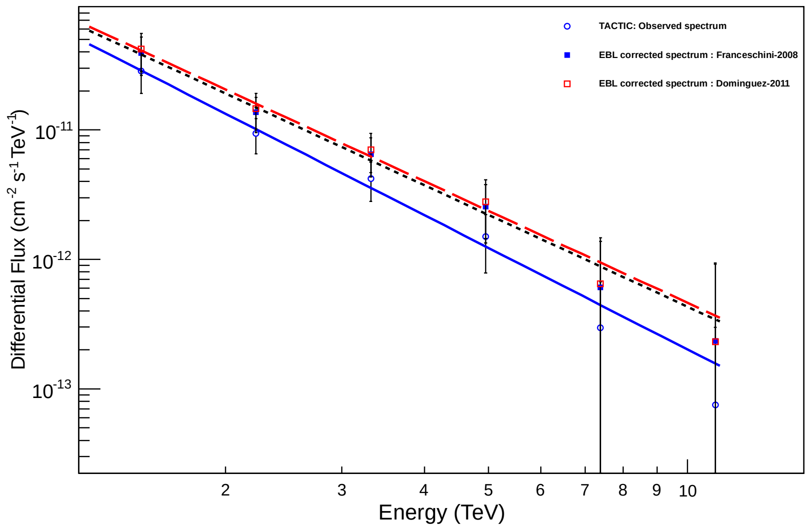

Figure 4.8: Differential energy Spectrum of Mrk 421 observed with *TACTIC* during the flare on February 16, 2010. De-absorbed source spectra for two EBL models are also shown.

time scale (t_{var}) using the relation:

$$R \approx \frac{ct_{var}\delta}{(1+z)} \tag{4.6}$$

where $\delta = [\Gamma(1 - \beta cos\theta)]^{-1}$, is the Doppler factor with β as the dimensionless bulk velocity and θ is angle between the jet axis and line of sight of the observer. Since blazar jet is aligned close to the line of sight, we can approximate $\delta = \Gamma$ corresponding to a viewing angle $\theta = cos^{-1}(\beta)$. Based on our temporal study, we consider $t_{var} \sim 1$ day to constrain the size of emitting region. The emission region is populated uniformly with a broken power law electron distribution described by:

$$N(\gamma)d\gamma = K\left[\left(\frac{\gamma}{\gamma_b}\right)^{p1} + \left(\frac{\gamma}{\gamma_b}\right)^{p2}\right]^{-1} d\gamma \quad ;\gamma_{min} < \gamma < \gamma_{max} \tag{4.7}$$

where K is the normalization, $\gamma_b m_e c^2$ is the break energy with m_e as the electron rest mass, $p1$ and $p2$ are the power law indices before and after the break energy $\gamma_b m_e c^2$. $\gamma_{min} m_e c^2$ and $\gamma_{max} m_e c^2$ are the minimum and the maximum electron energies of the distribution. The particles lose energy through synchrotron emission in a magnetic field B and synchrotron self Compton emission. The magnetic field energy density

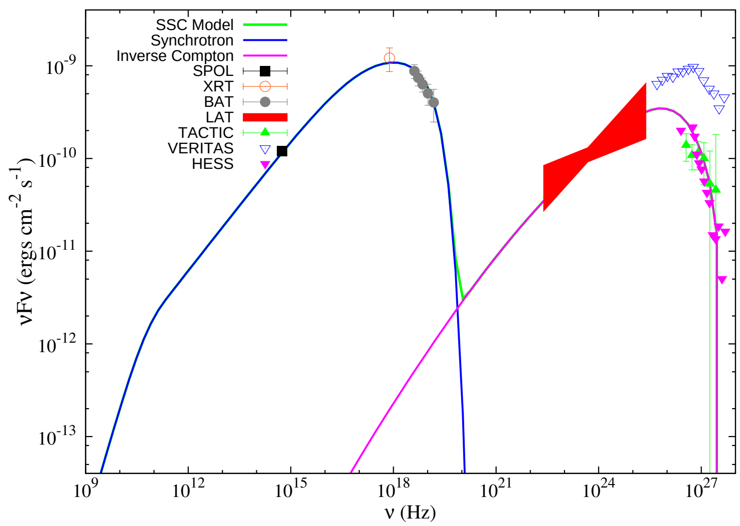

Figure 4.9: Spectral energy distribution of Mrk 421 using one-zone SSC model during flare on February 16, 2010 (MJD 55243). *TACTIC* flux points are corrected with Franceschini-2008 EBL model [4.70]. The VHE flux points obtained from *VERITAS* and *HESS* telescopes have been corrected for EBL absorption. The *VERITAS* flux points correspond to the observation on February 17, 2010 (MJD 55244) whereas *HESS* points are time averaged fluxes for observations during February 17-20, 2010 (MJD 55244-55246).

is considered to be in equi-partition with that of electrons,

$$U_B = m_e c^2 \int_{\gamma_{min}}^{\gamma_{max}} \gamma N(\gamma) d\gamma = U_e \tag{4.8}$$

where $U_B = B_{eq}^2/8\pi$ is the magnetic field energy density and U_e is the particle energy density. Due to relativistic bulk motion, the radiation from the emission region is Doppler boosted by δ^3. The main model parameters are constrained by the results obtained through our temporal and spectral studies and the resultant SED along with observed fluxes are shown in Figure 4.9. The parameter values estimated in the present work have been summarized in Table 4.6 and are consistent with the values reported in the literature [4.36, 4.51]. Due to large uncertainties in flux points, the LAT data are represented as butterfly plot in the figure. The VHE flux points reported by *VERITAS* and *HESS* telescopes are also shown in the figure and have been corrected for EBL absorption [4.70]. Source parameters derived from such modelling are very close to the real values. However, in our work, we have used near simultaneous multi-wavelength data averaged over one day to derive the broad band SED of the source. The parameters obtained from our modelling are the typical source parameters which may be slightly different from their realistic values.

4.5 Discussion and Summary

We have used TeV observations with *TACTIC* together with other multi-wavelength data on Mrk 421, to study the variability and spectral properties of the source during its high state of activity. Apart from analyzing the *TACTIC*, *Fermi*–LAT and *Swift*–XRT data during February 10–23, 2010 (MJD 55237–55250), we have also used simultaneous archival data for *Swift*–BAT, MAXI, optical (V-band) and radio (15 GHz) observations for our study. The highest flaring activity from the source in TeV energy band, as measured by *TACTIC* was detected on February 16, 2010 (MJD 55243) and an enhanced activity was also observed in HE γ–rays from *Fermi*/LAT and X–rays.

The variability studies in various energy bands suggest the emission to arise from the jet. Similar features observed in X-ray and TeV flare also support synchrotron and SSC origin of these emissions. The data statistics are not good enough to assert these interpretations strongly. Especially, the double flare seen in the X–ray energy band, conveys the level of complexity involved in these emission processes. Modelling such features may demand a detailed study involving various acceleration mechanisms driving blazar flares; however, this is beyond the scope of the present study. Recently, Dahai Yan et al. (2013) have investigated the electron energy distributions and the acceleration mechanisms in the jet of Mrk 421 by fitting the SED in different active states under the framework of single-zone SSC model [4.75]. They conclude that the shock acceleration is dominant in low activity state, while stochastic turbulence acceleration is dominant in flaring state. Whereas, Mastichiadis et al. (2013) have studied the origin of γ–ray emission in blazars within the context of the lepto-hadronic single zone model [4.76]. They find that γ–ray emission can be attributed to synchrotron radiation either from protons or from secondary leptons produced via photohadronic process. These possibilities imply differences in the X–ray and γ–ray variability signatures. The spectral index-flux correlation in the 1–10 keV energy band shows the hysteresis loop with a clockwise sense. This indicates (*i*) a soft lag during the spectral evolution and (*ii*) a cooling dominated electron spectrum present in the emission region. This also requires further study with good quality data.

The time averaged broad band SED of Mrk 421 during the flare can be well reproduced under the framework of simple one zone SSC model. The resulting parameters from the SED modeling are consistent with the source parameters used in SSC model reported in the literature [4.36, 4.51]. From these parameters we estimate the kinetic power of the jet (P_{jet}) by assuming that the emission region is also populated with cold protons equal in number as that of the non thermal electrons. The power of the jet can then be approximated as [4.77],

$$P_{jet} \approx \pi R^2 \Gamma^2 \beta c (U_p + U_B + U_e) \tag{4.9}$$

where U_p, U_B and U_e are cold proton energy density, magnetic field energy density and electron energy density in the rest frame of emission region respectively. The obtained jet power (P_{jet}=10^{44} erg/s) is consistent with the one generally assumed

Table 4.6: Optimized source parameters and properties of Mrk 421 obtained by fitting one day multi-wavelength data during flare on February 16, 2010 using simple one zone SSC model.

Parameter	Value
Blob Radius	2.37×10^{16}cm
Bulk Lorentz factor	14
Break energy of particle distribution	168 GeV
Particle energy density	2.42×10^{-3}erg/cm^3
Power law index before break	2.22
Power law index after break	3.80
Magnetic field	0.36 G
Jet Power	10^{44} erg/s
Radiated Power	10^{42} erg/s

for blazars and is much larger than the power released in the form of radiation (P_{rad}=10^{42} erg/s). Hence at blazar emission zone only a small fraction of the jet kinetic energy is utilized in radiation and most of the energy is spent in driving the jet upto Mpc scale. Eventhough, the obtained model parameters are consistent with the generally accepted values for Mrk 421, they differ considerably from the one reported by [4.64] during the same flaring episode. We note that the primary reason for this difference is due to the constraint introduced through equi-partition condition. Since equi-partition assures that the system is under minimum energy state (stable) [4.78], the parameters obtained in the present work may be the more probable ones. However, it is also to be noted that many blazars do not satisfy the equi-partition condition during a flare [4.79]. Most of these uncertanties regarding the emission models and underlying parameters can be resolved by detailed modelling of blazar light curves using complex algorithms. However such work would involve large number of parameters and future simultaneous multi-wavelength observations of blazars during flare can be used to estimate/constrain these parameters.

4.6 References

[4.1] A. Petrosian et al., 2007, ApJS, 170, 33

[4.2] B. E. Markaryan et al., 1981, APh, 17, 321

[4.3] G. Colla et al., 1972, A&AS, 7, 1

[4.4] M. H. Ulrich et al., 1975, ApJ, 198, 261

[4.5] B. A. Cooke et al., 1978, MNRAS, 182, 489

[4.6] B. Sbarufatti et al., ApJ, 635, 173

[4.7] M. Punch et al., 1992, Nature, 358, 477

[4.8] D. Petry et al., 1996, A&A, 311, 13

[4.9] B. G. Piner et al., 2010, ApJ, 723, 1150

[4.10] H. Teräsranta et al., 2004, A&A, 427, 769

[4.11] K. Niinuma et al., 2012, ApJ, 759, 84

[4.12] J. L. Richards et al., 2013, EPJWC, 61, 4010

[4.13] H. R. Miller, 1975, ApJ, 201, 109

[4.14] X. Guangzhong et al., 1988, A&AS, 72, 163

[4.15] F. K. Liu et al., 1997, A&AS, 123, 569

[4.16] W. A. Stein et al., 1976, ARA&A, 14, 173

[4.17] A. C. Gupta et al., 2004, A&A, 422, 505

[4.18] M. J. Ricketts et al., 1976, Nature, 259, 546

[4.19] R. F. Mushotzky et al., 1979, ApJ, 232, 17

[4.20] C. M. Urry et al., 1986, ApJ, 305, 369

[4.21] I. M. George et al., 1988, MNRAS, 232, 793

[4.22] T. Takahashi et al., 1996, ApJ, 470, 89

[4.23] L. Maraschi et al., 1999, ApJ, 526, 81

[4.24] W. Brinkmann et al., 2001, A&A, 365, 162

[4.25] M. Ushio et al., 2009, ApJ, 699, 1964

[4.26] G. G. Lichti et al., 2008, A&A, 486, 721

[4.27] A. Tramacere et al., 2009, A&A, 501, 879

[4.28] A. M. Levine et al., 1996, ApJ, 469, 33

[4.29] G. Fossati et al., 2008, ApJ, 677, 906

[4.30] I. Donnarumma et al., 2009, ApJ, 691, 13

[4.31] U. Barres de Almeida, 2011, ICRC, 8, 79

[4.32] Y. C. Lin et al., 1992, ApJ, 401, 61

[4.33] Y. C. Lin et al., 1996, A&AS, 120, 499

[4.34] R. C. Hartman et al., 1999, 123, 79

[4.35] W. Collmar et al., 1999, ICRC, 3, 374

[4.36] A. A. Abdo et al., 2011, ApJ, 736, 131

[4.37] P. L. Nolan et al., 2012, ApJS, 199, 31

[4.38] M. Ackermann et al., 2013, ApJS, 209, 34

[4.39] F. Acero et al., 2015, arXiv:1501.02003

[4.40] A. D. Kerrick et al., 1995, ApJ, 438, 59

[4.41] J. A. Gaidos et al., 1996, Nature, 383, 319

[4.42] J. A. Zweerink et al., 1997, ApJ, 490, 141

[4.43] F. Krennrich et al., 1997, ApJ, 481, 758

[4.44] F. A. Aharonian et al., 1999, A&A, 350, 757

[4.45] H. Krawczynski et al., 2001, ApJ, 559, 187

[4.46] F. Krennrich et al., 2002, ApJ, 575, 9

[4.47] P. F. Rebillot et al., 2006, ApJ, 641, 740

[4.48] J. Albert et al., 2007, ApJ, 663, 125

[4.49] D. Horan et al., 2009, ApJ, 695, 596

[4.50] K. K. Yadav et al., 2007, Astropart. Phys., 27, 447

[4.51] V. A. Acciari et al., 2011, ApJ, 738, 25

[4.52] J. Aleksić et al., 2012, A&A, 542, 100

[4.53] M. Tluczykont et al., 2007, JPhCS, 60, 318

[4.54] G. Fossati et al., 2000, ApJ, 541, 166

[4.55] C. Tanihata et al., 2004, ApJ, 601, 759

[4.56] E. Massaro et al., 2004, A&A, 422, 103

[4.57] A. Tramacere et al., 2007, A&A, 467, 501

[4.58] N. S. Kardashev, 1962, SvA, 6, 317

[4.59] K. Katarzyński et al., 2006, A&A, 453, 47

[4.60] B. Giebels et al., 2007, A&A, 462, 29

[4.61] C. Tanihata et al., 2001, ApJ, 563, 569

[4.62] L. Fortson et al., 2012, AIP Conf. Proc., 1505, 514

[4.63] M. Tluczykont et al., 2011, arXiv:1106.1035

[4.64] A. Shukla et al., 2012, A&A, 541, 140

[4.65] N. Isobe et al., 2010, PASJ, 62, 155

[4.66] G. Calderone et al., 2011, MNRAS, 413, 2365

[4.67] R. Edelson et al., 2002, ApJ, 568, 610

[4.68] J. Heidt & S. J. Wagner, 1996, A&A, 305, 42

[4.69] J. G. Kirk et al., 1998, A&A, 333, 452

[4.70] A. Franceschini et al., 2008, A&A, 487, 837

[4.71] A. Dominguez et al., 2011, MNRAS, 410, 2556

[4.72] S. Sahayanathan, 2008, MNRAS, 388, 49

[4.73] C. D. Dermer et al., 1993, ApJ, 416, 458

[4.74] S. Sahayanathan & S. Godambe, 2012, MNRAS, 419, 1660

[4.75] D. Yan et al., 2013, ApJ, 765, 122

[4.76] A. Mastichiadis et al., 2013, MNRAS, 434, 2684

[4.77] A. Celloti et al., 1997, MNRAS, 286, 415

[4.78] G. R. Burbidge, 1959, ApJ, 129, 849

[4.79] M. Böttcher et al., 2009, ApJ, 703, 1168

Chapter 5

Observation of 1ES 1218+304 with *TACTIC*

5.1 Motivation for observation

Since the detection of blazars as sources of HE γ–rays by *EGRET* and *Fermi*–LAT at present, the search for VHE counterparts of these sources has become a major goal for ground based observatories. Studies of VHE radiation from blazars are important in general to constrain the different γ–ray emission models. The blazar 1ES 1218+304 was predicted to be a TeV candidate blazar from the position of the synchrotron peak in its SED and is supposed to be a VHE γ–ray emitter detectable by ground based Cherenkov telescopes. Detection of VHE γ–rays from this source by *MAGIC* and *VERITAS* telescopes confirmed these predictions. Due to relatively large redshift (z=0.182) of the source, we expect a significant attenuation of VHE photons due to EBL absorption. This makes the source a good candidate for probing intensity and spectrum of EBL using VHE observations. Motivated by these considerations, we have selected 1ES 1218+304 for observation with *TACTIC* to explore its TeV γ–ray emission characteristics.

5.2 The Source: 1ES 1218+304

1ES 1218+304 first appeared in the literature in 1970 in the Bolonga radio catalog at 408 MHz [5.1]. Since then the source has been a target of many surveys at different wavelengths. For this reason it has acquired many different names. The name mainly used with the 1ES prefix, comes from the X-ray observations of the *Einstein Slew Survey*, version 1. Other popular names include B2 1218+30, 1H 1219+301, H 1219+305, PG 1218+304, FIRST J122121.9+301037, QSO B1218+304 and 2A 1219+305. The recent TeV catalog suggests the name TeV J1221+301, but the canonical 1ES 1218+304 will be used throughout this thesis.

5.2.1 Basic Properties

The source 1ES 1218+304 is a high synchrotron peaked (HSP) BL Lac type active galactic nuclei located at redshift $z = 0.182$ [5.2]. The source with equatorial coordinates: RA=$12^h\ 21^m\ 21.9^s$, Dec= $+30^\circ\ 10'\ 37''$ and galactic coordinates: l= 186.36°, b= 82.73°, is visible in northern hemisphere roughly from December to April. The morphology of the host galaxy is elliptical with luminosity M_R= -23.56 and a supermassive black hole of mass 10^9 $M_\odot$ [5.3]. The basic observational properties of the source are outlined below.

- First detected by the Ariel-5 X-ray satellite [5.4], 1ES 1218+304 was one of the earliest BL Lac objects to be discovered based on its X-ray emission [5.5].
- Initially identified with the high galactic-latitude X-ray source 2A 1219+305, the object was later classified as a BL Lac object using optical and radio counterparts [5.6].
- Optical observations using the Hubble Space Telescope (HST) [5.7] have resolved the host galaxy and found that the BL Lac nucleus is well centered in the main body of the host galaxy [5.8].
- Long-term optical monitoring of the source revealed that optical emission from 1ES 1218+304 typically varies on the timescale of months [5.9].
- Radio observations have confirmed that the source is compact on kiloparsec (kpc) scales with an upper limit on the size of the jet at 0.7 kpc and Doppler factor in the range of δ = 1.9–3.7 [5.10].

5.2.2 Previous Observations

The blazar 1ES 1218+304 has been particularly well-studied in X-rays, because it is a X-ray bright HBL [5.11]. Moreover, frequent target of opportunity observations are carried out by various X-ray observatories. Detection of VHE γ–ray emission above 100 GeV by ground based Cherenkov telescopes provides further evidence that X-ray bright HBLs tend to be strong VHE candidate sources. The source is also detected with *Fermi*-LAT with no evidence for variability. The multi-wavelength observations of 1ES 1218+304 in the past are briefly reviewed below.

- **Radio observations :** The blazar 1ES 1218+304 is a nearby low-power radio source. It was observed with the Very Large Array (VLA) at 1.4 GHz and Very Long Baseline Array (VLBA) at 5 GHz in 2002 to study the nuclear and large scale properties of the source [5.10]. These radio observations revealed the presence of a compact object and small jet in the source.
- **Optical observations :** The optical observations of the blazar 1ES 1218+304 performed with Hubble Space Telescope (HST), resolved a source of apparent magnitude 15.68±0.10 and an elliptical host galaxy of apparent magnitude

17.12±0.03 [5.3]. HST observations have also permitted an estimation of the mass of the central black hole in the source. As part of a blazar monitoring program, 1ES 1218+304 is routinely observed by the 1.03 m telescope at the Tuorla Observatory, Finland, and the 35 cm telescope at the KVA observatory on La Palma, Canary islands, Spain.

- **X-ray observations :** The source 1ES 1218+304 has been discovered as a candidate BL Lac object on the basis of its X-ray emission. It has been observed by the Einstein, ROSAT, BeppoSAX and XMM-Newton missions. The BeppoSAX X-ray Astronomy Satellite observed 1ES 1218+304 on July 12, 1999 in the energy range 2-10 keV and measured an integral flux of about 1.5×10^{-11} erg cm^{-2} s^{-1} [5.12]. The BeppoSAX spectral data is well described by a log-parabolic model. The *Swift* satellite observed 1ES 1218+304 twice in 2005, yielding a flux level similar to that observed by BeppoSAX [5.13]. Despite limited statistics, power law best fit to the *Swift* data shows a decrease in the flux level by 35% and a variation of the photon index. The *Suzaku* X-ray satellite observed 1ES 1218+304 in 2006 for a total of 79.9 ks [5.11]. During observation, *Suzaku* detected a prominent flare in the energy range 5-10 keV where the flux changed by a factor of ∼2 over a time scale of 5×10^4 s. The time profile of the flare changed with energy and the increase of the flux in hard X-rays lagged behind that for soft X-rays. This is a clear deviation from past observations where soft X-rays usually lagged behind hard X-rays. This could be attributed to the energy dependence of the acceleration time of electrons. From the position of synchrotron peak, located in hard X-rays, in the SED of 1ES 1218+304, the source was classified as an HBL [5.14].

- **HE γ–ray observations :** The *EGRET* experiment observed 1ES 1218+304 between 1991 and 1992 above 100 MeV. Subsequent non-detection placed the *EGRET* 95% confidence upper limit at 1.7×10^{-7} photons cm^{-2} s^{-1} [5.15]. *Fermi*-LAT also detected significant emission from 1ES 1218+304 during its first 2 years of exposure [5.16]. The *Fermi*-LAT spectrum of the source is described by a power law with index 1.71±0.07, making it one of the hardest spectrum sources in MeV-GeV range. From the first four years of observation with *Fermi*-LAT, spectral index of the source is observed to be 1.97±0.02 [5.17].

- **VHE γ–ray observations :** Based on its typical broad band characteristic with high radio and X-ray fluxes, the source 1ES 1218+304 was suggested as a promising candidate for detection at VHE γ–rays with ground based detectors. The source was first monitored with *Whipple* Observatory between 1995 and 2000. No successful detection was observed and an upper limit on the integral flux above an energy threshold of 350 GeV of 8.3×10^{-8} photons cm^{-2} s^{-1} (corresponding to 8% of the Crab Nebula flux) was reported by *Whipple* group [5.18]. *HEGRA* collaboration observed 1ES 1218+304 during 1996-2002 for 3.9 h and reported an upper limit on the integral flux above 840 GeV of

2.67×10^{-12} photons cm^{-2} s^{-1} (corresponding to 12% of the Crab Nebula flux) at 99% confidence level, considerably higher than previous upper limits [5.19].

The VHE emission from 1ES 1218+304 was first detected by the *MAGIC* telescope in 2005 [5.20]. In an observation time of 6.4 h, the *MAGIC* telescope observed a γ–ray signal from the source above 120 GeV with a significance of 6.4σ. The differential energy spectrum, with power law index of 3.0$\pm$0.4, was also reported by the *MAGIC* observations. The integral flux above 100 GeV was found to be (8.7$\pm$1.4)$\times$ 10^{-11} photons cm^{-2} s^{-1}, substantially smaller than the upper limits calculated by either *Whipple* or *HEGRA*. In May 2006, 1ES 1218+304 was the target of *HESS* observation campaign and the source was observed for 1.8 h at a zenith angle of 56° [5.21]. These observations did not yield any statistically significant signal (9 events, 1.2σ) from the source and the corresponding 99.9% confidence level limit on integral flux above 1 TeV was reported to be 17% of the *HESS* Crab Nebula flux. The *STACEE* detector monitored 1ES 1218+304 during 2006-2007 observations for 28 h above 160 GeV but did not observe any significant detection of VHE γ–rays from the source and an upper limit on the differential flux at 150 GeV was derived to be less than 5.2×10^{-6} photons m^{-2} s^{-1} TeV^{-1} [5.22]. In 2007, *VERITAS* telescope observed VHE emission from the source at a persistent level of 6% of the Crab Nebula flux [5.23]. The *VERITAS* Collaboration reported the detection of γ–rays above 160 GeV with a statistical significance of 10.4σ in an observation time of 17.4 h. The differential energy spectrum of the source was found to be compatible with a power law of spectal index 3.08$\pm$0.34. During December 2008 to May 2009 monitoring campaign of the blazar 1ES 1218+304, *VERITAS* telescope revealed a prominent flaring activity from the source at 20% of the Crab Nebula flux above 200 GeV [5.24]. From this observation, they reported an excess of 1155 events with a statistical significance of 21.8σ in an observation time of 27.2 h. The corresponding time averaged differential energy spectrum, in the energy range 0.2-1.8 TeV, was found to be a power law with a spectral index of 3.07$\pm$0.09. This flaring activity was characterized by variability time scale of days.

5.2.3 Variability studies

The VHE γ–ray light curves of 1ES 1218+304 from *MAGIC* observations in 2005 [5.20] and *VERITAS* observations in 2007 [5.23] did not show any evidence for significant time variability in VHE γ–ray emission from the source. However, the *VERITAS* observations of the source from December 2008 to April 2009 [5.24], indicated that 1ES 1218+304 is not a steady γ–ray source, but shows short-time variability. In 2010, Weidinger and Spanier showed that a time dependent model using self consistent treatment of electron acceleration is able to model the variability in *VERITAS* data [5.25], while the long time observations do not necessarily require a time resolved treatment. The kinetic equations for electrons and photons in a plasma blob were solved numerically including *Fermi* acceleration for electrons as well as synchrotron radiation and Compton scattering. An outburst of the timescale of roughly five days as measured from 1ES 1218+304 does not require a shock in jet model, which scales down to a few minutes depending on the model parameters, but may also be explained as different accretion states. Nevertheless, Weidinger and Spanier emphasized that the fundamental statement remains the same: long time observation of slightly variable blazars will result in a steady state emission, while an average over a single outburst will result in a significantly different SED for the source.

5.2.4 SED Modelling

The VHE γ–ray observations of 1ES 1218+304 with *MAGIC* in 2005 [5.20] along with other contemporaneous multi-wavelength data from X-ray and optical observations were used for the first time for spectral fitting of the source using one zone homogeneous synchrotron self Compton (SSC) model [5.11]. From the spectral fitting of multi-wavelength data, magnetic field strength B $\sim$ 0.047 G and emission region size R $\sim 3.0\times10^{16}$ cm were estimated for an appropriate beaming with a Doppler factor of $\delta = 20$. A time dependent SSC code [5.26] was also employed for modelling the contemporaneous multi-wavelength data of the blazar 1ES 1218+304 involving *MAGIC* [5.20] and *VERITAS* [5.23] observations. The input parameters of the model were used to infer physical parameters of the emitting region. An acceptable fit to the data as shown in Figure 5.1, was obtained by taking into account a stellar emission component in the optical regime due to the host galaxy. The physical parameters inferred from the fit were in line with particle acceleration due to the *Fermi* mechanism providing a particle spectral index of 2.1. A magnetic field of strength B $\sim$ 0.04 G and size of emitting region R $\sim 3.0\times10^{15}$ cm with a Doppler factor of $\delta = 80$ were estimated from this spectral fitting. A time dependent model with a self consistent treatment of electron acceleration [5.25] was developed to model the VHE outburst from the source detected with *VERITAS* [5.24]. This model predicted the magnetic field strength B $\sim$ 0.12 G, size of emission region R $\sim 3.0\times10^{15}$ cm and Doppler factor of $\delta = 44$ during the flaring state of the 1ES 1218+304. It was also concluded that the long time measurements can be explained by steady state emission from SSC model, but short outburst requires a time resolved treatment.

5.3 Search for VHE γ–ray emission from 1ES 1218+304 with *TACTIC*

The observations of 1ES 1218+304 were motivated primarily because of its unusually hard VHE spectrum despite its relatively large redshift. The source was monitored with *TACTIC* telescope from March 1, 2013 to April 15, 2013 (MJD 56352–56397) with the motivation of observing TeV γ–ray emission from the source.

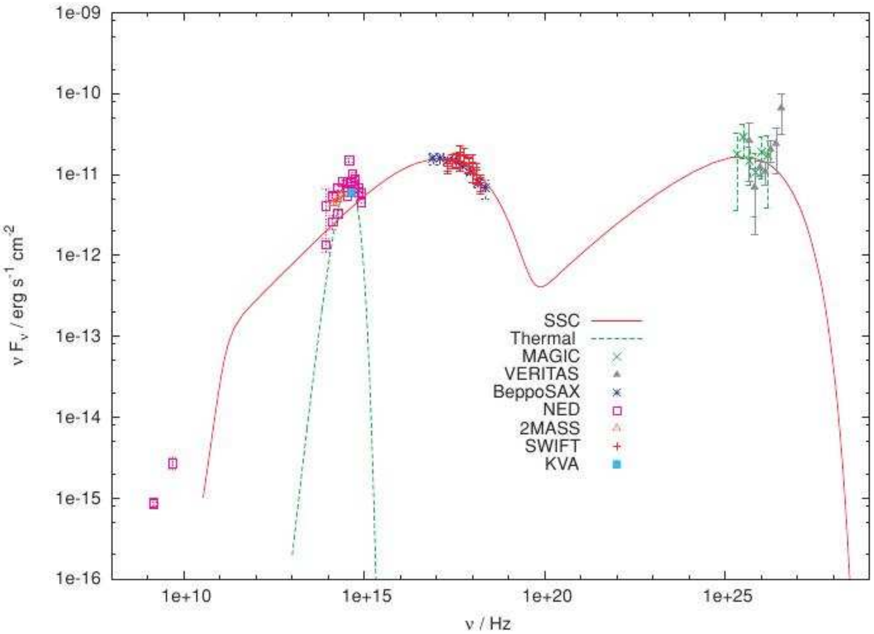

Figure 5.1: Spectral energy distribution of 1ES 1218+304 with time depenedent SSC model [5.26] using X-ray and VHE Observations.

5.3.1 Data Sample

The blazar 1ES 1218+304 was observed at zenith angles between 6° and 45° with *TACTIC* in tracking mode, during which the telescope continuously monitors the source. This mode of observation maximizes the source observation time and increases the possibility of detecting flaring activity from the source. About 54 h of data were collected during 18 nights of observations and the details are summarized in Table 5.1.

Table 5.1: Summary of *TACTIC* observations of 1ES 1218+304

Month	Observation dates	Observation Time (h)	Selected data (h)
March 2013	3,4,8,9,10,12,13,14,17,18,19	26.00	16.79
April 2013	6,7,9,10,11,12,13	28.00	22.83
Total	18 Nights	54.00	39.62

5.3.2 Data Analysis

Apart from excluding the observations during bad atmospheric conditions, several standard data quality tests have been applied to the raw data for selecting clean data for further analysis as described in Chapter 3. After applying the data quality checks the final data sample reduces to ≈ 39.62 h. For gamma/hadron separation we have followed the standard Hillas parameterization technique [5.27] where each Cherenkov image is characterized by its moments. The γ–ray selection criteria used in the present work are given in Table 5.2. These cuts have been optimized using 25 h of actual observation data on the Crab Nebula during November 2012. When applied to the remaining data on the Crab Nebula, the above cuts yield consistent detection of a γ–ray signal at a sensitivity level of $N_\sigma \sim 1.40\sqrt{T}$ (where T is the observation time in hours). The statistical significance of γ–ray like events is calculated using the methodology described in Chapter 3.

Table 5.2: Dynamic Supercuts selection criterion used for analyzing the *TACTIC* data.

Parameters	Cuts Value
L	$0.11^\circ \leq L \leq (0.1000 + 0.0520 \times \ln S)^\circ$
W	$0.06^\circ \leq W \leq (0.0850 + 0.0160 \times \ln S)^\circ$
D	$0.50^\circ \leq D \leq (1.27 \times \cos^{0.95}\theta)^\circ$ (θ=zenith angle)
S	$\geq$ 310 dc (digital counts)
α	$\alpha \leq 18^\circ$
F2	≥ 0.35
L/W	≥ 1.55
ASYM	≥ 0.0

In order to validate the proper functioning of the telescope and the data analysis methodology, we are collecting data on the Crab Nebula regularly. Although, during the observing season 2012-2013, the Crab Nebula was observed with *TACTIC* telescope right from November 2012 onwards we will present here, as a representative example, the results of our observations for approximately 11.33 h only which were carried out during March 1, 2013 to March 13, 2013. The main purpose of doing this is to compare the results of the Crab Nebula observations with that of 1ES 1218+304. There is an overlap of 6 nights when both the Crab Nebula and 1ES 1218+304 were observed one after the other. Figure 5.2(a) gives the α–distribution when the data collected on the Crab Nebula for 11.33 h is analyzed. The events selected after using the Dynamic Supercuts procedure yield an excess of 169±32 γ–ray like events with a statistical significance of 5.47σ. The corresponding γ–ray rate turns out to be (14.91±2.82)h^{-1}. Since the average zenith of 28° for 11.33 h data on the Crab Nebula is close to the average zenith of 21° for 39.62 h data on 1ES 1218+304, one can express the γ–ray rate observed from 1ES 1218+304 in Crab Unit (CU:1 CU ≡ 14.91± 2.82 h^{-1}). Figure 5.2(b) gives the α–distribution for the data collected on 1ES 1218+304 for 39.62 h. The data yields an excess of 2±56 γ–ray events with a statistical significance of 0.04σ. We do not have any evidence for a statistically significant γ–ray signal from the source during the period of our observations. The source was thus possibly in a low state which is below the sensitivity level of the *TACTIC* telescope. The upper limit on the integral VHE γ–ray

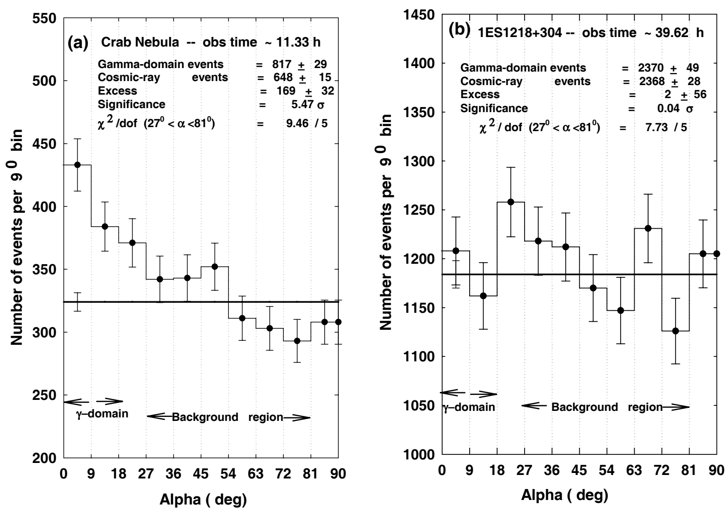

Figure 5.2: (a) On-source alpha plot of Crab Nebula for 11.33 h of data collected during March 1, 2013 to March 13, 2013 (b) On-source alpha plot of 1ES 1218+304 for 39.62 h of data collected during March 1, 2013 to April 15, 2013 (MJD 56352–56397). The horizontal lines in these figures indicate the expected background in the γ–domain obtained by using the background region with $27° \leq \alpha \leq 81°$.

flux from the source is described below.

5.3.3 Upper Limit on VHE γ–ray flux using *TACTIC* Observations

As discussed above, we do not find any evidence for a statistically significant VHE γ–ray signal from 1ES 1218+304 and thus we have accordingly calculated the upper limit on the integral flux at 99% confidence level. Using the probability density function of the number of excess events we have determined the upper limit on the excess events (N_{UL}) by using the methodology proposed by Helene [5.28] and the method involves solving the following equation for N_{UL},

$$\beta I\left(\frac{-N_{exc}}{\sigma_{exc}}\right) = I\left(\frac{N_{UL} - N_{exc}}{\sigma_{exc}}\right) \tag{5.1}$$

where (1-β)$\times$ 100% is the confidence level, N_{exc} is number of excess events with σ_{exc} as its standard deviation. The function I(x) is given by

$$I(x) = \frac{1}{\sqrt{2\pi}} \int_x^{\infty} e^{-t^2/2}\, dt = \frac{1}{2}\, erfc(\frac{x}{\sqrt{2}}) \tag{5.2}$$

where *erfc(x)* is the complementary error function. On solving Equation 5.1 with N_{exc}= 2, σ_{exc}= 56 (refer α–plot shown in Figure 5.2(b)) and β=0.01, we get N_{UL} $\approx$ 146 as 99% confidence level upper limit on the excess events from the source. Knowing that the γ–ray rate of (14.91$\pm$2.82)h^{-1} corresponds to 1 CU, the resulting 99% limit on the rate of excess events from 1ES 1218+304 translates to 3.68h^{-1} (i.e 146/39.62h or 0.25 CU). Alternatively, on dividing the upper limit on the excess events by the product of effective collection area after applying the Dynamic Supercuts (3.0$\times$ 10^8 cm^2) and observation time (39.62 h) we find the 99% upper limit on the integral flux to be 3.41$\times10^{-12}$ photons cm^{-2} s^{-1} at an average threshold energy $\sim$1.1 TeV. The values of effective collection area and threshold energy used above correspond to an average zenith angle of 25°. If we assume a source spectrum similar to that of the Crab Nebula (i.e dN/dE = 2.79$\times$ 10^{-11} $E^{-2.59}$ cm^{-2} s^{-1} TeV^{-1}; as measured by the *HEGRA* group [5.29]) and also found to match very well with the spectrum obtained from the *TACTIC* [5.30], the above 99% limit translates to an integral flux upper limit of 0.26 CU. Referring back to the upper limit, if we assume a steeper spectrum (i.e dN/dE $\propto$ $E^{-3.0}$) for 1ES 1218+304, similar to the one observed by *MAGIC* [5.20] and *VERITAS* [5.23] telescopes, the above upper limit on the integral flux corresponds to about 0.23 CU above a threshold energy 1.1 TeV. The differential flux upper limit at 99% confidence level is found to be 6.2$\times$ 10^{-12} photons cm^{-2} s^{-1} TeV^{-1}.

5.4 Multi-wavelength observations

For the study of multi-wavelength emission from the source, we use nearly simultaneous data in radio by *OVRO*, in optical and UV by *Swift*-UVOT, in X–rays by *Swift*-XRT, and in HE γ–rays by *Fermi*-LAT during March 1, 2013 to April 15, 2013 (MJD 56352–56397). The details of observation and data reduction for these instruments are described below.

5.4.1 *Fermi*-LAT data

The *Fermi*-LAT data for 1ES 1218+304 were retrieved from the publicly available NASA data base[1] during the period March 1, 2013 to April 15, 2013 (MJD 56352–56397). We selected the good quality events from the "source class" over the energy range 100 MeV–100 GeV and the events were extracted from a circular region of interest (ROI) with radius 15° centered at the source position (RA=12^h 21^m 23.5^s, Dec=30° 10′ 43.2″). In addition, we excluded the events observed with zenith angles > 100° to limit contamination from Earth limb γ–rays, and events detected while the spacecraft rocking angle was > 52° to avoid time intervals during which the bright limb of the Earth entered the LAT field of view.

The data obtained in this manner were analyzed using the standard *Fermi* Science-Tools software package (version v9r27p1). We used P7_SOURCE_V6 in-

[1] http://fermi.gsfc.nasa.gov/ssc/data/access

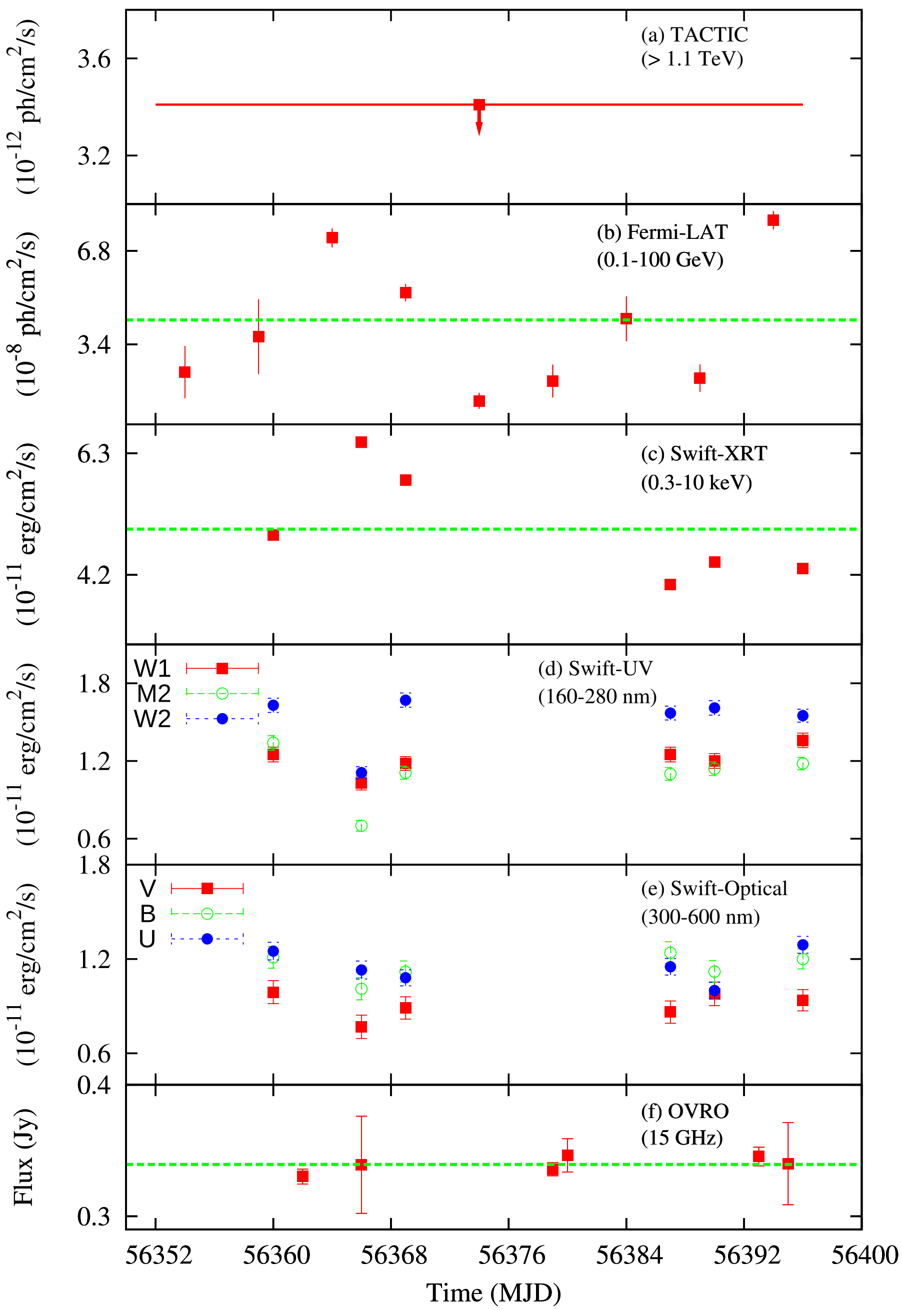

Figure 5.3: Multi-wavelength light curve of 1ES 1218+304 during March 1, 2013 to April 15, 2013 covering VHE γ–rays by *TACTIC*, HE γ–rays by *Fermi*-LAT, X–rays by *Swift*-XRT, UV/optical by *Swift*-UVOT instruments and radio by *OVRO* telescope. 99% confidence upper limit in VHE γ–rays by *TACTIC* is indicated as downward arrow. Each point in the 5 day binned light curve of *Fermi*-LAT in HE γ–rays corresponds to TS > 4. X–ray, UV/Optical and radio light curves represent daily flux values for 6 days of observations available during the monitoring of the source with *TACTIC*. The horizontal dotted lines (shown in (b), (c) & (f)) represent the average emission level in the respective energy bands.

strument response function with the galactic and isotropic diffuse emission models gal_2yearp7v6_v0.fits and iso_p7v6source.txt. All the point sources from *Fermi*-LAT second source catalog (2FGL) [5.16] within 20° of 1ES 1218+304, including the source of interest itself were considered in source model file. Sources within the ROI were fitted with power law models with the normalization as free parameter and spectral index set to the value given in second catalog (2FGL), while those beyond ROI had their models frozen to those as reported in second source catalog. An unbinned likelihood spectral analysis was performed to produce the light curve with the standard analysis tool *gtlike* implemented in Science-Tools software package. Since the source is not always detected at high statistical significance, we have produced the five day binned light curve with minimum statistical significance accepted for each time bin as TS ≥ 4, where TS is the test statistic defined as twice the difference of the log(likelihood) with and without the source respectively [5.31]. The time averaged spectrum of the source was obtained by fitting a power law model with normalization and spectral index as free parameters. The details of the source spectrum obtained in the present work from *Fermi*-LAT observations are described in Section 5.5.

5.4.2 *Swift*-XRT & UVOT data

During March 1, 2013 to April 15, 2013 (MJD 56352–56397) only six days of observations are available from *Swift* with XRT (X–Ray Telescope), covering the 0.3-10 keV enegy band [5.32], and UVOT (UV/Optical Telescope), covering 180-600 nm wavelength range [5.33]. In the following, we discuss the XRT data analysis together with the UVOT data.

Swift-XRT data were reduced following the standard procedure[2] using *FTOOLS*. The data were collected in window timing (WT) mode for all the observations. The task XSELECT (ver V2.4b) within the HEASOFT package (v6.13) with recent calibration files (ver. 20120209) was used to analyse the data. The spectra and light curves of the source were extracted using a circular region with radius 23″ around the source. The spectra and light curves of nearby background region were extracted within an annulus with inner radius of 24″ and outer radius of 45″ around the source. The corresponding exposure maps and ancillary response files (ARFs) were generated using task XRTEXPOMAP and XRTMKARF for all the observations, respectively. The spectra were binned using GRPPHA to ensure a minimum of 20 counts per bin to perform the χ^2–minimization for fitting the spectrum with model $phabs * zpowerlaw$ and fluxes were calculated using CFLUX. The best-fit parameters given in Table 5.3 were were derived for individual observation with a a neutral hydrogen column density fixed to its Galactic value 1.99×10^{20} cm^{-2} obtained from NASA/IPAC Extragalactic Database (NED)[3]. The best fit average parameters were also derived using simultaneous fitting of the spectra of six observations.

The source 1ES 1218+304 was observed with *Swift*-UVOT using all filters (V,

[2] http://www.swift.ac.uk/analysis/xrt/

[3] ned.ipac.caltech.edu

Table 5.3: Spectral analysis of *Swift*-XRT data during March 1, 2013 to April 15, 2013 using power law spectrum with neutral hydrogen density fixed at 1.99×10^{20} cm^{-2}.

MJD	Obs-ID	Photon index	Flux (10^{-11} erg cm^{-2} s^{-1})	χ^2_ν(dof)
56360	sw00030376021	$2.05^{+0.04}_{-0.04}$	$4.89^{+0.06}_{-0.06}$	1.23 (48)
56366	sw00030376022	$1.94^{+0.04}_{-0.04}$	$6.49^{+0.08}_{-0.09}$	0.90 (51)
56369	sw00030376023	$2.11^{+0.04}_{-0.03}$	$5.84^{+0.06}_{-0.06}$	0.80 (64)
56387	sw00030376024	$2.23^{+0.05}_{-0.05}$	$4.03^{+0.06}_{-0.06}$	0.93 (43)
56390	sw00030376025	$2.13^{+0.05}_{-0.04}$	$4.42^{+0.06}_{-0.06}$	1.43 (46)
56396	sw00030376026	$2.23^{+0.04}_{-0.04}$	$4.31^{+0.05}_{-0.05}$	1.38 (58)

Table 5.4: Summary of *Swift*-UVOT observed magnitudes during March 1, 2013 to April 15, 2013 in six filters.

MJD	V	B	U	W1	M2	W2
56360	16.15±0.08	16.78±0.06	15.86±0.05	15.85±0.05	15.59±0.04	15.83±0.03
56366	16.43±0.01	16.98±0.07	15.96±0.05	16.06±0.05	16.30±0.07	16.24±0.04
56369	16.27±0.08	16.87±0.06	16.01±0.05	15.91±0.05	15.79±0.05	15.80±0.03
56387	16.30±0.08	16.76±0.06	15.95±0.05	15.85±0.05	15.79±0.05	15.87±0.04
56390	16.17±0.08	16.86±0.06	16.10±0.05	15.89±0.05	15.76±0.05	15.84±0.04
56396	16.21±0.07	16.79±0.05	15.82±0.04	15.76±0.04	15.72±0.04	15.88±0.03

B, U, UVW1, UVM2, UVW2) in image mode over six days during *TACTIC* observations. The image mode level II data of all the filters were used in the present analysis with latest calibration files of UVOT [5.34]. The data were processed with the standard procedure[4] using UVOTMAGHIST task of HEASOFT package.The UVOT source counts were extracted from a 5″ sized circular region centered on the source position, while the background was extracted from a nearby larger, source free, circular region of 10″ radius. The observed magnitudes were converted into fluxes using conversion factors given in [5.35]. The observed magnitudes obtained in six filters during the period March 1, 2013 to April 15, 2013 are reported in Table 5.4.

5.4.3 OVRO data

The *OVRO* (Owens Valley Radio Observatory) is a fast cadence 15 GHz radio telescope with diameter of 40 m [5.36]. The telescope is a f/0.4 type parabolic reflector on an alt-azm mounting system and is equipped with dual beamed off axis optics and a cooled receiver installed at prime focus. The source 1ES 1218+304 was ob-

[4]http://www.swift.ac.uk/analysis/uvot/

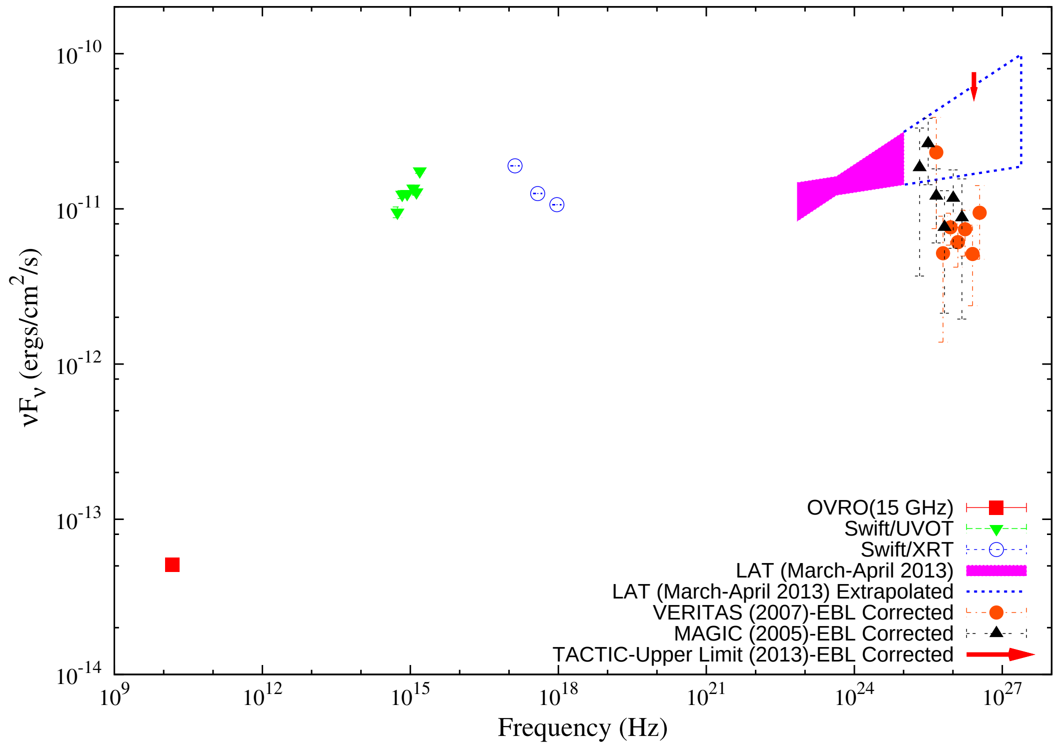

Figure 5.4: Multi-wavelength SED of 1ES1218+304 measured during March 1, 2013 to April 15, 2013. VHE points correspond to the fluxes measured by: *MAGIC* [5.20], *VERITAS* [5.23] telescopes along with *TACTIC* 99% flux upper limit at $\sim$ 1.1 TeV (present work). All the VHE flux points have been corrected for EBL absorption using Franceschini et al. (2008) model [5.37]. *Fermi*-LAT spectrum measured during March-April 2013 is shown as butterfly (filled curve) and same has been extrapolated in the *TACTIC* energy range 0.87–10 TeV (dotted lines). *Swift*-XRT points are time averaged fluxes for six days of observations. *Swift*-UVOT points correspond to time averaged fluxes meausered in all filters (V,B,U,W1,M2,W2). The time averaged radio flux at 15 GHz is taken from the *OVRO* observations.

served at 15 GHz using *OVRO* telescope[5] for six days during *TACTIC* observations as part of *Fermi* multi-wavelength blazar monitoring program and data of these observations are used in the present work.

5.5 Results

The results of VHE γ–ray observations of the blazar 1ES 1218+304 with the upgraded *TACTIC* from March 1, 2013 to April 15, 2013 (MJD 56352–56397) for a total observation time of 39.62 h are presented in the following subsections. No evidence for VHE γ–ray emission is found from the source in our study and as already mentioned the corresponding 99% confidence level upper limit on the integral flux

[5]www.astro.caltech.edu/ovroblazars/data

above an average threshold energy of 1.1 TeV is estimated to be 3.41 $\times10^{-12}$ photons cm^{-2} s^{-1} (i.e <23% Crab Nebula flux). The multi-wavelength data available during *TACTIC* observations show no unusual activity from 1ES 1218+304 in X–ray and HE γ–rays.

5.5.1 Light curve Analysis

The multi-wavelength light curve of 1ES 1218+304 observed by various instruments during March 1, 2013 to April 15, 2013 (MJD 56352–56397) is shown in the Figure 5.3. Since no significant γ–ray emission has been from the source with the *TACTIC*, we have shown the 99% confidence level upper limit on integral flux above 1.1 TeV for *TACTIC* observations in Figure 5.3(a). The five-day binned light curve of the source observed with *Fermi*-LAT during the same period is presented in Figure 5.3(b). All the points reported in the Figure 5.3(b) correspond to TS > 4. From the figure, it is evident that there is no statistically significant variation in the γ–ray activity in the energy range 100 MeV-100 GeV during *TACTIC* observations the average flux level during this period is found to be $(4.17\pm0.82)\times10^{-8}$ photons cm^{-2} s^{-1}. It is important to mention here that the source has been categorized as highly variable on monthly time scale in the second *Fermi* catalog [5.16] and thus some enhanced activity may be quite consistent with its past behavior.

Nearly simultaneous X–ray light curve observed by *Swift*-XRT for six days of monitoring of the source is depicted in Figure 5.3(c). From the Figure, we observe that the soft X–ray emission from the source is consistent with the average flux level $(5.01\pm0.34)\times10^{-11}$ erg cm^{-2} s^{-1}, except for some enhanced activity on March 15, 2013 (MJD 56366). During the enhanced activity on March 15 in X-rays, the HE activity is also observed to be slightly higher with respect to the average flux. We have also looked into the archival X–ray data in the energy bands 2-20 keV and 15-50 keV from *MAXI*[6] and *Swift*-BAT[7] instruments respectively and these data do not show any detection above 3σ. This indicates that during the period of *TACTIC* observations, the source was not active in hard X-ray regime. The simultaneous UV (W1,M2,W2 filters) and optical(V,B,U filters) light curves of the source for six days of observations are presented in Figure 5.3(d) and 5.3(e) respectively. The UVOT flux points included in the light curve have not been de-reddened. No unusual activity is observed in the source with *Swift*-UVOT instrument during the period of *TACTIC* observations. The radio observations at 15 GHz available for six days are shown in Figure 5.3(f). No significant variations are observed in radio emission from the source during this period.

5.5.2 Spectral Analysis

The spectral energy distribution of 1ES 1218+304 during March 1, 2013 to April 15, 2013 using broad band data discussed above is shown in Figure 5.4. For VHE γ–

[6] http://maxi.riken.jp/top/index.php
[7] http://heasarc.nasa.gov/docs/swift/results/transients

rays we plot the data from the observations with *MAGIC* and *VERITAS* telescopes along with the 99% CL upper limit on integral flux obtained from *TACTIC* telescope in the present work. The flux points reported by *MAGIC* group are based on the observations carried out during the period January 9-15, 2005 [5.20]. During the six days of observation, no flux variability on timescales of days was found and the time averaged spectrum was described by a power law with index 3.0±0.4. The *VERITAS* flux points taken from [5.23] correspond to observations during January–March 2007 for a total observation time of 17.4 h. The time averaged differential spectrum was described by a power law with photon index 3.08±0.34 and the integral flux above 200 GeV was 6% of the Crab Nebula flux. It is evident from the Figure 5.4 that the measured flux points are consistent with each other in the overlaping energy regime of the two telescopes. The VHE flux points measured with *MAGIC* and *VERITAS* telescopes as well as upper limit from *TACTIC* have been corrected for EBL absorption using the mean level density model proposed by Franceschini et al. (2008) [5.37].

The LAT data points have been obtained by dividing the energy range 0.1–100 GeV into four energy bands: 0.1–1 GeV, 1–10 GeV, 10–20 GeV and 20–100 GeV. The time averaged GeV spectrum measured by *Fermi*-LAT during this period is described with normalization factor f_0=(8.47±1.20)× 10^{-9} cm^{-2} s^{-1} GeV^{-1} and photon index $\Gamma = 1.87 \pm 0.08$. The HE photon index Γ=1.87±0.08 obtained in the present study is consistent with the value reported from quiescent state monitoring of 1ES 1218+304 by *Fermi*-LAT [5.38]. The photon index observed by *Fermi*-LAT during the first two years of observation of 1ES 1218+304 is 1.709±0.067 [5.16] and from first four years of observations is 1.97±0.02 [5.17].

The *Swift*-XRT flux points have been obtained from simultaneous fitting of the spectra of six observtaions in three energy bands: 0.3-1 keV, 1-2.5 keV 2.5–6 keV using CFLUX. Beyond 6 keV, *Swift*-XRT observations are not statistically significant to perform spectral analysis. The X-ray flux points measured with XRT as shown in Figure 5.4 have been corrected for Galactic absorption using a neutral hydrogen column density of 1.99×10^{20} cm^{-2} obtained from NED[8]. The time averaged soft X–ray spectrum measured with XRT during *TACTIC* observations is described by a power law with photon index 2.13±0.01. The X–ray emission level of (1.93±0.01)× 10^{-11} erg cm^{-2} s^{-1} in the energy range 2-10 keV, observed in our present study is below the flux level (2.64±0.02)× 10^{-11} erg cm^{-2} s^{-1} obtained from *XMM-Newton* measurements during 2001 observations [5.39].

The simultaneous optical and UV emission in the wavelength range 180-600 nm as measured by *Swift*/UVOT instrument in all six filters (V,B,U,W1,M2,W2) is shown in the Figure 5.4. The flux densities in all filters are estimated from the dereddened magnitudes with galactic absorption A_v=0.056 and R_v=A_v/E(B-V)=3.1, using the methodology proposed in [5.35]. The UVOT flux points have been obtained by multiplying the mean of flux densities with the bandpass (FWHM) of the corresponding filter [5.35]. Error in the mean density is obtained through the standard error propagation method. The radio flux point at 15 GHz obtained from

[8]ned.ipac.caltech.edu

OVRO telescope data archive[9] corresponds to the mean emission level from the source during *TACTIC* observations.

The broadband data points presented in Figure 5.4 indicate that the SED of the source can be described by two humps: first one peaking at X–ray energies and second at GeV energies. This implies that the multi-wavelength emission from 1ES 1218+304 can be possibly compared with the predictions of SSC model for blazar emission, but detailed SED modeling of the source is beyond the scope of this thesis.

Tang et al. (2010) have reproduced the SED of 1ES 1218+304 with the inhomogeneous jet model and the homogeneous SSC model [5.40]. They emphasize that the leptonic model is very successful in explaining multi-band emissions from the source and also point out that the VHE γ–ray data from *MAGIC* and *VERITAS* can be fitted with the strict lower-limit EBL model. Using the *Swift*, *MAGIC* and *VERITAS* data the SED of the source has been modeled in [5.26] by employing a time-dependent SSC code for obtaining physical parameters of the emission region. The short-time variability of the source has also been studied by Weidinger & Spanier (2010) [5.25] for reproducing the light curve observed by *VERITAS*. They suggest that the light curve can be reproduced by assuming a changing level of electron injection compared to the constant state.

5.6 Summary

Our γ–ray observations of 1ES 1218+304 (z=0.182) with the *TACTIC* telescope from March 1, 2013 to April 15, 2013 for a total observation time of $\sim$ 39.62 h do not show any evidence for a γ–ray signal. The multi-wavelength data in the X-ray and γ–ray energy bands, as measured by *Swift*-XRT (0.3-10 keV) and *Fermi*/LAT (0.1–100 GeV) also do not reveal any unusual activity from the source. The optical and UV emissions observed with *Swift*-UVOT instrument and radio observations at 15 GHz with 40 m *OVRO* telescope during *TACTIC* observations also do not indicate any flaring activity from the source. It is important to point out here that, because of the variable nature of blazars in general, the VHE emission from 1ES 1218+304 may increase significantly during future flaring episodes and may even easily exceed the limit reported in the present thesis. Hence the upper limit presented here only constrains the flux during our observation period.

5.7 References

[5.1] G. Colla et al., 1970, AAPS, 1, 281

[5.2] N. Bade et al., 1998, A&A, 334, 459

[5.3] C. M. Urry et al., 2000, ApJ, 532, 816

[9] http://www.astro.caltech.edu/ovroblazars/data/data.php

[5.4] B. A. Cook et al., 1978, MNRAS, 182, 489

[5.5] J. E. Ledden et al., 1981, ApJ, 243, 47

[5.6] A. S. Wilson et al., 1979, MNRAS, 187, 109

[5.7] J. H. Woo & C. M. Urry, 2002, ApJ, 579, 530

[5.8] R. Falomo et al., 2000, ApJ, 542, 731

[5.9] A. J. Pica et al., 1988, AJ, 96, 1215

[5.10] M. Giroletti et al., 2004, ApJ, 613, 752

[5.11] R. Sato et al., 2008, ApJL, 680, L9

[5.12] P. Giommi et al., 2005, A&A, 434, 385

[5.13] A. Tramacere et al., 2007, A&A, 467, 501

[5.14] D. Donato et al., 2001, A&A, 375, 739

[5.15] Y. C. Lin et al., 1996, A&ASS, 120, 499

[5.16] P. L. Nolan et al., 2012, ApJS, 199, 31

[5.17] F. Acero et al., 2015, arXiv:1501.02003

[5.18] D. Horan et al., 2004, ApJ, 603, 51

[5.19] F. A. Aharonian et al., 2004, A&A, 421, 529

[5.20] J. Albert et al., 2006, ApJ, 642, 119

[5.21] F. A. Aharonian et al., 2008, A&A, 478, 387

[5.22] C. Mueller et al., 2011, Astropart. Phys., 15, 121

[5.23] A. Acciari et al., 2009, ApJ, 695, 1370

[5.24] A. Acciari et al., 2010, ApJL, 709, 163

[5.25] M. Weidinger & M. Spanier, 2010, A&A, 515, 18

[5.26] M. Rüger et al., 2010, MNRAS, 401, 973

[5.27] A. Hillas, 1985, ICRC, 3, 445

[5.28] O. Helene, 1983, NIM A, 212, 319

[5.29] F. A. Aharonian, 2000, ApJ, 539, 317

[5.30] R. Koul et al., 2007, NIM A, 578, 548

[5.31] J. R. Mattox et al., 1996, ApJ, 461, 396

[5.32] D. N. Burrows et al., 2005, Space Sci. Rev., 120, 165

[5.33] P. W. A. Roming et al., 2005, Space Sci. Rev., 120, 95

[5.34] A. A. Breeveld et al., 2011, AIPC, 1358, 373

[5.35] T. S. Poole et al., 2008, MNRAS, 383, 627

[5.36] J. L. Richards et al., ApJS, 194, 29

[5.37] A. Franceschini et al., 2008, A&A, 487, 837

[5.38] A. A. Abdo et al., 2009, ApJ, 700, 597

[5.39] A. J. Blustin et al., 2004, A&A, 417, 61

[5.40] Y. Tang et al., 2010, RA&A, 10, 415

Chapter 6

Blazar Observations and Extragalactic Background Light

6.1 Motivation for study of Extragalactic Background Light

The extragalactic background light (EBL) is one of the fundamental observational quantities in cosmology. It plays a crucial role in cosmological tests for formation and evolution of stellar objects and galaxies. The EBL also plays an important role in the propagation of VHE γ–rays that are predominantly emitted by blazars. The VHE γ–rays are attenuated enroute to the Earth via pair production through ineteraction with low energy EBL photons. Thus the EBL affects spectrum of distant sources, specially blazars in the energy regime above 10 GeV. The knowledge of EBL spectrum and intensity will allow the determination of intrinsic blazar spectra in a crucial energy regime that can be used to test the particle acceleration mechanisms and VHE γ–ray production models. Conversely, knowledge of the intrinsic γ–ray spectrum and detection of blazars at increasingly higher redshifts will provide a unique tool to set strong limits on EBL and its evolution. The total EBL intensity can also be used to derive an estimate of the supernova rate and the resulting flux of supernova neutrinos because it is intimately connected to the diffuse X–ray, radio and supernova neutrino background. Therefore study of EBL is of fundamental importance both for understanding the entire process of star formation, galaxy evolution and VHE astrophysics in general.

6.2 Extragalactic Background Light

The EBL refers to the accumulation of energy released in the form of electromagnetic radiation from ultraviolet (UV) to infra-red(IR) through optical since the decoupling of matter and radiation at reshift z $\approx$ 1100 following the *Big-Bang*. Thus, the EBL comprises the integrated light from the resolved and unresolved extragalactic sources, and the light from any trully diffuse background, excluding cosmic

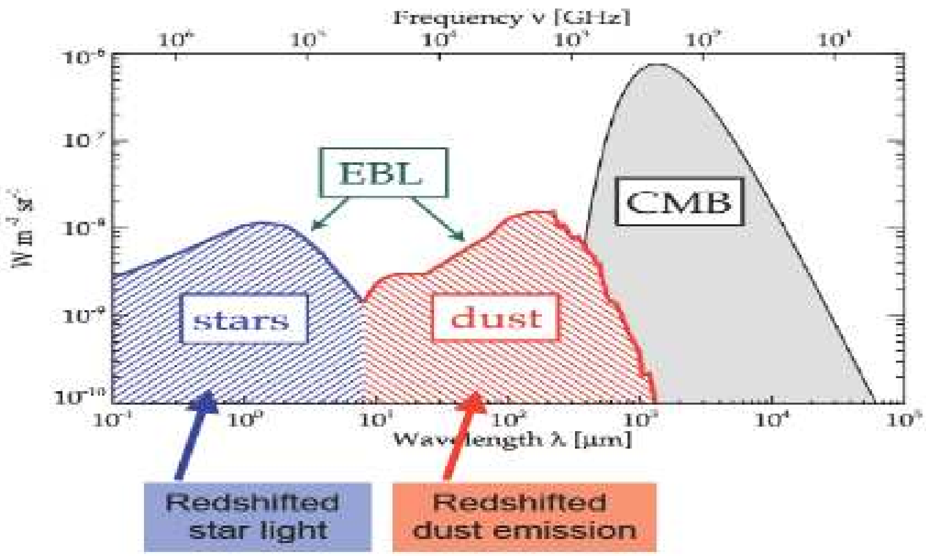

Figure 6.1: Illustration of two dominant backgrounds in the universe.(Credit: mpi-hd.mpg.de)

microwave backgound (CMB). The light emitted by stars and accreting compact objects through the history of the universe is encoded in the intensity of EBL. It is the second largest background after the CMB of 2.7 °K in terms of energy content in the universe [6.1]. A comparision of the two most important backgrounds in the universe is shown in Figure 6.1. While the CMB conserves the information about the structure of the univesre at the epoch of decoupling, EBL is the repository of all energy produced by nuclear and gravitational processes involving star and galaxy formation since the epoch of recombination. A significant fraction of EBL is shifted by cosmic expansion and by absorption and re-radiation by dust into IR wavelengths. Consequently, intensity and spectral shape of EBL hold key information about the formation and evolution of galaxies and their stellar and interstellar contents throughout cosmic history.

6.2.1 Main contributors to EBL

By definition, EBL does not include foreground radiation from the solar system, the Milky Way or other nearby galaxies, and CMB radiation. Background in the form of high energy radiation including X–ray and γ–ray is also not considered as a part of EBL. The conventional contributors to the EBL are redshifted starlight and dust-absorbed and re-radiated starlight and therefore it reflects the sum total of galactic luminosities integrated over the entire age of the universe. The main contributors to EBL intensity are outlined below:

- **Stellar Contributions :** Stars and the dust interacting with them are conventional contributors to EBL and most of the EBL intensity is powered by massive stars that end their life as core collapse supernova. The majority of EBL at UV to IR is produced by stars at all redshifts since the first stars formed. The UV light from galaxies is produced by the hot, massive stars, which are also responsible for most of the nuclear processing of Hydrogen into Helium and heavier elements generally called *metals*. The optical EBL includes the direct emission from stellar populations out to redshifts of $z = 10$. Finally, much of the stellar emission in the universe contribute to far-IR background through redshifted light from most distant or earliest generations of the stars. The dust grains (silicate and graphite with size 1 nm-10μm) and macromolecules, commonly identified as polycyclic aromatic hydrocarbons, in the emitting galaxy absorb UV-Optical photons and re-radiate as thermal radiation at IR wavelenghts $> 10\mu$m [6.1]. Dust attenuation of short wavelength light is very efficient and may prevent more than 30% of the star formation in the universe from being directly observed at wavelengths shorter than 1μm.

- **Pop III stars contribution:** The stars are classified by their heavy element abundance or metallicity (atomic number $Z > 2$), which correlates strongly with the age of star and with the type of galaxy where it can be found. Stars with high metallicity are referred to as *Population I* (Pop I) stars. Pop I stars are hot, young, and luminous, and are usually found in the arms of spiral galaxies. *Population II* (Pop II) stars have low metallicity, are cooler, older and less luminous, and are usually found in globular clusters. *Population III* (Pop III) stars have zero metallicity, and would have formed and died early in cosmic history. Over time, the remnants of these Pop III stars had enough metallicity to form the Pop I and II stars observed today. From simulations based on star formation, Pop III stars are expected to form differently from normal stellar population. In the aftermath of the *Big Bang*, the matter content of the universe consisted of Hydrogen and Helium only, with no heavy elements present by the end of the radiation era. It is believed that in this metal-free environment the first stars formed, radiated and finally exploded in violent supernovae giving origin to the first metals. This hypothetical stellar population is referred to as Pop III. Once formed, Pop III stars are expected to radiate close to the *Eddington limit* for most of their short lives (10^6 years). Their spectrum is described by black body radaition of temperature $\sim 10^5$ °K and net contribution to the EBL in the IR region could be significant [6.2,6.3,6.4,6.5].

- **Non-Stellar Contributions :** Non-stellar emission, such as the gravitational potential energy from accreting black holes and emission from decaying particles also contribute to EBL. A significant fraction of the baryons in the universe residing in a primordial intergalactic medium of ionized gas may also contribute to EBL. While hot gas (10^6 °K) would emit X-rays, and cold gas (10^4 °K) would produce dramatic absorption features in quasar spectra, gas at a temperature of 10^5 °K would be detectable only by its contribution to the EBL through redshifted HeII emission at 30.4 nm and $Ly\alpha$ at 121.6 nm.

- **Exotic Contributions :** The exotic and non-nuclear contributions to the EBL include radiation from AGN, brown dwarfs and the decay of primordial particles. The broadband energy output from AGN through release of gravitational energy associated with the accretion of matter represents the major non-nuclear contribution to the radiative energy budget of the universe [6.1]. Brown dwarfs are the gravitational energy sources that might contribute to EBL intensity. Brown dwarfs are the objects whose mass is below the minimum mass limit ($0.08M_\odot$) required for stable hydrogen burning. These objects radiating as black body contribute to EBL in the wavelength range 10-100 μm [6.6]. An additional non-nuclear contribution to the EBL might rise from radiative decay of primordial particles. By appropriately selecting the particle number density, mass, and decay redshift, wide range of background intensity at UV to far-IR wavelengths can be produced [6.7, 6.8], but no physical evidence favors one set of assumptions over the others, and the existence itself of such primordial particles remains highly conjectural.

6.2.2 Evolution of EBL

Understanding the evolution of background light with redshift is a key issue in observational γ–ray astronomy and cosmology. The diffuse EBL, as it is seen today, consists of integrated electromagnetic radiation from all epochs, which is redshifted, corresponding to the formation epoch, at which the radiation was produced. Due to the cosmic expansion of the universe, the light is redshifted resulting in an inexorable drift of radiated power from shorter to longer wavelengths. Also, the number and properties of the emitting sources change with time. The actual cosmic radiation background is not a static entity, it evolves continuously and the cosmic expansion should dilute the EBL by a factor $(1+z)^3$. The general behaviour of spectral densities is that of an increase in the photon proper density with redshift due to the Hubble expansion. However, such an increase is not simply proportional to the volume factor $(1+z)^3$ because photons are progressively generated by galaxy population during most of the Hubble time to the present, so that the photon comoving number density decreases with redshift [6.9]. Below redshift $z \leq 2$, EBL density increases with redshift due to rise in star formation rate and decreasing volume. At redshift $z \geq 2$, EBL density decreases because the total number of stars formed upto that redshift from $z = 6$ decreases. Thus from the phenomenological arguments, the redshift evolution can be accounted into the effective EBL photon number density by a factor $(1+z)^{3-k}$, where the parameter k is referred to as *evolution coefficient*. For $k = 1.2$, a good agreement is found between different approaches of cosmological evolution of EBL photon density [6.10].

6.2.3 Spectral Energy Distribution of EBL

The EBL photons lie in the wavelength range 0.1-1000 μm. The spectral energy distribution of EBL from UV to far-IR is characterized by a double hump structure with its two major components: cosmic optical backrgound (COB) and cosmic infrared background (CIB) [6.1]. The first component, COB peaks at $\sim 1\mu$m and is believed to originate directly from integrated starlight. The second component, CIB having its peak at $\sim 100\mu$m results mostly from reprocessing of direct starlight emission in UV to optical that is absorbed by dust inside the galaxies and re-emitted at higher wavelengths. The total energy density of EBL is almost equally shared by these two components COB (52%) and CIB (48%) as illustrated in Figure 6.1. Other contributions, like emission from AGN and quasars are expected to produce no more than 5 to 20 % of the total EBL density in the mid-IR region [6.11]. Thus it is obvious that the SED of EBL may be fitted with a combination of two or more modified black body spectra for its two distinct peaks at the optical and IR bands. The energy density from stellar populations include both older populations at low redshift and young populations at high redshifts. The existence of large amounts of cosmic IR radiation reveals that dust is common in the universe, since only dust can efficiently absorb a significant fraction of the power radiated by stars and accretion sources, and re-emit it at infrared wavelengths. The dominant energy source for EBL is apparently thermonuclear fusion reactions that convert hydrogen into heavier elements. The photometric results are usually presented in terms of νI_ν, where I_ν is the spectral intensity at frequency ν. The specific intensity of EBL is reported in units of nW $m^{-2}sr^{-1}$. The conversion of spectral intensity to energy density is given by

$$\epsilon^2 n_\epsilon(eVcm^{-3}) = 2.62 \times 10^{-4} \times \nu I_\nu(nWm^{-2}sr^{-1}) \tag{6.1}$$

where ϵ is the EBL photon energy in eV and n_ϵ is the photon spectral number density in photons $cm^{-3}eV^{-1}$. Also at a given wavelength λ , the photon spectral number density is calculated using the relation

$$n_\epsilon(cm^{-3}eV^{-1}) = 1.70 \times 10^{-4} \times \lambda^2(\mu m) \times \nu I_\nu(nWm^{-2}sr^{-1}) \tag{6.2}$$

The total intensity of EBL from UV to IR wavelengths lies in the range 45–170 nW m^{-2} sr^{-1}. The energy density in the wavelength range 0.16-3.5μm is quite uncertain with present limits of 19–100 nW m^{-2} sr^{-1}. The energy density in the 3.5–140μm range, 11–58 nW m^{-2} sr^{-1}, remains similarly uncertain because of the dominance of the interplanetary dust emission. The most certain background determination is in the range 140–1000μm containing (15$\pm$2) nW m^{-2} sr^{-1}. The nominal value for the total extragalactic background in the wavelength range 0.1–1000μm is 100 nW m^{-2} sr^{-1}.

6.2.4 Astrophysical and Cosmological Implications

One of the outstanding challenges in modern astrophysical cosmology is to explain the structure formation in the universe. The formation of stars and galaxies from matter and their evolution is accompanied by the release of radiant energy powered by gravitational and nuclear processes. The cosmic star formation rate density (SFRD), one of the fundamental quantities of cosmology, strongly evolves over the redshift range z= 0 to z= 2 with a peak expected at redshifts between 1 and 2. Stellar and dust emissions being dominant contributors to EBL, a precise measurement of EBL density can provide strong constraints on the SFRD [6.12]. The end of the dark ages of the universe, the epoch of reionization, is a topic of great interest in modern cosmology [6.13]. The first (Pop III) and second (Pop II) generation of stars are natural candidates for the sources of reionization. The Pop III stars are hot and massive, their UV photons emitted at $z > 5$ would be redshifted to near IR regime and could leave a unique signature on the EBL density [6.3]. If the EBL contribution from lower redshift galaxies is sufficiently well known, upper limits on EBL density can be used to probe the properties of early stars and galaxies [6.14]. Combining detailed model calculations with redshift dependent EBL denisty measurements could enable to probe the reionization history of our universe. Detection of spectral cutoffs in sources at very large redshifts ($z > 5$) would directly probe the evolving UV background at these redshifts, providing invaluable insight into the cosmic reionization epoch. While blazars may be difficult to detect much beyond $z \approx 2$, this may be feasible for GRBs which are the most luminous and distant γ–ray sources known in the universe.

6.3 EBL Measurements

The precise level of EBL density is not known accurately because its spectral energy distribution is a complex function of source characteristics, star and galaxy formation history in the Universe. Therefore, EBL lacks any spectral signature. Also, the EBL flux is very weak and the cumulative flux from foreground astrophysical sources is roughly 100 times that of the EBL. The EBL intensity from UV/optical to far IR can be determined in three ways: Direct measurements, Fluctuation analysis and Indirect constraints.

6.3.1 Direct Measurements

The direct measurements of EBL include observations with space or ground based instruments sensitive in specific wavelength bands. Since the atmosphere is opaque to UV light (100-250 nm), the observations in this wavelength range must be made from space. For optical (300-1000 nm) EBL measurement, the Earth's own atmosphere is the greatest impediment. The only successfully demonstrated method for dealing with atmospheric effects is to avoid it by conducting measurements of EBL from space. Measurement of EBL intensity in the UV-Optical wavelength regime is performed using two different procedures (i) light integration of extragalactic source counts and (ii) subtraction of the foreground of the sky brightness. Observations of IR ($10^3 - 10^6$ nm) EBL must be made from space with cryogenically cooled detectors because any warm body emits thermal radiation, including telescopes, the Earth's atmosphere and the Earth itself. Following techniques and analysis methods are used for direct measurement of EBL flux.

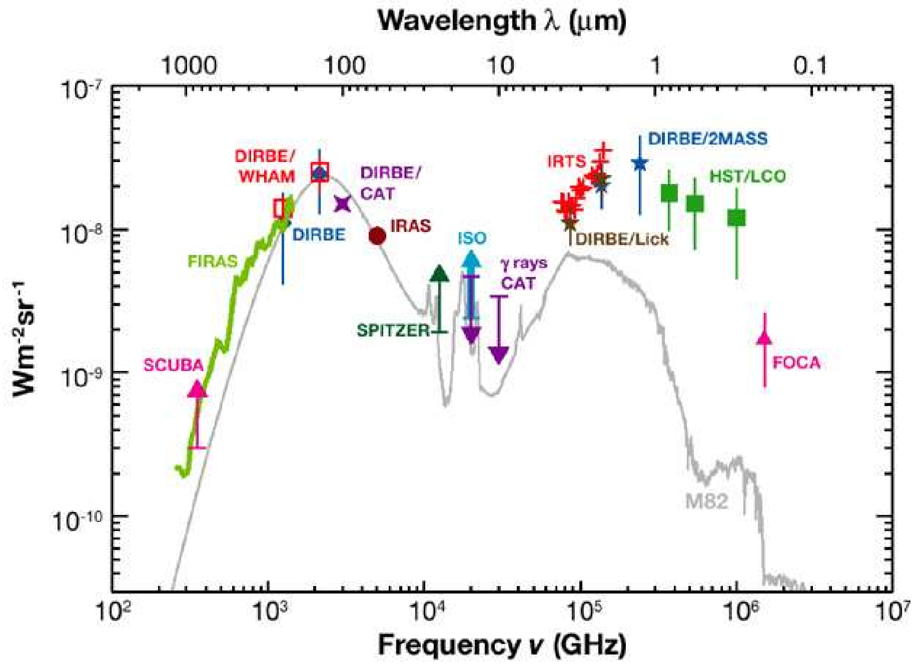

Figure 6.2: Complete EBL spectrum measured over three decades in wavelength by various instruments. (Figure adopted from [6.25])

- **Measurement of UV-EBL :** The early attempts to observe far UV background from rockets or space were inspired by the fact that the only bright foreground source documented at the time-*zodiacal light*-drops off sharply below 400 nm and becomes insignificant below 200 nm. However, the measurements were more difficult than expected and results varied by 3 orders of magnitude. With hindsight, it is clear that poor spatial resolution made subtraction of Galactic stars extremely difficult in these experiments and that the instrumental backgrounds were poorly understood. Rapid progress came around 1980, with the advent of UV detectors with better resolution and greater sensitivity. Results consistently show that the majority of UV background originates within the Galaxy, with only a small component being isotropic and therefore possibly extragalactic. Measurements and limits in the last 10 year have converged fluxes in the range 2–5 nW m^{-2} sr^{-1}, with a minimum estimate of 1 nW m^{-2} sr^{-1} from the cumulative flux in the detected sources.

- **Measurement of Optical-EBL :** The optical CCD detectors typically have sub-arcsecond resolution, which makes subtraction of stars in our own galaxy relatively easy. However, as in the UV, interstellar dust scatters incident starlight, producing diffuse galactic light at optical wavelengths. The dominant foreground source contributing from beyond the Earth's atmosphere is sunlight scattering off of the large dust particles ($\geq 10^4$ nm). As the solar system is harder to escape than the Earth's atmosphere, it is fortunate that scattering involved is well described by Mie scattering theory and is weakly wavelength dependent, with scattering becoming more efficient by $\sim 5\%$ per 100 nm toward longer wavelengths. The mean zodiacal light flux can therefore be measured using the strength of solar absorption features (Fraunhofer Lines) which are preserved in its spectrum. Ground based efforts to measure the optical EBL started in 1970s. Atmospheric emission or *airglow* was identified either by geometrical modelling or by beam switching between a clear line of sight and a dark dust cloud at high galactic latitude in order to isolate the foreground from background sources. In 1980, the *Pioneer 10 Explorer* obtained data not only from the above atmosphere but from beyond the zodiacal dust cloud at a large distance from the Sun. Detections of optical EBL at 300, 550 and 800 nm have been reported from *Hubble Space Telescope* (HST) and ground based spectroscopy.

- **Measurement of IR-EBL :** From space, thermal emission comes from dust trapped in the solar system and in the Galaxy. Rocket borne measurements of IR sky brightness continued into the 1990s from near to far IR wavelengths. The *Infrared Astronomical Satellite* (IRAS) carried out the first all sky survey in IR, mapping the sky at 12-100 μm [6.15]. The IRAS data clearly revealed large scale, diffuse emission components of the sky brightness from the solar system and galaxy. The most ambitious and successful IR measurement was undertaken with the *Cosmic Background Explorer* (COBE), launched in 1989. The COBE mission carried two instruments: *Diffuse Infrared Background Experiment* (DIRBE) and *Far Infrared Absolute Spectrophotometer* (FIRAS), designed to make absolute sky brightness measurements. The DIRBE was designed to search for CIB in the wavelength range 1.25-240 μm [6.16], whereas FIRAS was designed to measure the spectrum of the CMB and the far IR background from 125-5000 μm [6.17].

  Several recent instruments like *Near Infrared Spectrometer* (NIRS) onboard the *Infrared Telescope in Space* (IRTS), *Near Infrared Camera and Multi-Object Spectrometer* (NICMOS) onboard HST, *Infrared Space Observatory (ISO), Sub-millimeter Common User Background Array (SCUBA), Infrared Array Camera (IRAC) and Multi-band Imaging Photometer System (MIPS)* on board the *Spitzer* were also used to measure the IR background in the wavelength range 1.4-180 μm [6.18]. The NIRS measurements reported existance of near IR background excess, which was contradicted by NICMOS. The IRAC and MIPS measured galaxy contributions in the wavelength bands 3.6-8 μm and 24-170 μm respectively.

- **Challenges in Direct Measurement :** The direct measurements of EBL intensity as described above are very difficult and pose considerable technical and astronomical challenges. Technically, it requires absolute calibration of the instruments, and removal of all measurement uncertainties [6.1]. Astronomically, the measurements of EBL are possible only in the local universe, because it requires the removal of strong foreground emission from interplanetary dust particles, zodiacal light, airglow and from stellar and interstellar components in the Milky Way. The line emission from atoms and simple molecules at altitudes above 300 km and solar Lyα photons also contribute to the space based measurements of UV-EBL. Emission by atmosphere or airglow is also a source of foreground emission for ground based observations. It is not only at least 100 times brighter than the EBL but can also vary by several percent on timescales of minutes, as can atmospheric extinction.

6.3.2 Stacking/Fluctuation Analysis

At longer wavelengths, unresolved galaxies become a source of confusion, limiting the depth of the survey. Below a certain flux (the confusion limiting flux) individual sources become indistinguishable from the variation in the sky brightness caused by statistical fluctuations in the number of faint resolved or unresolved sources [6.20]. These limitations are partially circumvented by *stacking analysis.* Stacking of astronomical images of sources detected at one wavelength enhances their signal relative to the random background fluctuations at some other wavelengths [6.21]. The integrated light obtained by this method is closer to the EBL intensity than that obtained by integration down to the confusion limit. Most of the EBL is generated by discrete galactic or primordial stellar sources. Fluctuations in their number and their clustering properties will give rise to spatial fluctuations in the EBL intensity. Studies of the optical region of EBL via *fluctuation analysis* [6.22, 6.23] do not provide a direct measurement of EBL intensity. Spatial fluctuations in the EBL provide a different means of setting limits on its intensity. Fluctuation measurements of the EBL do not require absolute knowledge of its intensity, since the removal of foreground emission components is done on the basis of their distinct spatial properties rather than their absolute intensities. After the removal of all known resolved sources, any residual fluctuations will measure the EBL contribution from sources that may represent unknown or unresolved population of stars or galaxies. Fluctuation mesurements from *Spitzer and ISO* data have been used to derive limits on EBL at 100 and 160 μm [6.24].

6.3.3 Indirect Measurements

Indirect evidence for the intensity of EBL can be obtained from observation of the sources of γ–rays in the universe. VHE γ–ray photons traveling cosmological distances are annihilated by EBL photons through $\gamma-\gamma$ absorption and an electron-positron pair is created. This process introduces an attenuation in VHE spectra of γ–ray sources. These attenuation effects by EBL in principle provide an indirect but powerful tool to probe the EBL intensity at wavelengths corresponding to γ–ray observations. The method of probing EBL density indirectly using VHE spectra of blazars is discussed in detail in Section 6.6.

The general observations of EBL from near UV to far-IR using different instruments is shown in Figure 6.2. Only the most recent and strongly constraining measurements have been shown in the figure. From Figure 6.2, it is obvious that optical and IR components of EBL are well separated and the power in IR is comparable to the power in optical [6.25].

6.4 EBL Models

The EBL intensity and spectral shape depend on the star formation rate history, the stellar initial mass function, evolution of metallicity and the relative importance of energy released by nuclear and gravitational processes. In a dusty universe, the comoving luminosity density and total EBL intensity remain unchanged, however the energy is redistributed by absorption and re-emission processes over a large spectral range. Several distinct approaches have been used to model the intensity and spectral distribution of EBL at $z = 0$. They all represent different approaches for calculating the evolution of luminosity function (LF) with redshift. In the following, different models for EBL have been briefly discussed.

6.4.1 Backward Evolution Models

Backward evolution (BE) models start from the local determination of LF at $z = 0$, evolving it with redshift (back in time) using observed galaxy number counts at different wavelengths [6.1,6.26]. The EBL intensity and spectral shape are used as integral constraints on their evolution. Several distinct functional forms have been used to characterize the LF in the different IR wavebands. They are usually characterized by three parameters: normalization, characteristic luminosity (determining the transition point between the low and high luminosity behavior), and a power law index that determines the behavior of the LF at low luminosities. Evoultion in LF is introduced by adding a redshift dependence of the form $(1+z)^k$ to the basic parameters characterizing the LF. BE models are relatively simple, and their predictions can be easily compared to observed galaxy number counts, their magnitude-color and magnitude number density relations, and their redshift distribution. They are only loosely constrained by the physical processes.

6.4.2 Forward Evolution Models

Forward evolution (FE) models use the redshift dependence of the cosmic star formation rate (CSFR) to determine the LF and population synthesis with radiative transfer models to determine the distribution of energy over wavelengths [6.1,6.26]. Determination of the CSFR is complicated by extinction effects at UV and optical wavelengths, and by the implicit assumption that the IR luminosity is powered by stars and representative of the total bolometric luminosity of the galaxies. The most difficult part of this approach is determining the fraction of starlight that is absorbed by dust, and the spectrum of the re-radiated IR emission. The cosmological application of such models assumes that star formation is a monolithic process, in which in all galaxies star formation commenced at the same redshift and evolved quiescently until the current epoch. The models do not allow for galaxy interactions, stochastic star formation histories associated with merger events, or any morphological evolution of galaxies.

6.4.3 Chemical Evolution Models

Cosmic chemical evolution (CE) models are similar to BE and FE models except that they treat the universe as a closed system in which all galaxies within a large co-moving volume element are represented by their basic ingredients: stars, interstellar gas, metallicity, and radiation [6.1, 6.26]. Chemical evolution equations, analogous to those used to follow the chemical evolution of the Galaxy are used to follow the evolution of the average stellar, gaseous, and radiative contents in each comoving volume in a self consistent manner. Input parameters for CE models are the mean rest frame UV luminosity density as a function of redshift, and the mass of the interstellar medium gas as determined from HI column densities derived from studies of quasar absorption lines through damped Lyα systems.

6.4.4 Semi-analytical Models

Semi-analytical (SA) models follow the appropriate physical processes in a more general form for formation and evolution of galaxies to determine the LF in a cold dark matter Λ dominated (ΛCDM) universe [6.1,6.26]. These models then follow the growth and merger of dark matter halos, and the emergence of galaxies which form as baryonic matter falls into the potential wells of these halos. The fate of the infalling gas is determined by many different processes: the formation of stars in a multiphase interstellar medium, AGN and supernovae feedback processes that quench their formation, the evolution of the stellar radiation field, the heating and cooling of the interstellar medium and its chemical enrichment, the exchange of material with the intergalactic medium through infall and galactic winds, and the growth of the central black hole. SA models are inherently complex, incorporating a large number of physical processes, some poorly known, to derive galaxy properties.

6.4.5 Models used in our work

As in all EBL models discussed above, determination of the SED of galaxies is complicated by the detailed microscopic and large scale parameters needed to calculate the amount of starlight that is absorbed by dust, and the spectrum of the re-radiated emission. Recent SA models have combined the models for galaxy formation with radiative transfer models to determine the SED of galaxies. SA models are the most physically motivated models, and quite successful in reproducing a large number of observational constraints. Due to various assumptions and uncertainties in estimating the parameters, the EBL intensity suggested by various models differs considerably. Here we briefly describe some of EBL models used in our work.

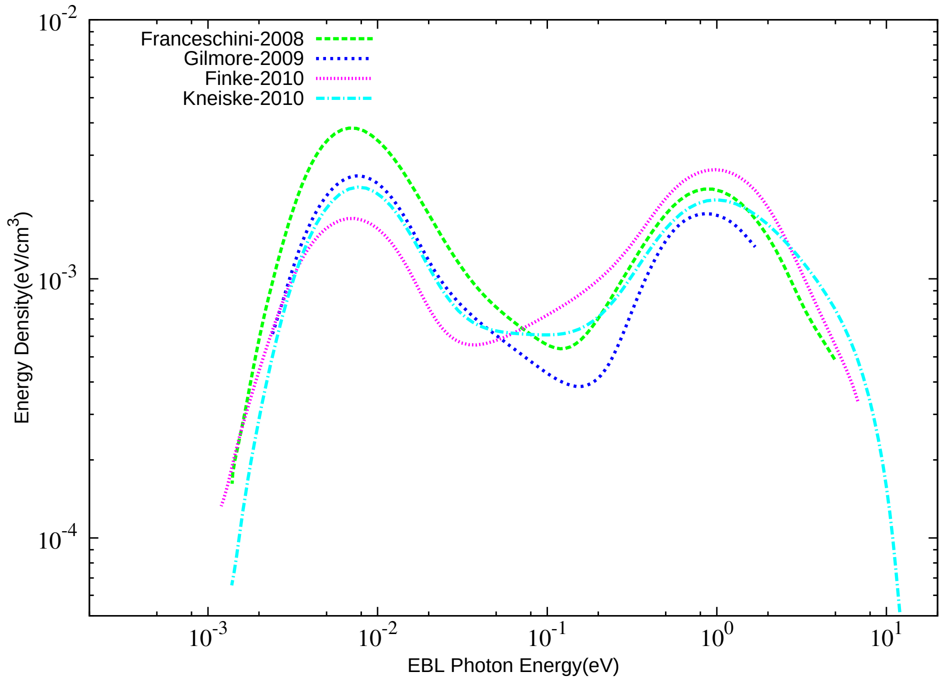

Figure 6.3: Spectral energy distribution of EBL predicted by four different models used in our work.

- **Franschini et al. (2008) :** Franschini et al. (2008) [6.27] used an empirical BE model to estimate EBL contribution using extensive data set available from *Spitzer Space Telescope IR camera* and ground based telescopes. They assumed the galaxy population is dominated by the evolution of spheroidal galaxies, spiral galaxies and merger systems. In case of spirals, the comoving number density remains constant after the formation at a given redshift but their luminosity evolves along with the evolution of their stellar content. For merger systems, they considered the evolution of both, luminosity and galaxy number density to be consistent with the observations. Spheroidal galaxies are assumed to be formed at moderate redshifts and their evolution is achieved by dividing them into seven sub-populations forming at various redshifts. Assuming the mass and luminosity functions do not vary among the sub-populations, they set their normalizations to reproduce the local luminosity function. The cosmological observables at near IR wavelength are then obtained by adding the contribution from these three galaxy classes. A synthetic spectral energy distribution is then used to extrapolate these observables to shorter wavelength. At longer IR wavelength, the photons are produced predominantly by the dust thermal emission present in the galaxy interstellar medium. Most luminous and massive galaxies are characterized by intense star formation and the emitted radiation is effectively reprocessed in to IR by dust rich medium. Hence they are bright in IR and their evolution is modelled similar to near IR wavelength.

- **Gilmore et al. (2009) :** Gilmore et al. (2009) [6.28] used SA approach to estimate the EBL by evolving the radiation released by galaxies and quasars starting from cosmological initial conditions. The UV luminosity density from galaxies are predicted using SA model of galaxy evolution. Their model also includes the formation of super massive black holes leading to quasars and AGN. However the properties of quasars and AGN predicted by their model is not yet tested with the observations and hence their contribution to UV background is added empirically. The emissivities due to galaxies and quasars are then integrated over redshifts to predict the evolving UV background of the Universe. The parameters of the SA model are constrained to reproduce the local galaxy observations. Along with this evolutionary model they also employ a radiative transfer code to estimate the absorption and re-emission of ionizing UV radiation by inter-galactic medium. The dust and stars are assumed to homogeneously fill the galaxies which are considered as oblate ellipsoids. The contribution of different components of the dust is set to reproduce the local IR background.

- **Finke et al. (2010) :** Finke et al. (2010) [6.29] predict the intensity of EBL directly from the stellar radiation and the reprocessed radiation by dust in the inter stellar medium without involving complex SA models. At shorter wavelengths, EBL is dominated by stellar emission which is treated as a blackbody. The stellar properties belonging to main sequence and off main sequence stars are obtained from approximate formulae given in [6.30]. Finally their contribution to EBL is estimated through initial mass function, stellar formation rate density and the fraction of photons escape from being absorbed by the dust in the interstellar medium. At larger wavelengths, the emission is dominated by dust which is approximated as a combination of three blackbodies. A warm component at temperature 40 K representing large dust grains found in and around star forming regions, a hot component at temperature 70 K representing small dust grains present in the disk of the spiral galaxies and emission from polycyclic aromatic hydrocarbons which is assumed as a blackbody at temperature 450 K. The resultant IR emission is calculated self consistently by equating the luminosity density from dust emission with the luminosity density from starlight absorbed by the dust.

- **Kneiske et al. (2010) :** EBL predicted by Kneiske & Dole (2010) [6.31] considers the evolution of star light using a simple stellar population model for different stellar masses. For a given initial mass function the evolution is mainly governed by the stellar formation rate density. The star forming regions are divided into two types namely “optical star forming region” with low dust extinction representing luminous infrared galaxies and “infrared star forming region” with high dust extinction representing ultraluminous infrared galaxies. The resultant SED produced by a population of stars is generated using a spectral synthesis model along with dust absorption/reemission model. The IR emission from the dust is again approximated as a combination of

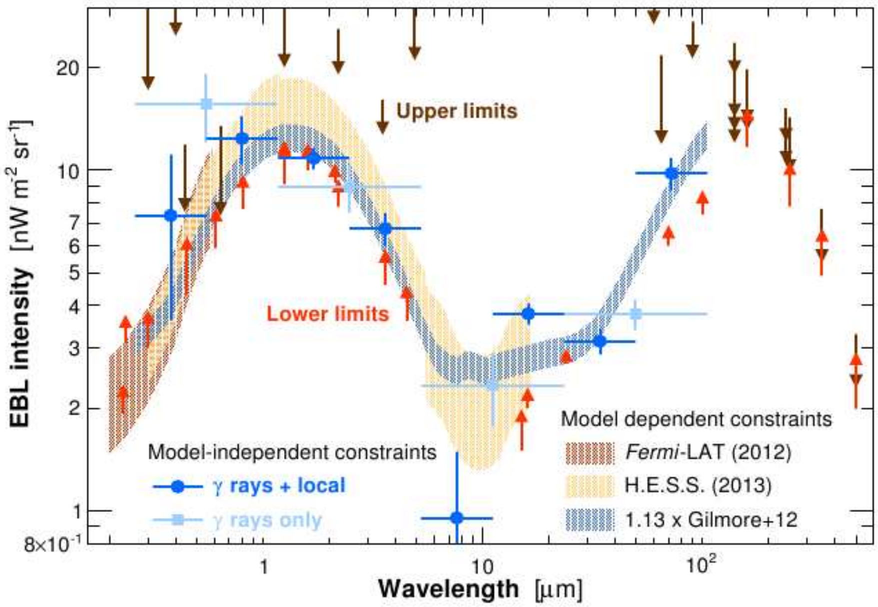

Figure 6.4: Constraints on the intensity of EBL at z=0 from various approaches. Lower and upper limits are shown with orange (upward) and dark brown (downward) arrows respectively. (Figure adopted from [6.53])

three black body spectra at different temperatures. The stellar formation rate density and dust parameters and then adjusted to reproduce the observed lower limit of EBL obtained through integrating the number counts of galaxy from deep sky survey and completeness correction.

The spectral energy density of EBL photons predicted by four EBL models as described above is depicted in Figure 6.3. These models for EBL intensity have been used for calculating the optical depth of VHE γ–ray photons at different redshifts in the present work.

6.5 Attenuation of VHE γ–ray photons and Indirect Constraints on EBL

The EBL is a source of opacity for VHE γ–ray photons travelling cosmological distances from source to the Earth. To date, the most numerous available GeV-TeV γ–ray sources are blazars in the universe. The intrinsic VHE γ–ray spectrum emitted from blazars is modified by EBL absorption because of the energy and distance dependence of opacity of the universe to TeV photons. The combined GeV-TeV and other multi-wavelength observations of blazars make it possible to study their intrinsic spectra over a large range of redshifts, thereby enabling the studies of EBL over a wide range of wavelengths. Dis-entangling the intrinsic blazar features and the EBL induced attenuation signature in the measured blazar spectra unambiguously lead to a precise measurement of EBL density. If EBL density is well measured, absorption in VHE spectra can be used as a distance indicator in VHE astrophysics, somewhat analogues to what is done for Supernovae of type 1A but with very different systematic uncertainties [6.32]. The evolution of such an attenuation signature with redshift would allow to put constraints on cosmological models and measure the Hubble parameter and cosmological densities. The inconsistancy between intrinsic VHE blazar spectra and known EBL density opens up a completely new window in particle and astroparticle physics since one of the two following options must be true: either the intrinsic source physics is fundamentally different than the models predict or the properties of γ–ray propagation through space are fundamentally different than we know today, which can become a major challenge for the modern physics.

6.5.1 EBL Absorption of VHE γ–ray photons

VHE γ-rays en route from source to the observer on the Earth suffer absorption by interaction with the low energy EBL photons via pair-production mechanism [6.33],

$$\gamma_{VHE} + \gamma_{EBL} \rightarrow e^- + e^+ \tag{6.3}$$

The above process is kinematically allowed provided following condition is satisfied by the energies of the two photons,

$$E\varepsilon(1 - cos\phi) = 2m_e^2c^4 \tag{6.4}$$

where E and ε are the energies of VHE γ-rays and EBL photons respectively, ϕ is the scattering angle between momenta of two photons in lab frame and m_e is the rest mass of electron. The total cross section for the pair creation process depends on the energy of two photons and the angle between them and is given by [6.34]

$$\sigma_{\gamma\gamma}(E_\gamma, \varepsilon, \phi) = \frac{\pi r_e^2}{2}(1-\beta^2)[(3-\beta^4)ln\frac{1+\beta}{1-\beta} - 2\beta(2-\beta^2)] \tag{6.5}$$

where r_e is the classical electron radius and β represents Lorentz factor in units of velocity of e^- or e^+. In the center of mass frame,

$$\beta = \left[1 - \frac{2m_e^2c^4}{E\varepsilon(1-cos\phi)}\right]^{1/2} \tag{6.6}$$

The optical depth, τ encountered by VHE γ-rays of energy E emitted from a source at redshift z_s due to EBL absorption is computed by convolving the EBL photon number density $n_{EBL}(\varepsilon$,z) with pair production cross section $\sigma_{\gamma\gamma}(E, \varepsilon, \phi)$. For cosmological applications, note that E and ε change along the line of sight in proportion to $(1 + z)$ due to the expansion of Universe. The three fold integral over the redshift

(z), scattering angle (ϕ) and the energy of EBL photons (ε) is given by

$$\tau(E,z_s) = \int_0^{z_s} \left(\frac{dl}{dz}\right) dz \int_0^{\pi} \left(\frac{1-cos\phi}{2}\right) sin\phi d\phi \int_{\varepsilon_{th}}^{\infty} n_{EBL}(\varepsilon,z)\sigma_{\gamma\gamma}(E,\varepsilon,\phi)d\varepsilon \quad (6.7)$$

The distance travelled by a VHE photon from source to observer in ΛCDM cosmology is expressed as,

$$\frac{dl}{dz} = \frac{c}{H_0}\frac{1}{(1+z)\sqrt{\Omega_\Lambda + \Omega_m(1+z)^3}} \quad (6.8)$$

where Ω_m and Ω_Λ are the density parameters for matter and vacuum (or dark) energy of the universe respectively and H_0 is Hubble constant at the present epoch. The threshold energy of background photons for pair production is given by

$$\varepsilon_{th}(E,\phi,z) = \frac{2m_e^2c^4}{E(1+z)^2(1-cos\phi)} \quad (6.9)$$

The optical depth of VHE γ-rays from a given source is estimated using equation (6.7) corresponding to different EBL models for $n_{EBL}(\varepsilon$,z) as described above. The intrinsic VHE γ-ray flux $\left(\frac{dN_\gamma}{dE}\right)_{int}$ emitted from the source is modified due to EBL absorption and the observed flux $\left(\frac{dN_\gamma}{dE}\right)_{obs}$ is related to intrinsic flux as

$$\left(\frac{dN_\gamma}{dE}\right)_{obs} = \left(\frac{dN_\gamma}{dE}\right)_{int} .e^{-\tau(E,z_s)} \quad (6.10)$$

Because the optical depth τ(E,z) mostly increases with energy for a given redshift for all expected EBL shapes, the absorption of VHE photons due to EBL makes the observed photon spectrum steeper than the intrinsic one. This steepening increases with redshift and EBL intenisty. Assuming that all the attenuation is attributed to EBL, several upper limits have been derived on EBL intenisty by making various assumptions on the intrinsic spectrum of blazars. The present status of different EBL limits obtained so far from blazar observations is described below.

6.5.2 Fixed Power law spectrum

Early observations of blazars suggested that their GeV-TeV spectra can be approximated by a single power law ($F(E) \propto E^{-\Gamma}$), and any deviations of the observations from the extrapolated power law to higher energies should be attributed to EBL attenuation. An EBL upper limit of 10 nW m^{-2} sr^{-1} in the wavelength range 1-5 μm was derived from the observation of Mrk 421, assuming that the power law extrapolation of *EGRET* spectrum with an index of $\Gamma = 1.96 \pm 0.14$ holds upto the TeV regime with index $\Gamma = 2.25 \pm 0.19$ measured by the Whipple telescope [6.35]. Strong EBL limits in the near and mid-IR were derived by fitting the spectrum of

Mrk 501 in the energy range 0.2-24 TeV (from HEGRA collaboration), with a range of possible absorptions assuming intrinsic power law spectra and varying levels of EBL intensity by scaling the lower limits from galaxy counts [6.36]. Later on, it was demonstrated that the absence of deviations from a power law does not preclude the presence of substantial absorption in the observed spectra. The main drawback of this assumption is that a single power law for the intrinsic blazar spectra does not hold true over a wide range in energy.

6.5.3 Hardness of blazar spectrum

A more relaxed assumption on the intrinsic blazar spectrum is that it can not be flatter than one with $\Gamma = 1.5$ [6.37] and it can be easily produced with standard *Fermi* shock acceleration and cooling mechanisms. In the spirit of this limit to the spectral index, an upper limit of 5 nW m^{-2} sr^{-1} at 10 μm was derived from Mrk 501 observations with the assumptions that the intrinsic spectrum of the source is concave ($\Gamma > 2.0$) above 4 TeV [6.38]. A breakthrough was achieved in 2005 with the HESS observations of two blazars namely 1ES 1101-232 (z=0.186) and H 2356-309 (z=0.165) in the energy range 0.2-3 TeV [6.39]. The strict assumption of $\Gamma \geq 1.5$ was used to derive upper limit of 14 nW m^{-2} sr^{-1} on 1-5 μm EBL, which is very close to the lower limits determined from integrated lights of galaxies and even closer to the most recent near IR estimates [6.40]. A comprehensive study of blazars over a redshift range from 0.08 to 0.18 has also explored a large number of hypothetical scenarios to set upper limits on EBL, with the requirement that intrinsic source spectra cannot be harder than Γ =1.5 or 2/3 [6.41]. The theoretical validity of a strict hardness limit of $\Gamma > 1.5$ has been discussed with no unanimous conclusion [6.42, 6.43]. Observational evidence has provided lower limits from galaxy counts that are higher than the previous ones [6.44, 6.45] and if these new limits are correct, they imply intrinsic spctra that are slightly harder than $\Gamma = 1.5$ [6.46].

6.5.4 Extrapolation of *Fermi*-LAT spectrum to VHE band

Fermi-LAT provides measurement of the intrinsic γ–ray spectrum in an energy range 0.1–100 GeV not affected by EBL absorption, for sources in the local universe. The extrapolation of *Fermi* spectrum into the VHE band can be assumed either a good estimate or upper limit for the intrinsic VHE spectrum of the source [6.47,6.48,6.49]. The rationale is that if both the emissions belong to the same SED hump, the flux and spectrum at VHE should always be lower and steeper than at the *Fermi* energy range. From the blazar observations, this assumption is not well justified because transition between HE and VHE bands is the energy range where γ–ray emission peaks and hence the spectrum tends to change the most [6.50]. For any given EBL model, data show that a simple extrapolation over more than one decade is rarely correct. The limits derived with this approach are usually more stringent than the *spectral hardness* limits. Recently, the imprint of EBL on a sample of γ–ray blazars out to a redshift of z$\sim$1.6 has been used to measure the EBL flux density at optical and ultraviolet wavelengths [6.50]. The models with minimal EBL density based on resolved galaxy counts are found to be acceptable description of *Fermi* data whereas models with larger intensity of EBL are incompatible with the *Fermi* observations. It is concluded that most of the EBL intensity can be explained by the measured galaxy emission.

6.5.5 SSC/EC modelling of blazar SED

A more realistic though model dependent approach for indirectly constraining EBL intensity is the prediction of intrinsic VHE γ–ray spectrum by modelling the complete blazar SED with SSC or EC models. This approach was pioneered in relation to the additional timing information that simultaneous observations of the synchrotron and IC emission can provide during flares [6.51]. These models for the intrinsic blazar spectrum have been used to determine the intensity of EBL in the 1-5 μm and 20-28 μm wavelength region [6.52]. A multi-wavelength fit to the X-ray and TeV data of Mrk 501 yielded an absolute upper limit on the EBL of 60 nW m^{-2} sr^{-1} and a most likely value of 20 nW m^{-2} sr^{-1} at 1 μm. However, it has also been pointed out that the lack of an absorption signature in the spectrum of Mrk 501, does not necessarily imply a lack of EBL absorption and opacity could be nearly constant in the transition region from near-IR to mid-IR EBL.

The most recent constraints on EBL intenisty using different approaches are shown in Figure 6.4. The EBL spectrum from mid-UV to far-IR is in good agreement with estimates based on galaxy counts.

6.6 Intrinsic VHE spectra of Blazars as a Probe for EBL

VHE γ-rays above $10'$s of GeV energy, emitted from distant blazars, are attenuated by photons from the EBL. Unfortunately, neither the EBL nor the intrinsic blazar spectrum is accurately known to derive one quantity from the other. We use a homogeneous one zone model synchrotron, SSC and EC emission mechanisms to estimate the intrinsic VHE spectra of blazars. The model is applied on three VHE blazars, namely PKS 2155-304, RGB J0710+591 and 3C 279, for which simultaneous multi-wavelength data are available from various observations. The predicted values of the intrinsic VHE fluxes are then compared with the observations by imaging atmospheric Cherenkov telescopes to determine the optical depth of VHE γ-rays. Comparision of these optical depth values with those predicted by different EBL models is used to probe the EBL predicted by four prominent EBL models described in Section 6.4.

6.6.1 Blazar Spectrum using SSC/ EC Model

We model the intrinsic spectrum of blazars extending from radio to VHE energies as a result of synchrotron and inverse Compton processes. The emission is assumed to originate from a spherical blob of radius R moving down the jet at relativistic speed with bulk Lorentz factor Γ. Since blazar jets are aligned close to the line of sight of the observer, we assume the Doppler factor $\delta = [\Gamma(1 - \beta_\Gamma cos\theta)]^{-1} \approx \Gamma$. Here β_Γ is the jet velocity in units of velocity of light c and θ is the jet viewing angle. The emission region is populated uniformly with a broken power law electron distribution described by:

$$N(\gamma)d\gamma = K\left[\left(\frac{\gamma}{\gamma_b}\right)^{p1} + \left(\frac{\gamma}{\gamma_b}\right)^{p2}\right]^{-1} d\gamma \quad ;\gamma_{min} < \gamma < \gamma_{max} \tag{6.11}$$

where K is the normalisation, $\gamma_b m_e c^2$ is the break energy with m_e as the electron rest mass, $p1$ and $p2$ are the power law indices before and after the break energy $\gamma_b m_e c^2$ and $\gamma_{min} m_e c^2$ and $\gamma_{max} m_e c^2$ are the minimum and the maximum electron energy of the distribution. A broken power law particle distribution can be the result of various physical conditions. For example, radiative cooling of a simple power law particle distribution can produce a broken power law with indices related by $p_2 = p_1 + 1$. The break energy γ_b then decides the age of the emission region [6.54]. If the radiation is due to synchrotron and/or inverse Compton processes, the observed spectral indices will differ by canonical 0.5. However, if the observed spectral indices fail to satisfy this condition, the underlying broken power law distribution can be an outcome of complex situations probably involving more than one acceleration processes [6.55]. In the present work, the indices $p1$ and $p2$ are considered as free parameters resulting from any of the above mentioned mechanisms. The synchrotron spectrum is obtained due to cooling of this particle distribution in a tangled magnetic field B_{eq}. The magnetic field B_{eq} and the relativistic particle distribution is assumed to be in equipartition

$$U_B = m_e c^2 \int_{\gamma_{min}}^{\gamma_{max}} \gamma N(\gamma) d\gamma = U_e \tag{6.12}$$

where $U_B = B_{eq}^2/8\pi$ is the magnetic field energy density and U_e is the particle energy density. The synchrotron emissivity at a given frequency ν is calculated by convolving the electron spectrum $N(\gamma)$ with single particle emissivity $P(\nu_s,\gamma)$ averaged over an isotropic distribution of pitch angles and is given by [6.56],

$$j_s(\nu_s) = \frac{1}{4\pi} \int_{\gamma_{min}}^{\gamma_{max}} N(\gamma) P(\nu_s, \gamma) d\gamma \tag{6.13}$$

High energy emission is attributed to inverse Compton emission where soft target photons are scattered to high energy by the electron distribution given by $N(\gamma)$. The target photons can be either synchrotron photons (SSC) or the photons external to the jet (EC). The inverse Compton emissivity is given by [6.57],

$$j_{IC}(\varepsilon,\Omega) = m_e c^3 \varepsilon \int_0^{\infty} d\varepsilon' \oint d\Omega' \int_{\gamma_{min}}^{\gamma_{max}} d\gamma (1-\beta cos\psi) n_{ph}(\varepsilon',\Omega') N(\gamma) \sigma(\varepsilon,\varepsilon',\Omega') \quad (6.14)$$

where ψ is the angle between the incident photon and electron directions, $\sigma(\varepsilon,\, \varepsilon',\, \Omega')$ is the scattering cross section and $n_{ph}(\varepsilon',\, \Omega')$ is the target photon distribution in blob frame. For an isotropic target photon distribution, $n_{ph}(\varepsilon',\, \Omega')$ can be replaced by an angle averaged distribution. Since BL Lac objects lack line/thermal emission we consider only synchrotron and SSC process to describe their broadband SED. Whereas, for FSRQ EC process should also be taken into consideration since line and/or thermal features are significant in their SED. Moreover modelling their broadband SED also demands the need of EC process to explain the γ–ray spectrum [6.58]. Further, FSRQ which are observed with a hard VHE spectrum suggest that the scattering process must be in Thomson regime. This condition can be achieved if the soft target photons are the IR photons from the dusty torus proposed by the unification theory [6.59, 6.60]. For SSC emission, the target photon distribution will be isotropic whereas for EC spectrum estimation it is assumed to be anisotropic. Finally, the total flux received by the observer is obtained considering relativistic and cosmological effects for the case of no enroute absorption using the relation [6.61],

$$F_{tot}(\varepsilon) \approx \frac{\delta^3(1+z)}{d_L^2} V' j' \left(\frac{(1+z)}{\delta} \varepsilon \right) \quad (6.15)$$

where ε is the observed energy, d_L the luminosity distance, z the redshift of the source, V' the volume of the emission region and j' is the emissivity due to different radiative processes.

6.6.2 Application of the model to individual blazar

The main parameters describing the intrinsic broadband blazar SED are the particle indices $p1$ and $p2$, magnetic field B, particle normalisation K, break energy of the particle distribution $\gamma_b mc^2$, size of the emission region R and bulk Lorentz factor Γ. In case of FSRQ, we have additional parameters describing the external photon field. Among these $p1$ and $p2$ can be obtained through the observed photon spectral indices. Using observed synchrotron and SSC fluxes, synchrotron peak frequency, variability timescale and equipartition, rest of the parameters can be constrained. For EC process we assume the external photon field to be blackbody radiation at temperature T which can be constrained using observed EC flux. The source parameters are optimized by reproducing the observed broadband SED of blazars excluding the VHE data since intrinsic VHE spectra is dependent on the EBL density. We apply this procedure for three blazars described below to study the transparency of VHE photons.

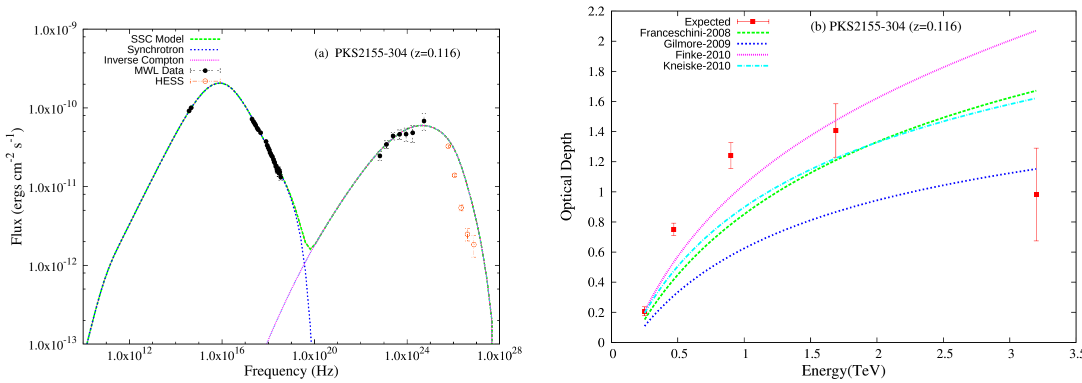

Figure 6.5: (a) Observed SED of PKS 2155-304 along with model curve. (b) Optical depth predicted through SED modeling and comapred with the one estimated for different EBL models.

- **PKS 2155–304 :** PKS 2155–304 is a high synchrotron peaked BL Lac object at redshift z=0.116. Dedicated multi-wavelength observations of this object including GeV and TeV observations with *Fermi*-LAT and $HESS$ are reported by Aharonian et al. (2009) [6.62]. We use this multi-wavelength data from optical to HE γ–rays to model the SED using synchrotron and SSC emission processes. The optimized parameters describing the SED of the source are given in Table 6.1. The resultant model curve along with multi-wavelength data including observed VHE fluxes by $HESS$ telescope is shown in Figure 6.5(a). The predicted intrisic VHE flux is more than the observed one and we account for this discrepancy as a result of absorption through pair production with EBL photons. From the ratio of these fluxes, we estimate the optical depth of this process and compare it with the one estimated through four EBL models discussed in Section 6.4.5. In Figure 6.5(b) we show the optical depth due to different EBL models and the one expected from broadband SED modeling.

- **RGB J0710+591 :** RGB J0710+591 is a high frequency peaked BL Lac (HBL) object at redshift z=0.125. This source was detected by $VERITAS$ telescope during the 2008-09 observation. Following this detection, an extensive multi-wavelength observation from optical to VHE γ–rays was initiated and the results were reported by Acciari et al. (2010) [6.63]. We use this multi-wavelength data from optical to HE γ–rays to model the SED of the source using synchrotron and SSC emission processes. The optimized source parameters are given in the Table 6.1. The observed SED of the source including VHE observations by VERITAS is shown in Figure 6.6(a) along with model curves. The optical depth estimated from the ratio of observed and intrinsic VHE fluxes is plotted in Figure 6.6(b) along with the one estimated for different EBL models. The large errors in optical depth values, especially at high energies, are due to the uncertainties in the observed VHE spectra.

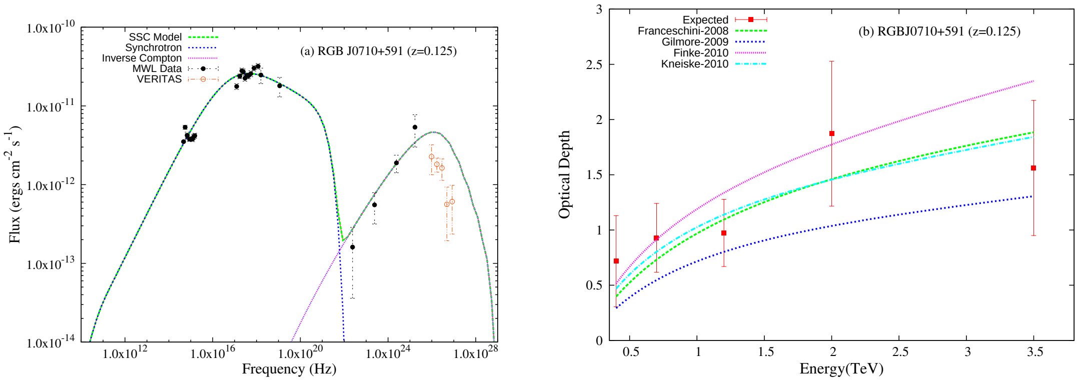

Figure 6.6: (a) Observed SED of RGB J0710+591 along with model curve. (b) Optical depth estimated from SED modeling and different EBL models.

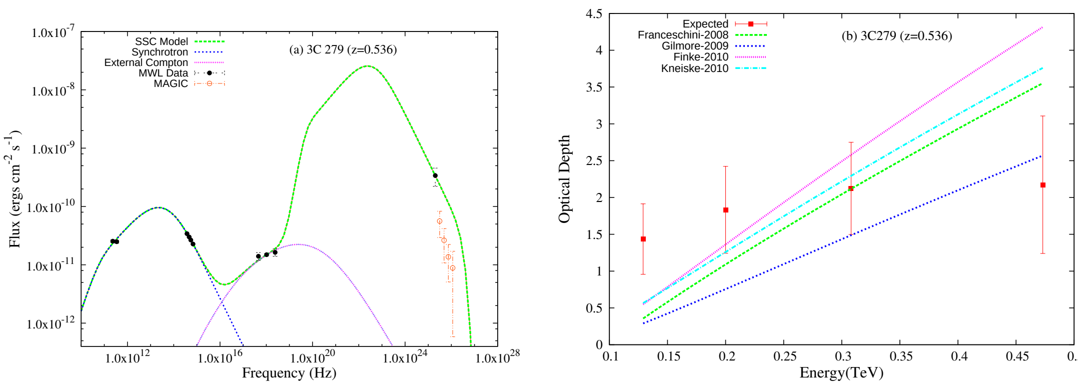

Figure 6.7: (a) Observed SED of 3C 279 along with model curve. (b) Optical depth estimated from SED modeling and different EBL models.

- **3C 279 :** 3C 279 is an FSRQ at a redshift of 0.536 and the farthest blazar detected in VHE till now. Hence, its intrinsic VHE γ–ray spectrum is modified considerably by EBL absorption. We use simultaneous observations from optical to VHE γ–rays during a γ–ray flare in 2006 to obtain the broadband SED of the source reported by Albert et al. (2008) [6.64]. Being an FSRQ, the SED of 3C 279 is reproduced by considering synchrotron, SSC and EC processes. Due to lack of simultaneous observations at MeV, we include VHE flux at 84 GeV in multi-wavelength data to obtain the optimized set of parameters governing the broadband spectrum. The source parameters are given in the Table 6.1 and the model spectrum of the source along with the multi-wavelength data upto VHE is given in Figure 6.7(a). The optical depth estimated from the ratio of observed and intrinsic VHE fluxes and for different EBL models is plotted in Figure 6.7(b).

6.6.3 Discussion

For all three blazars, a trend of deviation between the optical depth estimated through SED modeling from the one obtained from EBL models is observed. For two BL Lacs PKS 2155–304 and RGB J0710+591, which are closer compared to the FSRQ 3C 279, we have VHE information upto ∼3 TeV. For these two sources the difference between optical depths increases with the increase in energy, though for RGB J0710+591 we have large uncertainties. Moreover the largest deviation at 3.2 TeV in case of PKS 2155–304 and 3.5 TeV in case of RGB J0710+591 is obtained when the EBL model by Finke et al. (2010) is used. A closer examination suggests that at low energies the estimated optical depth is larger whereas the trend reverses as one moves to higher energies with maximum deviation at ∼3 TeV. Since these two sources are located at almost similar redshift, the evolutionary effects of EBL will not be prominent between them. Hence two possible interpretations can be made to understand this deviation. In the first case, if we assume the optical depth predicted by SED modeling to be the correct description of EBL intensity, then the EBL models under predict the EBL intensity at higher IR frequencies (corresponding to lower VHE photon energies) giving rise to less optical depth at lower VHE band. Whereas at higher VHE regime, the EBL models over predict the low energy EBL spectrum in IR band giving rise to large optical depth. In that case, the assumption made in estimation of IR component in these EBL models through absorption and re-emission of radiation and cosmological initial conditions may give rise to such discrepancies. On the other hand, if we assume that the optical depths predicted by these EBL models are correct, then the extrapolation of blazar SED using simple emission models may be erroneous. It means at VHE, the spectrum may not follow the simple power law expected from lower energies. Such a case is possible if the particle distribution hardens at high energies. A possible explanation of this feature can be due to the Maxwellian tail often encountered at high energies of an accelerated particle distribution where the escape time scale is longer than the cooling or acceleration time scales [6.65]. Presence of such features can be probed only by VHE observations describing the Compton tail of SED. The synchrotron regime of SED will not reflect this feature because the high energy tail of the same is often buried inside the Compton regime. Alternatively, understanding such features demand precise knowledge of EBL spectrum to obtain the intrinsic VHE spectra.

For 3C 279, we have information only upto 475 GeV. Being the farthest source, the evolution of EBL may be prominent and hence the deviation of optical depths will reflect the evolutionary history of the universe also. As expected the deviations are larger even at relatively lower VHE since the uncertainties regarding the evolution of EBL will also be folded into the uncertainties arising from the EBL spectrum and SED emission model. Even for this source we find a trend similar to BL Lacs that the estimated optical depth obtained using SED modeling is larger than the one predicted by EBL models at low VHE regime and the trend reverses as we move to high energies. Hence the two interpretations suggested earlier for BL Lacs will be applicable to this source also. However in this case, the evolutionary history of EBL may also be a prominent factor causing the deviation in optical depths. It is also to be noted that we have used multi-wavelength data available in the literature to reproduce the SED and to predict the VHE γ–ray emission from three sources. The data for these sources are not strictly contemporaneous. As we know that blazars are highly variable sources at all wavelengths, only simultaneous multi-wavelength observations would give the realistic SED and this would be another possible reason for the discrepancies observed in the optical depth values at different redshifts.

Recently, Abramowski et al. (2013) investigated the EBL absorption feature in the VHE spectra of $HESS$ detected blazars using maximum likelihood method [6.66]. They have assumed a smooth γ-ray spectra and estimated the EBL intensity through intrinsic spectral curvature. They used EBL shape proposed by Franceschini et al. (2008) and obtained the normalisation through fitting procedure. Yuan et al. (2012) have also used a Monte Carlo fitting procedure to obtain the model independent EBL intensities and intrinsic parameters of blazars [6.67]. Due to large uncertainties in their predicted EBL intensity, the derived optical depth will not differ considerably from the one obtained in the present work.

6.6.4 Limitations of the method

The SSC/EC process is a popular model for explaining the broad band SED of blazars with two peaks: the synchrotron peak at radio-UV-X-ray frequencies and IC peak at γ–ray energies. The spectrum of IC peak is modeled using parameters that produce the synchrotron peak and the unabsorbed part (HE $<$ 10 GeV) of the IC spectrum. Uncertainties in the parameters that determine the IC spectrum are the main drawbacks of using γ–ray emission models to constrain the EBL intensity. Furthermore, while SED of BL Lacs can be fitted well by SSC models, FSRQs require the inclusion of additional ambient radiation fields that make a contribution to γ–ray IC component. Additional complications arise from the fact that basic single zone models are not applicable for blazars exhibiting *orphan flares*, where only the VHE flux is enhanced while synchrotron emission remains unchanged. Finally, the biggest challenge for SSC/EC approach for constraining the EBL is to get simultaneous multi-wavelength observations of a large set of blazars at different redshifts.

6.7 Summary

A simple emission model considering synchrotron and inverse Compton emission mechanisms is used to reproduce the SED of blazars for which simultaneous multi-wavelength observations are available. The model is applied on three well studied VHE blazars at various redshifts. The model is then used to predict the intrinsic VHE spectra of these blazars. The source parameters are constrained using multi-wavelength data and are in close agreement with the values generally considered for blazars. The predicted intrinsic VHE flux by this model is used to estimate the optical depth for VHE γ–rays from the observed flux due to EBL absorption.

Table 6.1: Optimized source parameters from multi wavelength data and blazar modeling.

Sources	Parameters								
	z	R	Γ	γ_b	U_e	p_1	p_2	B	T
PKS2155-304	0.116	0.79	26.7	1.83×10^4	2.62	1.82	4.16	0.30	-
RGBJ0710+591	0.125	0.45	26.0	7.83×10^4	1.31	1.89	3.33	0.17	-
3C279	0.536	2.17	25.4	1.22×10^3	10.90	2.05	4.63	0.45	850

Notes– Col. 1: Source Name; Col. 2: Source Redshift;
Col. 3: Size of emission region (in units of 10^{-2}pc);
Col. 4: Bulk Lorentz factor; Col. 5: Break energy of particle distribution (in units of electron rest mass energy mc^2); Col. 6: Particle energy density (in units of 10^{-3}ergs cm^{-3}); Col. 7&8: Power law indices of particle distribution before and after the break respectively; Col. 9: Magnetic field (in units of Gauss); Col.10: Temperature of black body radiation in (K) for EC process.

We then compare this with optical depth obtained using four commonly used EBL models in VHE regime.

The deviation of optical depths is seen more at higher VHE regime with the optical depth predicted by SED modeling being lower. However the trend reverses at lower VHE regime though the deviation is not large as compared to the high energy end. We interpret this behaviour as an outcome of two possible scenarios. In the first case, the discrepancy may be due to under prediction of EBL intensity at higher IR frequencies and over prediction at lower IR frequencies by various EBL models. Alternatively, the deviation may also imply the failure of extrapolating the SED of blazars to VHE regime using simple emission models. In such case, the intrinsic VHE spectrum must be hard suggesting an excess in the high energy tail of the underlying particles distribution. With the poor statistics involving only three sources, we are not able to identify the more probable interpretation out of these two scenarios. However, we can forsee that identifying the correct EBL spectrum will be a potential tool to understand the intrinsic VHE spectrum of blazars which in turn explain the underlying particle acceleration mechanism. This can also be used to test different cosmological models enabling us to understand the Universe better. At the present epoch we are witnessing the rising number of VHE blazars due to various operational atmospheric Cherenkov telescopes, like *MAGIC*, *VERITAS* and *HESS* and this can constrain the EBL spectrum substantially.

6.8 References

[6.1] M. G. Hauser & E. Dwek, 2001, Annu. Rev. Astron. Astrophys., 39, 249

[6.2] J. Tumlinson et al., 2003, ApJ, 584, 608

[6.3] M. R. Santos et al., 2002, MNRAS, 336, 1082

[6.4] A. Kashlinsky et al., 2004, ApJ, 608, 1

[6.5] A. Cooray et al., 2004, ApJ, 606, 611

[6.6] A. Burrows & J. Liebert, 1993, Rev. Mod. Phys., 65, 301

[6.7] J. R. Bond et al., 1986, ApJ, 306, 428

[6.8] D. W. Sciama, 1998, A&A, 335, 12

[6.9] S. Razzaque et al., 2009, ApJ, 697, 483

[6.10] M. A. Malkan & F. W. Stecker, 1998, ApJ, 496, 13

[6.11] I. Matute et al., 2006, A&A, 451, 443

[6.12] M. Raue & M. Meyer, 2012, MNRAS, 426, 1097

[6.13] R. Barkana & A. Loeb, 2001, Phys. Rep., 349, 125

[6.14] M. Raue et al., 2009, A&A, 498, 25

[6.15] G. Neugebauer et al., 1984, ApJL, 278, 1

[6.16] M. G. Hauser et al., 1998, ApJ, 508, 25

[6.17] J. C. Mather et al., 1999, ApJ, 512, 511

[6.18] M. Noda et al., 1994, ApJ, 428, 363

[6.19] R. Thompson et al., 2007, ApJ, 657, 669

[6.20] H. Dole et al., 2004, ApJS, 154, 93

[6.21] H. Dole et al., 2006, A&A, 451, 417

[6.22] A. S. Shectman, 1973, ApJ, 179, 681

[6.23] A. S. Shectman, 1974, ApJ, 188, 233

[6.24] A. Penin et al., 2012, A&A, 543, 123

[6.25] E. Dwek & F. Krennrich, 2005, ApJ, 618, 657

[6.26] E. Dwek & F. Krennrich, 2013, Astropart. Phys., 43, 112

[6.27] A. Franceschini et al., 2008, A&A, 487, 837

[6.28] R. C. Gilmore et al., 2009, MNRAS, 399, 1694

[6.29] J. D. Finke et al., 2010, ApJ, 712, 238

[6.30] P. P. Eggleton, 1989, ApJ, 347, 998

[6.31] T. M. Kneiske & H. Dole, 2010, A&A, 515, 19

[6.32] O. Blanch & M. Martinez, 2005, Astropart. Phys., 23, 588

[6.33] R. J. Gould et al., 1967, Phys. Rev., 155, 1408

[6.34] G. Breit & J. A. Wheeler, 1934, Phys. Rev., 46, 1087

[6.35] F. W. Stecker & O. C. Jager, 1993, ApJL, 415, 71

[6.36] T. Stanev & A. Franceschini, 1998, ApJL, 494, 159

[6.37] M. A. Malkov & L. O. Drury, 2001, Rep. Prog. Phys., 64, 429

[6.38] C. Renault et al., 2004, A&A, 371, 771

[6.39] F. Aharonian et al., 2006, Nature, 440, 1018

[6.40] R. C. Keenan et al., 2010, ApJ, 723, 40

[6.41] D. Mazin & M. Raue, 2007, A&A, 471, 439

[6.42] F. W. Stecker et al., 2007, ApJL, 667, 29

[6.43] O. Zacharopoulou et al., 2011, ApJ, 738, 157

[6.44] L. R. Levenson & E. L. Wright, 2008, ApJ, 683, 585

[6.45] P. Madau & L. Pozzetti, 2000, MNRAS, 312, L9

[6.46] F. Krennrich et al., 2008, ApJL, 689, 93

[6.47] M. R. Orr et al., 2011, ApJ, 733, 77

[6.48] M. Georganopoulos et al., 2010, ApJL, 714, 157

[6.49] D. A. Sanchez et al., 2013, A&A, 554, 75

[6.50] M. Ackermann et al., 2012, Science, 338, 1190

[6.51] P. S. Coppi & F. A. Aharonian, 1999, Astropart. Phys., 11, 35

[6.52] J. Guy et al., 2000, A&A, 359, 419

[6.53] J. Biteau & D. A. Williams, 2015, arXiv:1502.04166

[6.54] S. Sahayanathan et al., 2003, ApJL, 588, 77

[6.55] S. Sahayanathan et al., MNRAS, ApJL, 388, L49

[6.56] G. B. Rybicki & A. P. Lightman, 1986, *Radiative Processes in Astrophysics*

[6.57] C. D. Dermer & R. Schlickeiser, 1993, ApJ, 416, 484

[6.58] R. C. Hartman et al., 2001, ApJ, 553, 683

[6.59] G. Ghisellini & F. Tavecchio, 2009, MNRAS, 397, 985

[6.60] S. Sahayanathan & S. Godambe, 2012, MNRAS, 419, 1660

[6.61] M. C. Begelman et al., 1984, Rev. Mod. Phys., 56, 255

[6.62] F. A. Aharonian et al., 2009, ApJL, 696, 150

[6.63] V. A. Acciari et al., 2010, ApJL, 715, 49

[6.64] J. Albert et al., 2008, Science, 320, 1752

[6.65] L. Starwaz & M. Ostrowski, 2002, ApJ, 578, 763

[6.66] HESS Collaboration and A. Abramowski et al., 2013, A&A, 550, A4

[6.67] Q. Yuan et al., 2012, arXiv:1212.5866

Chapter 7

Conclusions and Future Outlook

7.1 General Conclusions

VHE γ–ray astronomy using ground based IACTs has opened up a new window to the sky. The field began effectively in 1989 with the robust detection of the Crab Nebula in TeV γ–rays using 10 m IACT at the *Whipple* observatory. VHE γ–ray observation activity has grown rapidly to become one of the most productive subfields of astrophysics today with many discoveries by experiments like *HESS*, *MAGIC* and *VERITAS*. The remarkable achievements of observational γ–ray astronomy over the last two decades and recent theoretical and phenomenological studies of acceleration and radiative processes in astrophysical environments, fully justify further exploration of the sky in the VHE regime. Although, the main scientific motivations of γ–ray astronomy remain unchanged, the recent observational results have revealed new features which in many cases require revision of existing theoretical models and formulation of new concepts. It is expected that the ongoing operation of *Fermi*-LAT will be complemented by observations with the current IACTs like *MAGIC-I & II*, *VERITAS*, *HESS-II*, *TACTIC* and planned future experiments such as *CTA* (Cherenkov Telescope Array) and *MACE* (Major Atmospheric Cherenkov Experiment) telescope. The observations in the enormous energy range from 10^8 eV to 10^{15} eV will provide very deep insight into a number of problems of high energy astrophysics and fundamental physics.

The research work carried out in the present thesis deals with the VHE observations of two blazars Mrk 421 and 1ES 1218+304 with *TACTIC* gamma-ray telescope and other multi-wavelength observations using different instruments world wide. The thesis also involves application of blazar observations for probing the extragalactic background light, which is a very important cosmological quantity to understand the star and galaxy formation in the universe. The important findings of the thesis are highlighted below.

- The results reported on Mrk 421 have been obtained from multi-wavelength campaign of flaring activity observed in February 2010. The source was observed in its high activity state on February 16, 2010 with *TACTIC* at energies above 1.5 TeV. Near simultaneous multi-wavelength data collected during

February 10–23, 2010 are obtained from HE γ–ray observations with *Fermi*–LAT, X–ray observations by the *Swift* and *MAXI* satellites, optical V-band observation by SPOL at *Steward Observatory* and radio 15 GHz observation at OVRO 40 m telescope. The flaring activity of the source has been studied by investigating the properties of daily light curves from radio to TeV energy range along with the correlation and variability analysis in each energy band. The TeV flare detected by *TACTIC* on February 16, 2010 is observed to be well correlated with the activity in lower energy bands. Finally the broad band spectral energy distribution of the source in flaring state is reproduced using a simple emission model involving synchrotron and synchrotron self Compton processes. The spectral index - flux correlation in the 1-10 keV energy band with a hysteresis loop in clockwise sense indicates: (i) a soft lag during the spectral evolution and (ii) a cooling dominated electron spectrum present in the emission region. Although Mrk 421 is characterized by a dense duty cycle, even if it could be due to an observational bias related to the brightness of the source, proper understanding of the physical mechanism involved in the flare, requires good quality data.

- The second accomplishment of the thesis is the VHE observation of 1ES 1218+304 with *TACTIC* during March-April 2013 and other multi-wavelength observations by *Fermi*-LAT, *Swift*-XRT/UVOT and OVRO 40 m radio telescope. The blazar 1ES 1218+304 has been observed in the TeV energy range with the *TACTIC* from March 1, 2013 to April 15, 2013 and no evidence of TeV γ–ray activity was found from the source. The corresponding 99% confidence level upper limit on the integral flux above a threshold energy of 1.1 TeV is estimated to be 3.41×10^{-12} photons cm^{-2} s^{-1} (i.e < 23% Crab Nebula flux) assuming a power law differential energy spectrum with photon index 3.0, as previously observed by the $MAGIC$ and $VERITAS$ telescopes. For the study of multi-wavelength emission from the source, nearly simultaneous radio, optical, UV, X–ray and high energy γ–ray data have also been used. No significant increase of activity is detected from radio to TeV γ–rays from 1ES 1218+304 during the period from March 1, 2013 to April 15, 2013. It is important to point out here that, because of the variable nature of blazars in general, the VHE emission from 1ES 1218+304 may increase significantly during future flaring episodes and may even easily exceed the limit reported in the present work. Hence, the upper limit presented here only constrains the flux during the present observation period with the *TACTIC*. A long term monitoring with the ground based IACTs is essential in order to understand the variability of the source in VHE regime.

- An important finding of this thesis is the use of blazar observations as probe for extragalactic background light. We have used a homogeneous single zone model involving synchrotron, synchrotron self Compton (SSC) and external Compton (EC) emission mechanisms to estimate the intrinsic VHE spectra of blazars. The model is applied on three blazars, namely PKS 2155-304, RGB J0710+591 and 3C 279, for which simultaneous multi-wavelength data are available from various observations. The predicted values of the intrinsic VHE fluxes are then compared with the observations by ground based imaging γ–ray telescopes to determine the optical depth of VHE γ-rays. On comparing these optical depth values with those predicted by four different models for the intensity of extragalactic background light, a somewhat pronounced systematic deviation for PKS 2155-304 and 3C 279 at higher energies is observed, especially for the model proposed by Finke et al.(2010) [7.1]. This deviation is interpreted as an outcome of either the failure of the extrapolation of blazar spectrum to VHE energies and/or due to various assumptions buried in the extragalactic background light models. With the poor statistics involving only three sources, it is not possible to identify the more probable interpretation out of these two scenarios. However, it is observed that identifying the correct model for extraglactic background light will be a potential tool to understand the intrinsic VHE spectrum of blazars which in turn explain the underlying particle acceleration mechanism.

7.2 Unanswered Scientific Questions

The field of gamma-ray astronomy has become a very vibrant field with resolved source morphologies, well sampled light curves and energy spectra using large number of space and ground based observational facilities. Although significant progress in the understanding of particle acceleration in the universe and in the study of the origin of cosmic rays has been achieved in the past years, yet the field still has lots of open questions to be answered.

- After more than 100 years of research, most of the main issues related to cosmic rays like source identification, acceleration mechanism, propagation and composition are still open questions. The solution of these puzzles needs extensive studies involving astronomy, cosmology, nuclear physics and elementary particle physics together.

- The young supernova remnants, also known as *PeVatrons*, that can accelerate particles upto PeV energies and contribute to the high energy cosmic rays, have so far gone undetected.

- Among the 3033 sources in the third *Fermi* catalog, 2038 have associations or identifications with known astrophysical objects [7.2]. Although that number is greater than the total number of sources in the second catalog, 992 of the third catalog sources remain unidentified.

- At present, the observed VHE γ–rays could be understood by either leptonic or hadronic scenarios. However, it is hoped that as quality of data improves, observations may begin to unveil characteristics of γ–ray emission mechanisms in the universe. In addition, independent of the theoretical scenario, VHE observations would be capable of constraining the intrinsic spectra of emitting particles and thus casting light on the nature of particles and on acceleraion mechanisms.

- The extreme variability down to minute scale observed in VHE emission from blazars remains poorly understood till now. Measurement of blazar spectra on short time scales will provide a crucial tool for understanding the blazar physics and emission models.

- The formation of jets and its connection to the central black hole in the active galaxies and blazars in particular is one of the most important and basic problems in high energy astrophysics.

- Some recent observations of hard VHE spectra of distant sources are difficult to understand with conventional physics combined with the state of art extra-galactic background light models. Also, exact number density of extragalactic background light photons remains unknown today, as direct observations are difficult due to foreground emission.

- Recent discovery of VHE γ–ray emission from blazar PKS 1441+25 located at redshift z=0.939 [7.3,7.4] indicates that the universe is more transparent than previously thought. An alternative hypothesis, known as *Photon-ALP Oscillation* for transparency of universe needs to be properly understood in the framework of astrophysical observations [7.5,7.6].

- The problem of origin and strength of the intergalactic magnetic field is one of the long standing problems in astrophysics and cosmology [7.7,7.8]. Extremely weak and unamplified intergalactic magnetic fields have escaped detection upto now, however it is expected that the current and future generation γ–ray telescopes have a potential for detection of weak magnetic fields in the intergalactic medium.

- The peculiar high energy emission spectrum of the so-called *extremely high synchrotron peaked blazars* (EHSPs or EHBLs), characterized by very low magnetic field ($\sim 10^{-2}$-10^{-3} G) and hard spectral index (< 2) [7.9], challenges the standard emission models of blazars. Therefore, a unification scheme for blazar emission requires more source statistics in VHE regime with next generation telescopes.

- A major open question in modern cosmology is the nature of dark matter. If signatures of dark matter would appear in direct detection experiments, γ–ray observations may provide complementary information to identify its properties and mass [7.10]. In addition, the effects of quantum gravity [7.11] and other violations of Lorentz invariance related to fundamental physics are open issues in high energy astrophysics.

7.3 Upgraded TACTIC Telescope

In 2011, *TACTIC* underwent a major upgrade program to improve the over all performance of the telescope [7.12]. The main motivation for the upgrade of the *TACTIC* system is to increase its sensitivity and lower the threshold energy. Also, with a lower noise system the analysis energy threshold can be lowered, and the performance close to the threshold can be improved. The important steps taken to upgrade the sub-systems of *TACTIC* are described below.

7.3.1 Hardware

Most importantly, new compound parabolic concentrators (CPCs) were installed in the camera. New CPCs with square entry and circular exit in the telescope camera help to increase the photon collection efficiency. The reflectivity of new CPCs was measured to be $\sim 85\%$ in the wavelength range 400–550 nm. Apart from removing the dead space in between the photo-multiplier tubes, the use of new CPCs has also helped to improve the gamma/hadron segregation capability of the telescope. The signal and high voltage cables of the system readout were replaced. In addition, the trigger criteria were modified by including more nearest–neighbour collinear triplet combinations. A dedicated CCD camera was installed for conducting detailed point run calibrations and data collected had been successfully used for determining the position of the source in the image plane with an accuracy of better than ± 3 arc-min.

7.3.2 Data Analysis and γ/hadron separation

The data analysis procedure has been modified by incorporating the *ASYMMETRY* parameter so that the *head* and *tail* feature of Cherenkov images can be identified to further remove the hadronic background. The *ASYMMETRY* parameter is a measure of the skewness of Cherenkov light distribution relative to image centeroid and represents the third-order moment of the image along the major axis. The preliminary analysis of Crab observations during December 23-29, 2011 with the *TACTIC* after the hardware and software upgrade, yields an increase in the prompt coincidence rate at zenith angle of $0°$ from 2.4 Hz to $\sim$ 4.5 Hz. This translates to the reduction in the threshold energy of the telescope for cosmic rays from $\sim$ 1.8 TeV to $\sim$ 1.4 TeV and from $\sim$ 1.2 TeV to $\sim$ 0.8 TeV for the γ–rays. Simulation studies using *CORSIKA* (ver 6.971) also confirm these estimates. With the new cut values of image parameters derived from simulation, the sensitivity of upgraded *TACTIC* has improved from $N_\sigma \sim 1.0\sqrt{T}$ to $N_\sigma \sim 1.5\sqrt{T}$ (where T is the effective observation time). The γ–ray detection rate from the Crab Nebula has also increased from $\sim$ 9.2 h^{-1} to $\sim$ 15 h^{-1}. The upgraded telescope is now able to detect the TeV γ–ray emission from the Crab Nebula at 5σ significance level in an observation time of 12 h as compared to 25 h earlier.

The gamma/hadron separation using the potential of artificial neural network techniques [7.13] and random forest classification [7.14] further enhances the performance of the telescope after upgrade. The main advantage of artificial neural network methodology is that it is more effective at higher energies and this has led to determine the Crab Nebula energy spectrum in the energy range 1–24 TeV. Thus, the *TACTIC* telescope with significant improvement in its performance would help in the montoring of potential γ–ray sources in multi-TeV energy range during flaring activities for a short time and in quiescent state for a long time in future..

7.4 Future Outlook

Given the science goals (as described in Section 7.2) of gamma–ray astronomy, the primary objectives of the future experiments are to improve the point source sensitivity of the instrument in the energy range 100 GeV–50 TeV by more than one order of magnitude. In determining the optimum design of next generation experiments, it is necessary to start with the scientific drivers of the technique and to acknowledge that all the objectives of VHE γ–ray astronomy may not be achieved with a single instrument. Therefore, the new generation experiments suggest a dual approach for the future (i) development of high sensitivity IACTs in the energy range above 100 GeV where potential scientific return is well understood and (ii) development of an extensive air shower array with similar sensitivity and 100 to 1000 times larger effective area at 100 GeV than *Fermi*-LAT. While many γ–ray features identified by *Fermi* are intriguing, they also emphasize the need for improved energy resolution, position resolution and background rejection upto TeV energies and beyond. Some of the future γ–ray experiments coming over the course of next decade and longer are briefly outlined below.

7.4.1 Major Atmospheric Cherenkov Experiment

As a new Indian initiative for contributing significantly in the field of VHE gamma-ray astronomy, a 21 m diameter Major Atmospheric Cherenkov Experiment (MACE) telescope, is being set up at Hanle (32.8° N, 78.9° E, 4200 m asl) in the Ladakh region of North India under Himalayan Gamma Ray Observatory (HiGRO) collaboration. The *MACE* telescope as shown in Figure 7.1, is expected to see first light at Hanle by the middle of 2016. It is the second largest instrument after *HESS-II* (28 m diameter) in the world at the highest altitude. The Hanle site would offer an average of about 260 clear nights per year, providing a major advantage in terms of the sky coverage for γ–ray source observations.

The *MACE* telescope based on *alt-azm* mount will deploy a parabolic light collector of 25 m focal length and 21 m diameter. The light collector of the telescope comprises 356 panels each of $\sim$1 m$\times$1 m size. Each panel in the light collector consists of 4 diamond turned spherical metallic honeycomb mirror facets of ~ 0.5 m$\times$0.5 m size with uniform reflectivity more than 85% each. The mirror facets are aligned and fixed on the panels in such a way that each panel functions as a single spherical mirror. The radius of curvature of the mirror panels varies from $\sim$ 25 m to $\sim$ 26.5 m from the centre of light collector to its periphery respectively. The variation in the focal length of mirrors would help in minimizing the on-axis spot size of the light

Figure 7.1: Present status of the *MACE* telescope with its mechanical structure assembled and tested at ECIL Hyderabad, India.

collector. Each individual mirror panel will be mounted on the space frame using a 3–point support mechanism which has linear actuators with single and double ball joints coupled to it. The space frame is held by a structure with 6 wheels of 60 cm diameter which move on a 10 cm wide flat track of 27 m diameter. Out of 6 wheels, 4 wheels have elaborate gear mechanisms and drive systems coupled to them while 2 wheels function as idlers. The mechanical structure is designed to ensure enough load on the drive wheels to prevent slippage. The drive system is designed with an option of quick pointing in any direction in the sky within a maximum duration of 60 seconds. The drive system is capable of achieving pointing and tracking accuracy of better than 1 arc–min at wind speeds up to 30 km/h.

The imaging camera at the focal plane of the telescope will use 1088 photomultipliers arranged in a square matrix, covering a field of view of $4^\circ \times 4^\circ$ with a pixel resolution of 0.125°. The inner pixels within the field of view of $2.4^\circ \times 2.4^\circ$ will be used for trigger generation. The 38 mm diameter photomultiplier tubes (ETE make 9117 WSB) will be provided with hexagonal front aluminized plastic light concentrators for enhancing their light collection efficiency. The camera is designed in a modular manner with 68 modules of 16 channels each. Each individual 16 channel module has its signal processing electronics, first level trigger generation logic and signal digitization circuitry built into it. In order to ensure a wide dynamic range each photomultiplier signal is simultaneously amplified by a low gain and high gain factor. Detailed simulation studies carried out using *CORSIKA* (ver 6.971) package suggest that the gamma–ray threshold energy for the *MACE* telescope is $\sim$ 25

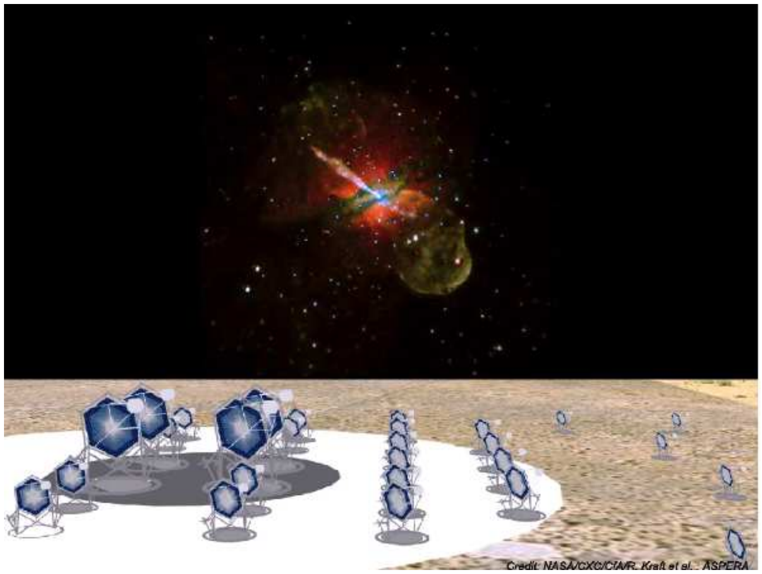

Figure 7.2: Artistic view of the *CTA* observatory.

GeV for a Nearest Neighbour Quadruplet trigger with single pixel threshold of 8 photo-electrons. Thus, the *MACE* telescope is expected to explore the γ–ray sky in the energy range 25 GeV–10 TeV, providing an excellent energy overlap with *Fermi*-LAT.

7.4.2 Cherenkov Telescope Array

The Cherenkov Telescope Array (CTA)[1] is a future observatory in the enterprise of VHE γ–ray astronomy consisting of one site per hemisphere granting full sky coverage [7.15]. The CTA site in southern hemisphere will focus on galactic and extragalactic sources and that in northern hemisphere will aim only at extragalactic studies. The planned operation and design concept of *CTA* as an open observatory is shown in Figure 7.2. With a large collaborative effort, *CTA* aims at the design of Cherenkov telescope array in the energy range 30 GeV-100 TeV, which will improve the sensitivity by about one order of magnitude with respect to the present generation major telescopes like *MAGIC, VERITAS & HESS*. At TeV energies, *CTA* will provide an increased sensitivity (mCrab fluxes with 5σ in 50 h), better angular resolution ($\sim$ 2 arc-min), superior energy resolution ($<$ 10%) and a wider field of view (6° to 8°) [7.16].

To fully explore the γ–ray sky in VHE regime, both *CTA* sites will deploy telescopes of multiple designs with different size as depicted in Figure 7.3. It is planned to have a large array in the southern hemisphere and a smaller array in the north. At the center of the array, there will be four units of 23 m diameter Large Size Telescopes (LSTs) with 100 m separation. The light collector diameter of LSTs ($\sim$

[1] http://www.cta-observatory.org/

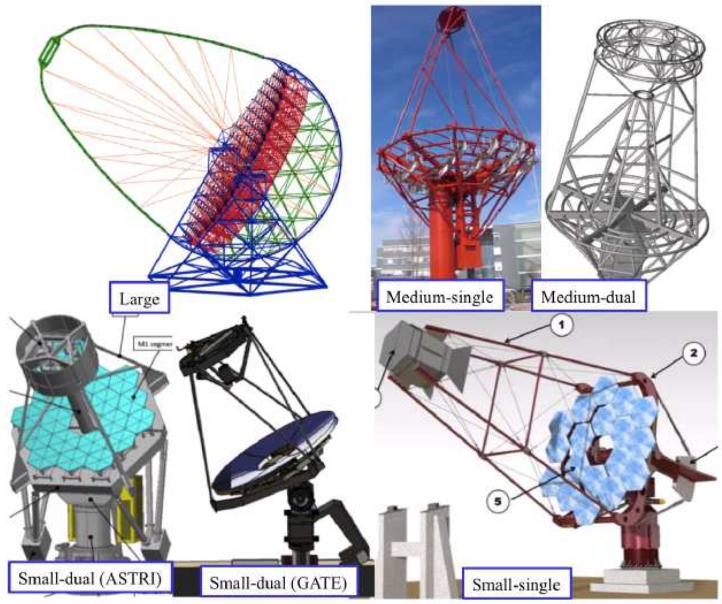

Figure 7.3: Design concept of different telescopes in development for CTA. (Figure adopted from [7.17]).

23 m) is optimized for $\sim$ 20–200 GeV and their design is based upon the *MAGIC* design with reduced weight through the application of new technologies and materials. The camera will consist of 2000 photomultiplier tubes. Medium Size Telescopes (MSTs) with 12 m diameter will provide deepest coverage of the mid-range of energies, centered around 1 TeV. A larger number (about 25 units) of MSTs separated by 150 m will cover larger area in the array. Two designs are envisaged for MSTs (i) single reflector Davies–Cotton design similar to *VERITAS* and (ii) dual mirror design using Schwarzschild-Couder optical system with a 9.5 m primary reflector. The high energy range of array, upto 100 TeV, will be covered by Small Size Telescopes (SSTs) with an aperture of 4 m. These telescopes will be the most numerous and most widely spaced in the array.

Above a few TeV, the Cherenkov light intensity is such that showers can be detected even well outside the light pool by telescopes significantly smaller than the MSTs. To achieve the required sensitivity at high energies, a huge area on the ground needs to be covered by SSTs with a field of view of about 10° and an angular resolution of about 0.2°, making the dual-mirror configuration very effective. The SSTs sub-array will be composed of 50–70 telescopes with a mirror area of about 5–10 m^2 and about 300 m spacing, distributed across an area of about 10 km^2. It is believed that *CTA* could offer one of the most powerful tools in the study of some of the most pressing questions in modern physics. In the next few years it may lead to a range of new observables, new methods and new theories. While the low end of the *CTA* energy coverage will close the current gap with the *Fermi*-LAT, its high energy coverage will open a new window in the γ–ray sky.

7.4.3 Space Telescopes

The launch of *Fermi* satellite has started an exciting period in the field of gamma–ray astronomy by outperforming expectations. The nominal all sky survey mode of *Fermi*–LAT is ideally suited to explore essentially all potential targets in the γ–ray sky. Although, the results obtained from the *Fermi* over the last six years of operation along with other γ–ray space telescopes in the past, are sufficiently intriguing, they have led to a wealth of information and also brought out the need for instruments with highly improved performance in the future.

Over the next decade and beyond, the *CALET* and *DAMPE* missions by NASA are expected to begin observations in the γ–ray sky. The CALorimetric Electron Telescope (*CALET*)[2] is a Japan–led project and it also involves Italian and American institutes. The instrument is expected to be launched in 2015 and will be installed on Japanese Experiment Module (JEM) on board the International Space Station (ISS). The DArk Matter Particle Explorer (*DAMPE*)[3] is one of the five satellite missions selected by the Chinese space program and is scheduled for launch in early 2016. Both instruments feature a deep calorimeter to reach a total of 30 to 33 radiation lengths, in order to provide excellent energy resolution (better than 3% above 100 GeV) in the energy range 1 GeV–10 TeV.

On a longer time scale (2019 and beyond), two other experiments will probe the high energy γ–ray sky : *GAMMA–400* and *HERD*. The Gamma Astronomical Multifunctional Modular Apparatus (*GAMMA–400*)[4] is a Russian satellite observatory, planned for launch in 2019. The baseline design of this instrument covers the energy range from 100 MeV to 10 TeV and is optimized for best performance around 100 GeV with 25 radiation length calorimeter. The High Energy cosmic Radiation Detector (*HERD*)[5] is an observatory planned for deployment on board the future China space station. Design studies are still at an early stage of development, though the two primary science goals are already defined as the search for dark matter signal and the origin of Galactic cosmic rays. The Alpha Magnetic Spectrometer (*AMS-02*)[6] will be operative on ISS for more than 10 years, collecting a huge amount of data to answer fundamental questions such as origin of dark matter and composition of cosmic rays in multi-TeV region of energy.

7.5 References

[7.1] J. D. Finke et al., 2010, ApJ, 712, 238

[7.2] F. Acero et al., 2015, arXiv:1501.02003

[7.3] R. Mirzoyan, 2015, ATEL# 7416

[2] http://calet.phys.lsu.edu
[3] http://dpnc.unige.ch/dampe
[4] http://gamma400.lebedev.ru
[5] http://english.ihep.cas.cn
[6] http://www.ams02.org/

[7.4] R. Mukherjee, 2015, ATEL# 7433

[7.5] A. de Angelis et al., 2007, Phys. Rev. D, 76, 121301

[7.6] M. Meyer et al., 2013, Phys. Rev. D, 87, 035027

[7.7] P. P. Kronberg, 1994, Rep. Prog. Phys., 57, 325

[7.8] L. M. Widrow, Rev. Mod. Phys., 2002, 74, 775

[7.9] L. Costamante et al., 2001, A&A, 371, 512

[7.10] M. Doro et al., 2013, Astropart. Phys., 43, 189

[7.11] G. Amelino-Camelia et al., 1998, Nature, 393, 319

[7.12] A. K. Tickoo et al., 2014, Pramana J. Phys., 82, 585

[7.13] V. K. Dhar et al., 2013, NIM A, 708, 56

[7.14] M. Sharma et al., 2015, NIM A, 770, 42

[7.15] The CTA Consortium, 2011, Exp. Astron., 32, 193

[7.16] B. S. Acharya et al., 2013, Astropart. Phys., 43, 3

[7.17] J. Holder, 2014, arXiv:1407.1080